

MODELLING AND DEVELOPMENT OF  
SUB-NANOSECOND INERTIAL FUSION DIAGNOSTICS

Thesis submitted for the degree of Doctor of Philosophy at  
the University of Leicester

by

Michael Steven Rubery MPhys  
Department of Physics and Astronomy  
University of Leicester



**2015**

AWE PLC © Crown Owned Copyright

## Abstract

This thesis discusses the modelling and development of the Cherenkov detectors fielded at the National Ignition (NIF) and Omega facilities to measure observables important for improving understanding of inertial confinement fusion (ICF). It begins with an overview of ICF together with an introduction to the relevant laser facilities, theory and detectors.

The Geometry and Tracking Version 4 (GEANT4), Monte Carlo Neutron Program (MCNP) and ACCEPT Monte Carlo codes were benchmarked and then validated experimentally at the high-intensity  $\gamma$  source facility using two Cherenkov detectors. GEANT4 was subsequently used for calculations of temporal response and light production from the Cherenkov detectors; thus allowing GRH's  $\pm 50$  ps uncertainty to be achieved and improved measurements of the DT  $\gamma/n$  strength ( $4 \pm 2 \times 10^{-5}$ ) and DT  $\gamma$  spectral shape to be made. Building on this, the novel Prompt Areal Density Diagnostic (PADD1) was also designed to enable measurements of remaining shell at peak fusion reactivity.

Limitations of the existing Cherenkov detectors are then introduced, specifically the photomultiplier tube (PMT) which limits bandwidth to 88 ps. Following an investigation into alternative technologies, Chemical Vapour Deposition (CVD) diamond emerged as a possible dynode candidate due to high secondary electron emission ( $> 20$ ), significantly better than lead glass (1–3) used in micro-channel plate (MCP) PMTs. A CVD diamond transmission dynode  $< 100$  nm thick could be incorporated into a PMT analogous to an MCP. Despite diamond's potential there are parameters, such as boron doping, surface termination and crystallinity which impact yield and require optimisation through experiment and simulation. A study of secondary electron modelling theory and limitations was thus performed, and an approach utilising an experimentally-derived dielectric function incorporated into the GEANT4 toolkit. This low-energy extension combined with measurements of diamond's emission characteristics will be used in the future to facilitate diamond's integration into a PMT.

# Acknowledgements

Firstly I wish to thank the Plasma Physics Department at AWE and Leicester University for funding me to play with such expensive toys and to tinker with codes for the duration of my doctorate. In particular, Colin Horsfield, Jim Andrew and Jon Lapington for their mentorship, knowledge and patience.

I would also like to thank my overseas colleagues Hans Herrmann, Yongho Kim, Carl Young, Joseph Mack, Scott Evans, Maria Gatu-Johnson, Tom Sedillo, Nelson Hoffmann, Wolfgang Stoeffl and Elliot Grafil for their time and effort during experiments which have taken us to Omega (Rochester NY, USA), NIF (Livermore CA, USA), HI $\gamma$ S (Durham NC, USA) and many other exotic locations; HTPD Wildwood NJ 2010 stands out as a particularly rainy, windy, desolate and deserted conference venue. I would also like to thank the tireless support staff at these facilities for their effort, attention to detail and for staying that extra hour to let us take a second ‘last’ shot of the day.

I would also like to say a huge thank you to those situated near my desk at AWE; in particular Dave Chapman, Damon Swatton, Steven Gales, Alex Leatherland, Andrew Simons, Matt Hill, Pete Allan, Steve James, Colin Brown, Verity Woolhead and Mike Bunce who have provided invaluable technical and grammatical advice, motivation and occasional lowbrow-office banter over the past four years.

And to those who I love...my beautiful, clever and patient Fiancé Beth, for supporting me through stressful times, for becoming a Skype expert during my many overseas trips to the US and for making me smile every day. Finally thanks to my Mum and Dad for setting me on the path towards being a scientist and for letting me spend my student loan on less-prudent frothy investments.

# List of Publications

1. Monte Carlo validation experiments for the gas Cherenkov detectors at the National Ignition Facility and Omega, Review of Scientific Instruments, AIP, 2013, 84, 073504. Rubery M., Horsfield C., Herrmann H., Kim Y., Mack J., Young C., Evans S., Sedillo T., McEvoy A. and Caldwell S.

*This publication is primarily associated with Section 2.5 and describes the measurements and subsequent Monte Carlo code-validation experiments performed at the high-intensity- $\gamma$  source (HI $\gamma$ S) facility, Durham, North Carolina, USA. The modelling and data analysis effort were led by the author.*

2. GEANT4 simulations of Cherenkov reaction history diagnostics, Review of Scientific Instruments, 2010, 81, 10D328. Rubery M., Horsfield C., Herrmann H., Kim Y., Mack J., Young C., Caldwell S., Evans S., Sedillo T., McEvoy A., Miller E. K., Stoeffl W., Ali Z. and Toebbe J.

*This publication is primarily associated with Section 2.1. The paper describes the initial benchmarking of the GEANT4 toolkit against the Integrated Tiger Series codes previously used exclusively to support the Cherenkov detectors at NIF and Omega.*

3. Diagnosing inertial confinement fusion gamma ray physics, Review of Scientific Instruments, 2010, 81, 10D333. Herrmann, H. W., Hoffman N., Wilson D. C., Stoeffl W., Dauffy, L., Kim Y. H., McEvoy A., Young C. S., Mack J. M., Horsfield C. J., Rubery M., Miller E. K. and Ali Z. A.

*The author provided experimentally-validated system response calculations for a variety of diagnostic configurations. A novel method for reporting  $\langle\rho R\rangle_{abl}$  using the GRH diagnostic was presented using these parameters when combined with the predicted  $\gamma$  spectrum emitted from the inertial-fusion implosion.*

4. ICF gamma-ray reaction history diagnostics, Journal of Physics: Conference Series, 2010, 244, 032047. Herrmann H. W., Young C. S., Mack J. M., Kim Y. H., McEvoy A., Evans S., Sedillo T., Batha S., Schmitt, M. Wilson D. C., Langenbrunner J. R., Malone R., Kaufman M. I., Cox B. C., Frogget B., Miller E. K., Ali Z. A., Tunnell T. W., Stoeffl W., Horsfield C. J. and Rubery M.

*This work relates to Section 3.1. The author was involved in the experimental preparation and measurements associated with the GRH timing calibration at NIF. In addi-*

*tion post-shot simulations were performed to compliment the analysis routines which resulted from this campaign.*

5. Determination of the deuterium-tritium branching ratio based on inertial confinement fusion implosions, Phys. Rev. C, American Physical Society, 2012, 85, 061601. Kim Y., Mack J. M., Herrmann H. W., Young C. S., Hale G., M. Caldwell S., Hoffman N. M., Evans S. C., Sedillo T. J., McEvoy A., Langenbrunner J., Hsu H. H., Huff M. A., Batha S., Horsfield C. J., Rubery M. S., Garbett W. J., Stoeffl W., Grafil E., Bernstein L., Church J. A., Sayre D. B., Rosenberg M. J., Waugh C., Rinderknecht H. G., Gatu Johnson M., Zylstra A. B., Frenje J. A., Casey D. T., Petrasso R. D., Miller E. K., Glebov V., Stoeckl C. and Sangster T. C.

*This work relates to Section 2.5. The author supplied modelling support to allow well-constrained measurements of the DT neutron/ $\gamma$  emission branching ratio to be made.*

6. Measurement of areal density in the ablators of inertial-confinement-fusion capsules via detection of ablator (n, n' $\gamma$ ) gamma-ray emission, Physics of Plasmas, 2013, 20, 042705. Hoffman N. M., Herrmann H. W., Kim Y. H., Hsu H. H., Horsfield C. J., Rubery M. S., Miller E. K., Grafil E., Stoeffl W., and Church J. A.

*This work relates to Section 3.3.1. The author supplied modelling support and data analysis assistance to develop a novel technique for measuring direct-drive ICF  $\langle\rho R\rangle_{abl}$ .*

7. Development and characterization of sub-100 ps photomultiplier tubes, Review of Scientific Instruments, 2010, 81, 10D318. Horsfield C. J., Rubery M. S., Mack J. M., Young C. S., Herrmann H. W., Caldwell S. E., Evans, S. C., Sedillo T. J., Kim, Y. H., McEvoy A., Milnes J. S., Howorth J., Davis B., O'Gara P., M. Garza I., Miller E. K., Stoeffl W. and Ali Z.

*The author provided support in the development and testing of 10 mm diameter micro-channel-plate Photomultiplier Tubes discussed throughout this thesis.*

# Contents

<b>1</b>	<b>Introduction</b>	<b>28</b>
1.1	Inertial confinement fusion . . . . .	28
1.2	The National Ignition Facility (NIF) . . . . .	32
1.3	The Omega laser facility . . . . .	40
1.4	Nuclear Physics . . . . .	42
1.4.1	Reaction Cross section . . . . .	42
1.4.2	Reaction Q Value . . . . .	44
1.4.3	Threshold energy . . . . .	45
1.5	Important fusion reactions . . . . .	45
1.6	Reaction History and bang time . . . . .	48
1.7	Inertial Confinement Fusion (ICF) radiation . . . . .	49
1.7.1	Neutron time-of-flight detector (nToF) . . . . .	50
1.7.2	Neutron Total Yield Diagnostic(NTYD) . . . . .	51
1.7.3	Charged Particle Spectrometer (CPS) . . . . .	53
1.7.4	Wedge Range Filter (WRF) . . . . .	54
1.7.5	Magnetic Recoil Spectrometer (MRS) . . . . .	54
1.7.6	Full-aperture backscatter diagnostic (FABS) and Near backscatter Imaging (NBI) . . . . .	56
1.7.7	Velocity interferometer for any reflector (VISAR) . . . . .	58
1.7.8	DANTE . . . . .	58
1.7.9	Filter fluorescer X-ray detector (FFLEX) . . . . .	59
1.7.10	Gated X-ray Detector (GXD) . . . . .	60

1.7.11	Cherenkov detectors . . . . .	62
1.8	Summary . . . . .	65
<b>2</b>	<b>Monte Carlo Codes</b>	<b>66</b>
2.1	Geant4 . . . . .	66
2.2	ITS: ACCEPT . . . . .	70
2.3	MCNP . . . . .	70
2.4	Benchmarking . . . . .	71
2.5	Validation at the high intensity $\gamma$ source . . . . .	75
2.5.1	HI $\gamma$ S Results . . . . .	80
2.5.2	Idaho LINAC facility . . . . .	83
2.5.3	Conclusions and discussions . . . . .	84
<b>3</b>	<b>Geant4 Cherenkov detector studies</b>	<b>88</b>
3.1	Bang-time as a function of gas fill pressure . . . . .	88
3.2	Detector light responses . . . . .	98
3.3	Measuring direct drive remaining ablator areal density using the GCD2 at Omega . . . . .	106
3.3.1	Introduction . . . . .	106
3.3.2	Theoretical considerations . . . . .	108
3.3.3	Precursor calibration factor $\alpha$ . . . . .	111
3.3.4	Precursor proportional to areal density . . . . .	114
3.3.5	September 2013 Knudsen campaign . . . . .	116
3.3.6	The Prompt-Areal-Density Detector 1 (PADD1) . . . . .	126
3.3.7	Conclusions . . . . .	141
3.4	Super GCD design . . . . .	143
3.4.1	GEANT4 output to LightTools 8.0 . . . . .	145
3.4.2	Aspherical secondary mirror . . . . .	148
3.4.3	Additional super GCD shielding . . . . .	150
3.4.4	Light output responses . . . . .	157
3.5	Summary . . . . .	162

3.5.1	Requirements for improved optical detectors . . . . .	163
<b>4</b>	<b>Cherenkov light detection</b>	<b>165</b>
4.1	Requirements for Cherenkov detectors . . . . .	165
4.2	Review of detector technologies . . . . .	166
4.2.1	Micro-channel plate photomultipliers . . . . .	166
4.2.2	Vacuum Photodiodes . . . . .	167
4.2.3	Semi-conductor photodiodes . . . . .	169
4.3	An alternative high-speed technology . . . . .	170
4.3.1	Design considerations . . . . .	171
4.3.2	Operational modes . . . . .	172
4.3.3	Experimental characterisation . . . . .	176
4.4	Summary . . . . .	179
<b>5</b>	<b>Diamond detector modelling using GEANT4</b>	<b>181</b>
5.1	Existing SEE models . . . . .	181
5.1.1	Dionne approximation . . . . .	181
5.1.2	Shih update to Dionne . . . . .	185
5.1.3	Dvorkin Model . . . . .	186
5.2	Electron transport considerations . . . . .	188
5.2.1	Secondary electron emission in diamond simulation (SEEDS)	189
5.3	GEANT4 adaptations for secondary emission process . . . . .	195
5.4	Geant4 diamond model . . . . .	196
5.4.1	Elastic scattering . . . . .	196
5.4.2	Inelastic scattering . . . . .	199
5.4.3	Energy-loss probability distribution . . . . .	203
5.4.4	Geometry and physics implementation . . . . .	205
5.5	Results and discussions . . . . .	209
5.5.1	Relation to incident primary angle . . . . .	209
5.5.2	SEE yield curve . . . . .	210
5.5.3	Secondary energy distribution . . . . .	214

5.6 Summary . . . . .	216
<b>6 Summary</b>	<b>218</b>
<b>Appendices</b>	<b>222</b>
<b>A Cherenkov Detector Gas Parameters</b>	<b>223</b>
<b>B Lindhard Dielectric Function</b>	<b>230</b>
<b>C Euler rotations</b>	<b>234</b>

# List of Tables

1.1	Table showing the fusion reactions pertinent to inertial confinement fusion experiments together with reaction $Q$ values, and cross sections at 10 and 100 keV where available. . . . .	46
3.1	Comparison between GEANT4, MCNP and an analytical calculation for the prominent n,n' $\gamma$ lines in carbon and oxygen. . . . .	110

# List of Figures

1.1	Direct-drive (a) and indirect drive (b) laser fusion approaches. . . .	29
1.2	Plot showing measured fuel $\rho R$ values at the Omega laser facility using the multi-picket with laser foot adiabatic shaping technique compared with predictions from the 1-dimensional LILAC code. The different laser profiles are included as inserts. . . . .	32
1.3	Schematic overview of the NIF laser system. . . . .	34
1.4	National Ignition Campaign (NIC) point design capsule in cross section form. The actual capsule is spherical with a 10 atm DT gas fill, followed by 68 $\mu\text{m}$ thick ice layer and then several layers of doped and undoped plastic. . . . .	35
1.5	Plot showing the four shock laser profile used on NIF at the commencement of the national ignition campaign together with the 3-shock high-foot laser profile. . . . .	35
1.6	Diagram of the NIC point design hohlraum. Twenty-four quads enter the hohlraum through a laser entrance hole in four groups: four at 23.5°, four at 30°, eight at 44.5°, and eight at 50°. The beams strike the gold wall and convert to X-rays which are used to implode the capsule. A low-Z gas (generally helium) fills the hohlraum to reduce the expansion of the wall over time. . . . .	37
1.7	Plot showing the reported radiated energy from the NIF laser for each shot fired during the NIC and high-foot campaigns. The blue and red fractions represent the contribution to the radiated energy from laser compression and alpha heating respectively. . . . .	38

1.8	Phase space plot of neutron yield against $\langle \rho R \rangle_{fuel}$ with alpha heating contours. The blue and green points represent experimental data from the NIC and high-foot campaigns respectively. . . . .	39
1.9	Diagram of the Omega laser large-aperture ring amplifier system consisting of $2\times$ rod amplifiers (two passes), $2\times$ disk amplifiers and a frequency conversion crystal. . . . .	41
1.10	Figure showing the binding energy per nucleon as a function of nuclear mass number $A$ . Fusion and fission are nuclear reactions resulting in higher binding energy; the former via the joining of two less stable isotopes to form a larger more stable nucleus, and the latter via the splitting of a single unstable heavy element into two more stable isotopes. The most stable element in the periodic table is $^{56}\text{Fe}$ .	43
1.11	Plot showing fusion cross sections of interest to the ICF community. The DD curve is the integral cross section for all three reactions listed in Table 1.1. . . . .	47
1.12	Reaction history of an igniting NIF capsule together with two failing implosions, simulated by D. Wilson (LANL). . . . .	50
1.13	Schematic of the neutron time-of-flight detector fielded at the Omega facility; the NIF variants, of which there are many, are similar in design with different scintillator and shielding configurations. . . . .	51
1.14	Schematic of the wedge range filter proton spectrometer. The spectrometer consists of a wedge-shaped filter with thickness varying along its length combined with a slab of CR-39. A small number of the incident protons have enough energy to pass through the wedge and cause localised damage sites. After etching into the front surface using sodium hydroxide each track is observable as a small hole with diameter proportional to the original proton energy. The proton energy distribution can be calculated by scanning the CR39, histogramming the tracks along the wedge axis and removing the stopping induced by the wedge thickness. . . . .	55

1.15	Schematic of the MRS detector fielded at the NIF facility. . . . .	56
1.16	Schematic of the NIF FABS and NBI configuration. . . . .	57
1.17	Diagram of the FFLEX diagnostic at NIF. The hard X-ray spectrum in the range 18-150 keV emitted during a laser-plasma interaction is recorded using 8 narrow-band channels consisting of a pre-filter, fluorescer, post-filter and photomultiplier system. . . . .	60
1.18	Photo of the GXD outside and inside the airbox; above and below respectively. . . . .	61
1.19	Not-to-scale schematic of the Gamma Reaction History (GRH) di- agnostic fielded at NIF and Omega. At NIF the diagnostic is lo- cated external to the vacuum chamber at approximately 6m from TCC. 3 mm of tungsten is placed in the nose to filter out X-rays from the implosion hot spot and laser-plasma interaction, followed by a 1 cm thick low-Z Compton conversion region to generate the high-energy electrons required to produce Cherenkov light. Three off-axis parabolic mirrors and a flat mirror are used to direct the Cherenkov light around four corners to the PMT. The optical relay was designed by Robert Malone (LANL) to produce identical path lengths for an ideal Cherenkov source placed immediately behind the converter. The second region of the diagnostic behind the pres- sure window is at air to accommodate the PMT. The routing has been designed to allow significant amounts of tungsten shielding to be placed between the laser plasma interaction and the PMT to in- crease signal-to-noise ratio. The detector can handle gas pressures of up to 215 psia CO <sub>2</sub> or SF <sub>6</sub> . . . . .	63

1.20	Not-to-scale schematic of the Gas Cherenkov Detector 1 (GCD 1) fielded at Omega inside a ten-inch manipulator (TIM). In this variant the PMT is placed immediately behind the pressure window inside an annulus of tungsten shielding (blue). The spherical primary and flat secondary mirrors focus the optical Cherenkov light onto a 12 mm disc at the photocathode. The large tungsten block removes the majority of high-energy $\gamma$ photons from directly interacting with the PMT. As with GRH there are a few millimetres of high-Z material in the nose to remove low energy X-rays followed by a 1 cm thick low-Z Compton conversion region. . . . .	64
1.21	Not-to-scale schematic of the Gas Cherenkov Detector 2 (GCD 2) fielded at Omega inside a ten-inch manipulator (TIM). In this version the PMT is located behind the gas cell inside a separate housing. This was initially conceived such that the parallel light from the detector could be routed to a streak camera away from the high-background environment of the target hall. The spherical primary and secondary mirrors produce a parallel light profile which is subsequently focused by an optic a short distance in front of the PMT. The large tungsten block removes the majority of high-energy $\gamma$ photons from directly interacting with the PMT. As with GRH there are a few millimetres of high-Z material in the nose to remove low energy X-rays followed by a 1 cm thick low-Z Compton conversion region. . . . .	64
2.1	Diagram of the test problem devised by J. Mack [LANL] used to compare the $\gamma$ Compton scattering and pair production processes and electron tracking algorithms. . . . .	73
2.2	Plot showing the energy-dependent (angle-integrated) results from the test case devised by J. Mack [LANL] described in Figure 2.1. GEANT4 and ACCEPT are shown in broken red and blue respectively.	74

2.3	Plot showing the angle-dependent (energy-integrated) results from the test case devised by J. Mack [LANL] described in Figure 2.1. GEANT4 and ACCEPT are shown in broken red and blue respectively.	74
2.4	Schematic of HI $\gamma$ S experimental configuration.	76
2.5	Photo of the HI $\gamma$ S NaI(tl) array used as the flux benchmark for cross-calibration with the plastic paddle detectors.	77
2.6	Plot showing the paddle intensity as recorded by the automated HI $\gamma$ S system and a manual record kept by A. McEvoy [LANL] during the $E_\gamma=16.86$ MeV, 65 psia CO <sub>2</sub> GRH translational measurement. The data shows the large fluctuations seen in the HI $\gamma$ S intensity over the course of a few hours.	78
2.7	Plot showing the PMT110-001 quantum efficiency folded with the general $1/\lambda^2$ Cherenkov emission spectrum. Comparing the area before and after folding yields a Cherenkov distribution-weighted QE of 17.5%. The QE data provided by Photek Ltd were interpolated to a regular abscissa before folding.	79
2.8	Plot showing several LED test can measurements of the peak height [mV] and area [nVs] for the PMT210-009 used in the GRH detector throughout the two-week campaign.	81
2.9	Plot showing an example of the two-part linear approximation to the PMT degradation used during the $E_\gamma=16.86$ MeV, 65 psia CO <sub>2</sub> GRH translational measurement.	82
2.10	Plot showing a comparison between experiment and GRH simulation for a 4.4 MeV $\gamma$ beam and a range of SF <sub>6</sub> gas-cell pressures.	83
2.11	Plot comparing the results of translating the HI $\gamma$ S beam across the GRH diagnostic with simulations. The beam energy was 4.4 MeV, and the gas and pressure were SF <sub>6</sub> and 200 psia respectively.	84
2.12	Plot showing the translation of the HI $\gamma$ S beam across the GRH diagnostic compared with simulations. The beam energy was 16.86 MeV, and the gas and pressure were CO <sub>2</sub> and 65 psia respectively.	85

2.13	Plot showing the intensity recorded by GCD during a 16.86 MeV HI $\gamma$ S pressure scan measurement compared with simulation between 10 and 100 psia. . . . .	86
2.14	Plot showing a comparison between the GCD and data obtained during the 2001 Idaho LINAC experiment. The electron source energy was varied between 8 and 18 MeV whilst holding the gas-cell pressure constant at 30 psia. Scaling factors have been applied to the simulations for illustrative purposes. PMT response parameters were not accurately known at this time making absolute comparisons difficult. The gradient however is a useful tool for validating the codes. . . .	86
3.1	Overview of the BT $\gamma$ measurement technique where two separate experiments are carried out. The first is a standard cryogenic DT ICF implosion and the second a silver ball target producing a fast-rising X-ray signal to clearly define the laser-interaction time. The optical timing fiducial is common to both recorded traces allowing the signals to be cross-timed with high precision. . . . .	90
3.2	GEANT4 linear approximation to the BC422 scintillator relative light yield compared with the published data sheet from Saint-Gobain Crystals. . . . .	91
3.3	GRH scintillation signals for $\tau_{RR}$ values of 0.5 ps, 8 ps, and 16 ps calculated using the GEANT4 model. . . . .	93
3.4	Plot showing FFLEX measured X-ray data from NIF (green triangles), exponential fit (broken red) and the temperature approximation used in the GEANT4 model (solid blue). . . . .	94
3.5	Plot showing a comparison between the 3:1 Hale spectrum calculated by C. Horsfield (AWE) and the source spectrum generated for the GEANT4 model in 0.25 MeV bins (the actual source term is at higher resolution than this spectrum sampled from the GCD1 nose cone). .	95

3.6	Plot showing temporal impulse responses of the gamma reaction history (GRH) diagnostic for a range of gas fill pressures. Also plotted is the temporal response of the GRH when configured to include a scintillator instead of a Compton converter. . . . .	96
3.7	Plot showing the temporal response peak location relative to the 30 psia peak as a function of gas fill pressure. This is the required scaling correction for the $BT_\gamma$ when changing GRH gas fill pressure. . . . .	97
3.8	Plot showing the FWHM of each impulse response as a function of gas fill pressure together with a linear least-squares fit. . . . .	98
3.9	Plot showing the $Y_{Ch}$ histogram produced by the GRH GEANT4 model for several $SF_6$ pressures and $E_\gamma$ values. The generated distribution shows a stronger dependence on $E_\gamma$ compared with gas pressure. The $\gamma$ source used to generate this spectrum was the parallel disc source used during the HI $\gamma$ S validation work described in section 2.5 . . . . .	100
3.10	Plot showing the laser-plasma interaction background measured at NIF by the GRH normalised to total laser energy with and without Pb shielding shadowing the sapphire pressure window. The shielding clearly reduces the background signal suggesting that a large proportion of the background originates from the sapphire window. . . . .	103
3.11	3D surface plot showing interpolated light response of the GRH detector when fielded at NIF as a function of two independent axes: pressure in psia and $\gamma$ energy $E_\gamma$ . Light response is defined as the number of Cherenkov photons recorded at the photocathode per source $\gamma$ . Generated using data from GEANT4 simulations and the IDL surface-fitting routine. . . . .	103

3.12	3D surface plot showing interpolated $e^-/\gamma$ statistics for the GRH detector when fielded at NIF as a function of two independent axes: pressure in psia and $\gamma$ energy $E_\gamma$ . $e^-/\gamma$ is the number of electrons leading to the detection of at least one Cherenkov photon at the photocathode, per incident $\gamma$ . Generated using data from GEANT4 simulations and the IDL surface-fitting routine. . . . .	104
3.13	3D surface plot showing interpolated Ch. photons/ $e^-$ statistics for the GRH detector when fielded at NIF as a function of two independent axes: pressure in psia and $\gamma$ energy $E_\gamma$ . Ch. photons/ $e^-$ is the mean number of Cherenkov photons recorded by the photocathode per productive electron. Generated using data from GEANT4 simulations and the IDL surface-fitting routine. . . . .	104
3.14	Plot showing the neutron-induced gamma spectrum from plastic and glass capsules calculated by GEANT4 and MCNP as discussed in Section 3.3.2. . . . .	109
3.15	Fraction of gammas emitted from the DT reaction and from carbon compared to the total. Beyond $\langle\rho R\rangle_{abl} = 4\text{mg}/\text{cm}^2$ inelastic carbon 4.44 MeV gammas become the dominant source. . . . .	111
3.16	Plot showing a 100 psia $\text{CO}_2$ shot recorded by the GCD1 diagnostic (broken black) at Omega with inferred areal density of $33\text{ mg}/\text{cm}^2$ . Also shown are the $33\text{ mg}/\text{cm}^2$ GEANT4 simulation; energy depositions are shown in broken red, optical photons in continuous blue and the combined result using the precursor model is shown in broken grey.	112
3.17	Plots showing precursor integral divided by the DT Cherenkov peak as a function of $\langle\rho R\rangle_{abl}$ with $\pm 1 \times \sigma$ uncertainty calculated for a neutron yield of $1 \times 10^{13}$ ; left plot shows the relation and statistical dependence with the tungsten central block removed and on the right as designed. The gas parameters for simulation and experiment were 100 psia $\text{CO}_2$ . . . . .	116

3.18	Plot showing the relative $\pm 1 \times \sigma$ in the precursor divided by DT Cherenkov peak as a function of yield, for several $\langle \rho R \rangle_{abl}$ values. . .	117
3.19	Plot showing the raw signal recorded by GCD2 for shot RID 70860 (shot 9 day 1) on the 4 <sup>th</sup> September 2013 during the Knudsen campaign at Omega. . . . .	118
3.20	Plot showing the analysed signal recorded by GCD2 for shot RID 70860 (shot 9 day 1) on the 4 <sup>th</sup> September 2013 during the Knudsen campaign at Omega. The raw signal is shown in solid black, Gaussian fit to the precursor signal above the 50 % point is shown in broken red, Gaussian fit to the rising background signal is shown in broken green and the raw GCD2 output after background subtraction is shown in broken blue. . . . .	119
3.21	Plot showing a comparison between the charged particle spectrometer, wedge range filter and GCD2 with $\chi/\sqrt{N} = 1.5$ . The CPS and WRF results were combined into a single result using an error-weighted algorithm by M. Gatu-Johnson (MIT). Left side comparison removes the two $R_i = 20 \mu\text{m}$ possible outliers (red) recorded by the charged particle detectors from the analysis; the right hand side comparison includes the possible outliers. . . . .	121
3.22	Plot showing a comparison between the GCD2 and GRH with $\chi/\sqrt{N} = 1.2$ . The same least-squares approach used in the GCD2 analysis has been performed for the GRH data. . . . .	121
3.23	Plot showing the X-ray emission from a $20 \mu\text{m}$ thick ablator D <sup>3</sup> He implosion. . . . .	122
3.24	Figure showing $\langle \rho R \rangle_{abl}$ measured by GCD2 (red triangles) together with initial shell thickness (blue diamonds) plotted against ion temperature. . . . .	123
3.25	Figure showing cross-calibrated GCD2 bang-times compared to values from the neutron temporal diagnostic. . . . .	124

3.26	Plot (left) showing $\langle \rho R \rangle_{abl}$ values cross-calibrated from the charged particle diagnostics during the September 2013 Knudsen campaign at the Omega laser facility. The right hand side data are error-weighted averages of the charged particle detector measurements. The independent axis is the initial capsule shell thickness measured prior to experiments. The various colour markers represent different fuel fill pressures in atmospheres. . . . .	124
3.27	Plot showing $\langle \rho R \rangle_{abl}$ values cross-calibrated from the charged particle results during the September 2013 Knudsen campaign at the Omega laser facility. Data on the right are error-weighted averages of the charged particle detector measurements. The independent axis in this case is the initial fuel fill pressure extrapolated from measurements taken during fabrication. The varying data markers represent the different initial shell thicknesses $R_i$ measured prior to the campaign.	125
3.28	Plot showing error-weighted average $\langle \rho R \rangle_{abl}$ values from the GCD2 diagnostic (circles) and the charged particle diagnostics (squares), plotted as a function of initial capsule fill pressure. Each error weighted data point comprises several measurements made with similar capsule conditions; varying colours correspond to different initial shell thicknesses. . . . .	125
3.29	Not-to-scale schematic of the novel $\langle \rho R \rangle_{abl}$ diagnostic. The essential components are the tungsten shielding to remove low-energy X-rays from LPI and hot spot, glass Cherenkov radiator to produce an optical signal proportional in intensity to the original gamma signal and a photomultiplier tube to amplify the optical signal. . . . .	127
3.30	FreeCad rendering of the PADD1 detector designed and fabricated in a joint collaboration between AWE and LLE. . . . .	128
3.31	Photo of the PADD1 comprising the mounting plate and the external housing. The internal PMT-glass housing, tungsten shield plate and port cover are removed. . . . .	129

3.32	Photo of the PADD1 5 cm thick glass and PMT110 coupled together as they are inside the housing. The outer surface of the glass is opaque as the machining grooves are still present at the request of the author. . . . .	129
3.33	Photo of the PADD1 5 cm glass and PMT de-coupled to allow observation of the input window conical protrusion used to couple the Cherenkov light to the PMT input window. . . . .	130
3.34	PADD1 1 mm thick 99 mm diameter 99.997 % pure tungsten filters (8 in total). The housing has room for an additional 2 filters however Goodfellow did not have the entire set in stock prior to the preliminary fielding, and the full compliment were not necessary for the August 2014 experiments. . . . .	130
3.35	GEANT4 predictions of the signal response of the PADD1 detector split into contributions from the DT gamma spectrum and inelastic gammas from neutron interactions with carbon in the capsule ablator, normalised for a yield of $1 \times 10^{13}$ . . . . .	132
3.36	GEANT4 predictions of the absolute timing of the GCD1 Cherenkov optical signal relative to PADD1. . . . .	133
3.37	Plot showing PADD1 data from F. Merrill's and C. Sangster's asymmetric drive (red and black solid) and cryogenic implosion (green solid) shot days respectively. . . . .	134
3.38	Plot showing the GCD2 $\langle \rho R \rangle_{abl}$ values against those reported by the novel PADD1 detector recorded during F. Merrill's asymmetric implosion shot day in August 2014. . . . .	136
3.39	Plot showing the PADD1 signals recorded during A. Zylstra's astrophysics campaign. All traces have been time-aligned such that the nuclear gamma arrival time appears at 22.75 ns for clarity. . . . .	139

3.40	Photo of the PADD1 detector with the full compliment of lead tape after A. Zylstra’s astrophysics campaign. The black tape was used to ensure the housing was light tight subsequent to the PMT change on F. Merrill’s shot day. . . . .	140
3.41	Cutaway view from the engineering CAD models of super GCD and GCD1 created using the SolidWorks eDrawings viewer. MOP stands for Maximum Operating Pressure. . . . .	143
3.42	Image produced by LightTools showing the starting locations (blue from GEANT4) in super GCD for a gas pressure of 220 psia in SF <sub>6</sub> . . . . .	146
3.43	Image produced by LightTools showing the starting locations (blue from GEANT4) in GCD1 for a gas pressure of 100 psia in CO <sub>2</sub> . . . . .	146
3.44	Temporal response of super GCD for 100 and 400 psia C <sub>2</sub> F <sub>6</sub> in red and black respectively. Broken lines correspond to the response with the aspherical mirror replaced with a flat mirror. The aspherical mirror offers slightly better light collection efficiency due to the collection of additional late-time paths. . . . .	147
3.45	Isometric view of the super GCD aspherical mirror produced by the visualisation software HepRApp. The blue rings consist of 49 cut cone volumes in GEANT4 with each edge approximating the curve shown on the right. . . . .	150
3.46	Plot showing the final aspherical mirror curvature optimised using the GEANT4 to LightTools technique. The aspherical coefficients are $C = -5.5381 \times 10^{-4}$ , $A = 1.522 \times 10^{-7}$ , $B = 3.790 \times 10^{-11}$ and $k = 0$ . . . . .	151
3.47	Plot showing the super GCD temporal response for several different annulus thicknesses at a CO <sub>2</sub> gas pressure of 30 psia. Raw GEANT4 data has been post-processed using the precursor model described in Section 3.3.3 and convolved with the impulse response function of a single stage Photek PMT (see Figure 4.3). . . . .	152

3.48	Plot showing the reduction in the precursor area as a function of annulus thickness. The plot shows that a 2 cm annulus drops the integral signal by > 20 %. The annulus does however reduce the signal more at later time therefore the improvement at the rising edge of the DT signal is better than 20 %.	152
3.49	Side view of the super GCD model from LightTools. Blue dots represent the Cherenkov birth locations predicted by the GEANT4 model and the red lines are the light rays with initial momentum vector also from the GEANT4 model.	153
3.50	Isometric view of the super GCD model from LightTools clearly showing the position and impact of the annulus. Blue dots represent the Cherenkov birth locations predicted by the GEANT4 model.	153
3.51	Plot highlighting the evolving precursor for several different shielding configurations with and without the aspherical mirror at a CO <sub>2</sub> gas pressure of 100 psia. Raw GEANT4 data has been post-processed using the precursor model described in Section 3.3.3 and convolved with the impulse response function of a single stage Photek PMT (see Figure 4.3). For comparison the GCD1 signal has been plotted in continuous grey.	154
3.52	Plot highlighting the evolving precursor for several different shielding configurations with and without the aspherical mirror at a CO <sub>2</sub> gas pressure of 100 psia. The plot is the same data as Figure 3.51 with the dependent axis expanded. Raw GEANT4 data has been post-processed using the precursor model described in Section 3.3.3 and convolved with the impulse response function of a single stage Photek PMT (see Figure 4.3). For comparison the GCD1 signal has been plotted in continuous grey.	155

3.53	Plot highlighting the evolving precursor for several different shielding configurations with and without the aspherical mirror at a CO <sub>2</sub> gas pressure of 30 psia. Raw GEANT4 data has been post-processed using the precursor model described in Section 3.3.3 and convolved with the impulse response function of a single stage Photek PMT (see Figure 4.3). For comparison the GCD1 signal has been plotted in continuous grey. . . . .	156
3.54	Super GCD light responses for several different gas pressures plotted as a function of incident $\gamma$ energy. Also plotted (broken lines) are the same response calculations performed for GCD1. . . . .	159
3.55	Super GCD light responses for several different gas pressures plotted as a function of incident $\gamma$ energy. Also plotted (broken lines) are the same response calculations performed for GCD1. Between the GEANT4 model and LightTools model there is a slight difference in predicted intensity observed by the PMT (likely related to the GEANT4 aspherical mirror implementation). This plot shows the super GCD responses from Figure 3.54 normalised to the LightTools values. . . . .	160
3.56	Figure showing a histogram of the Cherenkov birth locations for super GCD for several different gas types and pressures with and without the tungsten annulus in place. Also included is the histogram for a single line at 5.5 MeV. . . . .	161
3.57	Figure showing a comparison between histogrammed Cherenkov birth locations super GCD (red) and GCD1 (blue) at a CO <sub>2</sub> gas pressure of 100 psia. . . . .	161
4.1	Plot showing the radiant sensitivity in mA/W for a range of photocathode materials. . . . .	167
4.2	Diagram showing the layout and methodology of a MCP-based (two-stage in this diagram) photomultiplier tube (not to scale). . . . .	168

4.3	Unit response function (URF) of a single-stage MCP-based PMT with a FWHM of 123 ps. The URF in this case includes the 50' cableset used at the Omega laser facility. The coaxial line adds a small amount of broadening to the signal; this particular plot has been shown to highlight the general bandwidth of the system in this configuration. The actual minimum FWHM of the PMT by itself has been measured at approximately 88 ps. . . . .	169
4.4	Schematic diagram of a reflection dynode configuration. Each successive dynode stage is biased progressively more positive than previous stages, drawing any secondary electrons through the system. The accelerating voltage is high enough for the secondary electrons to cause further amplification at the next stage. . . . .	173
4.5	Schematic diagram of a transmission dynode configuration. The primary photoelectron is given sufficient energy to penetrate deep into the dynode material producing a large secondary population near the back surface. At the correct thickness and surface conditions the low energy secondaries can leak out of the surface where they can be accelerated towards the anode or into an additional dynode stage. .	175
4.6	Schematic diagram of a Venetian blind dynode configuration. Each layer is angled opposite to the previous to allow a route through the amplification stage. The layers must be packed close enough to remove the direct line of sight. This geometry can be thought of as a 2-dimensional micro-channel plate. . . . .	176
4.7	Schematic overview of the SEE characterisation equipment at Leicester University, used to measure the secondary electron emission properties of different dynode materials. . . . .	177

4.8	Photo of the equipment at Leicester University showing all the various components associated with the secondary electron emission measurement. Sub-image a) shows the exterior of the vacuum system, electrometers and vacuum monitoring sensors, b) shows the bespoke C++ software written by V. Taillandier (Leicester University) and PC, together with the electron gun controller unit. Sub-image c) shows the inside of the open vacuum chamber, Large Faraday Cup (LFC), target mounting holder and the associated manipulation arm and cabling. . . . .	178
5.1	Dionne reduced yield curves plotted as a function of multiples of the maximum primary energy. Solid/dotted lines are Dionne models and the filled region contains data from experiments. . . . .	185
5.2	SEE emission as a function of primary electron energy for a molybdenum sample. Higher yields are observed at larger angles relative to the normal. . . . .	186
5.3	Dvorkin's stopping points model(a) for energies of 10 keV (a), 20 keV (b) and 30 keV (c) and yield calculation for a reflection configuration(b). . . . .	188
5.4	Stopping function computed using the Lindhard dielectric function, from RPA theory. A four component polynomial fit was produced to parameterise the shape for use in the SEEDS code. . . . .	192
5.5	Energy loss relation and cumulative secondary electron emission predicted by the SEEDS model plotted as a function of depth, shown in broken black and red respectively. The SEEDS step resolution was 0.01 nm. . . . .	193
5.6	SEE for the reflection and transmission configurations, in blue and red respectively. The transmission simulation was performed for a 1 $\mu\text{m}$ thick diamond membrane. . . . .	194
5.7	Muffin tin potential for diamond obtained from Painter et al. in 1971.	198

5.8	Figures (a) and (b) show the differential elastic cross section in contour form. At low energy the elastic scattering is almost isotropic, however as the primary electron energy increases elastic scattering becomes forward lobed. . . . .	198
5.9	Elastic, inelastic and phonon cross sections calculated from this work compared with the inelastic cross section from Dimitrov et al. . . .	199
5.10	Plot of the diamond ELF in the $q = 0$ limit from Dimitrov et al. . .	200
5.11	Calculated inelastic mean free paths (IMFP) for diamond from this work, Ziaja et al., Ashley et al., and Tanuma et al. . . . .	202
5.12	Optical phonon scattering cross section obtained from Dimitrov's scattering rate data. . . . .	202
5.13	Probability distribution calculated for a 1 keV electron using equation 5.31 compared with the analytical result reported by Dimitrov.	204
5.14	Plot showing the SEE ( $\delta$ ) curve for moderately doped diamond at several incident electron angles predicted by the GEANT4 model; the second plot shows measured SEE data by Shih and Hor for a molybdenum sample. Note the surface coefficient for hydrogen-terminated diamond of 0.4 has not been applied to the GEANT4 data as the comparison is between two different materials and investigates the trend with angle not the absolute secondary yields. . . . .	210
5.15	Visualisation of a 500 eV electron from the Geant4 model. The visualisation tool used was HepRApp. . . . .	212
5.16	Comparison of the GEANT4 model (single crystal moderately boron doped diamond) with SEE measurements from Leicester University (polycrystalline, moderately boron doped and hydrogen terminated diamond) and Shih et al (hydrogen terminated and moderately boron doped diamond). The SEEDS code discussed in Section 5.2.1 is shown in broken green for comparison. . . . .	212

5.17	Plot showing the individual scattering totals for each process from the Geant4 model as a function of primary electron energy. The mean ionisation in eV (black) has also been included on the secondary axis.	213
5.18	Plot showing the secondary electron energy distribution for moderately doped diamond predicted by the GEANT4 model at several different primary energies $E_p$ . In addition the secondary electron distribution measured by Shih et al has been plotted for comparison. The differences highlight the need for a surface model treatment in the GEANT4 model. . . . .	214
5.19	Plot showing the fraction of primaries backscattered from the diamond as a function of primary energy $E_p$ predicted by the GEANT4 model. Simulation suggests that the backscatter fraction reduces to less than 5 % at energies below 100 eV. . . . .	215
A.1	Plot showing density scaling with respect to gas pressure for a temperature of 293.71 K, the NIF target hall nominal temperature. . .	224
A.2	Plot of the refractive index of SF <sub>6</sub> and C <sub>2</sub> F <sub>6</sub> (left) and CO <sub>2</sub> (right) at 1 atm. The Sellmeier fit for SF <sub>6</sub> was formed using a least-squares approximation to three separate experimental datasets. . . . .	225
A.3	Plot showing gamma energy threshold as a function of gas pressure.	227
A.4	Plot showing the transmission and reflection spectra used in the models of GRH and GCD 1. Dotted lines represent pressure window transmissions and solid lines mirror reflectances. . . . .	229
C.1	Diagram illustrating the primary electron and laboratory reference frames together with the 2D and 3D stages in the calculation of the scattered primary vector $V'(x', y', z')$ . . . . .	235
C.2	Diagram outlining the two steps involved with transforming the scattered primary electron vector $V'(x', y', z')$ from the primary electron frame to $V(x, y, z)$ in the laboratory frame . . . . .	236

# Chapter 1

## Introduction

### 1.1 Inertial confinement fusion

Inertial confinement fusion (ICF) is the implosion of a small plastic or glass capsule filled with low- $Z$  fuel at approximately  $5 \times 10^{-4}$  g/cm<sup>3</sup>, generally deuterium and tritium, using lasers [1]. The resulting high-temperature, density and pressure conditions generated in the imploded core are inertially confined for long enough to allow fusion reactions to occur. The National Ignition Facility (NIF) at Lawrence Livermore National Laboratory and Omega laser facility at the Laboratory for Laser Energetics both routinely conduct ICF experiments using 1.8 MJ 500 TW and 40 KJ 351 nm flashlamp-pumped neodymium-glass laser systems respectively. ICF is generally achieved through two different approaches: direct or indirect drive as shown in Figure 1.1 [2]. The former involves the laser beams interacting with the surface of the capsule and the latter the inner walls of a gold hohlraum containing the capsule; X-rays from the hot gold surface then drive the implosion. Investigations and computer modelling constrain the hohlraum dimensions to approximately 5-6 mm diameter 10 mm length cylinder with a 3 mm diameter laser entry hole [3]. Of critical importance is the requirement of a low- $Z$  gas inside the hohlraum to impede the expansion of the hohlraum wall during laser heating. Using a higher- $Z$  gas would generate energetic X-rays leading to capsule preheating and reduced

implosion quality. During the laser pulse the hohlraum gas turns to plasma; the creation of plasma waves represents a significant scattering source and must be minimised [4]. Direct and indirect drive ICF have pros and cons. Direct drive interactions are single-stage and therefore produce higher coupling efficiencies. However, Rayleigh-Taylor instability (RTI) [5] and asymmetry constraints limit the maximum achievable compression. Conversely during indirect drive 80 % of the laser light is converted to X-rays with the remainder deforming the walls of the hohlraum [6]. Only 12% of the generated X-rays deposit energy into the capsule ablator due to re-absorption in the hohlraum walls and losses from the laser-entry holes (LEH). The uniformity of the X-ray drive and subsequent implosion symmetry however are improved compared with the direct approach [7] [2].

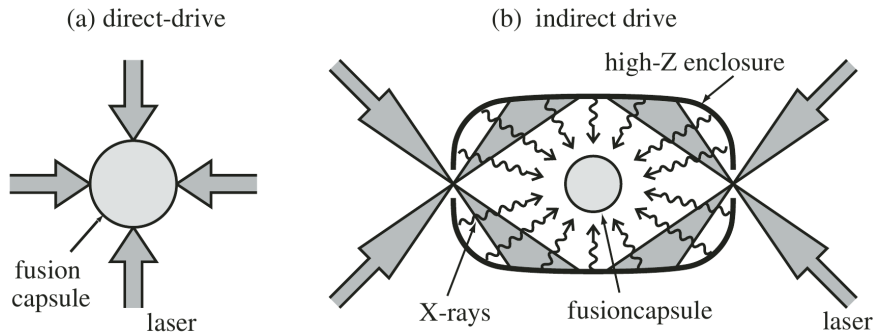


Figure 1.1: Direct-drive (a) and indirect drive (b) laser fusion approaches [2].

Current facilities can generate fuel pressures greater than 1 gigabar at temperatures of approximately  $10^8$  K during ICF experiments. The Lawson criterion for ignition [8] of  $P\tau = 10$  atm-s at  $10^8$  K implies the plasma be confined for  $< 1$  ns. During cryogenic ICF experiments at NIF a thin layer of  $0.25$  g/cm<sup>3</sup> ice near the triple point of DT at 18 K is formed on the inner surface of the plastic / beryllium / high-density carbon ablator leading to fuel areal densities  $\langle \rho R \rangle_{fuel}$  of 1-3 g/cm<sup>2</sup> or 1000 g/cm<sup>3</sup>, theoretically higher than achievable with a room-temperature gas fill.

To achieve a fuel density of 1000 g/cm<sup>3</sup> the laser profile is tuned to shock the capsule 4 times where each shock pressure  $P_n = 4 \times P_{n-1}$  and all are timed to

coalesce at the rear surface of the ablator at peak compression; the  $\times 4$  increase in pressure between stages allows maximum input of energy to the capsule whilst increasing density by the correct amount to minimise the change in entropy  $\Delta S$  between shocks. The total pressure applied across the laser profile is 100 Mbar producing a final shell implosion velocity of  $350 \text{ km s}^{-1}$ . As the shell implodes the DT gas and cryogenic layer are compressed by the in-falling ablator and heated to  $10^8 \text{ K}$ , high enough for fusion reactions to occur. The energy released during each  $\text{D(T,n)}^4\text{He}$  reaction is 17.6 MeV the majority of which is carried by a 14.1 MeV neutron. The alpha particle however is emitted with 3.5 MeV which quickly deposits this energy via electron ionisation within a few microns of its generation causing local heating of the fuel and consequently further fusion reactions. In an energy-generating facility lithium would be used around the target chamber to thermalise the fusion energy via neutron scattering for conventional conversion to electrical energy. In addition the reactions  $^6_3\text{Li(n,T)}^4_2\text{He}$  and  $^7_3\text{Li(n,T+n)}^4_2\text{He}$  are used to breed tritium for further use in the fuel cycle. The short  $< 1 \text{ ns}$  confinement time necessitates that diagnostics observing the different aspects of the implosion be extremely fast.

During direct-drive small non-uniformities in the laser beams and shell surface roughness produce mass inhomogeneities that seed RTI at the ablator-fuel interface which impregnates the fuel with cooling ablator material leading to reduced temperature and implosion performance. The impact of RTI could be mitigated by increasing the ablation-front velocity, which is achieved by reducing the density of the plastic or glass shell; however reducing the shell density increases the implosion isentrope which diminishes performance below the gains produced by reducing RTI. Laser techniques exist to reduce RTI through adiabatic shaping; this approach involves shocking the capsule with a laser prepulse or 'picket'. 1D calculations show that capsule performance depends strongly on low shell adiabat during the deceleration phase of the implosion; conversely, stability and implosion velocity depend strongly on a high adiabat in the ablated shell during the acceleration phase. An adiabat profile with a maximum at the outer surface and a minimum at the ablator-

fuel interface can be achieved using a laser prepulse [9]. During the prepulse a shock is launched into the ablator material which increases the shell density by a factor  $\times 4$  and sets the shell adiabat to a constant. At the end of the prepulse a rarefaction wave travels from the ablation front towards the shock front, eventually overtaking the initial shock which quickly decreases in strength together with the adiabat of the shocked material. Between the prepulse and main pulse foot, the rarefaction trailing edge expands outwards relaxing the shocked material, producing monotonically increasing pressure and density profiles from the outer ablated radius to the inner shock front. During the main pulse a strong shock is launched which initially interacts with the low-density trailing edge of the rarefaction wave, setting the outer material on a high adiabat. The shock then travels through the monotonically increasing density and pressure gradient with the post shock density increasing faster than the post shock pressure producing a low adiabat. Once the main shock reaches the prepulse shock front the adiabat profile has the desired shape of being large at the outer ablation region and a low value on the inner surface [10] [9]. Multi-picket adiabatic shaping combined with a main pulse foot has been used at the Omega laser facility to achieve fuel  $\rho R$  values of  $300 \text{ mg/cm}^2$  [11] as shown in Figure 1.2 and are also routinely used at NIF during direct and indirect drive experiments [12].

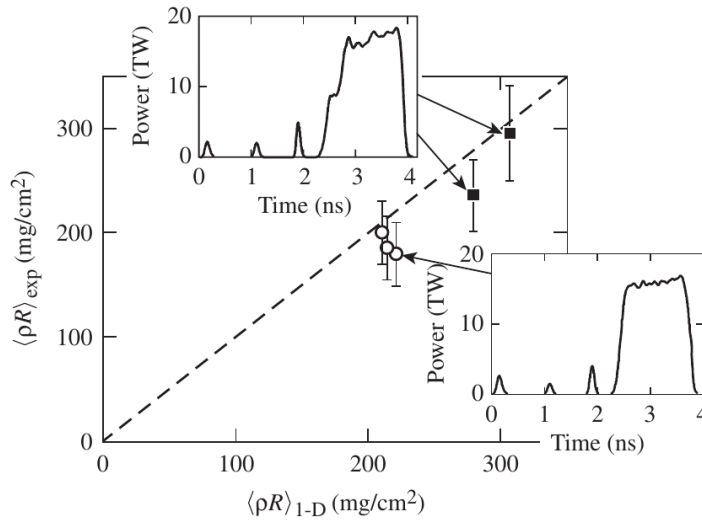


Figure 1.2: Plot showing measured fuel  $\rho R$  values at the Omega laser facility using the multi-picket with laser foot adiabatic shaping technique compared with predictions from the 1-dimensional LILAC code [11]. The different laser profiles are included as inserts.

## 1.2 The National Ignition Facility (NIF)

The national ignition facility based at the Lawrence Livermore National laboratory (Livermore, California, USA) is a neodymium-glass ICF laser system possessing 192 beams at a wavelength of 351 nm with a maximum on-target energy of 1.8 MJ (500 TW), designed using the CHAINOP numerical code. The NIF target chamber has an inner diameter of 10 m [13] and an outer 50 cm wall of borated gunite followed by 10 cm of aluminium [14]. The borated gunite is present to reduce the high-energy neutron distribution from activating the area surrounding the target chamber and the aluminium is used for strength, low permeability and conductivity. In addition aluminium does not generate any long-lived radioactive nuclei following high-energy neutron irradiation. 1053 nm laser light is picked off from the master oscillator and delivered to individual preamplifiers on single-mode polarization-preserving fibers. From the preamplifiers the beams are split into 48 separate bunches each known as

a 'quad' and transported to the multi-pass cavities via the boost-amplifier stages and the optical switch assembly. The flashlamps used to pump the glass laser slabs are energised with approximately 260 MJ of energy from a large capacitor bank. Each beam makes four passes through the cavity amplifiers; the pulses are then switched out, further amplified in the boost stage and subsequently transported to the target chamber.

At the target chamber there are  $48 \times$  final optics assemblies (FOA), which include the phase plates, vacuum window, focusing lens and debris shields amongst other components. Phase plates are required to transform the aberrated laser spatial profile into a relatively homogeneous distribution [13]. The debris shields protect the expensive optics from material ablated during the laser plasma interaction. Also present in the FOAs are the frequency conversion crystals; these frequency triple the 1053 nm light to 351 nm with 80 % conversion efficiency at a drive irradiance of  $3 \text{ GW/cm}^2$  (conversion efficiency is a non-linear function of irradiance). After entering the target chamber through the vacuum window the focused laser light is positioned on the hohlraum inner wall (indirect drive) or capsule surface (direct drive) with a positioning accuracy of  $50 \mu\text{m}$  [15]. Figure 1.3 shows a schematic overview of the NIF laser system including the 4- pass amplifier cavity and the FOAs mounted on the target chamber [16].

There are many detector systems used to diagnose different aspects of the implosion; these can be mounted on or near the target chamber, or located in a diagnostic insertion manipulator (DIM). There are three DIMs on NIF and they allow detectors to be situated at a tunable location relative to target chamber centre (TCC) inside the vacuum; the DIMs are also designed to be backward-compatible with the existing ten-inch manipulators at the Omega laser facility. DIMs are boxes made of an aluminium alloy bolted to the target chamber, inside which is a set of rails, a diagnostic cart and a vacuum flange / gate valve. A diagnostic with maximum diameter 30 cm, length of 300 cm and mass of 125 Kg can be bolted to the cart which itself can be driven along the rails using motors to a specified distance from TCC within  $\pm 250 \mu\text{m}$  and a lateral pointing accuracy of  $\pm 25 \mu\text{m}$  [17] relative to

TCC. Prior to insertion the entire airbox is pumped down to vacuum ( $1 \times 10^{-6}$  torr) and the gate valve subsequently opened; conversely the flange can be closed and the DIM let up to ambient pressure. A vacuum-compatible umbilical cable is used to provide power and other services to the detector. The DIM technology allows fast interaction with vacuum-based diagnostics without having to let the target chamber back up to air, saving time and effort.

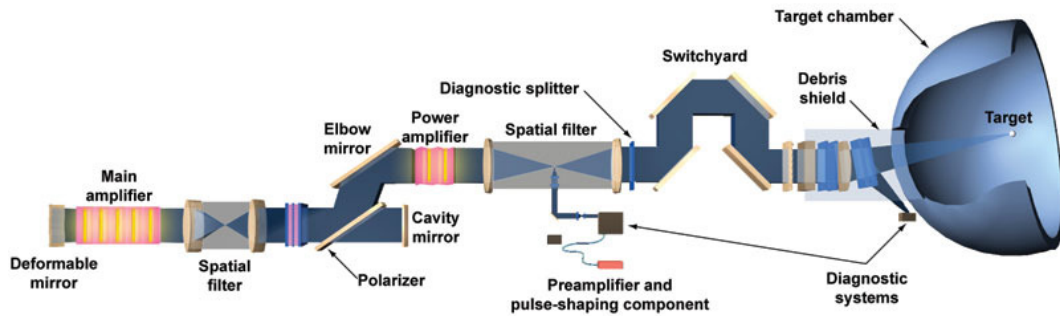


Figure 1.3: Schematic overview of the NIF laser system [16].

In 2011-2012 the national ignition campaign (NIC) began with the goal of ignition and thermonuclear burn in the laboratory for the first time, as part of a multi-institutional collaboration including Los Alamos (LANL), Sandia (SNL) and Lawrence Berkeley National Laboratories (LBNL), Laboratory for Laser Energetics (LLE, Rochester, NY), General Atomic (GA), Massachusetts Institute of Technology (MIT), Atomic Weapons Establishment (AWE) and Commissariat a lEnergie Atomique (CEA) [18].

Prior to the NIF several campaigns were conducted at the 20-beam 10 kJ Shiva and 10-beam 150 kJ NOVA facilities which were also located at the Lawrence Livermore National Laboratory before being dismantled in 1981 and 1999 respectively, to investigate the poorly understood processes critical to the pursuit of ignition. Investigations into ICF using the Shiva laser during the 1970s showed that the fundamental Nd:glass wavelength of 1053 nm coupled too strongly with electrons in the induced plasma leading to preheating of the fuel; heat from the core strongly

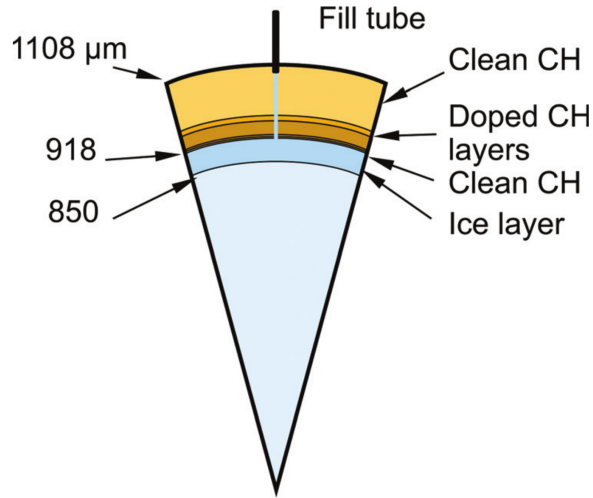


Figure 1.4: National Ignition Campaign (NIC) point design capsule in cross section form. The actual capsule is spherical with a 10 atm DT gas fill, followed by  $68 \mu\text{m}$  thick ice layer and then several layers of doped and undoped plastic.

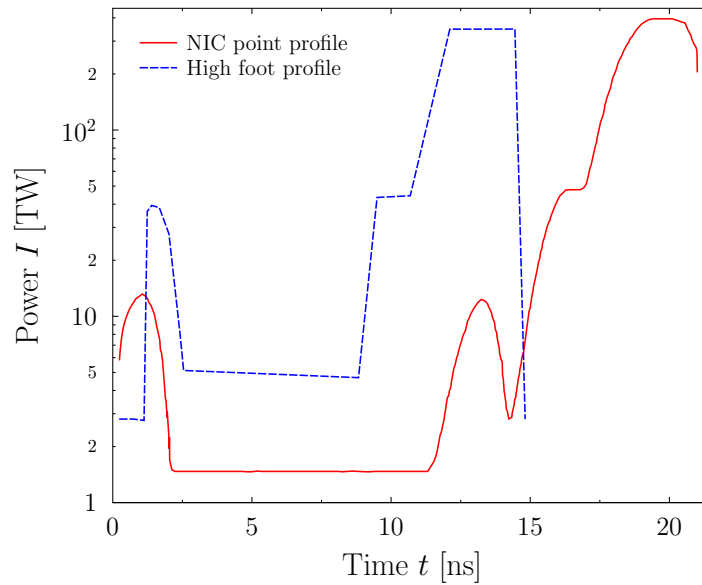


Figure 1.5: Plot showing the four shock laser profile used on NIF at the commencement of the national ignition campaign [19] together with the 3-shock high-foot laser profile.

opposes the inward-falling ablator material reducing the maximum achievable compression and moreover removes precious energy from the drive itself. The solution consisted of frequency-tripling the laser to 351 nm using potassium dihydrogen phosphate (KDP) crystals which significantly reduces the electron coupling and subsequent preheating [20]. Experiments, such as GASBIG and the first toroidal hohlraums, were designed to characterise the scaling of stimulated Brillouin scattering, stimulated Raman scattering, filamentation and hot electron preheating as a function of the high power laser drive [6]. The results suggested that these energy-depleting processes could be kept at tolerable levels through careful compensation in the plasma conditions required for inertial fusion.

At the commencement of the NIF ignition campaign the implosion was designed with a laser profile comprising 4 shocks as shown in Figure 1.5, the hohlraum shown in Figure 1.6 and the capsule shown in 1.4. The initial expectation was to begin at half the initial laser energy (approximately 0.8 - 1 MJ) and tune the symmetry of the implosion using images of the hot spot at peak compression recorded by the gated X-ray detectors and the neutron imaging diagnostic. Early results showed that the inner cone beams shown in Figure 1.6 were not providing sufficient drive at the capsule equator producing an implosion with positive  $P_2/P_0$  Legendre coefficients; an oblate compression [21]. The discrepancy between modelling and experiment was due to increased stimulated Brillouin scattering of the inner cone beams with the low-density helium plasma inside the hohlraum, in addition the gold hohlraum walls were expanding into the gas greater than expected further reducing the penetration of the inner cones. Moreover surface imperfections and dust contamination on the capsule seeded Rayleigh-Taylor instability (RTI) at higher than predicted levels allowing cold ablator material to mix with the fuel deforming the hot spot symmetry and compression.

The cross-beam energy transfer (CBET) laser-plasma interaction was used to compensate for the reduced drive at the equator [22]; this process allows energy to be transferred from the the outer beams to the inner beams by shifting the laser wavelength in the inner cones by approximately 1.8 Å through narrowband

tuning. The energy is transferred via stimulated Brillouin scattering in the low-density helium plasma at the hohlraum laser entry hole by means of an intermediary ion-acoustic wave; the resonance condition for transfer depends on the wavelength difference between the beams therefore the magnitude of transfer can be tuned by adjusting the wavelength separation between the inner and outer cones. Using CBET subsequent NIC experiments produced implosions within the  $\pm 7.5\%$   $P_2/P_0$  tolerance [22]. In addition, target fabrication developments significantly improved surface smoothness and reduced dust contamination; instability growth however was still producing intolerable levels of mix and the neutron yields remained below  $1 \times 10^{15}$ , several orders of magnitude below that required for gain.

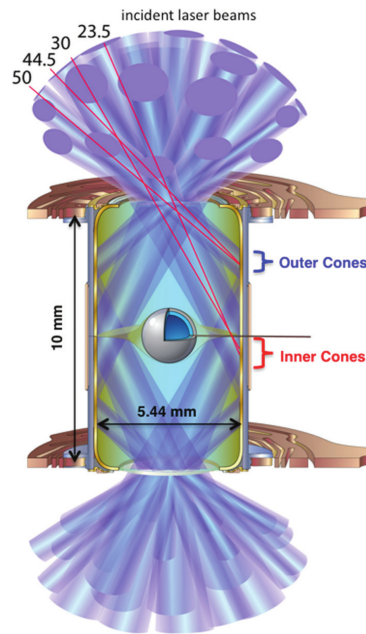


Figure 1.6: Diagram of the NIC point design hohlraum. Twenty-four quads enter the hohlraum through a laser entrance hole in four groups: four at 23.5°, four at 30°, eight at 44.5°, and eight at 50°. The beams strike the gold wall and convert to X-rays which are used to implode the capsule. A low-Z gas (generally helium) fills the hohlraum to reduce the expansion of the wall over time [23].

In 2013 the high-foot campaign began following on from the NIC campaign which attempted to improve the implosion symmetry and subsequent neutron yields by reducing the number of shocks to three, and utilising a laser profile comprising a

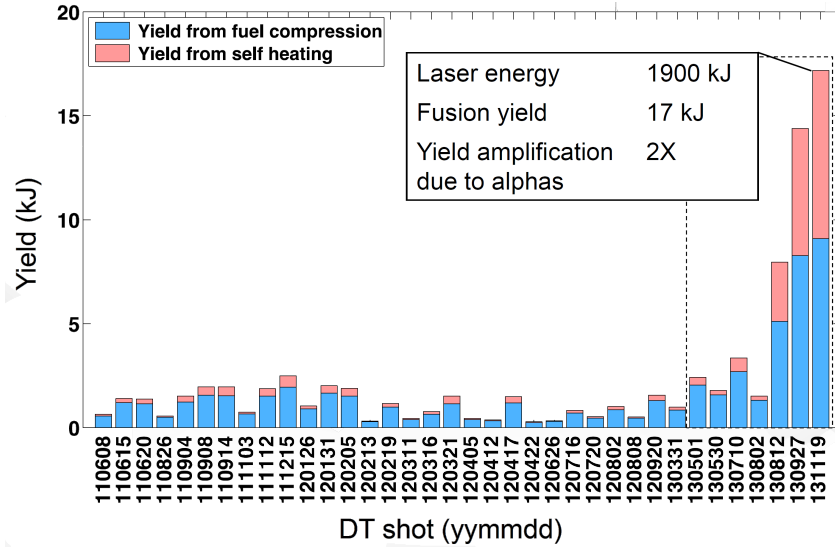


Figure 1.7: Plot showing the reported radiated energy from the NIF laser for each shot fired during the NIC and high-foot campaigns. The blue and red fractions represent the contribution to the radiated energy from laser compression and alpha heating respectively [24].

higher foot (the 2nd picket before the main laser drive pulse) as shown in Figure 1.5 [23]. The higher adiabatic ablator-fuel profile for the high-foot case is not predicted to produce the same high gain values as the 4-shock point design; initial experiments however show significantly reduced RTI growth, unmeasurable levels of mix and closer agreement with 1-D theory. On November 20<sup>th</sup> 2013 a 1.91 MJ (428 TW) shot was fired as part of the high-foot campaign which produced a record neutron yield of  $5.3 \times 10^{15}$ . Figure 1.7 shows all ignition shots conducted over the last two years with the compression yield contribution shown in blue and the yield due to alpha heating shown in red. The last seven shots in the Figure are from the high-foot campaign and the results show that self-heating from alpha particles emitted during the  $D(T,n)^4\text{He}$  reaction are now the dominant source of yield. Figure 1.8 shows the neutron yield versus  $\langle \rho R \rangle_{fuel}$  phase space plot with alpha heating contours together with experimental results from the high and low foot campaigns shown in green and blue respectively. The plot shows that the reduced RTI and improved symmetry achieved during the 3-shock high-foot campaign produce higher yields and significant alpha heating; the data also shows that the improved output comes at the

cost of reduced  $\langle \rho R \rangle_{fuel}$  due to the higher adiabat design of the implosion. The highly non-linear scaling of the implosion output means that small improvements in  $\langle \rho R \rangle_{fuel}$  and  $T_i$  can lead to significant yield enhancements suggesting that NIF may now be on the correct path towards ignition. Reducing the complexity of the implosion as demonstrated during the 3-shock high-foot campaign is likely the best method for understanding why the ignition campaign failed.

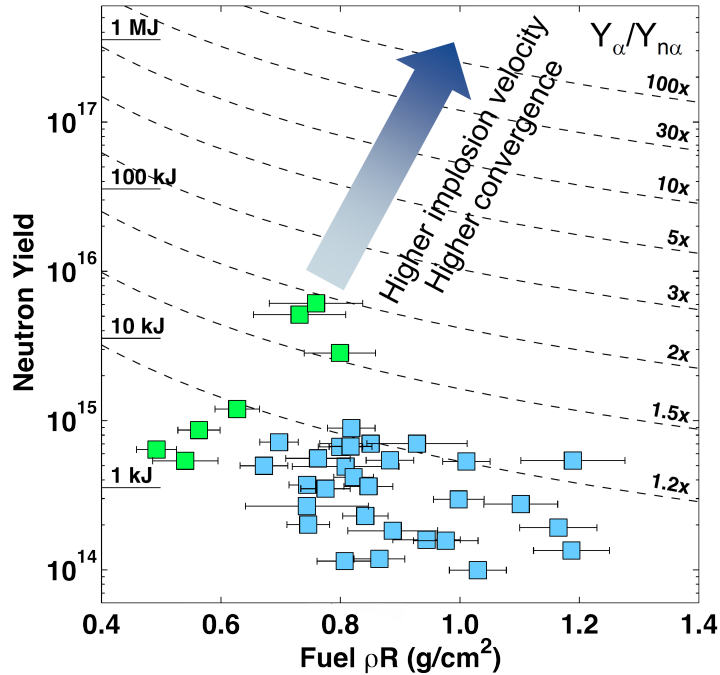


Figure 1.8: Phase space plot of neutron yield against  $\langle \rho R \rangle_{fuel}$  with alpha heating contours. The blue and green points represent experimental data from the NIC and high-foot campaigns respectively [24].

Beyond the high-foot campaign there are plans to introduce high-density carbon (HDC) diamond ablator materials, beryllium ablators and vacuum hohlraums. The benefit of using HDC for the ablator material comes from the increased density which allows the ablator to be thinner; the same amount of energy can be absorbed into a smaller volume leading to higher implosion velocities (400 km/s) [25] [26]. HDC surfaces are also smoother than plastic or beryllium which will lead to less Rayleigh-Taylor growth. The thinner HDC shells also allow a shorter period between laser pickets as the shocks have less distance to propagate; consequently,

a gas fill is not required in the hohlraum to hold back the gold wall decreasing laser-plasma radiative losses and simplifying the implosion modelling.

Beryllium has the benefit of having the lowest opacity that can be manufactured into a capsule which produces high ablation rates and therefore high implosion velocities, high core pressure and increased Rayleigh-Taylor ablative stabilisation [27]. The high ablation rate however may complicate the laser-plasma interaction of the inner cone beams affecting drive symmetry. The crystalline structure and melt point of beryllium also poses a problem for accurate modelling; in addition beryllium introduces toxic material handling complexities which must be mitigated before use in the NIF target chamber.

There are also plans for NIF to attempt ignition using polar direct drive. The laser beams at NIF are designed specifically to illuminate the inner surface of a hohlraum, as shown in Figure 1.6. To drive the capsule directly will require significant capsule design effort and modification of the laser system itself to mitigate the inherent asymmetry of the polar drive. The laboratory for laser energetics in Rochester, NY, have developed the polar-drive (PD) approach using the existing NIF beam configuration. Several modifications to the NIF infrastructure are required including: new phase plates, polarization rotators, and a polar-drive-specific beam-smoothing front end. The nominal design consists of a 1.5 MJ four-shock laser profile, similar to the NIF point indirect-drive design. 1D simulations predict a gain of 48 [28].

### **1.3 The Omega laser facility**

The Omega 60 beam frequency-tripled Nd:glass laser system designed for inertial confinement experiments is able to produce an on-target energy of 30 kJ (60 TW) [29], [30]. A commercially available mode-locked master oscillator produces 80 ps pulses at a frequency of 76 MHz in the oscillator room at a wavelength of 1054 nm; here complex pulse shapes are generated via low-intensity, integrated optics modulators at a bandwidth of between 6 and 9 GHz. The weak 1 nJ input pulses

fed via fibre-optic from the oscillator are amplified and stretched to the required length using feedback-stabilised regenerative amplifiers in the pulse-generation room (PGR) to an energy of 0.1 mJ after approximately 100 passes.

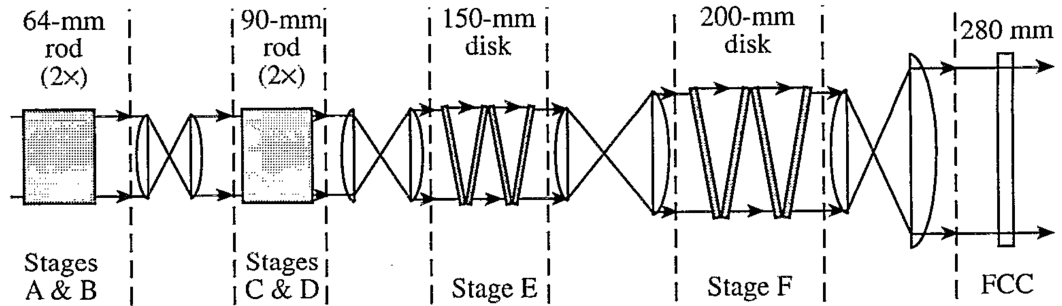


Figure 1.9: Diagram of the Omega laser large-aperture ring amplifier system consisting of  $2\times$  rod amplifiers (two passes),  $2\times$  disk amplifiers and a frequency conversion crystal.

The 0.1 mJ pulses are directed using a periscope and expanded onto the input of the large-aperture ring amplifier (LARA) system shown in Figure 1.9, which consists of two ND:glass rod amplifiers (64 mm and 90 mm) and two ND:glass disk amplifiers (150 mm and 200 mm); there are three individual LARA systems for the primary system, smoothing by spectral dispersion (SSD) and backlighter. Two passes are made through each rod amplifier and a single pass through the disk amplifiers producing a final energy of approximately 1000J at a gain of between 5000 and 10000 depending on the flash-lamp drive voltage. The beams are expanded by over a factor of 2 before the two disk amplifiers to keep the fluence below the damage threshold; the anti-reflection coating on the input lens of the final spatial filter will damage if the laser pulse reaches  $9.8 \text{ J/cm}^2$  [31].

Just before the target hall concrete wall the 1054 nm beams are converted to 351 nm using the frequency-conversion crystal (FCC) subsystem. The subsystem consists of an input polariser, three potassium dihydrogen phosphate (KDP) crystal optics and a UV absorption window. With the correct alignment and temperature the KDP crystal doubles the frequency of the incoming 1054 nm beam; the second crystal combines the doubled 527 nm light with the remaining 1054 nm light to

produce the final 351 nm beam. The third crystal is used for efficiently tripling the SSD beams, which are designed to shift any speckle pattern imprinted on the laser spatial distribution by a small amount over the duration of the pulse, thereby smoothing the on-target energy and uniformity.

The spherical aluminium Omega target chamber has an inner diameter of 1.56 m with 92 laser and diagnostic ports [14]. The GRH diagnostic discussed later in this thesis is located on port H8F; the GCD1, GCD2 and eventually the super GCD are designed to fit into ten inch manipulators (TIM) which are similar in design and purpose to the DIMs used at NIF.

## 1.4 Nuclear Physics

Nuclear reaction physics describes the interaction of the atomic nucleus with particles and energy [32]. The current state of the field combines theoretical and observational approaches to describe individual phenomena such as  $\alpha$  and  $\beta$  decay as well as fission and fusion reactions, amongst many others. In the next section, several basic nuclear concepts will be introduced including basic reaction energetics. These encompass the nuclear theory demonstrated and observed later in this work.

### 1.4.1 Reaction Cross section

The cross section, or effective area of the nucleus, is proportional to the probability for a given reaction to occur [32] [34]. In the reaction  $a(X, Y)b$ , the projectile  $a$  interacts with the parent  $X$  to produce the daughter nucleus  $Y$  and the ejectile particle  $b$ . If a flux of particles  $I_a$  is incident on the nucleus  $X$  the cross section is given by

$$R_b = \sigma I_a N, \tag{1.1}$$

where  $I_a$  and  $R_b$  are the incoming and outgoing particle fluxes respectively,  $\sigma$  is the cross section and  $N$  is the number of target nuclei per  $\text{cm}^2$  observable by the

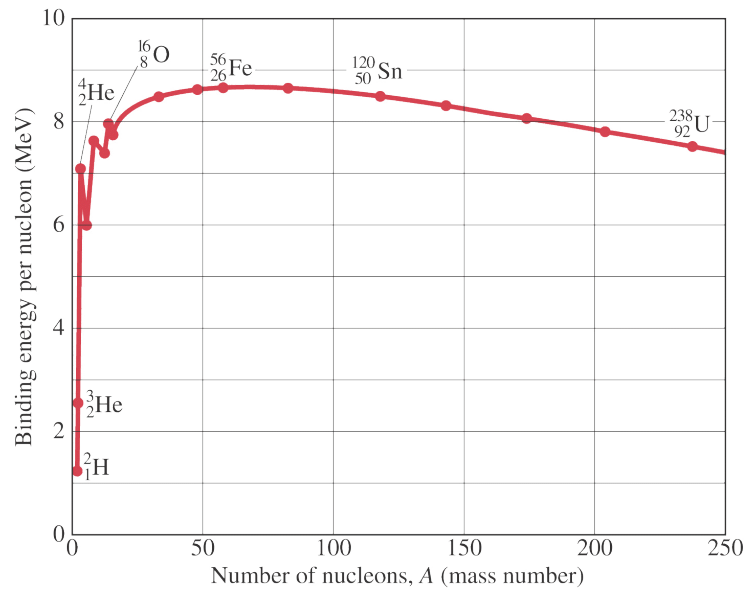


Figure 1.10: Figure showing the binding energy per nucleon as a function of nuclear mass number  $A$  [33]. Fusion and fission are nuclear reactions resulting in higher binding energy; the former via the joining of two less stable isotopes to form a larger more stable nucleus, and the latter via the splitting of a single unstable heavy element into two more stable isotopes. The most stable element in the periodic table is  $^{56}\text{Fe}$ .

incoming projectile within a small depth in which atom overlap can be neglected and over which the projectile energy and momentum can be assumed to remain unperturbed [32]. There are occasions where temporal information is limited and only the total number of incident and outgoing particles are known. Using integral quantities it can be shown that the total number of reactions occurring in a small thickness of material is,

$$N_R = \int_0^\infty \sigma(E)N(E)N_T dE, \quad (1.2)$$

where  $N_R$  is the total number of reactions,  $E$  is incident particle energy,  $\sigma(E)$  is the cross section at the incident particle energy,  $N(E)$  is the number of incident particles at that energy and  $N_T$  is the number of target nuclei as described above.

### 1.4.2 Reaction Q Value

The  $Q$  value for the nuclear reaction  $a(X, Y)b$  is defined as the initial mass energy minus the final mass energy

$$Q = (m_X + m_a - m_Y - m_b) c^2, \quad (1.3)$$

where  $m_X$  is the mass of the parent nucleus,  $m_a$  is the mass of the projectile,  $m_Y$  is the mass of the daughter nucleus,  $m_b$  is the mass of the ejectile and  $c$  is the speed of light. The discrepancy in mass between the initial and final nuclei arises from the difference in binding energy between the initial and final particles. The binding energy of a nuclear configuration is defined as the sum of the individual neutrons and protons minus the measured atomic mass of the nucleus, which is classically zero. A large binding energy corresponds to a light nucleus with respect to the mass of its constituent protons and neutrons. If a reaction process produces final products with large binding energy compared to the initial nucleus, the resulting  $Q$  value will be positive and the reaction is known as exothermic. The excess energy is released in the form of kinetic energy or excitation of ejectiles and daughter

particles. A negative  $Q$  value occurs when the total binding energy of the initial particles is greater than the final and is known as an endothermic reaction. In this case, the reaction requires a threshold amount of kinetic energy in the projectile or parent to initiate the reaction.

### 1.4.3 Threshold energy

Using the conservation of energy and momentum laws for the reaction  $a(X, Y)b$  it is possible to calculate a minimum threshold energy below which a reaction cannot occur,

$$T_{th} = (-Q) \frac{m_Y + m_b}{m_y + m_b - m_a} \quad (1.4)$$

In this equation the Coulomb barrier has been neglected. This approximation is valid where the projectile is a neutron, however for charged projectiles such as protons and deuterons, some energy will be lost overcoming the Coulomb barrier. Furthermore, quantum tunnelling, which allows charged particles to penetrate through classically prohibited potentials via the evanescent penetration of the wavefunction, is not relevant and is therefore ignored.

## 1.5 Important fusion reactions

Table 1.1 lists several of the most important reactions of interest to inertial confinement fusion community. The obvious choice for ICF is to use the  $D(T, n)^4\text{He}$  reaction with a  $Q$  value of 17.59 MeV and a cross section of  $> 30$  millibarns at the centre-of-mass (COM) temperatures ( $T_i = [14-24 \text{ keV}]$  [35]) routinely observed during ICF implosions. There are occasions when optimising the yield may not be the primary goal of an experiment; in some cases the high neutron background can reduce signal to noise values for other observables from the implosion, such as protons from  $D(D, p)T$  reactions (which will occur at a lower intensity during DT implosions), and alpha particles emitted directly from the fuel during DT experi-

ments with thin ablator materials known as exploding pushers. To constrain plasma and nuclear theory, and to validate the complex hydrodynamics simulations used to predict and optimise ICF implosions, experiments with different fuel fill ratios from Table 1.1 are required. Figure 1.11 shows the cross sections as a function of COM energy for a selection of the reactions in Table 1.1. Given the temperatures currently achievable during ICF experiments, the DT, TT, DD, D<sup>3</sup>He and D<sup>3</sup>He are of interest to the community. Fusion is possible with heavier nuclei; however the Coulomb barrier increases with each additional proton (charge) in the nucleus making nuclear reactions less probable at today’s achievable temperatures. In addition the higher temperatures required for higher-Z fusion produce more thermal X-rays leading to a less-efficient implosion.

Reaction	$Q$ Value [MeV]	$\sigma(10 \text{ keV})$ [barns]	$\sigma(100 \text{ keV})$ [barns]
$D + T \rightarrow \alpha + n$	17.59	$2.72 \times 10^{-2}$	3.43
$D + D \rightarrow T + p$	4.04	$2.81 \times 10^{-4}$	$3.3 \times 10^{-2}$
$D + D \rightarrow {}^3\text{He} + n$	3.27	$2.78 \times 10^{-4}$	$3.7 \times 10^{-2}$
$D + D \rightarrow \alpha + \gamma$	23.85	-	-
$T + T \rightarrow \alpha + 2n$	11.33	$7.9 \times 10^{-4}$	$2.4 \times 10^{-2}$
$D + {}^3\text{He} \rightarrow \alpha + p$	18.35	$2.2 \times 10^{-7}$	0.1
$p + {}^6\text{Li} \rightarrow \alpha + {}^3\text{He}$	4.02	$6 \times 10^{-10}$	$7 \times 10^{-3}$
$p + {}^7\text{Li} \rightarrow 2\alpha$	17.35	-	-
$p + {}^{11}\text{B} \rightarrow 3\alpha$	8.68	$4.6 \times 10^{-17}$	$3 \times 10^{-4}$
$p + p \rightarrow D + e^+ + \nu$	1.44	$3.6 \times 10^{-26}$	$4.4 \times 10^{-25}$
$D + p \rightarrow {}^3\text{He} + \gamma$	5.49	-	-
${}^3\text{He} + {}^3\text{He} \rightarrow \alpha + 2p$	12.86	-	-

Table 1.1: Table showing the fusion reactions pertinent to inertial confinement fusion experiments [8] together with reaction  $Q$  values, and cross sections at 10 and 100 keV where available.

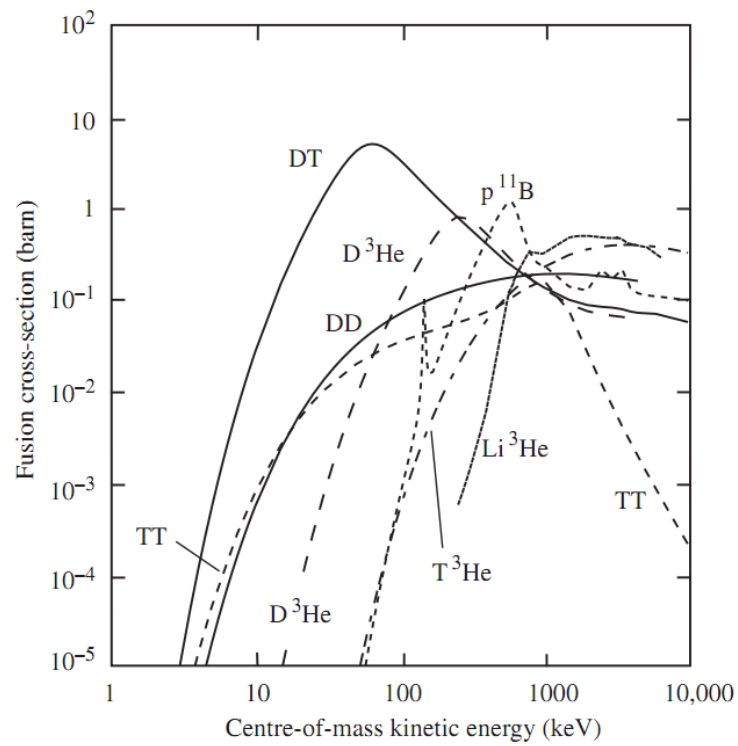


Figure 1.11: Plot showing fusion cross sections of interest to the ICF community [8]. The DD curve is the integral cross section for all three reactions listed in Table 1.1.

## 1.6 Reaction History and bang time

Reaction history (RH) is defined as the fusion neutron production rate as a function of time. Diagnosing the many orders of magnitude comprising the RH is fundamental to tuning ignition capsule, hohlraum and laser profile design and for identifying performance failure modes [36]. The 10 mm National Ignition Campaign (NIC) hohlraum point design shown in Figure 1.6 combined with the laser profile in Figure 1.5 were designed to X-ray drive the capsule in Figure 1.4 to compression using four shocks carefully timed to coalesce at the ablator-fuel interface at peak compression. The first three shock waves progressively drive the ablator and fuel to higher pressures; the fourth pulse contains the majority of the laser energy and therefore imparts the highest kinetic energy to the shocked fuel [37]. In a well-timed symmetric implosion the combined shock reaches the centre of the fuel producing an increase in the burn rate due to the rapidly increasing density and temperature. The pressure pulse reflects outward into the DT gas region previously heated and compressed by the combined shock-front causing a further increase in burn. When the outward-going reflected shock front meets the inward-falling dense DT ice layer the burn rate increases significantly; the region inside the reflected shock front and the DT ice layer is known as the hot spot.

All aspects of hydrodynamics modelling, target fabrication and laser-plasma interaction must come together seamlessly for the shocks to coalesce at the ablator back surface simultaneously and symmetrically. The smallest imperfections in the capsule or laser uniformity can produce density perturbations which can be amplified by the massive laser power driving asymmetry and instabilities. For example Figure 1.12 shows several simulated RHs for a NIF 1.8 MJ beryllium capsule folded with the 20 ps best Gaussian system response of a RH diagnostic: the red trace shows an igniting capsule with well-tuned shocks producing 9 MJ of fusion energy ( $G=5$ ); the solid black line shows a failing capsule RH with weak first pulse and the broken line is the opposite case where the first shock is too strong. The weak first pulse does not produce a compression sufficient to contain the alpha energy which

is lost to surrounding cold material; where the first shock is too strong it reflects off the ablator-fuel interface and begins to rarify the ablator before the later shocks arrive, again leading to poor compression and alpha heating.

Diagnostics commissioned to measure RH should aim to capture as many aspects of the 12 orders ( $1 \times 10^9$ - $1 \times 10^{20}$  neutrons/s) of magnitude present in Figure 1.12 [36]. At present RH is measured by the gamma reaction history (GRH) diagnostic and the neutron temporal diagnostic (NTD) with temporal resolutions of between 10 and 100 ps (30 - 3 GHz bandwidth equivalent); this represents 3-4 orders of magnitude during the peak intensity of the RH therefore significant detector development is still required in the low intensity ps regime.

An important parameter related to RH is the implosion bang-time (BT). BT is defined as the time between laser interacting with the hohlraum wall (indirect drive) or capsule (direct drive), and the peak in the RH. In the absence of a comprehensive reaction history the bang time provides an integrated perspective encompassing the implosion timing, shell velocity and compression for comparison with 1-D models and hydrodynamics models. At NIF the laser interaction term in the BT calculation is further specified as being the 2 % point in the rising edge of the first pulse (picket); at Omega conversely the BT is defined as being the 2 % of the peak laser energy [38] [39].

## 1.7 Inertial Confinement Fusion (ICF) radiation

During short sub-ns ICF experiments several radiations including: charged particles from the hot fuel region, X-rays from the laser-plasma interaction (LPI), and neutrons and gammas from nuclear reactions, can be emitted allowing measurements of different aspects of the implosion for comparison with and constraint of theoretical calculations. In addition, some diagnostics, such as velocity interferometer for any reflector (VISAR) and the gated X-ray detector (GXD), rely on probe lasers and backlighting radiography to make measurements.

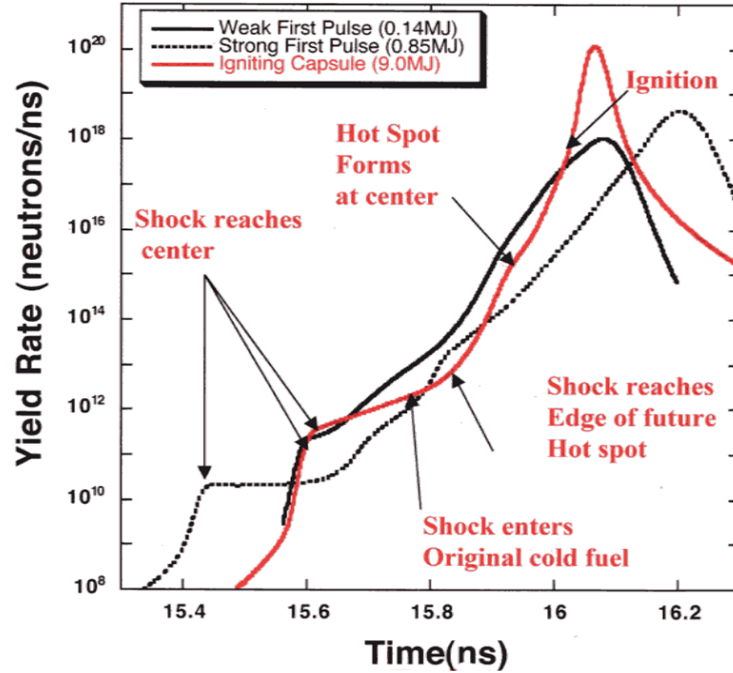


Figure 1.12: Reaction history of an igniting NIF capsule together with two failing implosions, simulated by D. Wilson (LANL) [37].

### 1.7.1 Neutron time-of-flight detector (nToF)

The neutron time-of-flight diagnostics are used during ICF implosions to measure the thermal broadening of the fusion neutron signal at large distances in order to infer the fuel ion temperature [40]. nToF diagnostics generally consist of a fast scintillator (BC422) coupled to a microchannel plate (MCP) PMT. The scintillator (1.3 ns decay time) and PMT (approximately 1 ns instrument response) are required to be sufficiently fast in order to temporally resolve the broadened neutron signal. The detector location must be carefully selected depending on the implosion characteristics: it must be close enough to subtend a statistically significant solid angle, far enough away to smear out the fusion reaction history, and far enough away to temporally spread the signal wider than the impulse response function of the scintillator, PMT, cables and oscilloscope. Consequently at NIF and OMEGA there are many nToF diagnostics at different distances, with varying scintillator geometries and PMT types to cover the various different temperatures, fusion burn

widths and neutron yields.

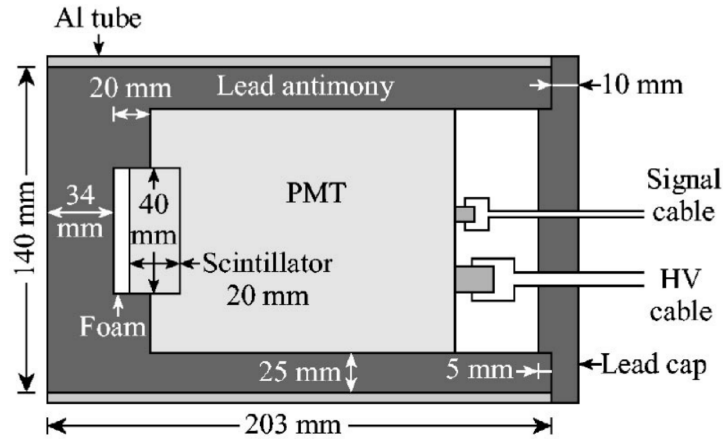


Figure 1.13: Schematic of the neutron time-of-flight detector fielded at the Omega facility from [40]; the NIF variants, of which there are many, are similar in design with different scintillator and shielding configurations.

In addition to recording thermal broadening, nToF detectors can also be used to measure other spectral features present in the neutron signal. These include the total down-scatter fraction which correlates well with  $\langle \rho R \rangle_{fuel}$  and is an important parameter in the Lawson criteria for fusion and the DD and TT reaction yields [41]. Down-scatter refers to 14.1 MeV fusion neutrons that lose energy inelastically via nuclear reactions with nuclei in the dense fuel.

### 1.7.2 Neutron Total Yield Diagnostic(NTYD)

The total neutron yield diagnostic (NTYD) infers the neutron flux at a specific location relative to TCC by measuring the neutron-induced activation in a copper or indium sample. The 2.5 cm diameter and 1 cm thick cylindrical samples are placed 4m from the NIF target chamber centre inside a cylindrical re-entrant tube and retracted pneumatically post-shot to a counting laboratory a short distance from the target hall. In the laboratory NaI scintillation detectors are used to measure the activity of the sample as a function of time; combined with timing signals from the laser system this allows the activity at  $t = 0$ , and therefore the total number of transmuted nuclei, to be calculated [42] [43].

For 14.1 MeV neutrons emitted from  $D(T,n)^4\text{He}$  the reaction  $^{63}\text{Cu}(n, 2n)^{62}\text{Cu}(\beta^+)$  with a half life of 9.74 minutes and threshold of 11 MeV is used; there is also a competing reaction  $^{65}\text{Cu}(n, 2n)^{64}\text{Cu}(\beta^+)$  which has a threshold of 10 MeV and a half life of 12.7 hours. The high threshold is required to remove reaction contributions from down-scattered, secondary and tertiary neutron sources. At  $E_n=14.1$  MeV the  $n, 2n$  cross sections for  $^{63}\text{Cu}$  and  $^{65}\text{Cu}$  are 454 mb and 906 mb; taking into account the 69.15 % and 30.85 % abundances this suggests that similar amounts of each reaction are likely to occur. The half life of  $^{64}\text{Cu}$  however is  $80\times$  longer therefore the early signal will be dominated by  $^{62}\text{Cu}$  radiation. Both  $^{62}\text{Cu}$  and  $^{64}\text{Cu}$  emit several characteristic  $\gamma$  photons during  $\beta$  decay however it is the 511 keV annihilation photon which is measured; each time a  $^{62}\text{Cu}$  or  $^{64}\text{Cu}$  nucleus decays to  $^{62}\text{Ni}$  and  $^{64}\text{Ni}$  respectively a proton is converted to a neutron through the weak interaction together with the emission of a positron and a neutrino. The positron is emitted with some fraction of the end-point  $\beta$  energy, which is lost through ionisation and bremsstrahlung before the positron finally annihilates with a local electron producing two approximately back-to-back 511 keV  $\gamma$  photons. Coincidence counting techniques are used to improve detection signal to noise ratio.

For 2.45 MeV neutrons emitted from  $D(D,n)^3\text{He}$  the  $^{115}\text{In}(n, n')^{115m}\text{In}$  reaction with a half life of 4.49 hours and threshold of 336 keV is used. The reaction product in this case is metastable, a state which decays slowly due to significant differences in nuclear structure compared to lower energy levels, and decays via  $\gamma$  emission with a strength of 45.8 %. The cross section at  $E_n=14.1$  MeV for production of the first excited state of indium is 13.32 mb making the material less sensitive than copper; the reduction in activity can be recovered by moving the sample closer to TCC to improve solid angle. Moreover, the 336 keV  $\gamma$  photon is not emitted time-synchronous with other photons therefore the signal to noise cannot be improved using coincidence counting techniques.

To infer the yield the induced activity per incident neutron must be known for the sample; there are two possible approaches used to do obtain this. A first principles calculation can be performed which must take into account the neutron

irradiation geometry, interaction cross sections, decay strengths, detector geometry,  $\gamma$  self absorption, detector efficiency and material abundances; this could be achieved using a validated Monte Carlo code, such as MCNP or GEANT4, together with efficiency measurements for the detector system. The second approach involves irradiating the sample with a known neutron field at the correct incident energy for a well-characterised period of time and measuring the induced activity. This approach can be carried out at an ion-beam accelerator facility and allows the induced activity for a specific dose to be measured directly, ruling out possible uncertainties in the Monte Carlo nuclear data and scattering algorithms.

At NIF the second approach is used due to the reduced error bars from empirically measuring the combined induced activity and detector efficiency conversion efficiency.

### 1.7.3 Charged Particle Spectrometer (CPS)

The charged particle spectrometers (CPS) mounted on ports at the Omega facility measure the energy distribution of charged particles during an ICF implosion with high resolution [44]. Charged particles enter the diagnostic through an adjustable aperture which can be set between 1 and 10 mm diameter depending on the predicted flux for the measurement; opening the aperture does however reduce energy resolution. Following the aperture is a 7.6 kG magnet designed to measure charged particles, such as protons, deuterons, tritons,  $^3\text{He}$  and  $^4\text{He}$ , in the range  $E(A/Z^2) = 0 - 30$  MeV; the resulting position of the charged particle depends on the magnetic field strength and the charge-to-mass ratio of the ion. Following the magnet is either an electronic particle detector or CR39. CR39 is now the preferred method due to 100 % detection efficiency and insensitivity to  $\gamma$  emission and transient inductance from EMF. For protons  $> 6$  MeV an aluminium block with a thickness of a few millimetres is required to range-down the energy due to a loss of detection efficiency above this energy. The preferred method for tuning the dynamic range is to increase or reduce solid angle by changing TCC-diagnostic separation.

The upper limit on dynamic range comes from the ability to distinguish pits on the CR39 which depends on the particle energy and etching condition. The CPS has a working yield range of approximately  $1 \times 10^7$  -  $1 \times 10^{13}$  per MeV and resolutions of 0.02 and 0.1 MeV at particle energies of 3 MeV and 15 MeV respectively.

#### **1.7.4 Wedge Range Filter (WRF)**

The wedge range filters (WRF) mounted on ports at the Omega laser facility measure proton energy distributions over a wide dynamic range using a wedge of varying thickness perpendicular to the TCC line of sight placed in front of a slab of CR39 material [44]. The aluminium wedge has a thickness varying from 400 to 1800  $\mu\text{m}$  covering an energy range of 8 to 18 MeV; the CR39 is generally cut into  $2 \times 2$  cm square pieces. The design is simple and compact, as shown schematically in Figure 1.14, therefore a large number can be fielded at different locations and distances simultaneously to cover a large range of possible yields; up to 8 at once have been fielded during Omega operations.

Absolute calibration of each wedge was required to compensate for fabrication uncertainties and for errors associated with modelling the proton stopping. This was conducted at a 2 MeV Van de Graaf accelerator using D,  $^3\text{He}$  or gold targets allowing a wide range of alpha and proton energies to be produced. The well-characterised charged particles were then used to generate a series of energy-response functions at each point along the wedge. Not including counting statistics, the absolute uncertainty for the WRF is  $\pm 0.1$  MeV in energy and  $\pm 12$  % in yield. Due to proton tracks overlapping in the CR39 it is not possible to use the WRF for charged particle yields greater than  $10 \times 10^{11}$  unless the detector is moved far from the OMEGA target chamber [44].

#### **1.7.5 Magnetic Recoil Spectrometer (MRS)**

The neutron magnetic recoil spectrometer is designed to measure the NIF neutron spectrum by converting neutrons to protons (CH-foil) or deuterons (CD foil). The

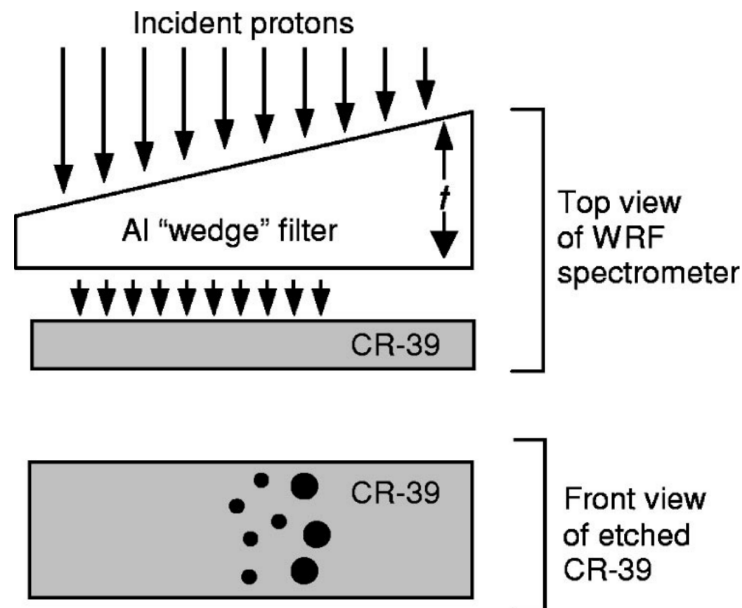


Figure 1.14: Schematic of the wedge range filter proton spectrometer [44]. The spectrometer consists of a wedge-shaped filter with thickness varying along its length combined with a slab of CR-39. A small number of the incident protons have enough energy to pass through the wedge and cause localised damage sites. After etching into the front surface using sodium hydroxide each track is observable as a small hole with diameter proportional to the original proton energy. The proton energy distribution can be calculated by scanning the CR39, histogramming the tracks along the wedge axis and removing the stopping induced by the wedge thickness.

charged particles are subsequently collimated to select a small energy range. Following collimation the particles are passed through a magnet to further separate by charge to mass ratio. The protons or deuterons are finally collected on a selection of CR39 detectors arranged along the focal plane of the collimator-magnet system [45]. CR39 is a solid-state poly allyl diglycol carbonate with good crystallinity and few defects making its use as a track detector favourable. When protons traverse the material damage tracks are created; following etching with sodium hydroxide the tracks are revealed as small holes with diameter proportional to the original proton energy. Consequently, CR39 can be used on its own to measure proton spectra. A schematic of the MRS employed at NIF is shown in Figure 1.15.

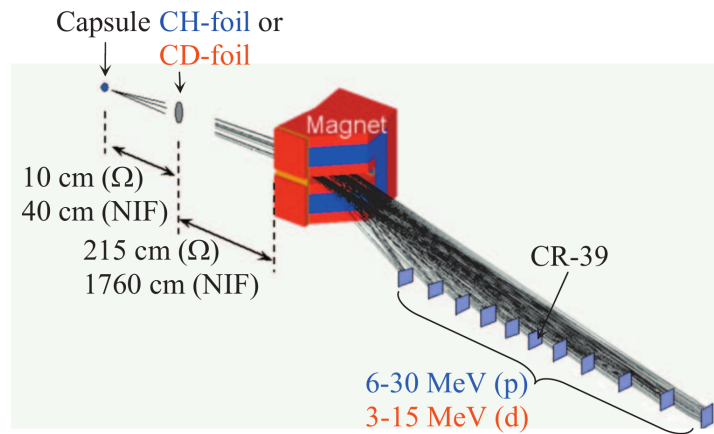


Figure 1.15: Schematic of the MRS detector fielded at the NIF facility [45].

From the neutron spectrum the MRS can report values for fuel areal density  $\langle \rho R \rangle_{fuel}$ , neutron yield  $Y_n$  and ion temperature  $T_i$ .

### 1.7.6 Full-aperture backscatter diagnostic (FABS) and Near backscatter Imaging (NBI)

The full-aperture backscatter diagnostic measures the power-time history and time evolution of the backscattered light into the incident aperture [46] [47]. The near backscatter imager measures the light scattered beyond the FABS aperture out to a cone angle corresponding to  $F/4.7$ . Results are used to constrain hydrodynamics

models and improve understanding of laser-plasma-interaction (LPI) instabilities. A NIF FABS and NBI system schematic is shown in Figure 1.16.

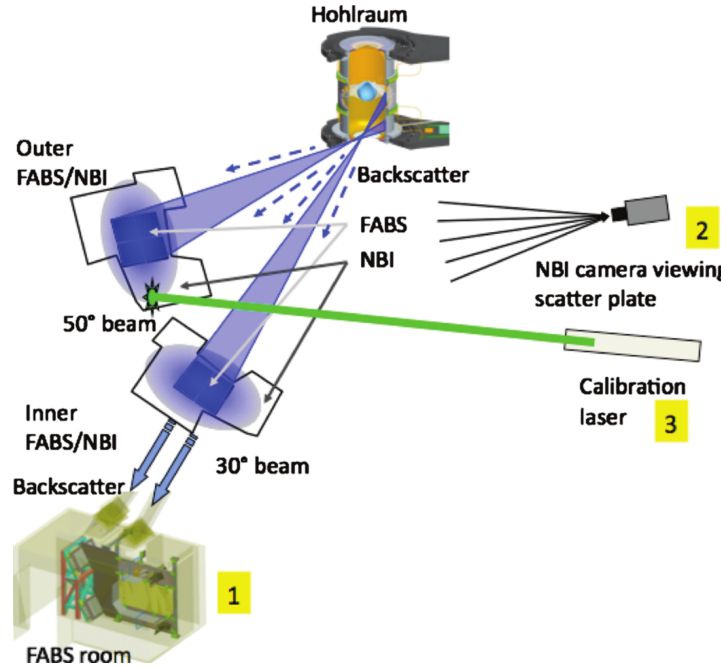


Figure 1.16: Schematic of the NIF FABS and NBI configuration.

Both NBI and FABS make separate measurements from two spectral bands; 350-353 nm corresponding to backscattered light from ion acoustic waves and stimulated Raman scattering in the range 450-750 nm from laser interactions with Langmuir waves. The combined uncertainty of the backscatter system is calculated to be  $\pm 15\%$ . There are two FABS detectors on NIF; one placed to measure the backscatter of one quad from the 'inner'  $30^\circ$  beams and the other to measure one quad of the 'outer'  $50^\circ$  beams. The backscattered light travels back up the NIF beam line and through the final turning mirror into the FABS optical system. At this point the light is diffused and then reduced in intensity further by locating a  $400\ \mu\text{m}$  fiber 2.5 m away from the diffuser with approximately  $6 \times 10^{-9}$  conversion efficiency. The low conversion efficiency is required to keep the recorded light below the damage threshold fluence of  $3\ \text{J}/\text{cm}^2$ . Two sets of four fiber pickoffs combined with filters are used to select the desired wavelength regions; the light from each pickoff is

converted to an electrical signal using a fast Hamamatsu photodiode (60-80 ps) and coupled to a Tektronix digitiser via a high bandwidth coax cable.

### **1.7.7 Velocity interferometer for any reflector (VISAR)**

The DIM-based VISAR diagnostic can measure the velocity of a moving surface, or shock-front by recording the induced Doppler wavelength shift; consequently VISAR was the primary method for tuning the timed shocks during the national ignition campaign [48] [49]. The probe consists of a 60 kW frequency-doubled Nd:YAG laser operating at 659.5 nm; special coatings and filters are required for the relay optics to reject the NIF drive laser wavelengths and to remove breakout and thermal light.

The probe light is delivered to TCC using three large-core 1-mm optical fibers combined with monitors to ensure the power is low enough to minimise Brillouin scattering. Reflected light from the capsule is collected by a triplet lens and routed out of the DIM through a 2" thick vacuum window. The preliminary image is picked up by an initial doublet lens and relayed to the interferometer table using a turning mirror. The interferometer utilises a delay etalon in one leg so that the recombined fringes move when the wavelength changes due to Doppler shift. A lens is then used to focus the recombined fringe image onto the input slit of a streak camera.

### **1.7.8 DANTE**

The NIF Dante diagnostic measures the changing X-ray emission of low-energy 50 eV-20 keV X-rays across 18 channels to report time-resolved temperature measurements during ICF experiments [50] [51]. The 18 channels combined with a complex fitting algorithm are used to produce a series of black body spectra as a function of time. In addition, integrating the recorded Dante black body spectrum provides the total X-ray drive power in the hohlraum at each recorded time.

A specific region of the X-ray emission from a hohlraum or direct drive target is selected using absolutely calibrated K- and L- edge filters and mirrors and converted to an electrical signal using a single X-ray diode (XRD) with Au photocathode

per channel. The high fluxes emitted during hohlraum experiments at NIF require additional attenuation compared to the same system on Omega to keep the recorded signals within the linearity of the XRD. The attenuation cannot be achieved using filters or by reducing the XRD aperture size: the former because additional filtering would reduce the signal to noise between the desired low-energy X-ray range and m-band gold contaminant X-rays, the latter is because the non-linearity of the XRD scales proportionately with the area of the photocathode. The solution is to place a well-calibrated pinhole array (sieve) in front of the XRD which can be changed to attenuate the X-ray emission to the correct fluence for the XRD.

The large separation between photodiode and oscilloscope require that the broadening due to the non-ideal behaviour of the transmission line be calibrated; this is calculated by sending a known 10 ns square pulse down the signal line and recording the broadened signal. The transfer function can be unfolded from the signal and used to deconvolve experimental signals.

### 1.7.9 Filter fluorescer X-ray detector (FFLEX)

The port-mounted FFLEX diagnostic is designed to measure time-integrated hard X-rays in the range 18-150 keV across 8 channels emitted from an implosion target [52].

A schematic of the FFLEX setup for one of the eight channels is shown in Figure 1.17. X-rays from the implosion are initially filtered to remove the low energy component of the emission; a fluorescer and post-filter made from the same material are then used to complete the system narrow-pass filter. For example tantalum ( $K$ -shell  $\approx 67$  keV) and ytterbium ( $K$ -shell  $\approx 61$  keV) are used as the pre-filter and fluorescer/post-filter in channel 5 respectively. The channel response is obtained from the product of the transmission spectrum for the pre and post filter together with the fluorescence cross section.

After filtering the X-ray signal is recorded using a NaI(Tl) scintillator combined with a PMT. Signal rise time is dominated by the NaI scintillator material and is

on the order of 230 ns; fall time is approximately 100  $\mu$ s.

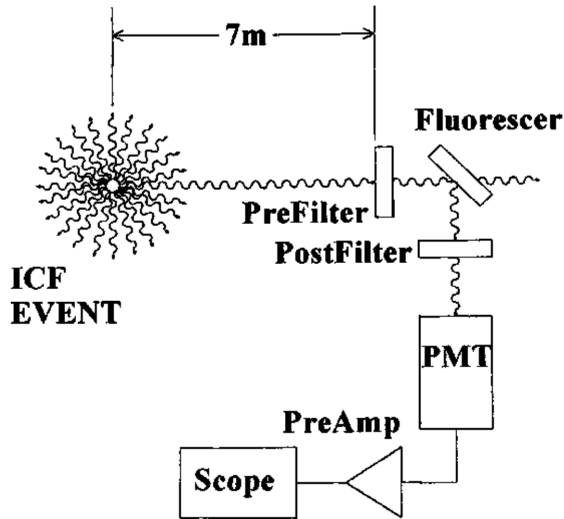


Figure 1.17: Diagram of the FFLEX diagnostic at NIF from the literature [52]. The hard X-ray spectrum in the range 18-150 keV emitted during a laser-plasma interaction is recorded using 8 narrow-band channels consisting of a pre-filter, fluorescer, post-filter and photomultiplier system.

### 1.7.10 Gated X-ray Detector (GXD)

The gated X-ray detector is designed to measure temporally resolved X-ray images of the implosion using a pin-hole array, gold photocathode, MCP, phosphor electron-photon converter and CCD. The NIF GXDs are designed to work in a diagnostic instrument manipulator (DIM) at NIF or ten inch manipulator (TIM) at Omega (or AWE's ORION facility). Detector spectral sensitivity is between 0.2 to 10 keV depending on filter type and temporal resolution ranges from 40 ps to a few ns depending on the MCP voltage stripline. The GXD is generally fielded with the nose cone array 1.5 m from TCC; at this close proximity the complex electronics required to trigger the MCP, phosphor and CCD are susceptible to electromagnetic interference and induction. Consequently the entire diagnostic is contained within a sealed aluminium airbox which acts as a Faraday cage around the electrical components. Several feedthroughs are required to provide the detector with 28 V power, signal and trigger cables, and water coolant [53].

The signal recorded by GXD is generated by first filtering the broad-energy X-ray emission to obtain the desired X-ray cutoff. The signal then passes through a pinhole at the specific distance required to obtain a particular magnification. Beyond the pinhole array a gold photocathode is used to convert the X-ray signal into a low-energy electron signal. The MCP is manufactured with four stripline electrodes designed to handle the 3kV output from the gating module. Each stripline can be fired at any time during the experiment with a tolerance of  $\pm 40$  ps i.e. simultaneously, sequentially or any other combination. Once triggered the 3 kV voltage pulse travels the length of the stripline in a minimum of 200 ps, which is tunable using interchangeable pulse-forming modules. The gain produced by the microchannel plate is a function of the voltage as it transits across the stripline, this combined with the pinhole array produces several X-ray images at different times from a single strip of the MCP. The amplified electron signal then encounters a P43 phosphor ( $\lambda=540\text{nm}$ ) coated fiber-optic faceplate which simultaneously receives a voltage trigger and converts the electron images into visible light. The light is subsequently coupled to a Spectral Instruments SI-1000 charge-coupled device (CCD) camera where it can be digitally downloaded and manipulated post shot.

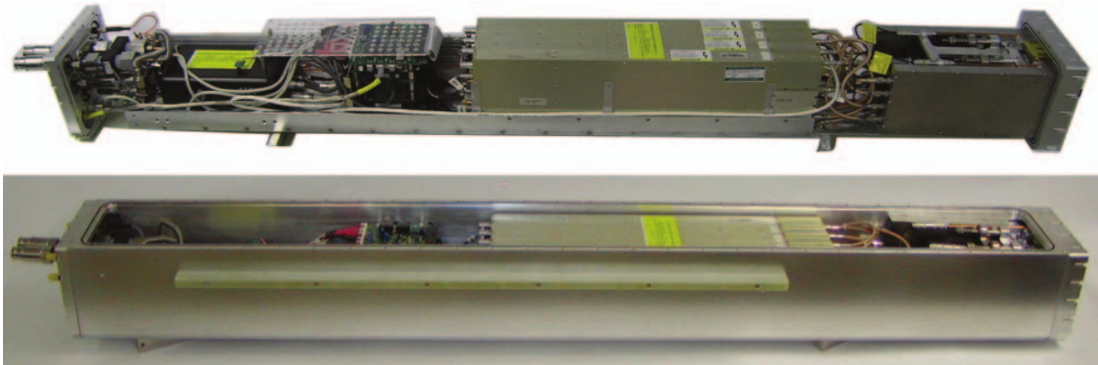


Figure 1.18: Photo of the GXD outside and inside the airbox; above and below respectively.

### 1.7.11 Cherenkov detectors

The Cherenkov detectors at NIF and Omega are designed to measure reaction history (RH) and bang-time (BT) to within 50 ps using  $\gamma$  photons emitted at low intensity during the  $D(T,n)^4\text{He}$  reaction [54]. The dominant branch in  $D(T,n)^4\text{He}$  reaction involves the emission of a 14.1 MeV neutron and a 3.5 MeV  $\alpha$ ; however there is a competing channel which proceeds through a  $3/2^+$  resonance in  $^5_2\text{He}$  via an electromagnetic dipole transition to either the  $3/2^-$  ground state or  $1/2^-$  1st excited state [55]. The strength of these competing gamma decay branches is much reduced relative to the neutron emitting channel; nucleon emission is a far quicker decay mechanism and therefore the relative branching ratio [35] for the combined gamma emitting channel is  $(4.2 \pm 2) \times 10^{-5}$ . During routine ICF implosion experiments at Omega DT reaction yields measured using the nToF diagnostic reach over  $1 \times 10^{13}$  and therefore  $\times 10^8$  DT gammas are also emitted. Measuring the gamma emission has several advantages over particle-based approaches: gammas travel at the speed of light (SOL) and arrive at the detector before much of the  $n,n'\gamma$  and  $n,\gamma$  background, and gammas suffer no thermal time-of-flight spreading therefore preserving the implosion reaction history at large source-detector separations. Gammas do however arrive approximately time-synchronous with any thermal or fast-electron X-ray emission from the laser plasma interaction.

The non-nuclear X-ray background can be mitigated using a Cherenkov-based gamma detector system [56]. The detection principle involves the gamma signal first being converted to an electron distribution in a thin low- $Z$  metal converter. The electron distribution heading in the forward direction retains most of the original gamma energy with the maximum transfer occurring for  $E_{e^-}(\theta = 0^\circ) = E_\gamma - \frac{m_e c^2}{2}$ . The electron distribution is then channelled through a high-pressure gas with an appropriate refractive index for the emission of Cherenkov light. Depending on the space and mass constraints on the detector the light can be reflected and focused via a series of optical components onto a fast MCP-based PMT [57] [58] as shown in Figures 1.19 and 1.20 and 1.21.

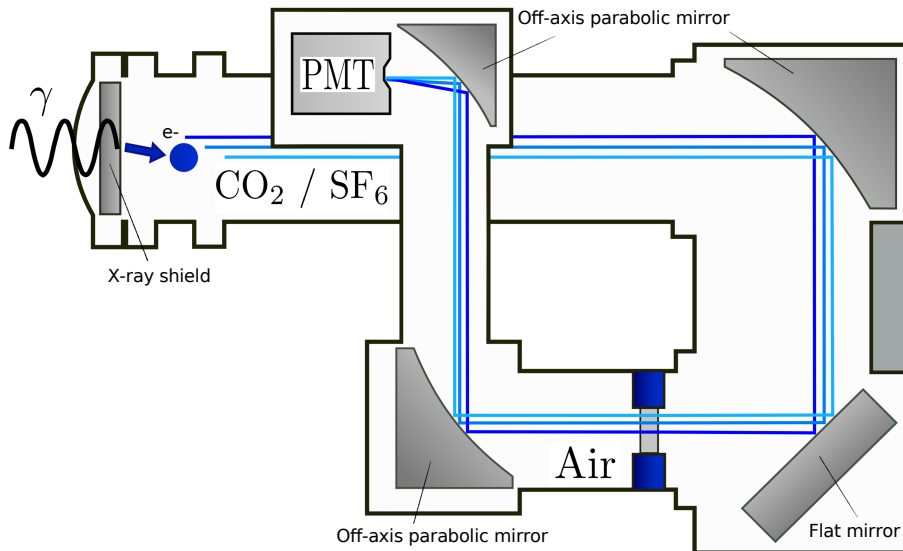


Figure 1.19: Not-to-scale schematic of the Gamma Reaction History (GRH) diagnostic fielded at NIF and Omega. At NIF the diagnostic is located external to the vacuum chamber at approximately 6m from TCC. 3 mm of tungsten is placed in the nose to filter out X-rays from the implosion hot spot and laser–plasma interaction, followed by a 1 cm thick low–Z Compton conversion region to generate the high–energy electrons required to produce Cherenkov light. Three off-axis parabolic mirrors and a flat mirror are used to direct the Cherenkov light around four corners to the PMT. The optical relay was designed by Robert Malone (LANL) to produce identical path lengths for an ideal Cherenkov source placed immediately behind the converter. The second region of the diagnostic behind the pressure window is at air to accommodate the PMT. The routing has been designed to allow significant amounts of tungsten shielding to be placed between the laser plasma interaction and the PMT to increase signal–to–noise ratio. The detector can handle gas pressures of up to 215 psia  $\text{CO}_2$  or  $\text{SF}_6$ .

An important consideration for the Cherenkov detectors is the relation between gas pressure, density and refractive index. Appendix A contains a review of the literature and parameterised fits for the gases  $\text{CO}_2$ ,  $\text{SF}_6$  and  $\text{C}_2\text{F}_6$ .

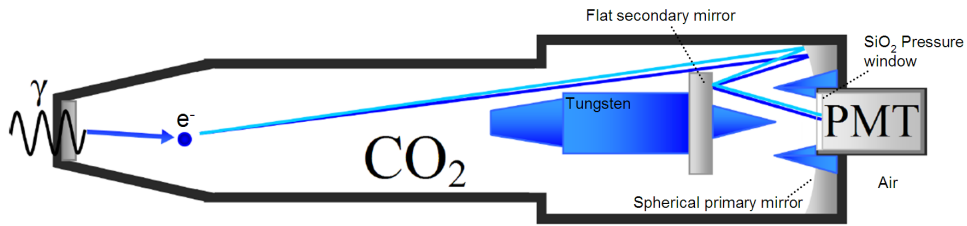


Figure 1.20: Not-to-scale schematic of the Gas Cherenkov Detector 1 (GCD 1) fielded at Omega inside a ten-inch manipulator (TIM). In this variant the PMT is placed immediately behind the pressure window inside an annulus of tungsten shielding (blue). The spherical primary and flat secondary mirrors focus the optical Cherenkov light onto a 12 mm disc at the photocathode. The large tungsten block removes the majority of high-energy  $\gamma$  photons from directly interacting with the PMT. As with GRH there are a few millimetres of high-Z material in the nose to remove low energy X-rays followed by a 1 cm thick low-Z Compton conversion region.

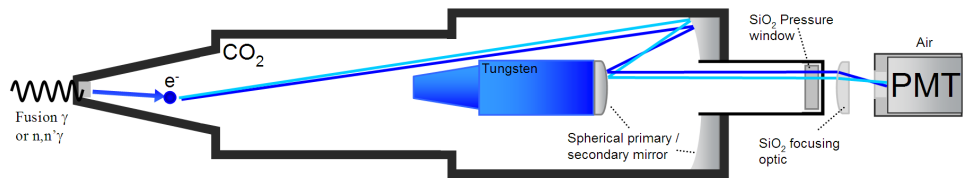


Figure 1.21: Not-to-scale schematic of the Gas Cherenkov Detector 2 (GCD 2) fielded at Omega inside a ten-inch manipulator (TIM). In this version the PMT is located behind the gas cell inside a separate housing. This was initially conceived such that the parallel light from the detector could be routed to a streak camera away from the high-background environment of the target hall. The spherical primary and secondary mirrors produce a parallel light profile which is subsequently focused by an optic a short distance in front of the PMT. The large tungsten block removes the majority of high-energy  $\gamma$  photons from directly interacting with the PMT. As with GRH there are a few millimetres of high-Z material in the nose to remove low energy X-rays followed by a 1 cm thick low-Z Compton conversion region.

## 1.8 Summary

The preceding chapter has introduced the Omega and NIF laser facilities, and the difficulties encountered in the pursuit of ignition during the high and low foot campaigns. Significant physics design and modelling work was performed by the community in support of this goal; it is evident however that at the time of writing the NIF is far from producing excess energy in the form of thermonuclear burn from an ICF implosion. Consequently efforts must be focused on diagnosing the failure modes of current designs using the latest technology. The next chapters will focus mainly on development and characterisation of the Cherenkov detectors at NIF and Omega using Monte Carlo techniques. Improvements in the accuracy of bang time measurements and reaction history reported by these detectors constrain the modelling efforts throughout the ICF design community.

# Chapter 2

## Monte Carlo Codes

### 2.1 Geant4

Geometry and tracking 4th edition (GEANT4) is a particle physics Monte-Carlo toolkit for modelling radiation interactions with detector materials [59]. Written by researchers at CERN and SLAC, amongst others, the C++ object-oriented code allows user's to define complex detector geometries by performing Boolean subtractions, unions and intersections on volumes, such as cylinders, boxes and spheres. Physics packages include electromagnetic, nuclear, high-energy particle and optical physics, with a low energy limit occurring at approximately 250 eV. The user however must implement the relevant individual physics packages for their simulation; in addition each physical process may have several models available with overlapping energy regimes and at different accuracies. These are implemented at the users discretion. Particles are tracked in a dynamic stepwise manner; dynamic in this case refers to the modification of the time-step depending on the shortest mean free path of the instantiated processes. Consequently, tracking resolution evolves to match the requirement of the current material. Visualisation and ray tracing, important components of detector modelling, are handled through several packages [60]: HepRApp, OpenGL, DAWN, RayTracer, VRML, gMocren, QT and openInventor. Each has unique qualities and a full discussion is beyond the scope of

this thesis. HepRApp is currently used and useful aspects include: 3D interactive detector visualisation, ray-tracing, trajectory cuts, detector hierarchy interrogation and export to various file formats.

An additional consideration for the Monte Carlo modelling is the ability to correctly predict nuclear interactions with the detector geometry, such as elastic, inelastic and capture interactions of neutrons down to thermal energies. Consequently the high-precision elastic, capture and inelastic processes were added to the neutron particle at startup. The high-precision inelastic processes use data from the Evaluated Nuclear Data Files version 6 (ENDF/B-VI) for incident neutron energies between 0 and 20 MeV and include the final states:  $\gamma$ ,  $n'\gamma$  (discrete and continuum), np, nd, nt,  $n^3\text{He}$ ,  $n\alpha$ ,  $nd2\alpha$ ,  $nt2\alpha$ ,  $n2p$ ,  $n2\alpha$ ,  $np\alpha$ ,  $n3\alpha$ ,  $2n$ ,  $2np$ ,  $2nd$ ,  $2n\alpha$ ,  $2n2\alpha$ ,  $nX$ ,  $3n$ ,  $3np$ ,  $3n\alpha$ ,  $4n$ , p, pd,  $p\alpha$ ,  $2p d$ ,  $d\alpha$ ,  $d2\alpha$ , dt, t,  $t2\alpha$ ,  $^3\text{He}$ ,  $\alpha$ ,  $2\alpha$ , and  $3\alpha$  [61].

The GEANT4 toolkit is constructed such that each part of the simulation is compartmentalised into classes or objects which can share variables, functions and subroutines. Most classes are provided as part of the source code and include: standard Monte Carlo geometric shape descriptions and combinatorial manipulation, particle descriptions, GEANT4 run manager, tracking algorithms, physics modules and pre-built lists, isotope and materials, run management, visualisation packages and example simulations to name a few. To produce a working simulation the user must create a separate directory containing at minimum a main c++ program (this is common to all c++ programming) which must include the instantiation of the GEANT4 run manager, a detector construction class containing a description of the simulation geometry, world and materials, a physics list containing particles and their associated physics processes (a pre-built list from the source code can be called instead) and a primary generator containing the commands and algorithms associated with generating the particle source. Throughout this thesis the GEANT4 simulations for the Cherenkov detectors and other systems are generally constructed in the same way. The list below outlines the classes and their purpose

- **Main program** includes creation of the run manager, detector construction,

physics list, primary generator, event action, stepping action, visualisation and GEANT4 interactive session objects. In addition arguments are read into the main program from command line and passed to other parts of the simulation, for example variable parameters that modify parts of the geometry or source between runs. After the aforementioned classes are instantiated the user must instruct the run manager to run a specific number of events.

- **Detector construction** includes isotope and material definitions, volume (logical and physical) definitions including boolean operations, material property tables, such as refractive index and optical reflection as a function of energy, and sensitive detector definitions.
- **Physics list** contains definitions of particles used (only those pertinent to the simulation are defined to save memory), physics models attached to specific particles, such as Compton scattering and pair production for  $\gamma$  photons, and particle cut information which specifies the energy or range at which a particle ceases to produce secondary particles. In some cases throughout this thesis the pre-built QGSP\_BERT\_HP physics list is used instead of a user-generated version for simplicity.
- **Primary Generator** Contains commands and algorithms associated with generating the particle source. The interactive program called General Particle Source (GPS) can be used which has pre-written sources for a variety of scenarios which can be adjusted for a specific requirement; it is however inflexible when dealing with complex source terms. The preferred approach used throughout this thesis is the particle gun method which allows the user to specify all aspects of the source, such as particle type, location, time, energy, direction, by any means available in a modern programming environment. This may involve random numbers or reading in a source term from file generated elsewhere, to mention two. This approach is obviously powerful but requires validation effort to ensure errors are not introduced.

- **Sensitive Detector** Specific volumes in the detector geometry can be set as sensitive. GEANT4 then allows the user access to pre and post step data for all particles entering the volume during the simulation. Without any sensitive detector, or alternative, GEANT4 is a silent code that runs efficiently. Step information consists of any attribute that can be imagined for a particle. Commonly required attributes are: name, kinetic energy, global/local time, ionisation, direction, atomic mass/number, current volume. This information can then be used to populate user-defined arrays passed from other parts of the simulation, such as a temporal array recording the time of optical photons passing the boundary of a sensitive volume (photocathode or pressure window for example), or an array containing the energies of  $\gamma$  photons passing the boundary of a sensitive volume. There are pre-built methods for creating histograms in GEANT4; however significant Monte Carlo experience and physics understanding can be gained by creating bespoke histograms combined with complex logical conditions.
- **Event action** allows the user access to the simulation before and after each event. An event is defined as the completion of one single source term defined in the primary generator action; this may involve more than one particle for complex source terms such as  $\beta$  decay. This class can be used to periodically inform the user of the status of the simulation, write histograms generated inside the sensitive detector to file or to reset boolean flags and variables used to indicate the meeting of a logical condition elsewhere in the simulation.
- **Run action** analogous to event action this class gives the user access to the simulation before and after the run. This is generally where arrays are initialised and resolutions defined to be passed to the sensitive detector and event action objects later in the simulation. In addition run action can be used to perform the final writing out of histograms to file at the end of the run.
- **Stepping action** A stepping action class contains the same functionality as

the sensitive detector class however the object is instantiated for every step occurring in the simulation, in contrast to a specific detector logical volume. The stepping action class is a powerful tool when it comes to debugging a simulation but produces poor efficiency when running large numbers of source particles. Care must also be taken to ensure the volume information is contained in any output to avoid confusion and misleading results.

In exceptional cases additional classes may be used and these will be discussed throughout this thesis where required.

## **2.2 ITS: ACCEPT**

The integrated tiger series of codes are a set of powerful software packages written in Fortran 90 designed to model through Monte Carlo methods linear-time-independent coupled electron/photon radiation transport within spatially dependent macroscopic electric and magnetic fields [62] [63]. The user selects one of the many ITS codes through the preprocessor directive. Particle scattering is approximated by employing accurate cross sections, sampling distributions, and physics models for describing the production and tracking of  $e^-/\gamma$  interactions from 1.0 GeV to 1.0 keV. The availability of source code permits the more sophisticated user to tailor the simulation to specific applications and to extend the capabilities of the codes to more complex applications.

ACCEPT, one of many ITS models originally released in 1979, is a general 3-dimensional transport code utilising the combinatorial-geometry technique originally developed to investigate the nuclear and conventional vulnerability of armoured military vehicles such as the US M60A1 tank [64].

## **2.3 MCNP**

The Monte Carlo neutron particles (MCNP) code written in Fortran 90, developed and maintained by Los Alamos National Laboratory is the benchmark for investi-

gating the transport and effect of incident neutrons and  $\gamma$  photons through complex geometries via the Monte Carlo method [65]. Neutron interaction cross sections are obtained from the ENDF/B-VI library; thermal neutrons are treated through either the free gas formalism or the  $S(\alpha, \beta)$  technique. The code also supports coupled transport i.e. the production of secondary  $\gamma$  photons from neutron interaction, and also comprises continuous stopping and bremsstrahlung / X-ray line emission for electrons produced either as a primary particle or following  $\gamma$  scattering interactions.  $\gamma$  physics includes incoherent (Compton) / coherent (Rayleigh) scattering, photoionisation and pair production (with subsequent 511 keV annihilation emission). The code uses an arbitrary 3-dimensional configuration of materials in geometric cells bounded by 1<sup>st</sup> and 2<sup>nd</sup> -degree surfaces and 4<sup>th</sup> -degree elliptical tori [66].

Unlike GEANT4 and ACCEPT, the MCNP source code is not freely available; therefore modifying physics processes or creating unique tallying algorithms is currently impossible. Geometry, source, physics and tally structures are defined in an input deck or macro to be read by the executable at run time which reduces the versatility of the code. Nonetheless MCNP is the world's leading Monte Carlo code for the simulation of neutron interactions for the energy-regime discussed in this thesis.

## 2.4 Benchmarking

Prior to the author's involvement in the ICF community in 2008, modelling of the Omega and NIF Cherenkov detectors had been performed using two codes from the Integrated Tiger Series: CYLTRAN and ACCEPT. It was decided that the Monte Carlo code GEANT4, produced by a different physics community, would augment the existing models and provide additional capabilities associated with a modern object-oriented code.

Before embarking on the complex Cherenkov detector geometries and source terms a simple test problem was created for the purpose of benchmarking some of the relevant physics [67]. Figure 2.1 shows the side view of a 1.5 cm thick beryllium

cylinder with 3.5 cm radius and density of 1.85 g/cm<sup>3</sup>. The source term was a  $\gamma$  photon with  $E_\gamma = 17$  MeV starting 5 cm in front of the beryllium cylinder with starting vector [0,0,1] where the  $z$  is in the same direction as the cylinder thickness. The low energy cut-off (ACCEPT) and secondary production threshold (GEANT4) were both set at 1 MeV. The standard electromagnetic processes were used for both codes (GEANT4: G4EmStandardPhysics). The tallying structure consisted of a surface on the rear of the beryllium cylinder with a radius of 3.5 cm and measured absolute particle numbers divided by the number of source  $\gamma$  photons. A tally surface is allowed in the ITS ACCEPT code; in GEANT4 however a cylindrical sensitive detector was placed behind the beryllium converter and a logical statement written to record only the first step (always the volume boundary) of  $e^{-/+}$ s in the volume. Three scenarios would be simulated to investigate the  $\gamma$  conversion process: the first simulation involved the invocation of all  $\gamma$  conversion processes (Compton scattering, pair production and photo-ionisation), the second with pair production turned off and Compton scattering on, and the third with Compton scattering off and pair production on. Any differences observed in the output would highlight areas for investigation, and possibly require the use of different physics modules.

The two parameters investigated were the angle of  $e^{-/+}$  emission integrated over all energies in 2° bins, and the  $e^{-/+}$  energy spectrum integrated over all angles in 1 MeV bins. The number of source particles for each simulation was not explicitly stated. Figure 2.2 shows the code comparison for the angle-integrated energy-resolved case with GEANT4 in broken red and ACCEPT in broken blue. Agreement is good for all process permutations with the small differences due to counting statistics as opposed to the underlying physics processes. The reduction in counts observed in GEANT4 relative to ACCEPT at 1 MeV in the angle-integrated comparison is due to the difference in definition of threshold between the codes and does not represent incorrect simulation of the physics. In GEANT4 the number of counts increases to match the ACCEPT value if the threshold is reduced to 0.1 MeV. Both GEANT4 and ACCEPT predict the Compton scattering peak to occur at 14 MeV. Figure 2.3 showing the code comparison for the energy-integrated

angle-resolved case with GEANT4 in broken red and ACCEPT in broken blue. As with the energy-resolved case the agreement is good for all process combinations. The peak at  $\theta = 5.5^\circ$  however is lower in the GEANT4 model by approximately 5%; examining the individual processes suggests that the small difference originates from the Compton scattering process. The pair production comparison shows good agreement.

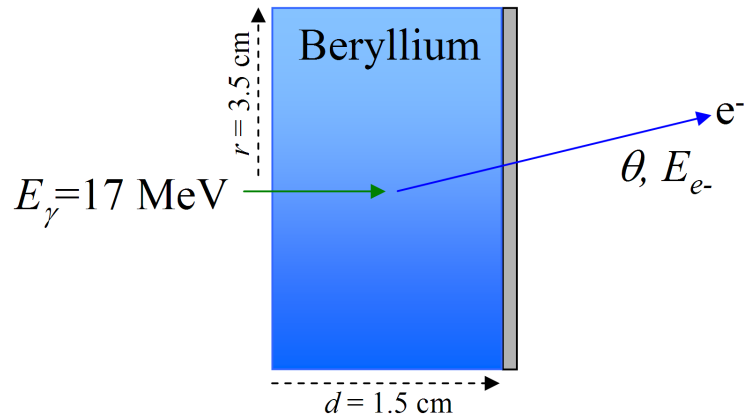


Figure 2.1: Diagram of the test problem devised by J. Mack [LANL] used to compare the  $\gamma$  Compton scattering and pair production processes and electron tracking algorithms.

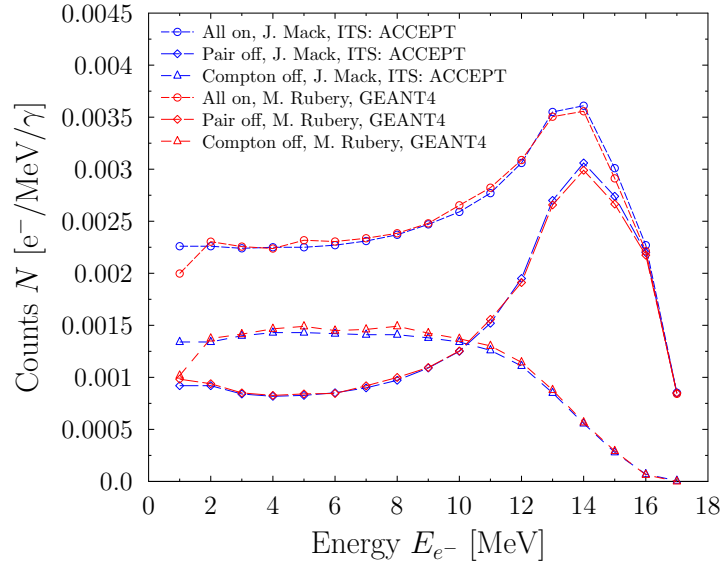


Figure 2.2: Plot showing the energy-dependent (angle-integrated) results from the test case devised by J. Mack [LANL] described in Figure 2.1. GEANT4 and ACCEPT are shown in broken red and blue respectively.

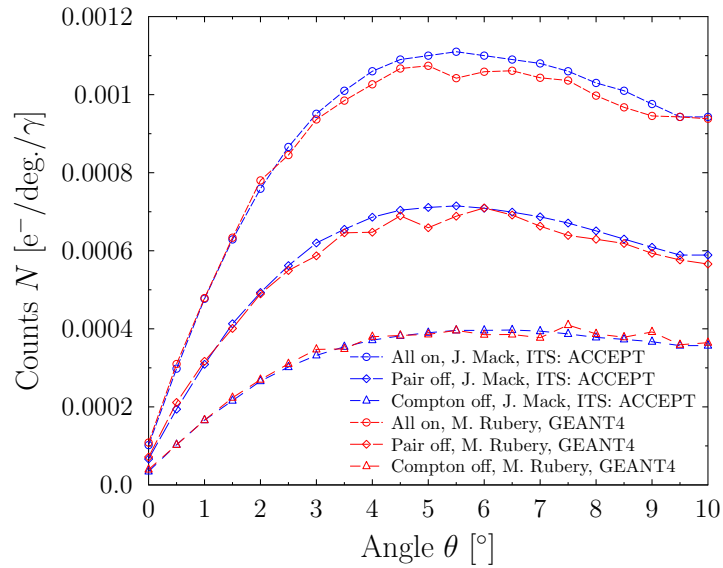


Figure 2.3: Plot showing the angle-dependent (energy-integrated) results from the test case devised by J. Mack [LANL] described in Figure 2.1. GEANT4 and ACCEPT are shown in broken red and blue respectively.

## 2.5 Validation at the high intensity $\gamma$ source

There are scenarios where parameters and functions required for post-processing measured data are inaccessible, such as bandwidth limitations, physical restrictions, costs and time constraints. This is where particle physics Monte Carlo codes are useful. For example, to measure the time-response of the GRH Cherenkov detector to the  $\gamma$  DT spectrum would require a maximum 1 ps  $\gamma$  source (with the correct spectral shape) and the detector to be connected to a fast  $< 5$  ps streak camera with a dynamic range of at least 100 and a S/N of better than 10. This is a feasible measurement however with significant human effort, cost and time. A more time and cost-efficient approach would be to use a Monte Carlo code, such as GEANT4 and ACCEPT. The codes however should be treated with caution and consequently significant effort has been spent to validate the models as discussed in the next section, and to cross-calibrate the underlying physics as discussed in Section 2.4

A series of experiments were designed to characterise the response of the detectors to several source configurations for comparison with the Monte Carlo models. Furthermore, additional modelling support conducted by C. S. Young [LANL] using the ACCEPT code and an independently generated GEANT4 model of the GRH detector by E. Grafil [LLNL] are presented.

The high-intensity  $\gamma$  source at Duke University, North Carolina, USA [68], can supply a mono-energetic  $\gamma$  signal between 2-60 MeV at an intensity of up to  $1 \times 10^9 \gamma s^{-1}$  with a beam diameter of  $\approx 1$  cm. Ultraviolet photons are up-shifted to multi-MeV energies through an inverse Compton interaction with high-energy electrons from an accelerator storage ring. The GRH (fielded at NIF [69] and OMEGA [70]) and GCD (fielded at OMEGA) were brought to the facility with the intention of measuring the response of the diagnostics to the calibrated  $\gamma$  signal for a range of pressures and geometries for comparison with simulation. The objective was to validate two aspects of the models: the relationship between observed optical intensity and gas-cell pressure, and optical intensity with diagnostic location and orientation. The first 'pressure' comparison validates the algorithms used to calcu-

late density and refractive index and the second 'translational' approach confirms the accuracy of the user-built geometry and optics. Figure 1.19 and 1.20 show the GRH and GCD respectively in schematic form; both utilise the same physical principles. High-energy  $\gamma$  radiation normally from an ICF implosion is incident on the converter region where it converts to an electron distribution through Compton scattering and pair production with efficiency depending on the energy of the original photon [71]. The electron distribution is then channelled through a high-pressure (0-220 psia) gas cell. The portion of the electron distribution travelling above the gas-cell light velocity will emit Cherenkov radiation; this radiation is subsequently re-directed using one or more optics onto a micro-channel-plate (MCP) based photomultiplier tube (PMT) [57].

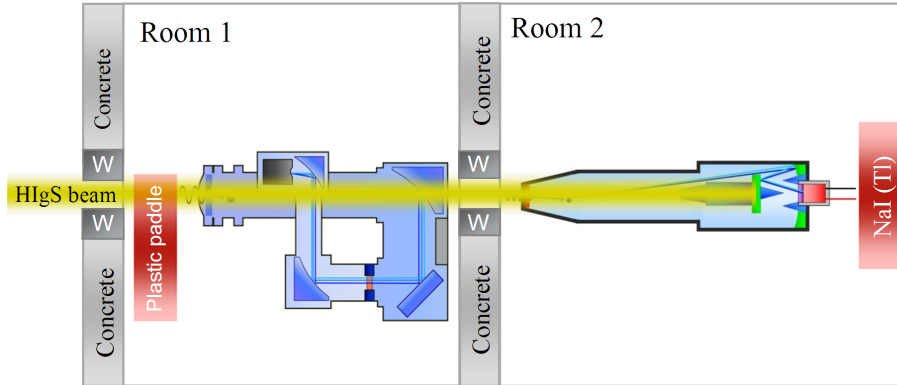


Figure 2.4: Schematic of HI $\gamma$ S experimental configuration.

During the HI $\gamma$ S experiment current from a single or double stage microchannel-based Photek PMT was recorded using a Keithley picoamp electrometer. Electrometer and PMT dark currents were continually monitored over the course of the two-week experiment and never exceeded 10% of the signal. The  $\gamma$  intensity was continually monitored using a stack of 5 sheet plastic paddle detectors, thin enough to record intensity without scattering or depleting the beam during use. Coincidence counting techniques were also implemented to reduce background signals. The paddle detector was calibrated against a large 10''  $\times$  12'' sodium-iodide NaI(tl) crystal detector prior to the experiment. A linear relationship was supplied by the



Figure 2.5: Photo of the HI $\gamma$ S NaI(tl) array used as the flux benchmark for cross-calibration with the plastic paddle detectors.

HI $\gamma$ S facility to convert the recorded paddle intensity  $J_\gamma$  to  $[\gamma\text{s}^{-1}]$  with a different scaling factor for each of the three energies used throughout the campaign. These were 16.86 MeV, 10 MeV and 4.43 MeV; the first and last were chosen to replicate the primary peak of the DT  $\gamma$  spectrum and the 4.4 MeV  $^{12}\text{C}$  n,n' $\gamma$ , and the second chosen as an intermediate value.

$$P_\gamma = MJ_\gamma, \quad (2.1)$$

where  $P_\gamma$  is the paddle flux in  $[\gamma\text{s}^{-1}]$ . The conversion factors were  $M(16.86 \text{ MeV}) = 68.1 \pm 7$ ,  $M(10 \text{ MeV}) = 61 \pm 6$  and  $M(4.43 \text{ MeV}) = 85 \pm 9$ .

In the GEANT4 model the array resolution for the refractive index was 10 nm between 200 nm and 800 nm, with a linear interpolation performed by the toolkit at run time. The upper limit of 800 nm was introduced due to the negligible quantum efficiency of the S20 photocathode (PC) beyond this wavelength. During simulations Cherenkov photons crossing the PC surface were recorded per source  $\gamma$  for comparison with experiment, data in this form will be referred to as 'response' from this point onward. Errors for all simulations were obtained by running the simulation a minimum of 10 times and calculating the standard deviation in the

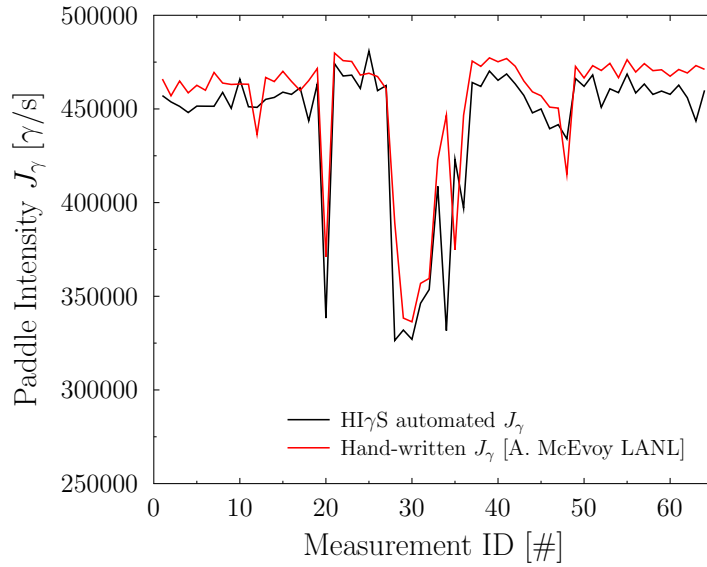


Figure 2.6: Plot showing the paddle intensity as recorded by the automated HI $\gamma$ S system and a manual record kept by A. McEvoy [LANL] during the  $E_\gamma=16.86$  MeV, 65 psia CO $_2$  GRH translational measurement. The data shows the large fluctuations seen in the HI $\gamma$ S intensity over the course of a few hours.

desired parameter; consequently simulation errors do not include uncertainties in the dispersion, density, geometry or transmission/reflectance spectra. Response values recorded during the HI $\gamma$ S experiment consisted of a measured electrometer charge between some recording limits  $t_1$  and  $t_2$  together with a varying paddle flux measurement over the same period. Figure 2.6 shows the paddle intensity recording using two different methods during the  $E_\gamma=16.86$  MeV, 65 psia CO $_2$  GRH translational measurement. The black data was produced using an automated routine by the HI $\gamma$ S facility and the red generated by A. McEvoy [LANL] by continuously monitoring the paddle counter; investigations by the HI $\gamma$ S facility suggest the second approach shows the best correlation with NaI(tl) calibration crystal. Nonetheless the agreement is good between the two approaches. To convert the measured value to the same form as the output from simulation the following relation is required

$$R = \frac{\int_{t_1}^{t_2} I_m(t) dt}{QGeM \int_{t_1}^{t_2} P_\gamma(t) dt}, \quad (2.2)$$

where  $R$  is response,  $I_m$  is electrometer charge,  $P_\gamma$  is measured paddle flux,  $e$  is electron charge,  $Q$  is spectrally-averaged quantum efficiency,  $G$  is PMT gain and  $M$  is paddle conversion value. The spectrally-averaged quantum efficiency  $Q$  was obtained using

$$Q = \frac{\int_{\lambda_{200nm}}^{\lambda_{800nm}} Q(\lambda) \frac{1}{\lambda^2} d\lambda}{\int_{\lambda_{200nm}}^{\lambda_{800nm}} \frac{1}{\lambda^2} d\lambda}, \quad (2.3)$$

where  $Q(\lambda)$  is the spectrally dependent quantum efficiency. The process of folding the  $Q(\lambda)$  with the general Cherenkov  $1/\lambda^2$  spectrum is displayed in Figure 2.7 for the single-stage PMT110-001 used in GCD. Following the folding process  $Q$  was found to be  $17.5 \pm 10 \%$ . The large error in folded quantum efficiency is due to uncertainties in the final Cherenkov spectrum following interactions with mirrors and pressure windows, and in the response status of the photocathode at a specific point in time which degrades at different rates across its working spectral range as a complex function of dose and dose rate, as discussed in the next paragraph.

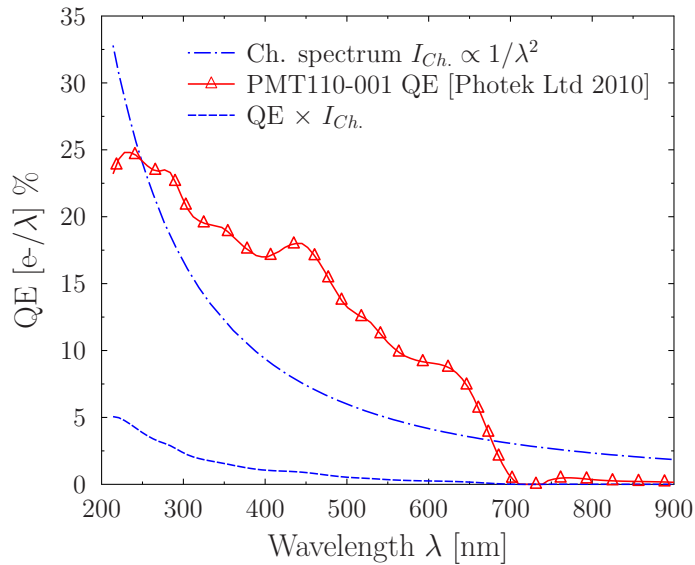


Figure 2.7: Plot showing the PMT110-001 quantum efficiency folded with the general  $1/\lambda^2$  Cherenkov emission spectrum. Comparing the area before and after folding yields a Cherenkov distribution-weighted QE of 17.5%. The QE data provided by Photek Ltd were interpolated to a regular abscissa before folding.

The PMTs for both diagnostics were continually monitored throughout the course of the two week campaign using a dedicated LED test can (TC). The TC has 3 LED colours: red, blue and green, allowing relative measurements of  $Q(\lambda)$ . TC measurements for both PMTs were made several times per day to quantitatively indicate the state of the S20 photocathode, the PMT component most sensitive to prolonged exposure to radiation. Over the two weeks the PMTs were observed to reduce in sensitivity primarily in the red region of the  $Q(\lambda)$  spectrum; the degradation was accounted for in calculations of response. Figure 2.8 shows several of the test can measurements of the peak height and area response to the calibration LED test can for the PMT210-009 used by the GRH detector. The degradation over the two week campaign is clearly evident for the blue, green and red components of the quantum efficiency; the peak height and area track together as expected. The green signal area is larger than the blue due to the long decay time of the green LED used in the test can. Discussions with the manufacturer Photek suggest that the degradation is proportional to total dose and is caused by ions escaping from the micro-channel plate, accelerating in the internal PMT field and modifying the photocathode surface. The total dose observed during the campaign at HI $\gamma$ S was higher and more prolonged compared with shots at NIF and Omega; PMT degradation is therefore not predicted to be an issue during ICF experiments. Figure 2.9 shows a two-part linear approximation to the PMT degradation used for the  $E_\gamma=16.86$  MeV, 65 psia CO<sub>2</sub> GRH translational measurement. Similar approximations were used during all measurements and detectors.

### 2.5.1 HI $\gamma$ S Results

Figure 2.10, 2.11 and 2.12 contain comparisons between code and dark-current-subtracted HI $\gamma$ S electrometer data for a GRH pressure-varying experiment and two GRH translational experiments. In Figure 2.10 agreement is good above the predicted 4.4 MeV Cherenkov threshold of 110 psia across the pressure scan. Below threshold some signal is still observed due to electrometer dark-current drift

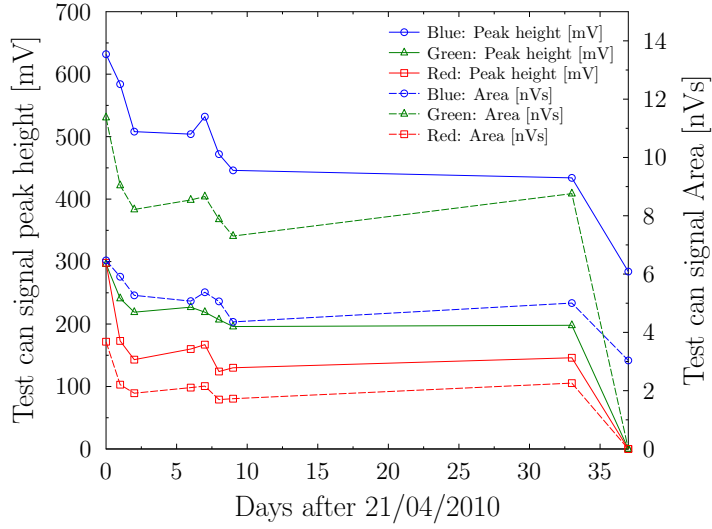


Figure 2.8: Plot showing several LED test can measurements of the peak height [mV] and area [nVs] for the PMT210-009 used in the GRH detector throughout the two-week campaign.

and high-energy bremsstrahlung emission from GeV synchrotron electrons in the  $\times 10^{-11}$  torr rest gas. Bremsstrahlung intensity is estimated at  $\times 10^{-5}$  of the desired monoenergetic  $\gamma$  signal however at such energies conversion to Cherenkov light is extremely efficient. Two translational scans were performed for  $E_\gamma = 4.4$  MeV at 200 psia SF<sub>6</sub> and  $E_\gamma = 16.86$  MeV at 65 psia CO<sub>2</sub> and are shown in Figures 2.11 and 2.12. Agreement is good between measurement and simulation for both scenarios; all models reproduce the shape asymmetry with the peak seen at a beam displacement of approximately -2cm. The peak lies on the side furthest from the second off-axis parabola and is an artefact of the focusing optics [72]. Some electrometer signal still remains when the HI $\gamma$ S beam translates beyond the 12.5 cm diameter gas cell; again this is attributed to  $\gamma$  scattering towards the PMT from the side walls and converter region; direct interactions of  $\gamma$  photons with the PC and MCP are not included in the models therefore the signal disappears from the simulations beyond the side walls of the GRH.

Figure 2.13 contains a comparison between the GCD experiment and simulation

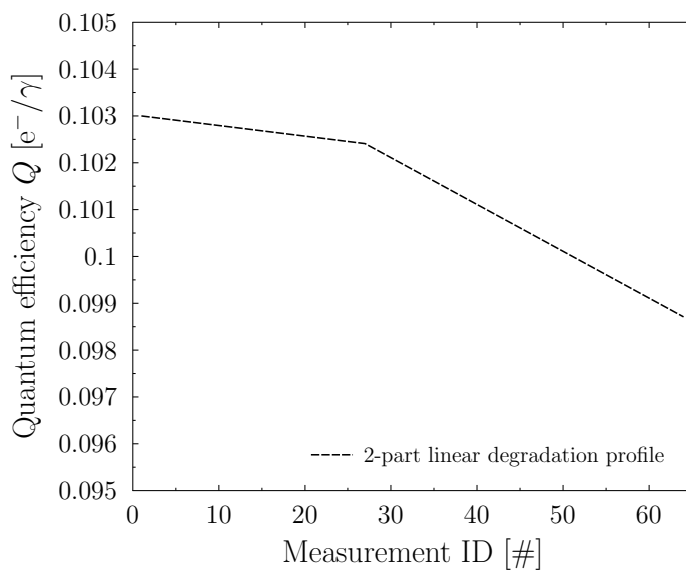


Figure 2.9: Plot showing an example of the two-part linear approximation to the PMT degradation used during the  $E_\gamma=16.86$  MeV, 65 psia CO<sub>2</sub> GRH translational measurement.

over a range of CO<sub>2</sub> pressures for a HI $\gamma$ S beam energy of 16.86 MeV. Measurements were complicated by the GCD being fielded behind the GRH along the beam axis. Consequently the denominator in equation 2.2 must be multiplied by a further attenuation constant  $A_G = 2.5$ , which was obtained by moving the GRH in and out of the beam for the 10 MeV and 16.86 MeV gamma energies. During the experimental campaign it was not possible to take measurements of  $A_G$  for all GRH pressures and orientations; consequently the uncertainty in  $A_G$  is estimated to be  $\pm 20\%$  from Monte Carlo simulations. The agreement between experiment and simulation in Figure 2.13 is good for shape with both codes reproducing the pressure threshold of approximately 18 psia. The intensity comparison required a correction of 0.65 for both models; this is likely due to uncertainties in  $Q$ ,  $A_G$ ,  $P_\gamma$ ,  $G$  and  $M$  which produce a combined error of  $\pm 30\%$ . The purpose of these measurements is to obtain a calibration factor for application to ICF experiments at the NIF and Omega.

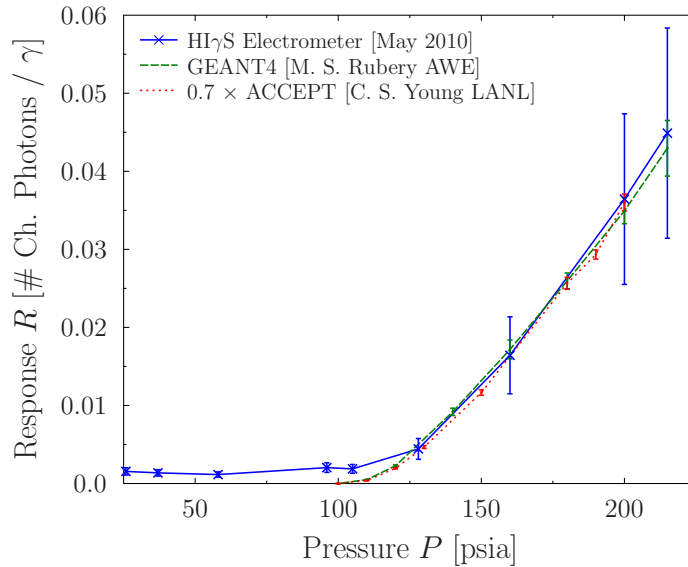


Figure 2.10: Plot showing a comparison between experiment and GRH simulation for a 4.4 MeV  $\gamma$  beam and a range of SF<sub>6</sub> gas-cell pressures.

## 2.5.2 Idaho LINAC facility

The Idaho Accelerator Centre [36] (IAC) at Idaho State University, Pocatello, Idaho can provide a monoenergetic electron source at  $\mu\text{A}$  current levels. In 2001 the GCD was taken to the IAC with intention of measuring the response of the diagnostic to the calibrated source for comparison with the ACCEPT code; GEANT4 modelling of the Cherenkov detectors did not begin until 2010. Set up and data analysis for the 2001 IAC experiment does not form part of this thesis; however the results from the campaign compliment the conclusions from the HI $\gamma$ S comparison. During this experiment the source was not  $\gamma$  radiation but multi-MeV electrons. To allow the electrons to enter the gas cell the aluminium nose cone, Be converter and lead X-ray shield were removed and replaced with a 4 mm thick aluminium plate. This allows electrons to enter the gas cell with a well-defined energy loss and minimal straggling whilst maintaining the pressure boundary. Despite neglecting the  $\gamma$  to electron conversion process, the LINAC configuration allows the output of the diagnostic to be measured for a range of electron energies at a constant pressure. Obtaining

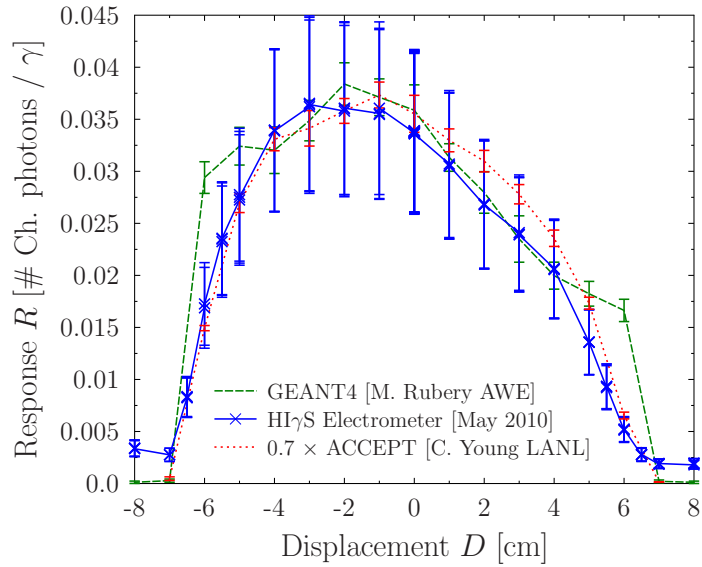


Figure 2.11: Plot comparing the results of translating the HI $\gamma$ S beam across the GRH diagnostic with simulations. The beam energy was 4.4 MeV, and the gas and pressure were SF<sub>6</sub> and 200 psia respectively.

good agreement for the IDAHO configuration would provide good validation for the optics and gas parameters. Figure 2.14 shows a comparison between electrometer data extracted from the PMT and the most recent versions of the ACCEPT and GEANT4 models. Despite requiring a scaling factor of approximately  $\times 0.6$  for both codes the relation between electron energy and response correlate well. The intensity discrepancy is likely due to uncertainties in the PMT quantum efficiency and gain which were not characterised to the same degree of precision as during the HI $\gamma$ S campaign, and the IAC electron beam which was assumed to be a uniform mono-energetic source with  $2^\circ$  dispersion starting from a lead collimator a short distance in front of the diagnostic.

### 2.5.3 Conclusions and discussions

Following the two week experimental campaign at the high intensity  $\gamma$  facility at Duke University and the 2001 Idaho LINAC experiment the Monte Carlo particle

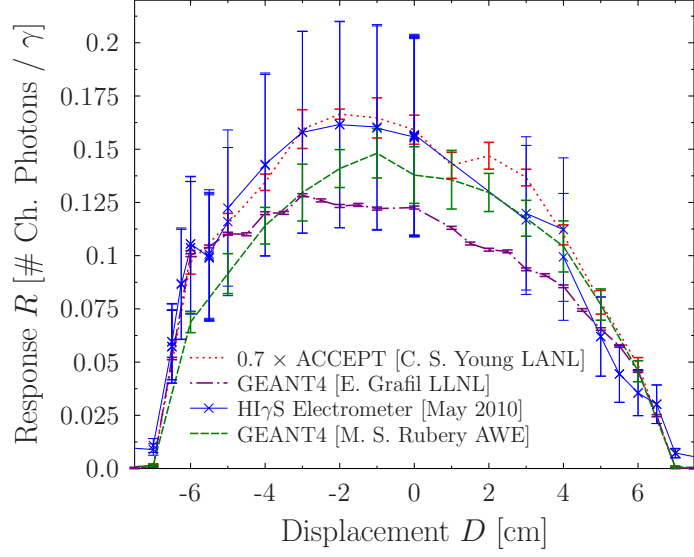


Figure 2.12: Plot showing the translation of the HI $\gamma$ S beam across the GRH diagnostic compared with simulations. The beam energy was 16.86 MeV, and the gas and pressure were CO<sub>2</sub> and 65 psia respectively.

physics codes were able to provide diagnostic parameters for use in inertial fusion experiments at the National Ignition Facility and the Omega laser facility. The code validation process described in this work for the GEANT4 model shows that simulations of the GRH involving a single  $\gamma$  energy absolute response can be used with a confidence of  $\pm 30\%$  across the working pressures range of the diagnostic (0 - 225 psia) during ignition and implosion physics experiments. The  $\pm 30\%$  is a conservative uncertainty due to several diagnostic parameters which were not fully characterised or well understood at the time, such as the mirror/window transmissions and reflectances, HI $\gamma$ S source energy/spatial profile and intensity, and HI $\gamma$ S paddle conversion factors. Future code-validation experiments will require a more in-depth characterisation of these parameters if the uncertainty is to be reduced. For GCD the uncertainty comprises the same issues as above but is slightly higher at  $\pm 50\%$  due to the GCD being fielded down-beam from the GRH during measurements. The uncertainty could be reduced in the future by restricting measurements to periods where the GRH is removed from the line of sight. An important criteria

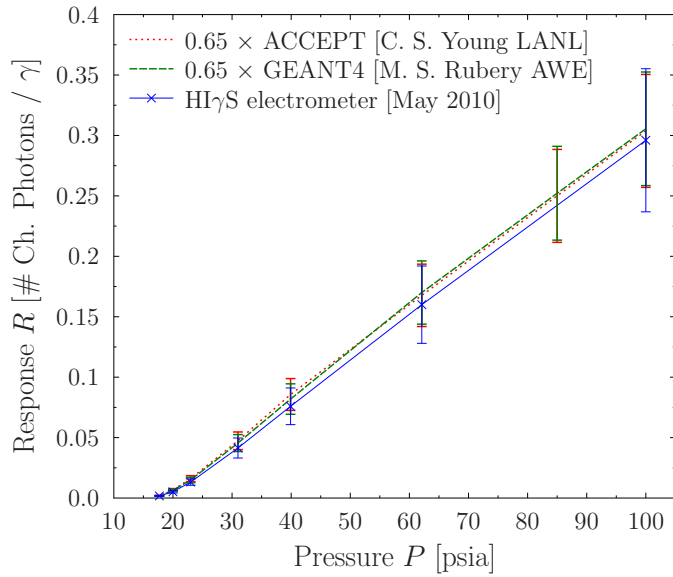


Figure 2.13: Plot showing the intensity recorded by GCD during a 16.86 MeV HI $\gamma$ S pressure scan measurement compared with simulation between 10 and 100 psia.

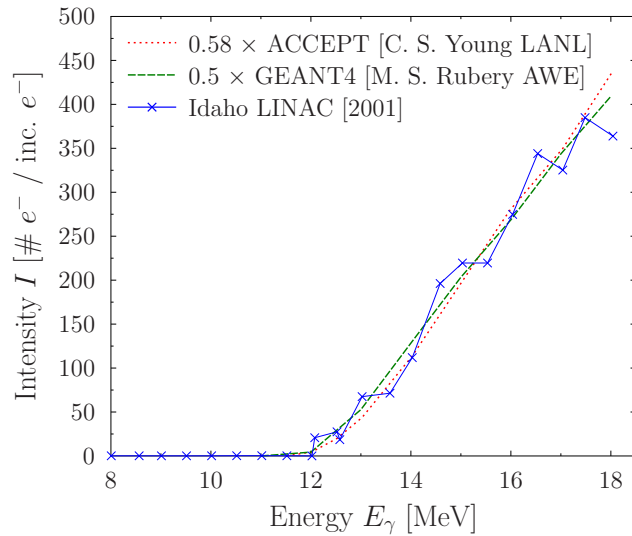


Figure 2.14: Plot showing a comparison between the GCD and data obtained during the 2001 Idaho LINAC experiment [73]. The electron source energy was varied between 8 and 18 MeV whilst holding the gas-cell pressure constant at 30 psia. Scaling factors have been applied to the simulations for illustrative purposes. PMT response parameters were not accurately known at this time making absolute comparisons difficult. The gradient however is a useful tool for validating the codes.

for the experiments was to demonstrate the scaling of intensity with pressure and response to validate the algorithms used to calculate density and refractive index for CO<sub>2</sub> and SF<sub>6</sub>; all the comparisons show good agreement in shape with required scaling never exceeding a factor of 2. The models can now be used with a well-defined degree of confidence for further physics experiments, such as the D-T  $\gamma$  branching ratio investigation [74] and D-T spectral analysis.

# Chapter 3

## Geant4 Cherenkov detector studies

### 3.1 Bang-time as a function of gas fill pressure

At the onset of the national ignition campaign (NIC) the gamma reaction history diagnostic was required to report  $\gamma$  bang-time  $BT_\gamma$  with a tolerance of  $< 50$  ps [56].  $BT_\gamma$ , also known as nuclear bang time is an important parameter used to assess implosion quality and is related to reaction history (RH), discussed in Section 1.6. To report  $BT_\gamma$  to such high accuracy requires many aspects of the detector to be characterised to high precision, some of which are unmeasurable; consequently the GEANT4 and ACCEPT models must be used to fill in gaps. The temporal response of the detector is one such characteristic.

At NIF and Omega a dedicated laser timing shot is required to calibrate the 2 % point in the rising edge of the first picket (NIF) or maximum laser power (Omega). This shot requires a gold or silver ball target in place of the hohlraum or capsule. The gold target with no fuel fill is used to generate an X-ray signal with effectively instantaneous rise time producing a temporal history indicative of the laser pulse; X-ray generation from plastic or glass is slow in comparison and would smear out features in the laser profile. The two diagrams in Figure 3.1 describe

schematically the method for calculating  $BT_\gamma$  using the GRH diagnostic. During the dedicated timing shot the scintillation signal which results from the deposition of X-ray energy (charged particles actually deposit the energy following scattering interactions) in BC422 is recorded alongside an optical timing fiducial picked off from the NIF laser at the diagnostic splitter shown in Figure 1.3. The scintillation signal is deconvolved with the appropriate detector and PMT system response to recover the laser profile; calculation of the system response is discussed in the next section. The timing fiducial is fed into the GRH detector via fibre optics located at the centre of the GRH flat mirror and directed towards the pressure window. During a shot requiring a  $BT_\gamma$  measurement the Cherenkov signal is recorded alongside the ever-present timing fiducial; deconvolution is again used to recover the implosion RH, this time with a different detector and PMT system response. The fiducial is then used to align the RH and laser profile on the same time base;  $BT_\gamma$  is calculated by measuring the separation between the 2 % point in the rising edge of the first laser picket, and the peak in the RH.

As discussed in Section 1.7.11 all the Cherenkov detectors are insensitive to X-rays even at the maximum rated fill pressure of 215 psia for GRH at NIF and Omega. Consequently the low-Z aluminium  $\gamma$  to  $e^-$  converter at the front of the the detector must be replaced with a scintillator sensitive to the X-rays. For this purpose BC422 was chosen due to a fast rise time of  $< 20$  ps and decay constant of 1.4 ns respectively [76] [77]. In the literature Lerche and Phillon report 20 ps as a conservative estimate as the observed rise time was close to their system response. With the GRH in this configuration it is possible to record the laser profile as a function of time. Despite the fast time response of BC422, a non-negligible broadening is imposed on the X-ray signal. In order to calculate the 2 % point in the rising edge of the first laser picket the scintillator needs to be deconvolved with the detector system temporal response, which includes broadening introduced by the BC422 and the various optical paths around the 3 off-axis-parabolas (OAP) and single flat mirror. To measure this experimentally would require a minimum 10 ps FWHM  $> 100$  keV X-ray signal and the optical signal from GRH to be fed

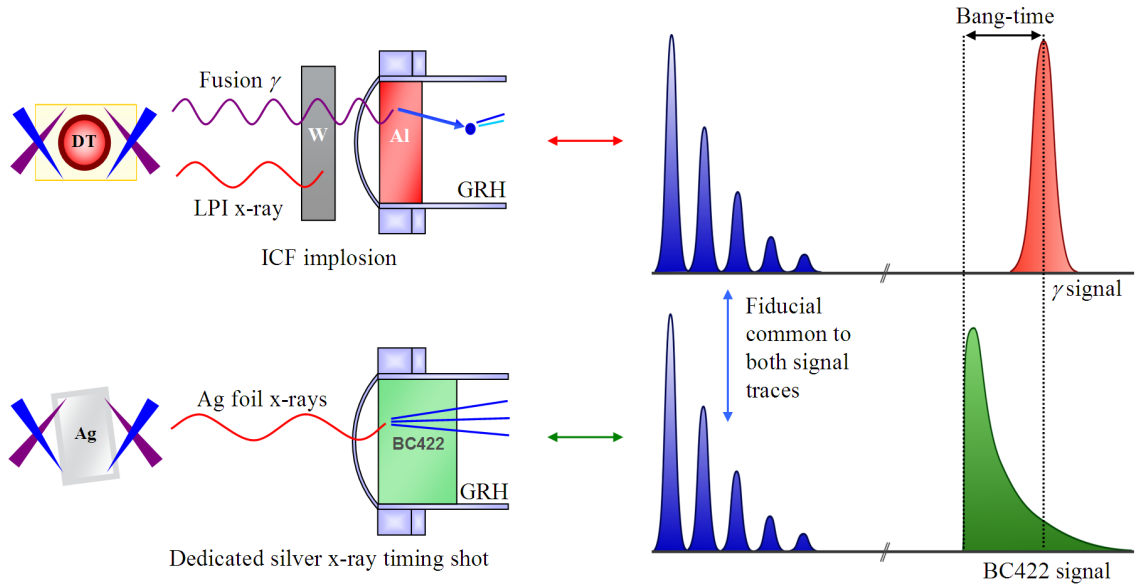


Figure 3.1: Overview of the  $BT_\gamma$  measurement technique where two separate experiments are carried out. The first is a standard cryogenic DT ICF implosion and the second a silver ball target producing a fast-rising X-ray signal to clearly define the laser-interaction time. The optical timing fiducial is common to both recorded traces allowing the signals to be cross-timed with high precision [75].

to a streak camera. Generating the short X-ray signal is possible with a short-pulse laser, such as Omega EP, however at NIF the advanced radiography system (ARC) which will utilise chirped-pulse amplification (CPA) technology to generate sub-ps pulses is not commissioned (at the time of writing). In addition there is currently no method for coupling the GRH optical system to a streak camera. There are preliminary plans for a GRH at 15m outside the concrete shield wall which is designed to split the optical signal to a PMT, photodiode and streak camera to cover a large dynamic range whilst maximising system bandwidth. Unfortunately this design also requires neutron yields much larger than currently achievable and would require several years of design work before commissioning. Consequently the validated GEANT4 model was used to generate the system response for the existing GRH system.

The nominal nose of GRH is comprised of a 0.325 cm thick dome (spherical surfaces can withstand higher gas pressures) made from aluminium; inside the dome

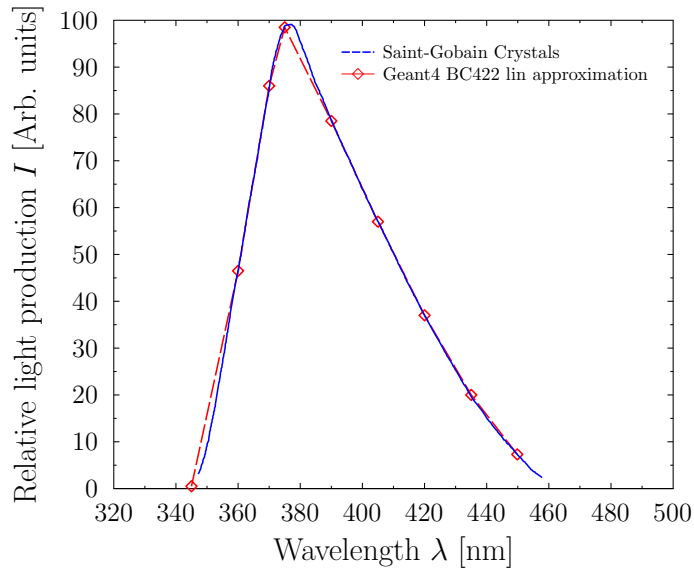


Figure 3.2: GEANT4 linear approximation to the BC422 scintillator relative light yield compared with the published data sheet from Saint-Gobain Crystals [78].

sits a 0.927 cm thick 12.7 cm diameter aluminium converter (0.9 cm thickness and 12.7 cm diameter on the Omega GRH variant). A 5 mm thick tungsten shield used to stop X-rays interacting with the detector is placed a few cms in front of the GRH between the port cover and nose cone. This configuration has been optimised to produce the highest number of forward-travelling high-energy electrons and positrons in order to maximise Cherenkov production and minimise temporal spreading [79]. To make the GRH sensitive to X-rays from the laser-plasma interaction, the 5 mm tungsten shield was removed and the aluminium converter replaced with a 0.3 cm thick and 12.7 cm diameter BC422 scintillator. The GEANT4 GRH geometry was modified to reflect the above changes. In addition the scintillation properties of BC422 were required for the correct production of light. The default GEANT4 scintillation model does not include a rise time model; in most experimental cases it is faster than the bandwidth of the recording system and isn't required. For the GRH detector response calculation however the rise time is important. At the request of the author and Martin Goettlich (Deutsches Elektronen-Synchrotron

DESY/FLC) an addition was made to the G4Scintillation class allowing the user to specify a finite rise time using the ‘FASTSCINTILLATIONRISETIME’ class property. The sampling algorithm for the new model is based on the function

$$I(t) = e^{-t/\tau_D} (1 - e^{-t/\tau_R}), \quad (3.1)$$

where  $\tau_R$  and  $\tau_D$  are the rise and fall time of the scintillator respectively. The rise time constant  $\tau_R$  in equation 3.1 is not the same rise time as defined by Lerche and Phillon, who define rise time  $\tau_{RR}$  as the time between 10 % and 90 % in the rising edge. A short derivation can be used to reconcile  $\tau_R$  and  $\tau_{RR}$ . Assuming that the decay time is long compared to the rise time, at small  $t$  we get  $e^{-t/\tau_D} = 1$  and consequently  $I(t) = (1 - e^{-t/\tau_R})$ . A simple rearrangement produces

$$t = -\tau_R \ln(1 - I(t)). \quad (3.2)$$

Inserting  $I(t) = 0.1$  and  $I(t) = 0.9$  into two separate equations and subtracting one from the other produces

$$t_2 - t_1 = \tau_R (\ln(0.9) - \ln(0.1)) \quad (3.3)$$

where  $t_2 - t_1$  is the rise time as defined using the 10 % and 90 % points. Substituting  $t_2 - t_1 = t_{RR}$  where  $t_{RR}$  is the 10 % to 90 % rise time produces

$$\tau_R = \tau_{RR} / \ln(9). \quad (3.4)$$

Using the rise time conversion in equation 3.4 the correct constants can be used with the new GEANT4 scintillation model [80]. Private discussions with R. Lerche

suggest that  $\tau_{RR} = 8$  ps is a reasonable estimate for the real rise time of BC422 [81]. In the 1992 experiment, broadening resulting from the streak camera and acceptance angle of the flat mirror, the many possible optical paths through the system and scattering effects from the volumetric source (6 mm diameter 5 mm thick) imply that the real rise time is closer to  $\tau_{RR} = 8$  ps. Consequently  $\tau_R$  was set to 3.6 ps for the GRH scintillation calculations.

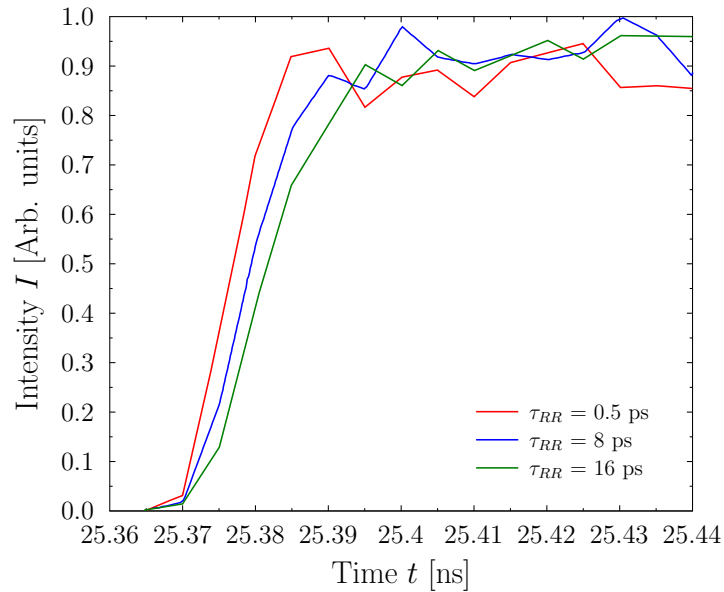


Figure 3.3: GRH scintillation signals for  $\tau_{RR}$  values of 0.5 ps, 8 ps, and 16 ps calculated using the GEANT4 model.

Additional properties for the scintillator required for the GEANT4 model are the wavelength dependence of the light production, refractive index ( $n = 1.58$ ) and the light yield (8400 photons per MeV [82]). Figure 3.2 shows the relative light yield distribution published by Saint-Gobain [78] together with the linear approximation used in the GEANT4 model. Other non-optical parameters for the BC422 are the density of  $1.032$  g/cm<sup>3</sup> and elemental composition (1.1:1 hydrogen atoms to carbon atoms). To calculate the temporal response from the gold ball X-ray signal a source term had to be written to approximate the laser-plasma emission. A representative X-ray spectrum as measured by the Filter-Fluorescer Diagnostic

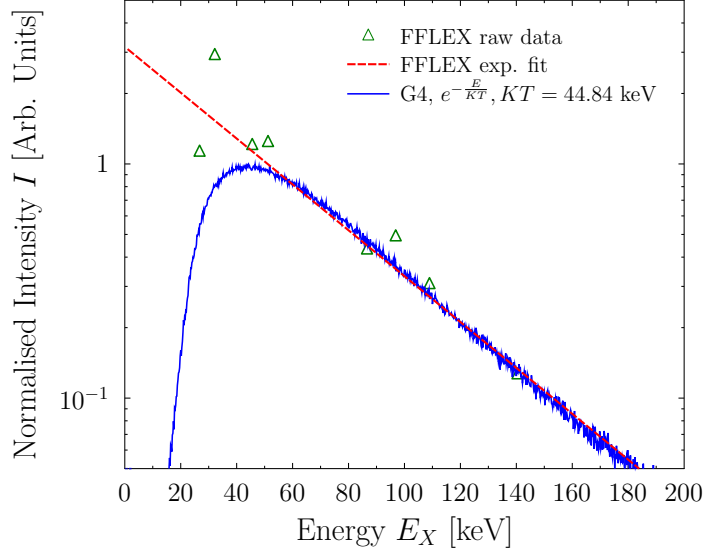


Figure 3.4: Plot showing FFLEX measured X-ray data from NIF (green triangles), exponential fit (broken red) and the temperature approximation used in the GEANT4 model (solid blue).

System (FFLEX) was provided by S. Le Pape [LLNL] [83]. Figure 3.4 shows the FFLEX X-ray spectrum (green triangles) together with a simple exponential fit (broken red) with exponent equivalent to a temperature of 44.8 keV. The GEANT4 general particle source was used to generate a temperature distribution of the form  $F(E) = e^{-E_x/K_B T_e}$  where  $E$  is X-ray energy,  $K_B$  is the Boltzmann constant,  $T_e$  is the electron temperature (same as ion temperature for thermal equilibrium), with  $K_B T_e = 44.8$  keV. The scintillator was set as a sensitive volume and used to tally X-rays as a function of energy to ensure the distribution was correct; the result is plotted in Figure 3.4 (solid blue) and shows good agreement with the FFLEX data and exponential fit. With the source term in place, the model was set up to record the scintillation photons at the photocathode between the predicted 25 and 30 ns arrival time in 5 ps bins. To obtain adequate statistics the simulation was run on the Atomic Weapons Establishment (AWE) WILLOW supercomputer which allows  $16 \times$  parallelisation. Figure 3.3 shows the change in the rising edge at several different values of  $\tau_{RR}$ . Even with  $\tau_{RR} = 0.5$  ps the rising edge is not instantaneous; the edge

is broadened by the many possible paths through the GRH optical system and by the many different light-producing X-ray and electron scattering trajectories observed in the scintillator. The 8 ps data in Figure 3.3 was combined with the appropriate PMT temporal response and used by the GRH team at NIF to deconvolve the laser profile during the NIC timing calibration shots.

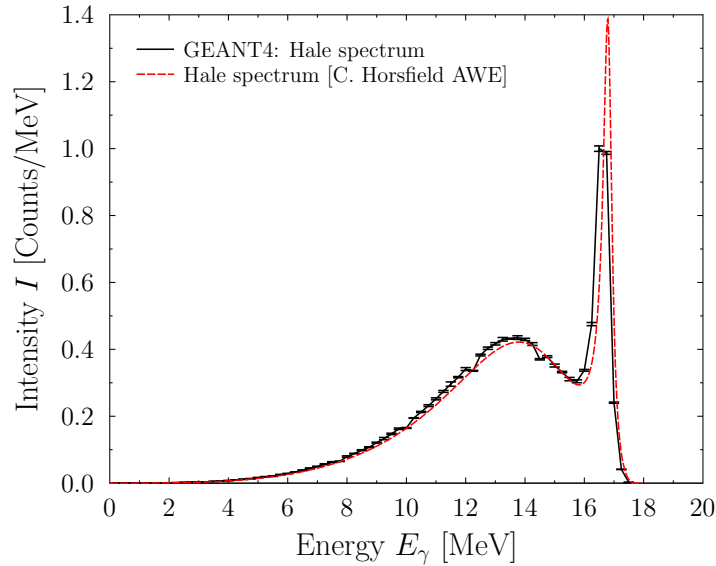


Figure 3.5: Plot showing a comparison between the 3:1 Hale spectrum calculated by C. Horsfield [AWE] [84] [85] and the source spectrum generated for the GEANT4 model in 0.25 MeV bins (the actual source term is at higher resolution than this spectrum sampled from the GCD1 nose cone).

The second temporal profile used in the  $BT_\gamma$  deconvolution is the detector system response for a DT shot. The source distribution used for a shot of this type was generated from a Hale distribution supplied by C. Horsfield [AWE] [84] [85]. To ensure the spectrum was sampled correctly the converter was set as a sensitive volume and  $\gamma$  photons recorded between 0 and 20 MeV in 0.25 MeV bins. Figure 3.5 shows a comparison between the supplied spectrum and the  $\gamma$  distribution recorded in the GEANT4 model at the target-chamber-centre (TCC)-facing side of the converter. Good agreement is observed; however the intensity of the GEANT4 16.75 MeV line is split between two 0.25 MeV bins and therefore appears low. The

sampling resolution of the source term is much higher than the 0.25 MeV bin width used to tally  $\gamma$  photons therefore the actual spectrum observed by the detector in the model has better agreement than Figure 3.5.

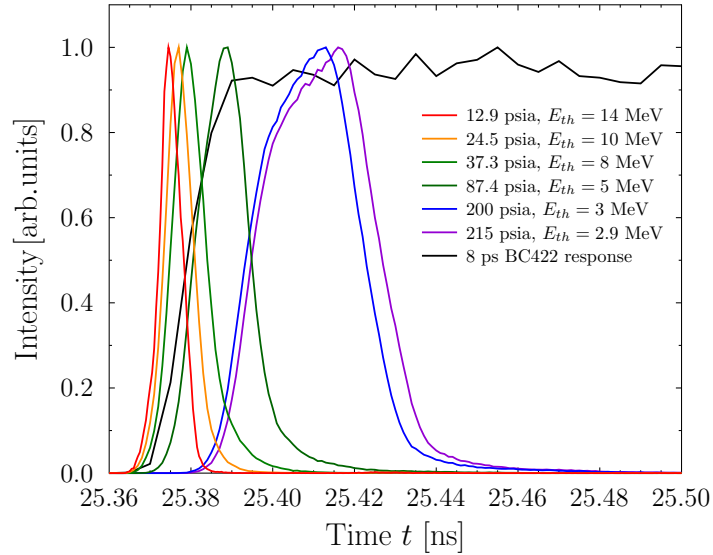


Figure 3.6: Plot showing temporal impulse responses of the gamma reaction history (GRH) diagnostic for a range of gas fill pressures. Also plotted is the temporal response of the GRH when configured to include a scintillator instead of a Compton converter [75].

With the source term created, a parameter study was performed to investigate the dependence of the detector response to the DT Hale source term for a range of pressures. As discussed in Section A changing the gas pressure modifies the refractive index and the density of the gas. An increase in refractive index  $n$  has the effect of widening the Cherenkov emission angle and slowing down the optical photons as they travel around the optical system. A higher density increases the probability of electrons scattering events, such as ionisation and bremsstrahlung, altering the trajectory of the Cherenkov-producing tracks throughout the gas cell. A higher density will also increase the possibility of unconverted  $\gamma$  photons Compton scattering or pair producing further down the gas cell, creating additional Cherenkov photons away from the converter region. Figure 3.6 shows the scintillation signal generated

by the  $\tau_{RR} = 8$  ps source term (solid black) compared with detector responses generated using the 3:1 DT Hale distribution source term at several different pressures (various colours); the binning resolution was 5 ps to facilitate simple post-processing with a PMT impulse response (also at 5 ps resolution) if required. As predicted the higher pressure simulations, corresponding to higher gas density and refractive index, produce detector response functions delayed in time due to the reduced light speed and show significant broadening relative to lower pressures.

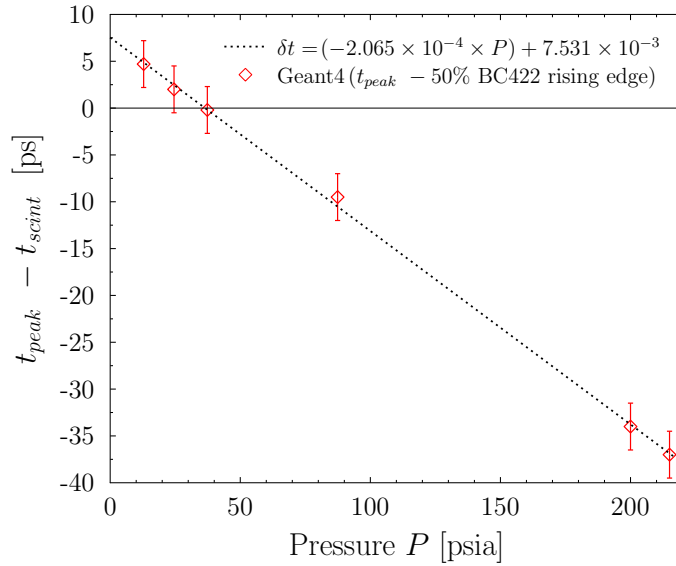


Figure 3.7: Plot showing the temporal response peak location relative to the 30 psia peak as a function of gas fill pressure. This is the required scaling correction for the  $BT_\gamma$  when changing GRH gas fill pressure [75].

The red diamonds in Figure 3.7 shows the shift in detector response peak relative to the 50 % point in the scintillator rising edge as a function of gas fill pressure. The simple linear fit  $\delta t = (-2.1 \times 10^{-4}P) + 7.5 \times 10^{-3}$  has been used to fit the data. Across the working range of the detector 1 psia to 215 psia the peak shifts by  $t(E_\gamma = 250 \text{ MeV}) - t(E_\gamma = 2.95 \text{ MeV}) = 7 \text{ ps} + 37 \text{ ps} = 44 \text{ ps}$ ; the induced shift is comparable to the  $\pm 50$  ps uncertainty specified for GRH  $BT_\gamma$  calculations. Consequently the GEANT4 detector response functions must be included in the signal deconvolution together with the PMT impulse response function to correctly

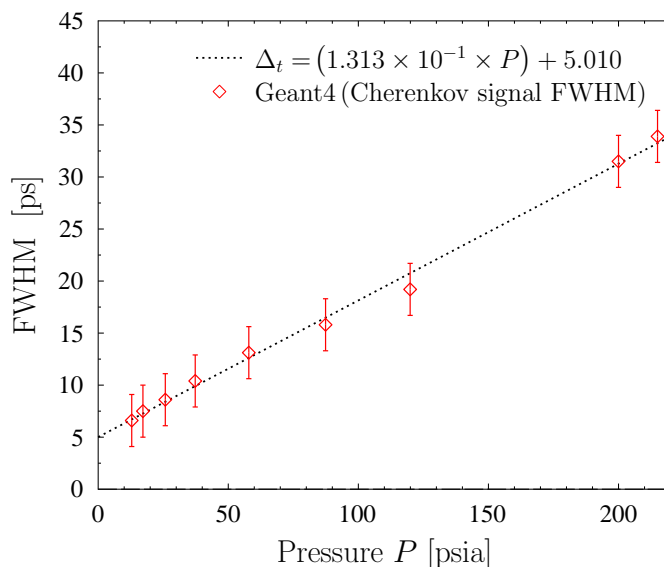


Figure 3.8: Plot showing the FWHM of each impulse response as a function of gas fill pressure together with a linear least-squares fit [75].

locate the peak in the RH. Figure 3.8 shows the FWHM of the detector response as a function gas pressure together with the linear fit  $\Delta t = (1.3 \times 10^{-1}P) + 5.0$ . The FWHM is the absolute full-width at half maximum, no Gaussian fit was performed due to the asymmetry of the response function. Over the range 1 psia to 215 psia the detector response broadens from 5 ps to 33 ps, an increase of 28 ps. The significant asymmetry and broadening of the detector response observed with increasing gas pressure further emphasises the need for individual detector responses at each gas configuration for use in the  $BT_\gamma$  signal deconvolution.

## 3.2 Detector light responses

The temporal profile produced by the Cherenkov detectors is not the only parameter important for calculations at the NIF and Omega facilities. The amount of light produced by the detector combined with associated conversion statistics are essential for predicting PMT voltages, unfolding spectral components and reporting error for a given measurement. The three specific parameters investigated in this

section are light response  $R$ , number of productive  $e^-$  per incident gamma  $Y_{e^-}$  and number of Cherenkov photons per productive electron  $Y_{Ch}$ . The first parameter  $R$  has been discussed previously. The second  $R_{e^-}$  and third  $Y_{Ch}$  produce the light response when multiplied together, and are important for calculating uncertainty and detector noise floor. The uncertainty in a particular measurement does not come from the number of Cherenkov photons recorded by the PMT, it is related to the original number of  $\gamma$  photons converted to Cherenkov light and subsequently detected by the photocathode which is subtly different. For example the GRH subtends a relative solid angle of  $2.72 \times 10^{-5}$ ; during a shot with a neutron yield of  $1 \times 10^{13}$  and using  $B_{DT\gamma} = 4.2 \times 10^{-5}$  this corresponds to  $11 \times 10^3$  DT Hale  $\gamma$  photons interacting with the detector. At a  $\text{CO}_2$  gas pressure of 100 psia the response has been calculated at  $R = 0.09$  Ch. photons/ $\gamma$  leading to  $1 \times 10^3$  Cherenkov photons interacting with the photocathode, which appears to be sufficient for a  $\pm 3\%$  yield measurement; in truth the uncertainty is worse. The number of electrons producing at least one photon of light which reaches the photocathode is approximately  $Y_{e^-} = 0.01 \gamma/e^-$  and the average number of photons emitted per productive electron  $Y_{Ch}$  is approximately 10 Ch. photons/ $e^-$ . With this gas configuration the GRH only detects  $\approx 100$  gammas which has a counting error of  $\pm 10\%$ , three times higher than the value calculated using the Cherenkov signal. In reality the error is more complex still; the  $\sqrt{N}/N$  error of  $\pm 9\%$  is the intrinsic error associated with a measurement where discrete Poisson statistics apply. However, the GRH involves two conversion steps:  $\gamma$  to  $e^-$  and  $e^-$  to Cherenkov light and for each conversion there is an additional uncertainty which must be added in quadrature with the  $\sqrt{N}$ . To fully understand the detector these parameters and conversions are required as a function of incident  $E_\gamma$  and gas pressure, and temperature to a lesser extent. This represents a massive parameter space which would require unfeasible resources to fill experimentally. Consequently the next section will discuss how the parameters have been calculated using the validated GEANT4 models. Data for GCD1, GCD2, GRH (NIF), GRH (Omega) and super GCD have been supplied to the teams working at the Omega and NIF facilities, however throughout the next

section the GRH (NIF) will be used to demonstrate the approach. The simulation approach and class structure developed to record the parameters used throughout this section are discussed in Section 2.1.

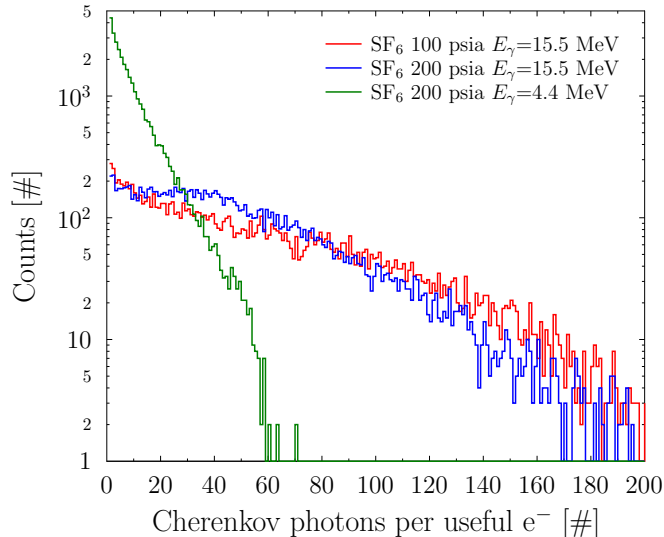


Figure 3.9: Plot showing the  $Y_{Ch}$  histogram produced by the GRH GEANT4 model for several SF<sub>6</sub> pressures and  $E_\gamma$  values. The generated distribution shows a stronger dependence on  $E_\gamma$  compared with gas pressure. The  $\gamma$  source used to generate this spectrum was the parallel disc source used during the HI $\gamma$ S validation work described in section 2.5

Light response  $R$  is defined as the number of Cherenkov photons recorded at the photocathode per incident  $\gamma$  photon. The photocathode is used instead of the glass input window to be consistent with measurements of PMT quantum efficiency, which systematically account for the effect of the glass input window. The sensitive detector used in Section 3.1 was modified to calculate the  $R$  the integral of the temporal response between 25 and 27.5 ns, divided by the number of source  $\gamma$  photons. The situation is not quite so simple for the other parameters  $Y_{e^-}$  and  $Y_{Ch}$ . The first process was to write a G4UserSteppingAction class to gain access to all G4Step information for each step occurring in the simulation, this reduces computational efficiency by a factor of approximately  $\times 2$ . Two histograms (G4int arrays) were created to tally  $Y_{e^-}$  and  $Y_{Ch}$  throughout the entire simulation. The simpler of the tallies

is the number of Cherenkov photons per productive electron  $Y_{Ch}$ . Using the `EndOfEventAction` method of the `G4UserEventAction` class the number of Cherenkov photons recorded at the photocathode was used to increment the appropriate bin of the  $Y_{Ch}$  histogram. The Cherenkov photon count was implemented by setting a global counting integer (`opPhotonCollection`) to zero in the `BeginOfEventAction` method and incrementing `opPhotonCollection` each time a photon was recorded in the `G4VSensitiveDetector` class using the `extern` keyword. To obtain  $Y_{e^-}$ , each time a Cherenkov photon was created in the `G4UserSteppingAction` class three global variables: `currentTrackId`, `CurrentParentId` and `eventID` were updated to those of the optical photon. Inside the `G4VSensitiveDetector` a logical statement using the `currentTrackId`, `CurrentParentId` and `eventID` integers is used to increment another counting integer `NumberOfParents` (also set to 0 in the `BeginOfEventAction` method) in the case where the `CurrentParentId` is different to the previous recorded optical photon for the current event. This complexity is required because occasionally a source  $\gamma$  can produce more than one productive  $e^-$  through secondary and tertiary scatters.

Figure 3.9 shows the histogram generated for several  $\text{SF}_6$  pressures and  $E_\gamma$  values; the number of Cherenkov photons per productive electron parameter  $Y_{Ch}$  is the mean of this spectrum. The  $\gamma$  source used to generate this spectrum was the parallel disc source used during the HI $\gamma$ S validation work described in Section 2.5. Halving the pressure for a constant  $E_\gamma$  has little impact on the shape of the distribution except slightly reducing the observation frequency of large Cherenkov bunches; reducing  $E_\gamma$  from 15.5 MeV to 4.4 MeV however alters the spectrum dramatically. No Cherenkov bunches greater than 75 are observed. This is because the lower-energy Compton- and pair-produced electrons from the small  $E_\gamma$  quickly fall below the speed of light due to losses from ionisation and bremsstrahlung, which reduces the track length over which Cherenkov light is produced. The histogram associated with  $Y_{e^-}$  is of less interest as the overwhelming majority of counts fall within the first bin, with occasional counts falling in the 2<sup>nd</sup> and 3<sup>rd</sup> bin.

During the NIC campaign it quickly became evident that running the simula-

tion each time a gas configuration was requested was inefficient; new simulations were required when the measured pre-shot gas pressure deviated from previously calculated values or when planning future experiments outside the original scope of the detector. A new method was required which would allow the calculation of detector parameters for any gas and at any any pressure. Consequently, a bash script was written to submit  $45\times$  individual simulations to the AWE supercomputer WILLOW, at pressures between 5 and 225 psia at 5 psia intervals separately for SF<sub>6</sub> and CO<sub>2</sub>, each producing a single file containing  $P$ ,  $R$ ,  $Y_{e^-}$  and  $Y_{Ch}$  as a function of  $E_\gamma$  in steps of 0.25 MeV. The results were combined using an IDL routine to produce a single file for each gas containing  $P$ ,  $E_\gamma$ ,  $R$ ,  $Y_{e^-}$  and  $Y_{Ch}$  values. To allow calculation of the statistics at any pressure or energy a surface fit to the 3D dataset was used to convert the irregularly spaced data to a regular grid. The IDL procedure GRIDDATA was combined with the TRIANGULATE function to produce  $3\times$  2D linearly-interpolated  $4000\times 4000$  arrays for  $R$ ,  $Y_{e^-}$  and  $Y_{Ch}$  between pressures and energies of 5 to 225 psia and 2 to 20 MeV respectively. A smoothing of 40 nearest neighbours was used after the calculation. A command-line interface was written to allow the user to enter a gas, pressure and energy resolution; the IDL program would subsequently search the high-resolution grid and find the nearest two gas pressures and then perform a nested linear interpolation to report the parameters at the specific pressure and energy resolution. Finally the IDL program was modified to allow the user to produce a 3D surface plot for all or one of the parameters following the 2D interpolation; the CG\_SURFACE procedure from the COYOTE library was used for this purpose which is a modification to the built-in IDL routine SHADE\_SURF with additional functionality and control.

Figures 3.11,3.12 and 3.13 show the surface plots of  $R$ ,  $Y_{e^-}$  and  $Y_{Ch}$  produced using the COYOTE CG\_SURFACE procedure as a function of two independent axes: pressure in psia and  $\gamma$  energy  $E_\gamma$ . All surfaces show a smooth transition to 0 below the threshold values predicted in Figure A.3 except for  $Y_{Ch}$  in Figure 3.13 which exhibits spikes between 1 and 10 for  $E_\gamma < E_{Th}$ , which suggest a low-intensity source of optical light reaching the photocathode not originating from the gas. The

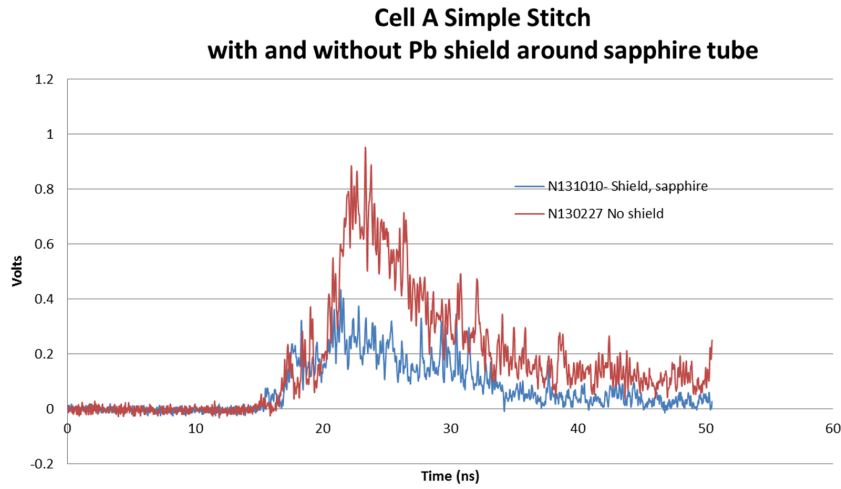


Figure 3.10: Plot showing the laser–plasma interaction background measured at NIF by the GRH normalised to total laser energy with and without Pb shielding shadowing the sapphire pressure window. The shielding clearly reduces the background signal suggesting that a large proportion of the background originates from the sapphire window. Data courtesy of LLNL/LANL [86].

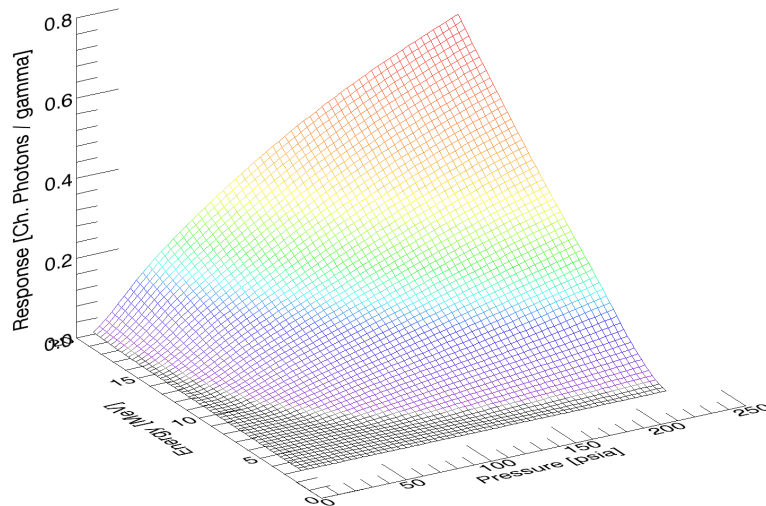


Figure 3.11: 3D surface plot showing interpolated light response of the GRH detector when fielded at NIF as a function of two independent axes: pressure in psia and  $\gamma$  energy  $E_\gamma$ . Light response is defined as the number of Cherenkov photons recorded at the photocathode per source  $\gamma$ . Generated using data from GEANT4 simulations and the IDL surface–fitting routine.

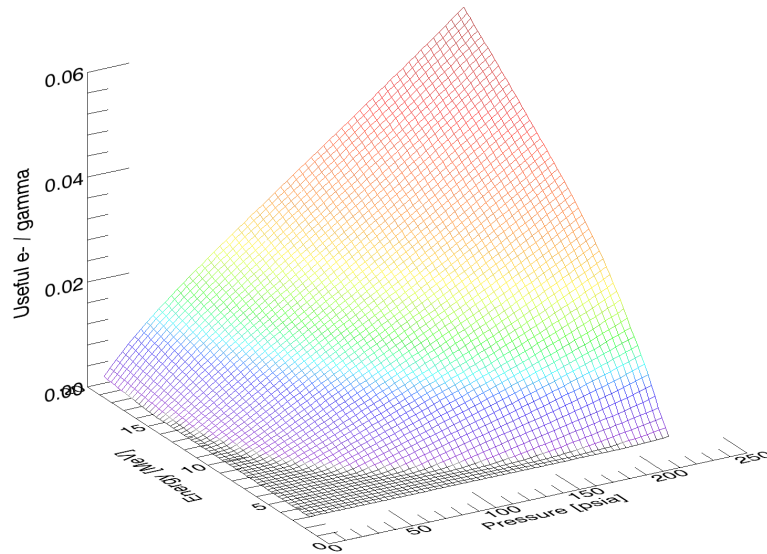


Figure 3.12: 3D surface plot showing interpolated  $e^-/\gamma$  statistics for the GRH detector when fielded at NIF as a function of two independent axes: pressure in psia and  $\gamma$  energy  $E_\gamma$ .  $e^-/\gamma$  is the number of electrons leading to the detection of at least one Cherenkov photon at the photocathode, per incident  $\gamma$ . Generated using data from GEANT4 simulations and the IDL surface-fitting routine.

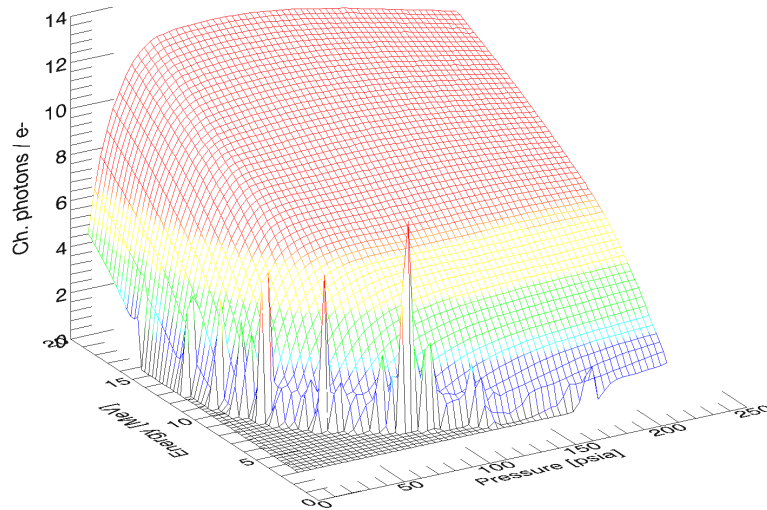


Figure 3.13: 3D surface plot showing interpolated Ch. photons/ $e^-$  statistics for the GRH detector when fielded at NIF as a function of two independent axes: pressure in psia and  $\gamma$  energy  $E_\gamma$ . Ch. photons/ $e^-$  is the mean number of Cherenkov photons recorded by the photocathode per productive electron. Generated using data from GEANT4 simulations and the IDL surface-fitting routine.

source files used to generate the  $R$  and  $Y_{e^-}$  surfaces also show response below threshold several orders of magnitude smaller than the gas-based Cherenkov production, however the signal is lost in the interpolation process. The below-threshold response is caused by Cherenkov production in the sapphire pressure window and glass PMT input window. These regions are shadowed by shielding placed outside the detector, occasionally however a scattered low-energy electron can navigate to the volume and emit large amounts of Cherenkov light. The Cherenkov production threshold can be calculated by combining the Lorentz factor  $\gamma = 1/\sqrt{1 - v^2/c^2}$  with the relativistic kinetic energy equation  $E_k = (\gamma - 1) m_0 c^2$  producing

$$E_{e^-} = \left( \frac{1}{\sqrt{1 - \frac{1}{n^2}}} - 1 \right) m_e c^2, \quad (3.5)$$

where  $1/n^2 = v^2/c^2$ . Substituting  $n = 1.5$  produces a Cherenkov threshold of 430 keV; it is not unfeasible that a scattered  $\gamma$ , electron or positron of this energy could reach the pressure window or PMT input window. In addition, the 1.8 MJ drive at NIF produces a significant amount of laser-plasma interaction hard X-rays which will also generate electrons above this energy. During the NIC campaign a significant background signal was observed before, during and after the expected arrival time of the DT Cherenkov signal. Figure 3.10 shows the reduction in background signal observed when placing 2 mm of lead shielding tape around the cylindrical cell surrounding the pressure window; the reduction further confirms the below-threshold Cherenkov observed in the IDL GRH parameter calculator.

Following the success of the IDL GRH parameter calculator after dissemination to colleagues at AWE, LANL and LLNL additional data files were produced for GCD1, GCD2 and super GCD using the same methodology. The user can now produce a  $R$ ,  $Y_{e^-}$  and  $Y_{Ch}$  response for any diagnostic, at any pressure in the working range, and as a function of an arbitrary  $E_\gamma$  resolution at NIF or OMEGA.

## 3.3 Measuring direct drive remaining ablator areal density using the GCD2 at Omega

### 3.3.1 Introduction

Areal density is an important indicator of compression and implosion quality [87] during ICF experiments. Throughout the implosion 14.1 MeV fusion neutrons interact with materials in the remaining ablator leading to the emission of inelastic gammas. The resulting gamma intensity provides a direct measure of the remaining ablator areal density  $\langle \rho R \rangle_{abl}$  at bang time, which shows good correlation with fuel areal density, an important variable in the Lawson criteria for fusion. Overly large  $\langle \rho R \rangle_{abl}$  values correspond with a slow shell velocity leading to poor compression and performance; small  $\langle \rho R \rangle_{abl}$  values correlate with increased hydrodynamic instability and undesired preheating of the fuel [87]. Several approaches exist to measure  $\langle \rho R \rangle_{abl}$  including the magnetic recoil spectrometer discussed in Section 1.7.5, charged particle spectrometer discussed in Section 1.7.3 and a multi-faceted inference technique [88] developed using the gamma reaction history (GRH) diagnostic discussed in Section 1.7.11. In the next section we discuss the measurement of the inelastic gamma radiation, and therefore  $\langle \rho R \rangle_{abl}$ , directly using a previously undesired background signal observed by the gas Cherenkov diagnostics at the Omega laser facility, Rochester, NY.

There are currently three Cherenkov diagnostics as discussed in Section 1.7.11 routinely fielded at Omega and a fourth super GCD currently under development by a collaboration led by LANL to be fielded at Omega and NIF. GCD2 differs from GCD1 in that the Cassagrainian focusing produces a parallel beam after the secondary mirror instead of focusing down to the input window of a PMT. This was originally designed to allow the optical signal to be routed away from the high-background region of the target chamber and coupled to the input slit of a well-shielded streak camera, potentially increasing the bandwidth of the system. Currently GCD2 has been re-engineered with an additional focusing optic and PMT

directly behind the diagnostic. The original design and specification precluded the requirement for shielding inside the radius of the primary Cassagrainian optic; consequently background signals in GCD2 are larger in its current configuration. It is this increased background signal that is of interest to this work. As discussed in Section 1.7.11 the unwanted detection of lower energy X-rays can be mitigated by selecting a high gas threshold; this solution however does not remove the possibility of direct X-ray interactions with the photocathode and MCP of the PMT. This can be avoided by placing 3-5 mm of high-Z material, such as lead or tungsten, at the front of the diagnostic. The remaining sources of background then come from neutron interactions with the remaining capsule ablator and large diagnostic masses located close to the ICF capsule, such as the target positioner and diagnostics requiring large solid angles. The latter are measured by the Cherenkov detectors at late time relative to the gamma signal due to the slow neutron time-of-flight; the former is emitted almost time-synchronous with the gamma signal due to capsule compression at bang-time. The energies of the  $n,\gamma$  and  $n,n'\gamma$  background generally range from 0-10 MeV and include intense lines corresponding to nuclear resonances and a continuum contribution reducing significantly with increasing energy. The small thickness of high-Z material in the nose is not sufficient to block direct interactions from these sources with the PMT or Cherenkov production in the glass pressure and PMT input windows ( $n = 1.48$ ); the gas pressure can be set appropriately to reduce Cherenkov optical contributions from inelastic gammas, as shown in Figure A.3. These background interactions from  $n,\gamma$  and  $n,n'\gamma$  emissions are observed 0.5 ns early with respect to the desired Cherenkov signal due to the extra time of flight introduced by the Cassagrainian optics.

14.1 MeV neutron interactions with plastic ablator material produce a low intensity background continuum spectrum together with a prominent 4.44 MeV emission from the  $2^+$  4.44 MeV state in carbon (solid black and broken blue in Figure 3.14); the glass spectrum is more complex consisting of a relatively large continuum with several oxygen peaks in the 6-7 MeV range (broken red and orange in Figure 3.14). Given that the attenuation coefficient of the chosen high-Z shielding material tung-

sten goes through a minimum around 4-7 MeV and that for routine ICF shots at Omega there are significantly more gammas emitted from the ablator material compared with fusion gammas as shown in Figure 3.15 it is likely that remaining ablator emission contributes the majority of statistics to the background signal, therefore providing a direct proportionality to the remaining  $\langle \rho R \rangle_{abl}$  at bang time. At Omega areal densities of  $30 \text{ mg/cm}^2$  are routinely observed; using  $B_{DT_\gamma} = (4.2 \pm 2) \times 10^{-5}$  this translates to approximately  $10\times$  more carbon 4.44 MeV gammas interacting with the detector. To investigate this further the validated Monte Carlo codes will again be used study the background signal, which will be called ‘precursor’ from this point onward.

### 3.3.2 Theoretical considerations

GEANT4 and MCNP models were created with a 1 cm radius sphere of ablator material (plastic or glass) with a density of  $1 \text{ mg/cm}^3$  producing a  $\langle \rho R \rangle_{abl}$  of  $1 \text{ mg/cm}^2$ . 14.1 MeV neutrons were emitted isotropically from the centre of the sphere to mimic the compressed capsule at bang time. A spherical 0.1 mm thick shell was created around the capsule sphere to tally gammas emitted from neutron interactions with the ablator material. The gamma spectra produced by MCNP and GEANT4 for plastic and glass are shown in Figure 3.14. The GEANT4 and MCNP models, which both utilise cross sections from the ENDF database predict  $1.49 \times 10^{-5}$  and  $1.06 \times 10^{-5}$  carbon 4.44 MeV gammas per neutron per  $\text{mg/cm}^2$  of areal density respectively. It should be stated that the GEANT4 model incorrectly predicts the emission of carbon gammas at 3.2, 9 and 13 MeV as shown in Figure 3.14 which originate from levels above the alpha separation energy. Particle emission occurs on much shorter time-scales compared to electromagnetic emissions therefore the intensity of these gammas would be much lower in reality, consequently these high energy emissions are ignored. Furthermore, the 3.2 MeV gamma is emitted as part of a cascade which also emits a 4.44 MeV gamma which is likely the reason the total intensity predicted by GEANT4 for that line is large compared with

MCNP. For glass the three oxygen lines at 6.13, 6.92 and 7.12 MeV were recorded at  $2.33 \times 10^{-6}$ ,  $1.21 \times 10^{-6}$  and  $6.78 \times 10^{-7}$  gammas per neutron per  $\text{mg}/\text{cm}^2$  of areal density by GEANT4 and  $3.45 \times 10^{-6}$ ,  $1.02 \times 10^{-6}$  and  $1.34 \times 10^{-6}$  gammas per neutron per  $\text{mg}/\text{cm}^2$  of areal density by MCNP respectively.

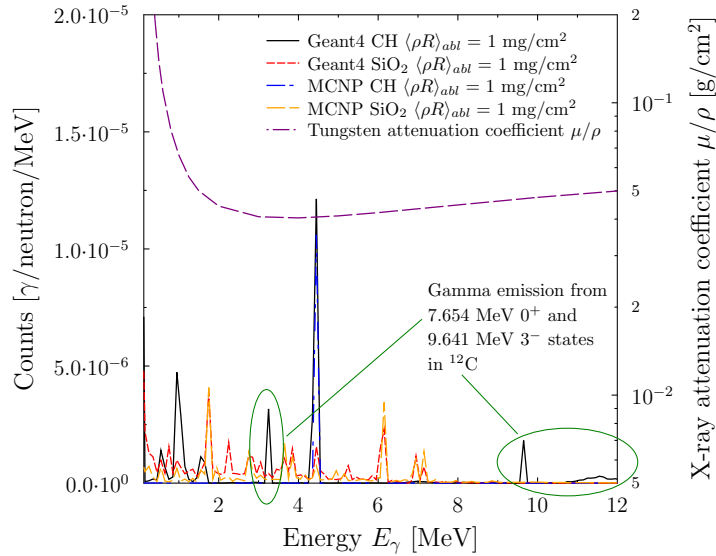


Figure 3.14: Plot showing the neutron-induced gamma spectrum from plastic and glass capsules calculated by GEANT4 and MCNP as discussed in Section 3.3.2.

To verify the plastic and glass Monte Carlo results an analytical calculation was also performed for the prominent 4.44 MeV line in carbon, and the three lines in Oxygen. To calculate the number of reactions occurring in a material we use

$$R = \sigma N_n N_T, \quad (3.6)$$

where  $R$  is the number of reactions,  $\sigma$  is the level cross section at  $E_n = 14.1$  MeV,  $N_n = 1$  is the number of neutrons interacting with the material and  $N_T$  is the number of target nuclei per  $\text{cm}^2$  observable by the incoming projectile within a small depth in which atom overlap can be neglected and over which the projectile energy and momentum can be assumed to remain unperturbed [32]. The areal density of  $1 \text{ mg}/\text{cm}^2$  can be obtained through many combinations of  $\Delta R$  and density; in this

case  $\rho = 0.01 \text{ g/cm}^2$  and  $\Delta R = 0.1 \text{ cm}$ . For carbon the number of  $^{12}\text{C}$  atoms per  $\text{cm}^2$ , taking into account the 98.93 % abundance of the  $^{12}\text{C}$  isotope, in this depth was calculated to be  $4.97 \times 10^{19}$ . Combining equation 3.6 with the conclusions over the previous lines and a cross section of 210.4 mb [89], a  $^{12}\text{C}$  4.44 MeV gamma emission intensity of  $1.1 \times 10^{-5}$  per neutron was calculated for an areal density of  $1 \text{ mg/cm}^2$  in good agreement with MCNP and slightly lower than GEANT4. For oxygen, cross sections of 95.3 mb, 23.3 mb and 49.7 mb were obtained for the three lines. Using the same approach described previously and the 53.3 % mass-fraction of oxygen in  $\text{SiO}_2$ , values of  $3.57 \times 10^{-6}$ ,  $8.74 \times 10^{-6}$  and  $1.87 \times 10^{-6}$  gammas per neutron per  $\text{mg/cm}^2$  of areal density were obtained for the 6.13, 6.92 and 7.12 MeV lines in oxygen respectively. The analytical and Monte Carlo estimates agree to within a factor of  $\times 2$  for all lines except the 7.12 MeV line estimated by GEANT4 which differs by almost  $\times 3$ . Table 3.1 contains a summary of the nuclei and lines analysed during the previous section together with the Monte Carlo results and analytical calculations.

Line [MeV]	Nucleus	Cross section [mb]	GEANT4 [ $\gamma/n/\langle\rho R\rangle_{abl}$ ]	MCNP [ $\gamma/n/\langle\rho R\rangle_{abl}$ ]	Calculation [ $\gamma/n/\langle\rho R\rangle_{abl}$ ]
4.44	$^{12}_6\text{C}$	210.4	$1.49 \times 10^{-5}$	$1.06 \times 10^{-5}$	$1.1 \times 10^{-5}$
6.13	$^{16}_8\text{O}$	95.3	$2.33 \times 10^{-6}$	$3.45 \times 10^{-6}$	$3.57 \times 10^{-6}$
6.92	$^{16}_8\text{O}$	23.3	$1.21 \times 10^{-6}$	$1.02 \times 10^{-6}$	$8.74 \times 10^{-7}$
7.12	$^{16}_8\text{O}$	49.7	$6.78 \times 10^{-7}$	$1.34 \times 10^{-6}$	$1.87 \times 10^{-6}$

Table 3.1: Comparison between GEANT4, MCNP and an analytical calculation for the prominent n,n' $\gamma$  lines in carbon and oxygen.

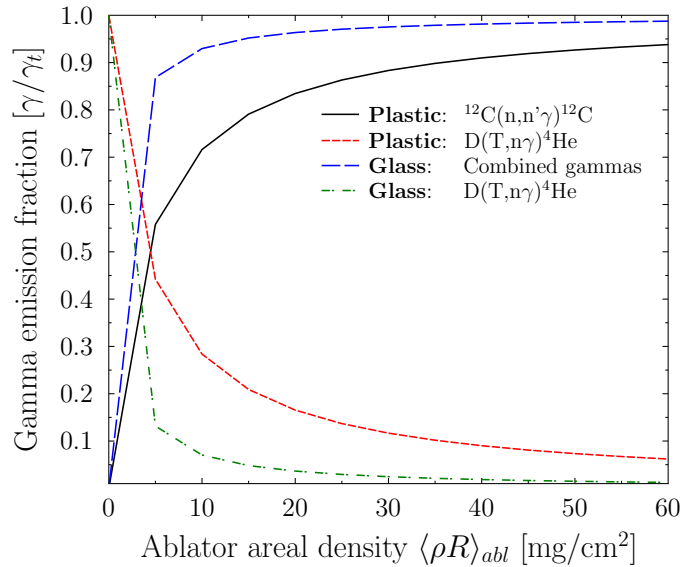


Figure 3.15: Fraction of gammas emitted from the DT reaction and from carbon compared to the total. Beyond  $\langle \rho R \rangle_{abl} = 4 \text{ mg/cm}^2$  inelastic carbon 4.44 MeV gammas become the dominant source.

### 3.3.3 Precursor calibration factor $\alpha$

To investigate the origin and statistical uncertainty in the precursor, the experimentally validated [90] GEANT4 simulations of GCD1 and GCD2 were used. At the time of writing a full set of engineering drawings does not exist for the GCD2 therefore the GEANT4 model is a best estimate from existing information. A 10 mm diameter and 1 mm thick cylindrical volume was created behind the PMT glass input window to represent the photocathode. This volume was set sensitive and an algorithm written to record time-resolved (5 ps bins) track-integrated energy deposition from electrons and positrons together with a separate tally for optical photons recorded following Cherenkov production in the gas and glass pressure window. The electrons/positrons originate from Compton scattering, pair production and photo-ionisation of gammas and high-energy X-rays with materials close to the PMT. The secondary particle production threshold was set at 5 keV; this was optimised to sufficiently down-scatter the source gamma signal to lower energy electrons whilst maintaining good computational efficiency required to cover

the large yield and  $\langle \rho R \rangle_{abl}$  parameter space. Figure 3.16 (broken green) shows RID=58164 (plastic ablator) at the Omega laser facility (Shot 8: 25th May 2010) recorded by GCD1 with a measured areal density of  $33 \pm 11 \text{ mg/cm}^2$  as reported by the GRH. The recorded signal is produced via the MCP-based charge amplification of electrons ejected from the photocathode surface inside the PMT coupled to a high-bandwidth transmission line and oscilloscope. To compare simulation with Figure 3.16 a method must be devised to combine the optical and energy deposition components that are recorded during the Monte Carlo simulation. A first principle approach could be used to model the low-energy electron ionisation events in the photocathode material; however this is difficult without full knowledge of the dielectric response, band structure and surface work function. Another approach is to calculate a calibration factor  $\alpha$  from the experimental data in Figure 3.16 where the  $\langle \rho R \rangle_{abl}$  was known.

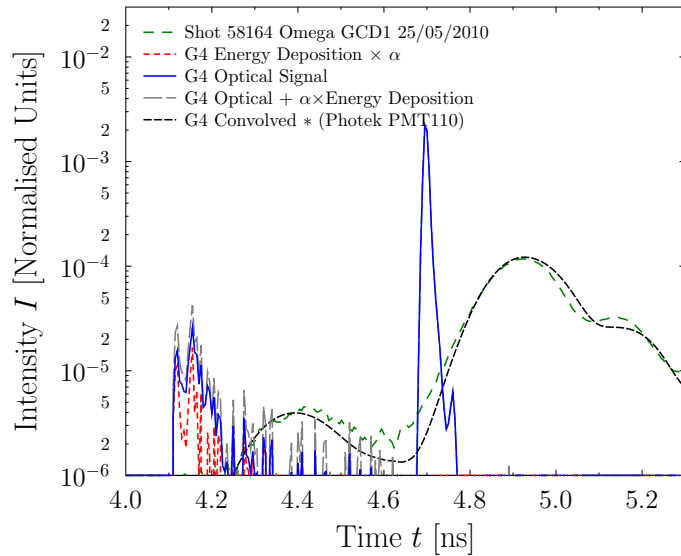


Figure 3.16: Plot showing a 100 psia  $\text{CO}_2$  shot recorded by the GCD1 diagnostic (broken black) at Omega with inferred areal density of  $33 \text{ mg/cm}^2$ . Also shown are the  $33 \text{ mg/cm}^2$  GEANT4 simulation; energy depositions are shown in broken red, optical photons in continuous blue and the combined result using the precursor model is shown in broken grey.

To calculate the measured precursor ratio  $R_p$  we integrate between 4.65 ns and 6 ns and then divide the result by the integral between 4.2 and 4.65 ns. Consequently  $R_p = 24.3$ . The optical signal arriving at the photocathode is well understood and was discussed earlier in Section 2.5 [90]. The primary Cherenkov signal is proportional to the DT  $\gamma$  signal emitted during ICF implosions; the precursor however is a combination of Cherenkov light produced in the pressure window of the diagnostic and input window of the PMT, and energy deposited from  $dE/dX$  electron and positron tracks originating from down-scattered high-energy gammas. GEANT4 simulations can be used to model both the optical component and the background electron tracks; combining the two signals on a single trace however requires the conversion to electrons of all the integrated  $dE/dX$  tracks traversing the photocathode. The combination results in photocathode electrons due to the conversion of optical photons to electrons in the photocathode at the quantum efficiency. To combine the time resolved energy deposits with the recorded optical signals we use  $R_p$  which consists of

$$R_p = \frac{I_{DT}}{I_{OPC} + \alpha I_{EDPC}} \quad (3.7)$$

where  $I_{DT}$  is the integral of the DT Cherenkov signal,  $I_{OPC}$  is the optical integral of the precursor,  $I_{EDPC}$  is the integral of the energy deposits during the period of the precursor and  $\alpha$  is the calibration factor.

The branching ratio for gammas emitted from the DT Hale spectrum is  $4.2 \pm 2 \times 10^{-5}$  per neutron; it was also shown earlier from MCNP and an analytical calculation that  $1.1 \times 10^{-5}$  carbon 4.44 MeV gammas are emitted per neutron for every  $1 \text{ mg/cm}^2$  of areal density. In shot 58164 the plastic areal density was  $33 \text{ mg/cm}^2$  therefore  $3.63 \times 10^{-4}$  gammas were emitted per neutron in this shot. By running a GEANT4 simulation with a source term consisting of 10.4 % DT Hale spectrum gammas and 89.6 % 4.44 MeV gammas the correct ratio of gammas will interact with the diagnostic for a  $\langle \rho R \rangle_{abl} = 33 \text{ mg/cm}^2$  implosion. Recording optical

photons and energy deposited in the photocathode as a function of time allows  $I_{DT}$ ,  $I_{OPC}$  and  $I_{EDPC}$  to be calculated; the results of the simulation are shown in Figure 3.16. Combining the simulation output and  $R_p = 24.3$  produces an  $\alpha$  of 750.61 electrons/MeV of deposited energy. The PMTs used inside other Cherenkov detectors fielded at Omega, such as GCD2 and GCD3 (in design), are the same as GCD1 therefore the calibration factor  $\alpha$  will also be applicable to these diagnostics.

### 3.3.4 Precursor proportional to areal density

As mentioned in Section 1.7.11 the background precursor signals in GCD2 are larger than those seen in GCD1 due to the omission of shielding inside the primary Casagrainian mirror. Consequently the counts observed in the GCD2 precursor should show the best statistical proportionality of the available detectors to the  $\langle \rho R \rangle_{abl}$  signal. To further increase the counting statistics from this point forward the central tungsten block will also be removed for  $\langle \rho R \rangle_{abl}$  measurements. The precursor model and GEANT4 simulation were used to investigate the statistical proportionality of the precursor to  $\langle \rho R \rangle_{abl}$  and yield. The GEANT4 source term was modified such that a  $\langle \rho R \rangle_{abl}$  value could be specified at run time. The required fraction of precursor gammas, in this case for a plastic ablator, was calculated from

$$F_{C-12} = \frac{1.1 \times 10^{-5} \langle \rho R \rangle_{abl}}{1.1 \times 10^{-5} \langle \rho R \rangle_{abl} + B_{DT\gamma}} \quad (3.8)$$

where  $F_{C-12}$  is the fraction of carbon 4.44 MeV gammas emitted relative to the total gamma source. A random number can be thrown and if  $R_1 \leq F_{C-12}$  a 4.44 MeV gamma is emitted and where  $R_1 > F_{C-12}$  a gamma selected from the Hale distribution [85] is emitted into the Monte Carlo geometry. The same equation was also used for glass capsules; however the constant changes to  $3.14 \times 10^{-5}$ . This represents the integrated number of gammas per neutron per  $\text{mg}/\text{cm}^2$  of  $\langle \rho R \rangle_{abl}$  between 0 and 20 MeV from the glass MCNP n,n' $\gamma$  simulation which showed closer agreement with the analytical calculation for the prominent oxygen lines. For the

glass precursor simulation, a gamma is sampled from a probability distribution calculated from the glass MCNP spectrum in Figure 3.14.

$\langle \rho R \rangle_{abl}$  values over the range 0 mg/cm<sup>2</sup> to 100 mg/cm<sup>2</sup> were chosen to assess the proportionality. In addition, the number of source gammas per simulation was chosen such that the total number of DT Hale gammas was equivalent to a neutron yield of  $1 \times 10^{13}$ , allowing the statistical dependence of a routine shot on Omega to be investigated. For example, if  $\langle \rho R \rangle_{abl} = 30$  mg/cm<sup>2</sup> then the DT fraction translates to  $1 - F_{C-12} = 0.071$ , the relative solid angle subtended by GCD2 is 0.0122 using

$$\Omega_{rel} = \frac{1}{2} (1 - \cos(\theta_{GCD2})) \quad (3.9)$$

where  $\theta_{GCD2} = \arctan(4.5/20) = 12.68^\circ$ , and using  $B_{DT\gamma}$  this results in  $5.1 \times 10^6$  DT gammas interacting with the diagnostic. The total number of gammas required for a full DT + carbon 4.44 MeV gamma simulation would be  $5.1 \times 10^6 / 0.071 = 72 \times 10^6$  split 92.9 % : 7.1 % between carbon 4.44 MeV and DT Hale gammas respectively. 16× parallel simulations were run at  $\langle \rho R \rangle_{abl}$  values between 0 mg/cm<sup>2</sup> and 100 mg/cm<sup>2</sup> in steps of 5 mg/cm<sup>2</sup>. Values and uncertainties from this point forward are the mean and  $1 \times \sigma$  error calculated from 16 parallel simulations with different initial random seeds.

Figures 3.17a and 3.17b show the dependence of the precursor on  $\langle \rho R \rangle_{abl}$  for plastic and glass capsules using the precursor model combined with the GEANT4 source term with and without the detector central tungsten shielding block. With the block removed the largest  $1 \times \sigma$  uncertainty of 10 % occurs at  $\langle \rho R \rangle_{abl} = 0$  mg/cm<sup>2</sup>; at this value the precursor is solely generated from DT Hale gammas. The uncertainty reduces to 3 % at  $\langle \rho R \rangle_{abl} = 100$  mg/cm<sup>2</sup>. GCD2 configured with and without the central tungsten block shows a strong correlation with  $\langle \rho R \rangle_{abl}$  for both plastic and glass ablaters; however the uncertainty increases by a factor of  $\times 4$  with the tungsten shield in place. Figure 3.18 shows the  $1 \times \sigma$  error calculated by

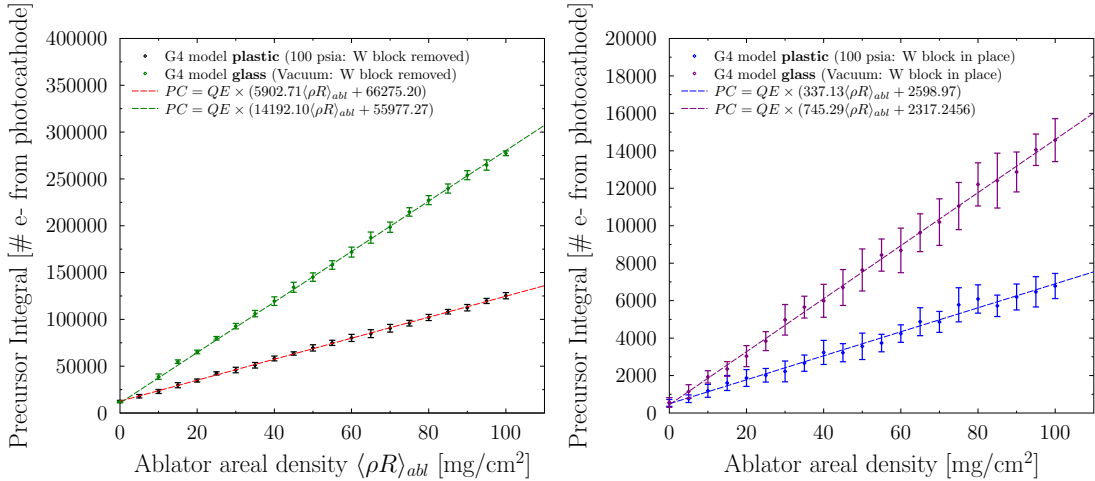


Figure 3.17: Plots showing precursor integral divided by the DT Cherenkov peak as a function of  $\langle \rho R \rangle_{abl}$  with  $\pm 1 \times \sigma$  uncertainty calculated for a neutron yield of  $1 \times 10^{13}$ ; left plot shows the relation and statistical dependence with the tungsten central block removed and on the right as designed. The gas parameters for simulation and experiment were 100 psia CO<sub>2</sub>.

GEANT4 as a function of neutron yield for several plastic capsule  $\langle \rho R \rangle_{abl}$  values. The plot shows that for neutron yields as low as  $1 \times 10^{12}$  the uncertainty is less than 20.0 % for  $\langle \rho R \rangle_{abl}$  values greater than 20 mg/cm<sup>2</sup>. The error analysis in the subsequent section is based on the uncertainties calculated by the GEANT4 precursor model.

### 3.3.5 September 2013 Knudsen campaign

During September 2013 a LANL-led team conducted an investigation into the Knudsen effect [91] using a variety of fuel fill pressures and initial shell thickness; the Knudsen effect is the loss of high-energy ions from the hot-spot Maxwellian tail to the cold ablator material at peak compression. One-dimensional modelling suggests that the losses should be observable and separable from competing mix losses over the ablator thicknesses and fill pressure ranges 7 - 30  $\mu\text{m}$  and 2 - 15 atm respectively. This represented the ideal opportunity to test the new technique as  $\langle \rho R \rangle_{abl}$  values were predicted to cover a wide range; furthermore the charged particle spectrom-

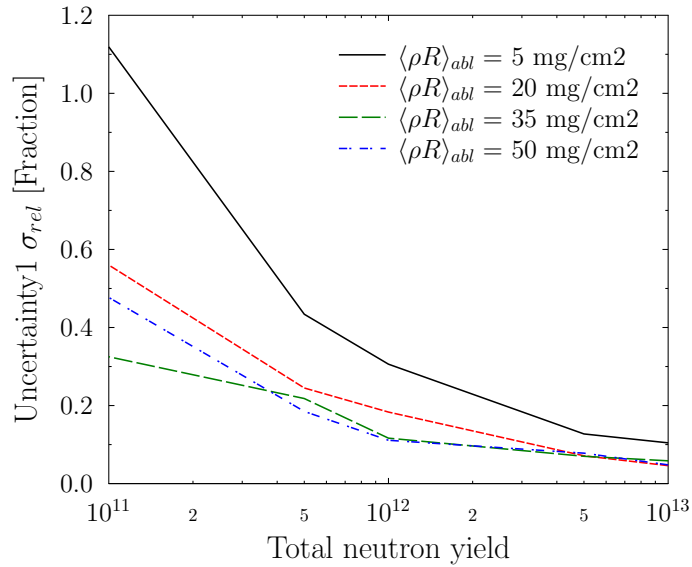


Figure 3.18: Plot showing the relative  $\pm 1 \times \sigma$  in the precursor divided by DT Cherenkov peak as a function of yield, for several  $\langle \rho R \rangle_{abl}$  values.

eter (CPS) and GRH diagnostics were also fielded allowing cross calibration and comparison. The GCD2 was fielded with the central tungsten shield removed. A Photek single-stage PMT was coupled to 2 separate SCD5000 [92] oscilloscopes via a 40 foot 3/4 inch foam-flex high-bandwidth cable and a single N-type impedance-matched splitter. Two oscilloscopes were used to increase dynamic range. The Photek PMT110 used to record data was held constant at 4900V, and therefore constant gain, to remove additional uncertainty in the measurement. Characterised N-type attenuators were used to cover the wide range of neutron yields predicted for the experiment ( $N_y = 1 \times 10^{11}$  to  $3 \times 10^{13}$ ). During the entire campaign the integrated charge drawn from the PMT to the right hand side of the precursor signal never exceeded 5.2 nVs, below the 10 nVs calculated in past experiments to be the non-linear limit for a single stage 10 mm diameter MCP-based PMT.

Figure 3.19 shows shot RID 70860 (shot 9 day 1) recorded by the GCD2 during the Knudsen campaign. The precursor signal has been highlighted in blue and shows good temporal separation from the rising background signal caused by n,n' $\gamma$

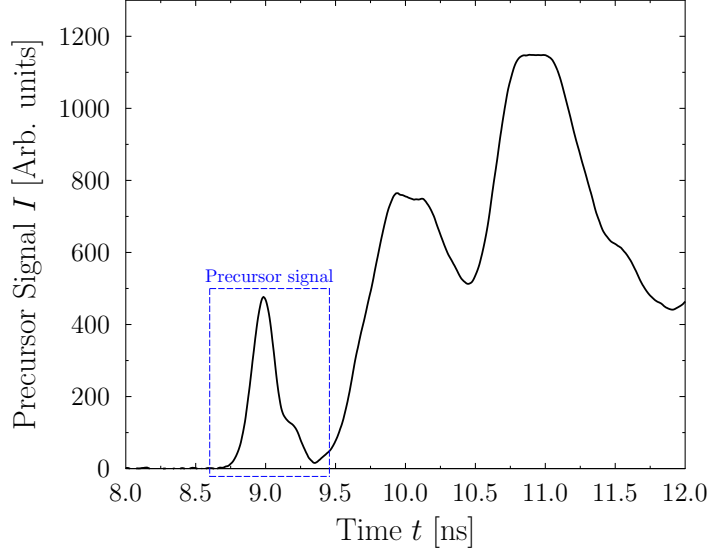


Figure 3.19: Plot showing the raw signal recorded by GCD2 for shot RID 70860 (shot 9 day 1) on the 4<sup>th</sup> September 2013 during the Knudsen campaign at Omega.

interactions from the Sydor framing camera at 4 cm, gated X-ray imager at 4 cm, neutron temporal diagnostic at 15 cm and the GCD1 at 20 cm. The rising background signal occurs where the Cherenkov signal would have been had there been pressurised gas in the GCD2, further validating the choice to run the detector evacuated. Figure 3.20 shows the raw precursor signal in continuous black from RID 70860 together with the post-processed traces. Two different approaches were used to analyse the data. The first approach was to fit the Gaussian shown in broken red to the signal above the 50 % point; the integral was then calculated using the product of the Gaussian full-width at half maximum and peak height. The second approach, which was used for the following discussions, involved fitting the Gaussian shown in broken green to the rising edge of the background signal and subtracting to leave the corrected signal shown in broken blue. The integration region was calculated based on a consistent method using the left-hand-side baseline and the minimum of the post-signal region after background subtraction. Several shots with less-favourable signal to noise values required 5-10 point smoothing to

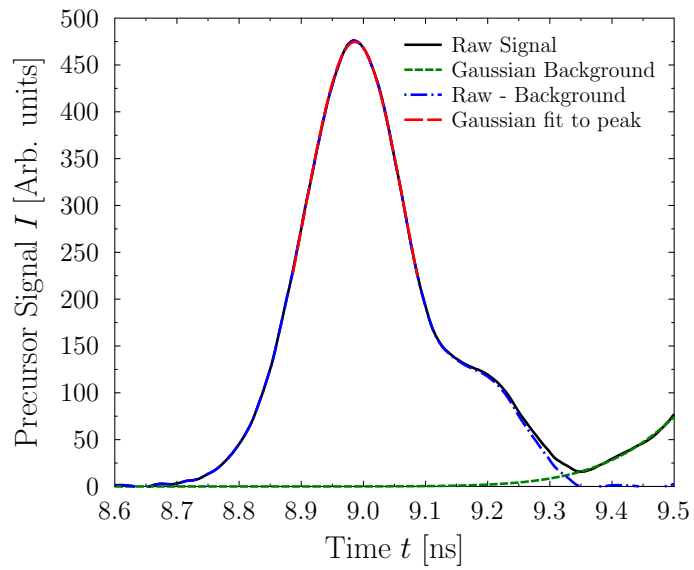


Figure 3.20: Plot showing the analysed signal recorded by GCD2 for shot RID 70860 (shot 9 day 1) on the 4<sup>th</sup> September 2013 during the Knudsen campaign at Omega. The raw signal is shown in solid black, Gaussian fit to the precursor signal above the 50 % point is shown in broken red, Gaussian fit to the rising background signal is shown in broken green and the raw GCD2 output after background subtraction is shown in broken blue.

meet the requirements of the analysis routine. Both analysis approaches produce the same results following cross calibration to  $< 3 \%$ . After integration a least-squares algorithm was written to minimise the deviation between the GCD2 and MIT data assuming the offset linear fit predicted by the GEANT4 precursor model shown in Figure 3.18. The MIT data consists of an error-weighted average of the available data from the CPS1, CPS2, WRF1 and WRF2 charged particle diagnostics analysed by M. Gatu-Johnson (MIT). Averaging over all charged particle diagnostics removed the possibility of comparing to individual diagnostics. Following the least-squares minimisation the resulting  $m$  and  $C$  constants were found to be 3960.2 and 21556.6 respectively. Values for  $m$  and  $C$  calculated from the GEANT4 model were 5902.7 and 66275.2; within a factor of 2 for the gradient and approximately a factor of 3 for the precursor signal associated with the DT spectrum. The model predictions could be improved if a full set of engineering drawings were produced for the GCD2. In addition neither the GCD1 or GCD2 models includes the ten-inch manipulator (TIM) which will introduce additional scattered sources. The model does however allow the statistical uncertainty of the precursor to be estimated; errors associated with each measurement during the Knudsen campaign are a quadrature combination of the uncertainty from background subtraction, signal integration and model.

Figure 3.21 shows a comparison between the MIT and GCD2 data with a reduced  $\chi/\sqrt{N} = 1.5$ . Good agreement is observed for the dataset except for shot RIDs 70870 and 70877. Closer inspection of the CPS and WRF data suggest the charged particle diagnostics were close to their noise floors for both shots which could cause the deviation. The measured yields from the neutron time of flight diagnostic were  $1.41 \times 10^{12}$  and  $2.95 \times 10^{11}$  for shot RIDs 70870 and 70877, an order of magnitude lower than the predicted yields of  $1 \times 10^{13}$  and  $3 \times 10^{12}$  respectively. Consequently the diagnostic distance from TCC, which is the only method of modifying dynamic range for the charged particle diagnostics, may not have been optimal. At present the GCD2 least-squares includes these possible outliers, however they may be removed in the future following further discussions with MIT. After removing the possible outliers the reduced  $\chi/\sqrt{N} = 1.2$ . Figure 3.22 shows a comparison

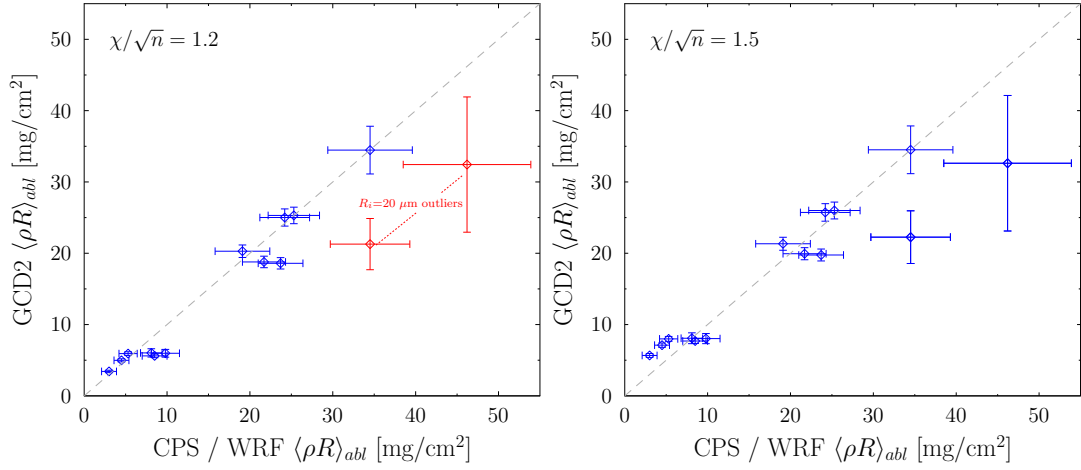


Figure 3.21: Plot showing a comparison between the charged particle spectrometer, wedge range filter and GCD2 with  $\chi/\sqrt{N} = 1.5$ . The CPS and WRF results were combined into a single result using an error-weighted algorithm by M. Gatu-Johnson (MIT). Left side comparison removes the two  $R_i = 20 \mu\text{m}$  possible outliers (red) recorded by the charged particle detectors from the analysis; the right hand side comparison includes the possible outliers.

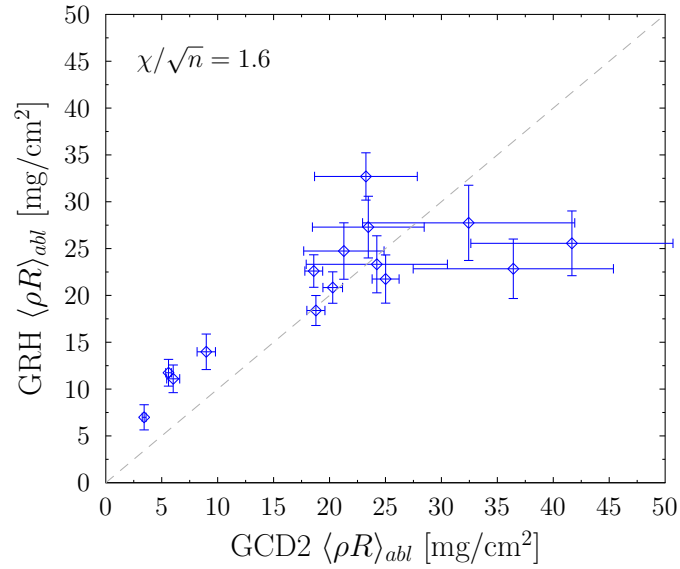


Figure 3.22: Plot showing a comparison between the GCD2 and GRH with  $\chi/\sqrt{N} = 1.2$ . The same least-squares approach used in the GCD2 analysis has been performed for the GRH data.

between  $\langle \rho R \rangle_{abl}$  values from GCD2 and GRH with  $\chi/\sqrt{N} = 1.2$ . GRH values were calculated using the carbon puck method described in the literature [87] and were post-processed using the same least-squares approach implemented in the GCD2 analysis.

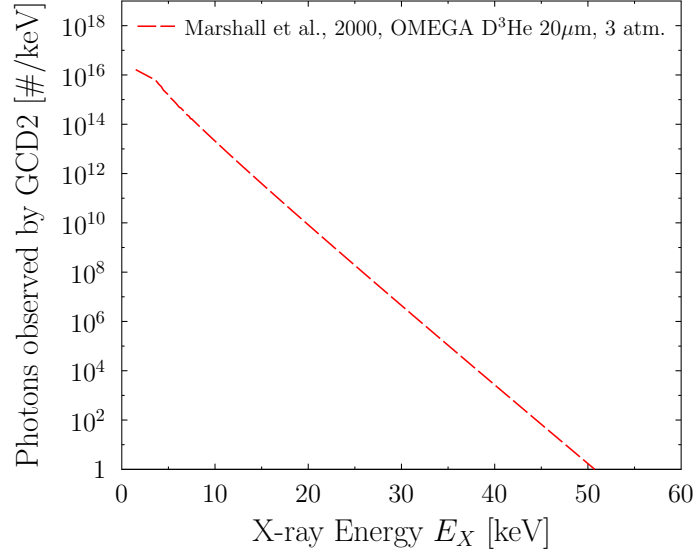


Figure 3.23: Plot showing the X-ray emission from a 20  $\mu\text{m}$  thick ablator  $\text{D}^3\text{He}$  implosion.

To rule out possible contamination of the precursor signal from X-rays generated in the hot spot at peak compression, the precursor model was again used. Plot 3.23 shows an X-ray spectrum generated from the hot spot at peak compression for a  $\text{D}^3\text{He}$  implosion with  $T_I = 1\text{keV}$  and a CD shell thickness of  $20\mu\text{m}$  recorded at the Omega laser facility [93]; unfortunately an X-ray spectrum for a DT implosion on OMEGA could not be found in the literature. The  $\text{D}^3\text{He}$  X-ray spectrum reduces below 1 photon/keV at approximately 50 keV. A GEANT4 simulation sampling X-ray photons from this spectrum was performed and subsequently combined with the precursor model; no energy deposition or optical photons were recorded at the photocathode. The X-ray emission from a DT implosion is unlikely to produce a significantly different spectrum, therefore hot spot X-rays are not contaminating the

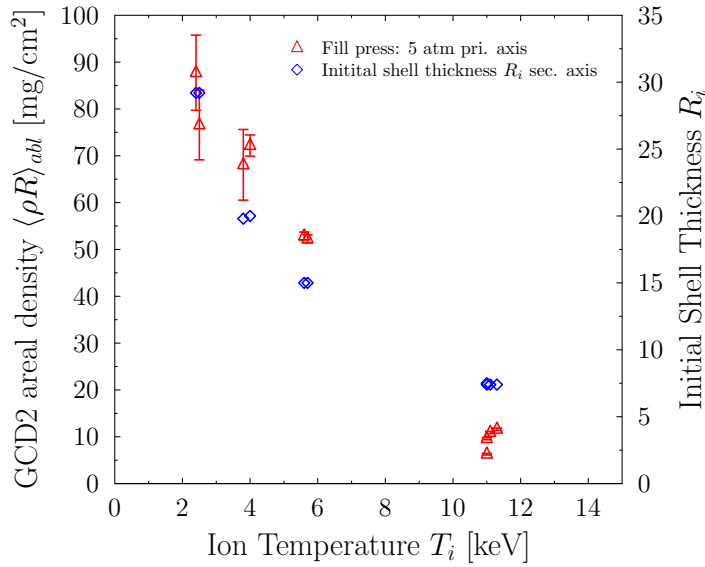


Figure 3.24: Figure showing  $\langle \rho R \rangle_{abl}$  measured by GCD2 (red triangles) together with initial shell thickness (blue diamonds) plotted against ion temperature.

GCD2  $\langle \rho R \rangle_{abl}$  measurement. In addition Figure 3.24 shows a comparison between  $\langle \rho R \rangle_{abl}$  values reported by GCD2 and the measured initial shell thicknesses against ion temperature for the 5 atm capsule fill dataset. If high-energy X-rays from the hot spot region were contaminating the  $\langle \rho R \rangle_{abl}$  measurement the values would likely increase with increasing ion temperature; however the opposite trend is observed.

Figure 3.25 shows a comparison between the bang time values recorded using the GCD2 and neutron temporal diagnostic NTD. The GCD2 diagnostic does not have an absolute timing fiducial from the laser system therefore the error has been estimated at  $\pm 50$  ps and the values cross-calibrated using the NTD data; relative timing however should be better than the conservative error estimate. The plot clearly shows agreement between the GCD2 and NTD; this constrains the origin of the precursor to a nuclear signal emitted at peak compression. If the precursor signal was generated from high-energy laser-plasma interactions (LPI) no correlation would be observed with the NTD bang-time results.

Several interesting trends were observed during the Knudsen campaign. Figure

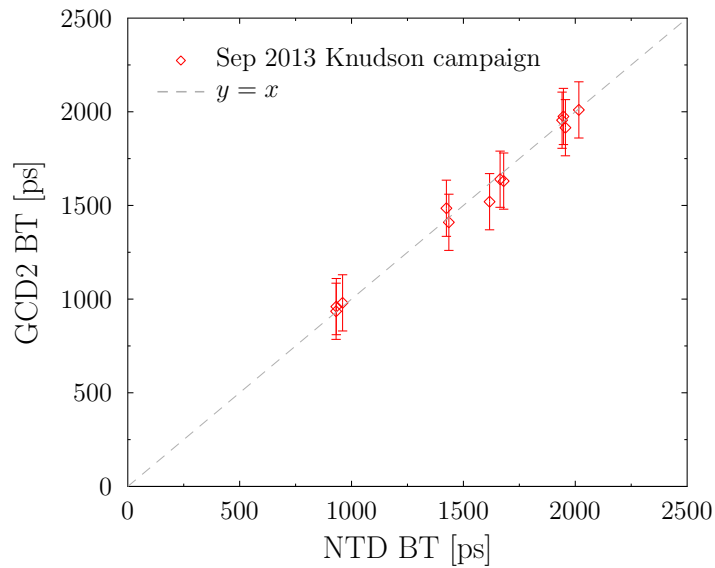


Figure 3.25: Figure showing cross-calibrated GCD2 bang-times compared to values from the neutron temporal diagnostic.

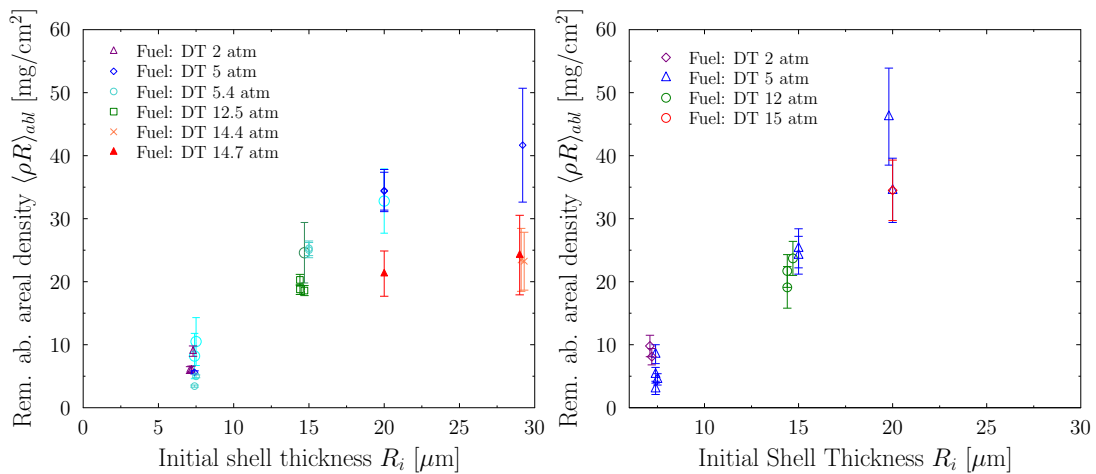


Figure 3.26: Plot (left) showing  $\langle \rho R \rangle_{abl}$  values cross-calibrated from the charged particle diagnostics during the September 2013 Knudsen campaign at the Omega laser facility. The right hand side data are error-weighted averages of the charged particle detector measurements. The independent axis is the initial capsule shell thickness measured prior to experiments. The various colour markers represent different fuel fill pressures in atmospheres.

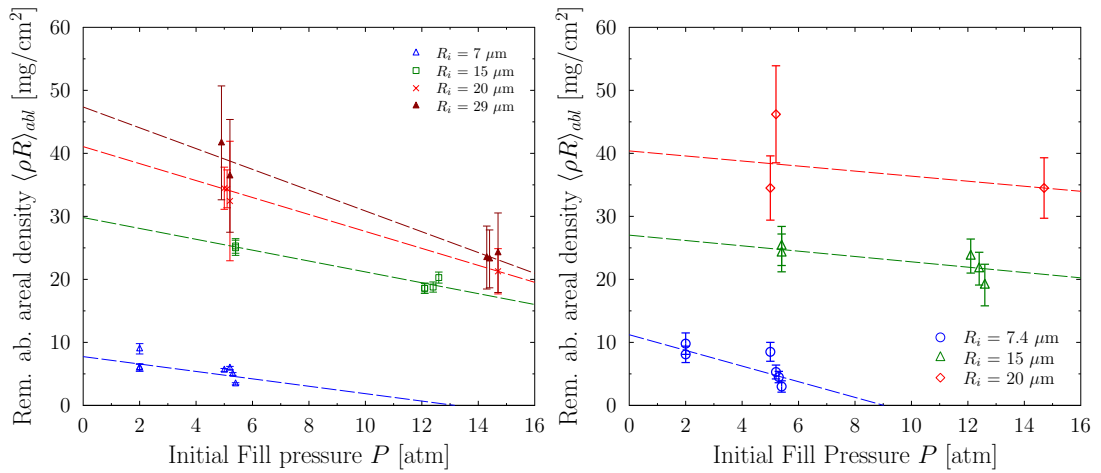


Figure 3.27: Plot showing  $\langle \rho R \rangle_{abl}$  values cross-calibrated from the charged particle results during the September 2013 Knudsen campaign at the Omega laser facility. Data on the right are error-weighted averages of the charged particle detector measurements. The independent axis in this case is the initial fuel fill pressure extrapolated from measurements taken during fabrication. The varying data markers represent the different initial shell thicknesses  $R_i$  measured prior to the campaign.

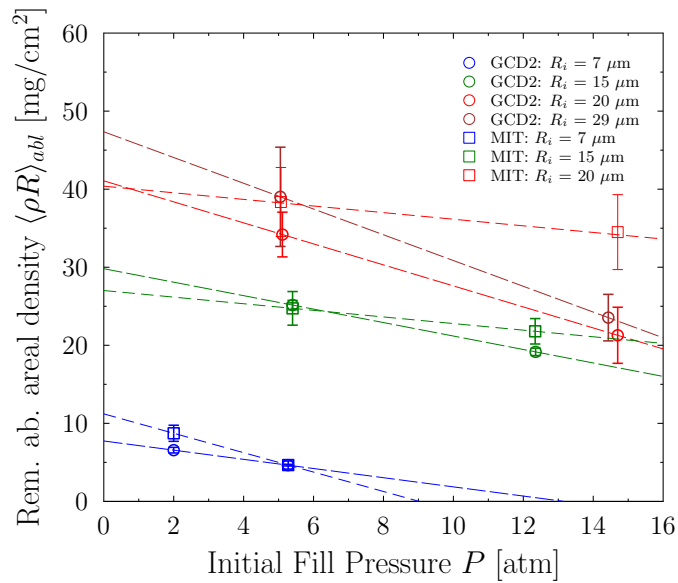


Figure 3.28: Plot showing error-weighted average  $\langle \rho R \rangle_{abl}$  values from the GCD2 diagnostic (circles) and the charged particle diagnostics (squares), plotted as a function of initial capsule fill pressure. Each error weighted data point comprises several measurements made with similar capsule conditions; varying colours correspond to different initial shell thicknesses.

3.26 shows  $\langle \rho R \rangle_{abl}$  against initial shell thickness, colour-coded by fill pressure. Figure 3.27 shows  $\langle \rho R \rangle_{abl}$  against fill pressure colour-coded by initial shell thickness. As expected  $\langle \rho R \rangle_{abl}$  increases with initial shell thickness; however in the GCD2 data there is a clear additional dependence on fill pressure. The same analysis from the GRH neither confirms or discounts the trend due to relatively large scatter at each capsule initial condition. Figure 3.28 shows error-weighted average  $\langle \rho R \rangle_{abl}$  values from the GCD2 diagnostic (circles) and the charged particle diagnostics (squares), plotted as a function of initial capsule fill pressure. Each error weighted data point comprises several measurements made with similar capsule conditions. The contour lines are linear fits to the resulting data-points for constant  $R_i$ . The plot clearly shows  $\langle \rho R \rangle_{abl}$  reduced with increasing capsule fill pressure, for constant shell thickness, throughout the Knudsen campaign. During 2002 however, a similar experiment with measurements made using the CPS diagnostics and several wedge range filter diagnostics reported no dependence on fill pressure [94], although the error bars on the three measurements may be too large to rule out a soft dependence.

### 3.3.6 The Prompt-Areal-Density Detector 1 (PADD1)

Accurate measurement of  $\langle \rho R \rangle_{abl}$  using an evacuated gas Cherenkov detector has been demonstrated; it follows that the same principles can be applied to a more compact diagnostic without the complexities of mounting a large 1+ metre long detector in a ten-inch manipulator or routing cabling through vacuum interfaces. The important aspects of the approach require a high-Z X-ray shield to block LPI and hot-spot X-rays, some lighter-Z bulk material to convert the 4.44 MeV gammas to electrons and positrons, a Cherenkov or scintillation radiator to convert the electrons and positrons to optical light, and a PMT to amplify the signal. The design philosophy is shown in Figure 3.29 and could be incorporated onto a port, located in a re-entrant tube or for low yields could be designed for use in a TIM. The diagnostic itself is similar in concept and design to the existing hard X-ray detectors (HXRD) currently fielded at NIF and Omega [95].

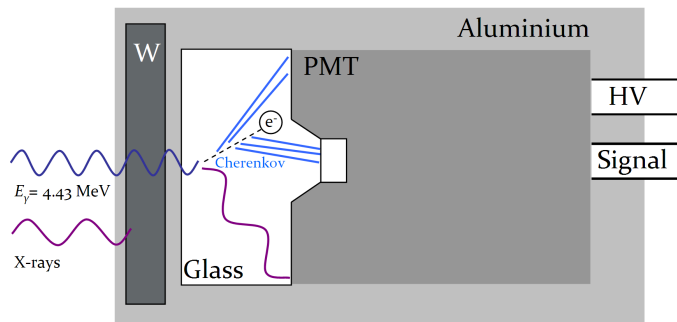


Figure 3.29: Not-to-scale schematic of the novel  $\langle \rho R \rangle_{abl}$  diagnostic. The essential components are the tungsten shielding to remove low-energy X-rays from LPI and hot spot, glass Cherenkov radiator to produce an optical signal proportional in intensity to the original gamma signal and a photomultiplier tube to amplify the optical signal.

Given the simplicity of the diagnostic a request was made to the Laboratory for Laser energetics (LLE) in July 2014 to assist in the design and fabrication of the detector, with a view to a first fielding during several high-yield shot days on the 26<sup>th</sup>, 27<sup>th</sup> and 28<sup>th</sup> August 2014. The individual campaigns were F. Merrill et al’s asymmetric implosion campaign designed to develop and characterise the neutron imaging system (NIS) and X-ray imaging systems, C. Sangster’s cryogenic implosion campaign with a modified laser pulse shape designed to optimise fuel areal density  $\langle \rho R \rangle_{fuel}$ , and A. Zylstra’s astrophysics campaign aimed at reducing the S-factor uncertainty in the H-D reaction as described briefly in Section 3.4, respectively. LLE agreed to field the diagnostic at a preliminary qualification status as a ride-along detector provided that the hard-X-ray detector (HXRD) design was leveraged to reduce complexity and impact on local resources. LLE would produce engineering drawings and handle the machining of individual aluminium components and tungsten HD18.5 (purchased from Mi-Tech Metals), except for the UV-grade SiO<sub>2</sub> glass which was contracted to CVI Melles Griot and the 8 × 1 mm thick tungsten plates which were procured from Goodfellow Ltd and cut to size by Panmure Instruments Ltd. The Photek Limited PMT110-B1140124 and PMT210-23100811 PMTs used over the 3 days were provided by AWE. A schematic of the final design rendered using FreeCad [96] is shown in Figure 3.30 with components

annotated for clarity. A photo of two sections of the machined PADD1 housing are also shown in Figure 3.31. Specific aspects include a reduced port cover thickness of 0.6 mm (from 19.05 mm) to allow maximum control of the line of sight mass external to the chamber, two Thorlabs threaded retaining rings to hold the tungsten filters and PMT housing in place, a polyamide foam to provide a soft landing for the polished glass during install, up to 10 mm of tungsten (6 mm was the default thickness during August, 8 of which are shown in Figure 3.34) and a light-tight housing courtesy of a rear plate and o-ring combination. Figures 3.32 and 3.33 show the PADD1 glass coupled with the PMT and de-coupled respectively. The detector would be installed on the 4" diameter port H11G. The initial name was Prompt Areal Density Diagnostic 1 (PADD1), pronounced 'Padawon'. However, due to a conflict with an existing similarly name PADD detector the name was changed to Diagnostic for Areal Density (DAD) by LLE to avoid confusion. The final name will be decided permanently by AWE at the final design review stage, which will take place following the preliminary fielding. For the remainder of this section the detector will be referred to as PADD1.

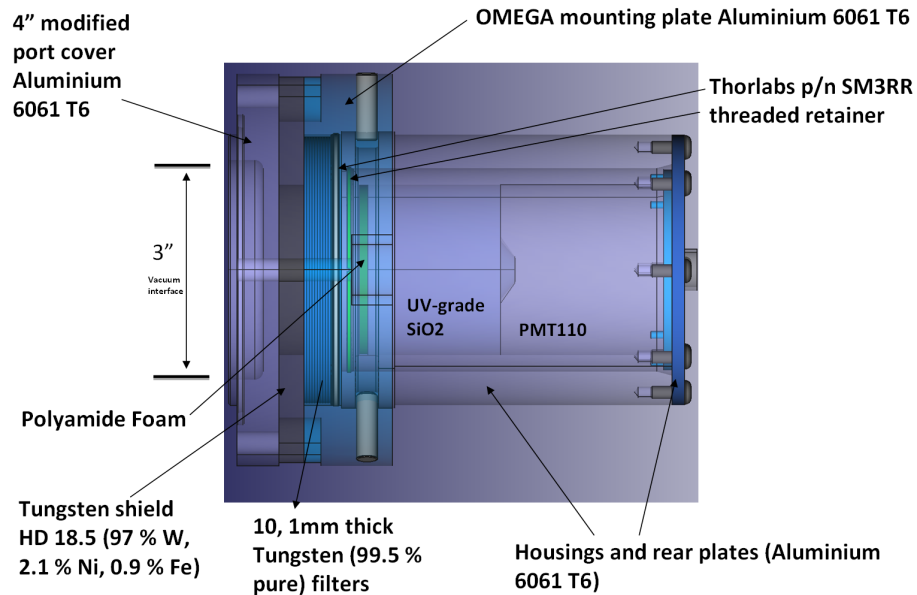


Figure 3.30: FreeCad [96] rendering of the PADD1 detector designed and fabricated in a joint collaboration between AWE and LLE.

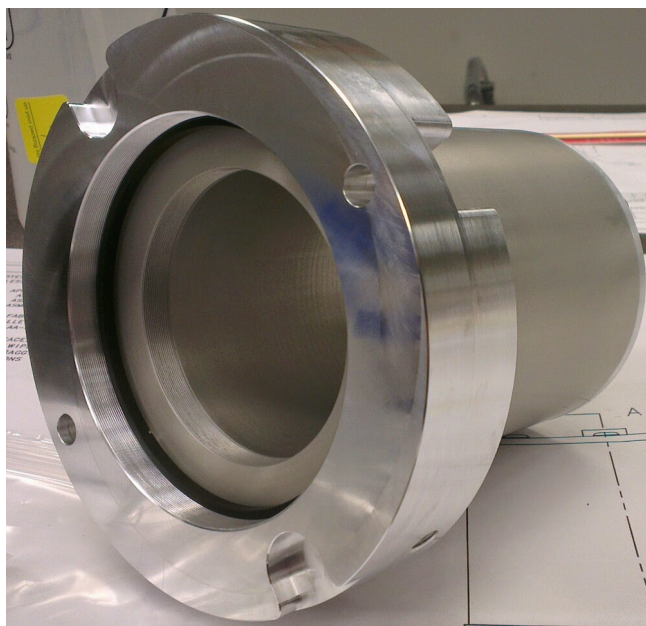


Figure 3.31: Photo of the PADD1 comprising the mounting plate and the external housing. The internal PMT-glass housing, tungsten shield plate and port cover are removed.

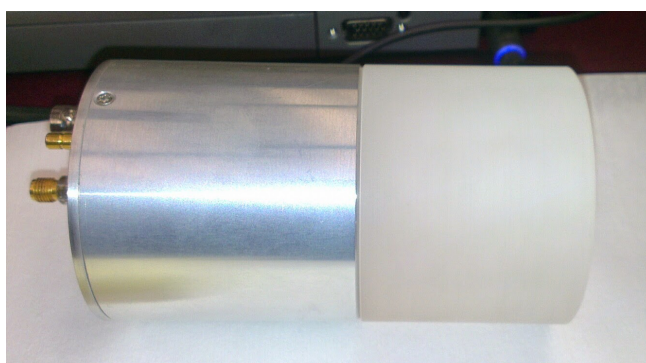


Figure 3.32: Photo of the PADD1 5 cm thick glass and PMT110 coupled together as they are inside the housing. The outer surface of the glass is opaque as the machining grooves are still present at the request of the author.



Figure 3.33: Photo of the PADD1 5 cm glass and PMT de-coupled to allow observation of the input window conical protrusion used to couple the Cherenkov light to the PMT input window.



Figure 3.34: PADD1 1 mm thick 99 mm diameter 99.997 % pure tungsten filters (8 in total). The housing has room for an additional 2 filters however Goodfellow did not have the entire set in stock prior to the preliminary fielding, and the full compliment were not necessary for the August 2014 experiments.

The PADD1 transmission line matches the Cherenkov detectors with a 40 foot 3/4 inch N-type foam-flex high-bandwidth cable combined with 10-20 feet of flexible SMA cable coupled to a SCD5000 oscilloscope. The extra SMA cable is used to reduce stress on the PMT and oscilloscope input connectors. In addition a Stanford Research Systems PS350 power supply together with an SHV cable were used to provide voltage and current to the PMT. The SCD5000 oscilloscope, signal cables and power supply were provided by LANL.

The aims for the preliminary fielding were to firstly identify the signal requiring pre-shot timing and peak voltage estimates, potentially followed by a cross-calibration to the GCD2 detector which was also being fielded in  $\langle \rho R \rangle_{abl}$  measurement configuration, and finally an optimisation of the line of sight tungsten filtering. Figure 3.35 shows intensity predictions from a GEANT4 simulation based on the CAD model shown in Figure 3.30. The PMT geometry used in the simulation was the same as used in the previous section for the GCD2  $\langle \rho R \rangle_{abl}$  measurements. The same post-processing technique was used to convert energy deposition into photocathode electrons. The output was then normalised to a neutron yield of  $1 \times 10^{13}$ , quantum efficiency of 18 %, gain of  $2 \times 10^4$  and combined with a signal temporal width of 200 ps to produce a predicted PMT peak voltage for a  $\langle \rho R \rangle_{abl}$  of  $1 \text{ mg/cm}^2$ . This was then scaled to higher  $\langle \rho R \rangle_{abl}$  values and combined with the constant DT signal associated with a neutron yield of  $1 \times 10^{13}$ . The capsule design used on Merrill's 26th August shot day were 15  $\mu\text{m}$  thick plastic with a 15 atm DT fill pressure producing expected yields between 2.5 and  $5 \times 10^{13}$ . Figure 3.28 predicts a  $\langle \rho R \rangle_{abl}$  value of approximately  $25 \text{ mg/cm}^2$  for this design. A PMT gain of  $7.32 \times 10^3$  at 4475 Volts was chosen. Combining a quantum efficiency of 18 % and a neutron yield of  $5 \times 10^{13}$  produces a PMT voltage of 63.5 V, which for a 200 ps pulse is marginally larger than the Photek-advised non-linear 10 nVs upper limit of the PMT. The actual signal is expected to be slightly lower than the ideal GEANT4 predictions for several reasons: CVI Melles Griot were unable to provide the requested  $L/2$  and 60 – 40 surface Figure and scratch dig in time for the experiment due to the short timescales, a design tolerance mismatch between the depth of the PMT in-

put window and the conical transmission region meant that a 100  $\mu\text{m}$  air gap was likely between the two surfaces reducing signal transmission by up to 30 %. The loss in transmission was calculated using a GEANT4 simulation with and without the gap and occurs due to the difference in refractive index between air and glass. This could be mitigated in the future using an index-matching membrane or fluid. The post-processing approach used for GCD2 over-predicted the output voltages by greater than a factor of 2; a similar over-prediction was likely for PADD1 therefore the PMT bias voltage was increased slightly to compensate for the combined loss mechanisms. The SCD5000 window, offset and CRT intensity, focus and background settings combine to allow a peak voltage of approximately 1-3 volts with a rise time of approximately 60-70 ps; consequently a 30 dB (30  $\times$ ) attenuator was used to reduce the peak voltage to within the optimal range.

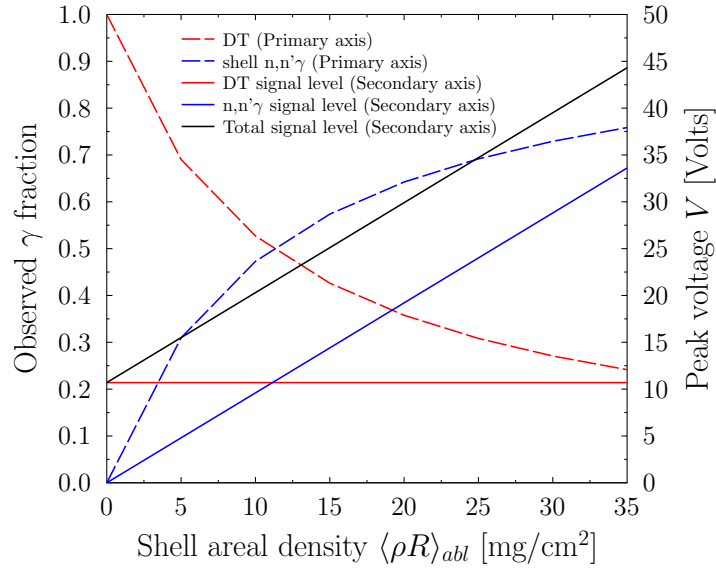


Figure 3.35: GEANT4 predictions of the signal response of the PADD1 detector split into contributions from the DT gamma spectrum and inelastic gammas from neutron interactions with carbon in the capsule ablator, normalised for a yield of  $1 \times 10^{13}$ .

In addition to the measured signal voltage the trigger timing of the scope is required. The impulse response functions of the GCD1 and PADD1 diagnostics

calculated using the GEANT4 model are shown in Figure 3.36; a delay of approximately 1.3 ns is observed between the two detectors. The trigger settings required to measure a GCD1 signal when combined with SCD5000 scope are well known. Consequently a second SCD5000 was cross-timed to the primary GCD1 SCD5000 using a signal generator and trigger/signal cables with the same length (internal trigger delay may vary between individual SCD5000 scopes by up to 15 ns). The second scope was then set to match the GCD1 SCD5000 with 1.3 ns of additional trigger delay.

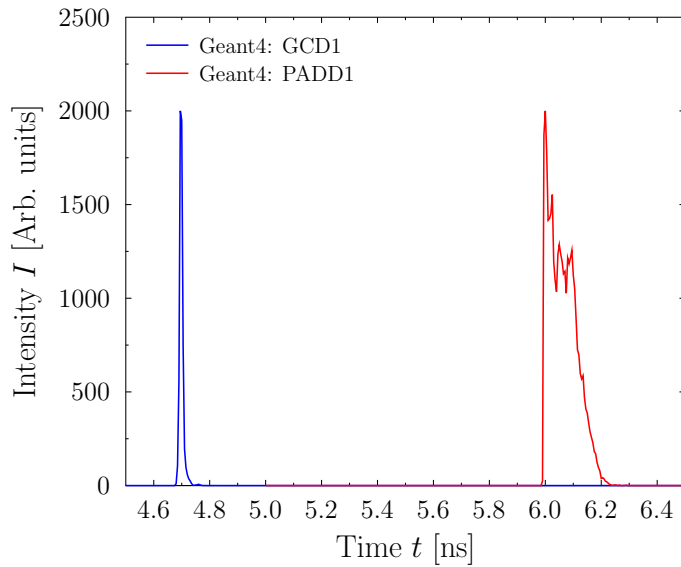


Figure 3.36: GEANT4 predictions of the absolute timing of the GCD1 Cherenkov optical signal relative to PADD1.

Figure 3.37 shows the entire dataset for F. Merrill’s shot day on the 26th August (red and black) together with the four cryo shots from C. Sangster’s campaign. The first set of data was taken using PMT110-B1140124 (black); unfortunately after the 5<sup>th</sup> shot the PMT failed due to an internal arc discharge. The PMT was then swapped out for PMT210-23100811 (red) which worked without incident for the remainder of the 2.5 days. As discussed previously in Section 3.3.4 the GCD2 and PADD1 detectors observe a constant background from the DT  $\gamma$  after the signal

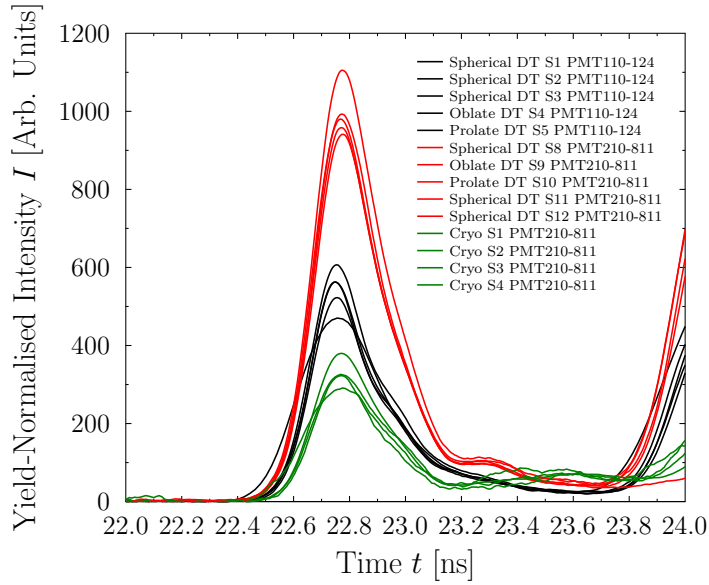


Figure 3.37: Plot showing PADD1 data from F. Merrill’s and C. Sangster’s asymmetric drive (red and black solid) and cryogenic implosion (green solid) shot days respectively.

has been normalised by neutron yield. After subtracting this constant contribution the remaining signal is produced from  $n,n'\gamma$  reactions with the remaining ablator material. During Sangster’s cryogenic implosions the capsules were designed such that the surrounding plastic material is fully ablated during the laser pulse leaving only the inner cryogenic surface to accelerate inwards and compress the fuel, leaving no measurable  $\langle \rho R \rangle_{abl}$ . In theory this should provide the ideal platform to measure the constant background from the DT  $\gamma$  without contributions from the remaining ablator. The green dataset in 3.37 shows the cryogenic PADD1 data after neutron yield normalisation (to  $1 \times 10^{13}$ ) and oscilloscope background subtraction. The S/N of the cryogenic dataset is not optimal as the neutron yields for the four shots were a factor of 10 lower than pre-shot predictions. In addition, on the first of the four shots the SCD5000 was configured to a 10 ns wide window further reducing S/N, to account for a possible 3 ns bang-time delay. Despite the yield and S/N limitations the average contribution from the DT  $\gamma$  was calculated from the four shots to be 22310 electrons with a standard deviation of  $\pm 8\%$ . Electrons in this case refers to

the number of electrons liberated from the photocathode which is calculated from the voltage on the SCD5000 trace using  $N = \frac{\delta t V}{50 G q}$  where  $\delta t$  is the resolution of the scope (5 ps in this case),  $V$  is the measured voltage, 50 (ohms) is the transmission line impedance,  $G$  is the PMT gain and  $q$  is the electron charge. The cryogenic shots were recorded using PMT210-23100811 therefore the calibration would not be valid for the failed PMT110-B1140124. With the constant background calculated the neutron-normalised data from the previous shot day could then be cross-calibrated to the GCD2. After subtracting the DT contribution the remaining signal integrals for shots 8 to 12 were divided by the  $\langle \rho R \rangle_{abl}$  values calculated by GCD2 to produce five calibration factors. The mean calibration factor was then calculated to be 1920 electrons per  $\text{mg}/\text{cm}^2$  with a standard deviation of  $\pm 5 \%$ . This average calibration factor was then re-applied to the original remaining integrals to produce the PADD1 reported  $\langle \rho R \rangle_{abl}$  values. For shots 1 to 5 the situation wasn't as straight forward due to the use of a different PMT for which the background calibration from the cryogenic shot day was not applicable. Shots 3 and 9 were measured to be  $24.63 \text{ mg}/\text{cm}^2$  and  $24.44 \text{ mg}/\text{cm}^2$  by GCD2 respectively therefore one would expect the constant DT background to be approximately the same for shots 3 and 9. Fortunately PADD1 did take data on shot 9 and using the cryogenic calibration the DT contribution was calculated to be 30.67 %. In the absence of a measured alternative the DT background was assumed to contribute the same percentage to the PADD1 signal for shots 3 and 9. The absolute DT contribution for shots 1-5 was thus calculated to be 12029 electrons. The remaining shell signal could then also be calculated for shots 1, 2, 4 and 5 using the same approach as before. Individual calibration factors were calculated using GCD2 results and averaged to produce 1089 electrons per  $\text{mg}/\text{cm}^2$  with a standard deviation of 7 %. The averaged calibration factor was then used to produce  $\langle \rho R \rangle_{abl}$  values for the failed PMT dataset. Data from the cryogenic implosions combined with the results on Merrill's campaign show that at approximately  $25 \text{ mg}/\text{cm}^2$  the DT background contributes 30 %; this compares extremely well with the GEANT4 pre-shot predictions of 30.8 % shown in Figure 3.35. In addition the integral signal predicted by the GEANT4 simulation

for a  $25 \text{ mg/cm}^2$   $\langle \rho R \rangle_{abl}$  implosion with a yield of  $1 \times 10^{13}$  was 43369 electrons liberated from the photocathode; shot 2 with a  $\langle \rho R \rangle_{abl}$  of  $25.4 \text{ mg/cm}^2$  generated 39700 electrons from the photocathode producing a deviation between experiment and simulation of less than 10 %. The agreement between PADD1 and GEANT4 is likely better than the GCD2 model due to the simplicity of the new detector. The GCD2 has a Cassagrainian optical system with primary and secondary mirrors combined with a lens which, if slightly misaligned or degraded, may produce the overestimate discussed in Section 3.3.5. PMT non-linearity throughout the shot day was not an issue as the largest observed neutron yield was half the maximum expected at  $2.91 \times 10^{13}$ .

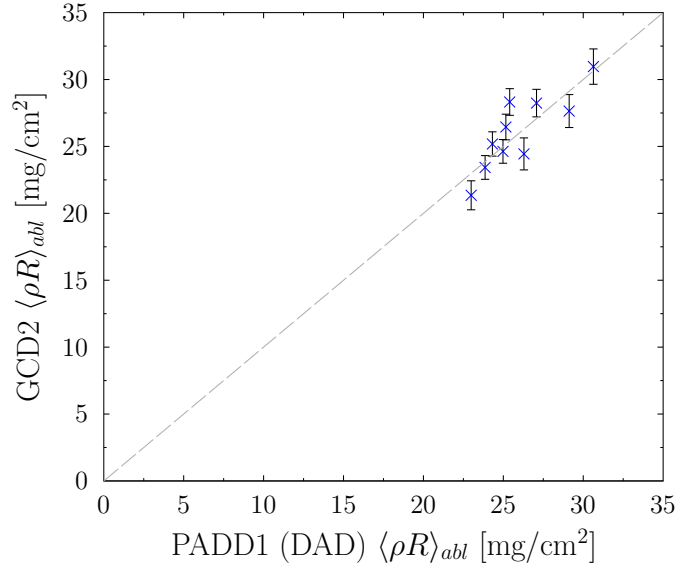


Figure 3.38: Plot showing the GCD2  $\langle \rho R \rangle_{abl}$  values against those reported by the novel PADD1 detector recorded during F. Merrill’s asymmetric implosion shot day in August 2014.

The  $\langle \rho R \rangle_{abl}$  values from PADD1 and GCD2 are compared in Figure 3.38 and show good agreement following cross-calibration. The largest deviation between the two detectors of 10.32 % was observed on shot 2. A full error analysis of the PADD1 as a function of yield and  $\langle \rho R \rangle_{abl}$  similar to the approach in Figure 3.18 will be performed once the final design review has taken place and the finished

design is commissioned. Given the agreement observed during the August shots the uncertainty is likely to be at least as good as GCD2.

The final shot day in August 2014 was A. Zyltra's astrophysics experiment consisting of plastic shells filled with  $D_2$ ,  $H_2$ ,  $DH$  and  $D^3He$ . The aim of the campaign was to measure the HD 5.5 MeV  $\gamma$  yield using the recently commissioned super GCD diagnostic at 400 psia and therefore constrain the astrophysical S-factor for the reaction which is currently known to only a factor of 3 precision. No fusion 14.1 MeV neutrons would be produced during these implosions therefore the PADD1 was not able to make  $\langle \rho R \rangle_{abl}$  measurements. Instead the shot day would be used to investigate the sensitivity to laser-plasma interaction (LPI) and hot spot X-rays which if high enough in energy may penetrate the nominal 6 mm of tungsten at the front of the diagnostic, or scatter around the 147.32 mm diameter 9.4 mm thick HD18.5 X-ray shield. Note the X-ray shield has an empty inner section with radius 63.5mm which is filled using the tunable tungsten filter plates. The target chamber outside the diameter of the X-ray shield is 76.2 mm thick aluminium which at 200 keV would let through 8 % of any signal. These X-rays would only require a single scatter to the glass and PMT housing. Low intensity nuclear  $\gamma$  photons were predicted for the  $D_2$ ,  $DH$  and  $D^3He$  implosions which PADD1 should be able to observe albeit with poor statistics and unknown sensitivity; these would be used qualitatively to investigate the S/N relative to any X-ray contributions. The  $H_2$  implosion is predicted to emit few or no high-energy  $\gamma$  photons and would therefore be used as a  $\gamma$  null for the day. To ascertain the magnitude of any direct X-ray interactions the line of sight tungsten shield would be varied between 4 mm and 8 mm. The yields were predicted to be more than  $200\times$  smaller than those observed during the previous high-yield DT implosions therefore the 30 dB attenuation was removed and the PMT bias increased to 4600 V from 4475 V, increasing total sensitivity by  $225\times$ . Figure 3.39 shows a selection of the recorded signals from the shot day. Each shot has not been normalised to particle yield as the signal may be proportional to laser energy which was constant at approximately 26 kJ throughout the entire day. The  $\gamma$  peak for each implosion has been corrected to 22.75 ns using the estimated bang

times and data from the previous shot days. The first signal of interest is the H<sub>2</sub> implosion with 6 mm tungsten filter (green) which shows no signs of a  $\gamma$  signal but contains multiple contributions from X-rays prior to the projected  $\gamma$  arrival time through to late time. The tungsten line of sight filters were subsequently increased to 8 mm for the HD implosion and were seen to have no effect. There is however a signal at 22.75 ns with poor S/N due to the background which may contain contributions from the 5.5 MeV HD  $\gamma$  and 24 MeV DD  $\gamma$ . The filtering was reduced to 4 mm for the subsequent HD implosion again with no impact on the background pedestal. The fact that the line of sight filtering has no impact and the signal begins early relative to the  $\gamma$  arrival time suggests that the signal originates from the laser-plasma interaction and is scattering off the chamber around the X-ray shield towards the glass and PMT region. Consequently over the next series of shots lead tape was progressively wrapped around the housing. Thicknesses are approximate as the lead was applied in between shots quickly for qualitative purposes. The red trace in Figure 3.39 shows that with just 1.2 mm of tape the background X-ray signal is reduced by over a factor of 2. The lead tape was then further increased to a total of 2.5 mm on shot 13 (blue). The S/N for this shot is 6.5 and represents a significant improvement over the earlier shots. Figure 3.40 shows the housing with full compliment of lead tape following A. Zylstra's astrophysics campaign.

Whilst the nuclear signals at 22.75 ns in Figure 3.39 are not the primary objective of the PADD1 detector the results from A. Zylstra's campaign show that with shielding modifications  $\gamma$  signals 200 $\times$  lower in intensity than those recorded during high-yield DT shots can be observed. Consequently the PADD1 designs are currently being modified to include a HD18.5 tungsten mounting plate and housing. The modifications will produce a minimum of 20 mm tungsten shielding between the target chamber scattering annulus and the PMT-glass housing, 8 $\times$  more than the thickest lead tape used earlier with the additional benefit of 60 % increase in density. Further modifications as the diagnostics moves from preliminary qualification status to final design review include: index-matching fluid for the glass-PMT input window interface to maximise light transmission, a flash aluminium coating

for the target-chamber-facing surface of the glass to collect backward-propagating Cherenkov light and a cable stress-relief system at the rear of the PMT to mitigate the risk of an LLE technician damaging the connections through impact. At the time of writing the PADD1 detector is one month away from final design review with a projected second fielding during ICF implosions at Omega in May 2015; this may occur earlier if a suitable high-yield cryogenic campaign can be identified.

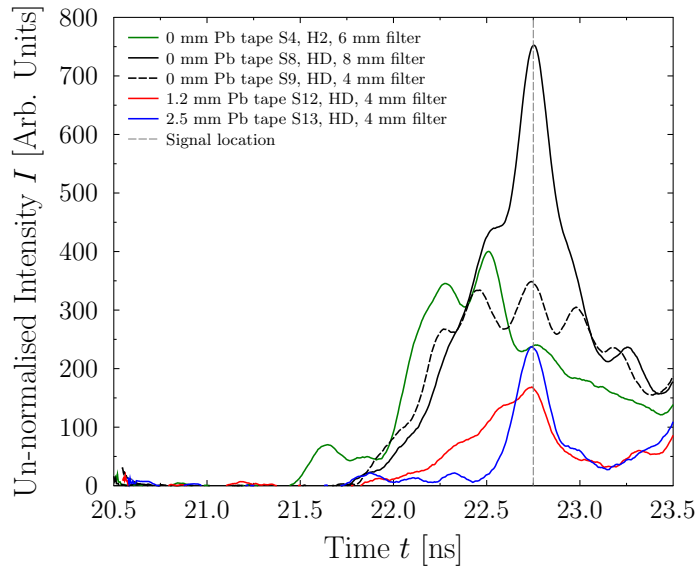


Figure 3.39: Plot showing the PADD1 signals recorded during A. Zylstra's astrophysics campaign. All traces have been time-aligned such that the nuclear gamma arrival time appears at 22.75 ns for clarity.

Moving on from direct drive experiments at Omega,  $\langle \rho R \rangle_{abl}$  measurements at NIF may be possible if PADD1 could be optimised to temporally separate the optical signal from undesired hohlraum gammas at similar energies using a Photodiode, for example a Photech PD010 with a response of approximately 65 ps. This would involve thinning the glass to minimise the temporal impulse response; neutron yields would be high enough to recover any associated reduction in sensitivity. In addition the shielding would need to be significantly increased to mitigate the massive background from laser-plasma-induced X-rays ( $67\times$  more on-target energy than Omega). The contribution from carbon and gammas may be separable in time



Figure 3.40: Photo of the PADD1 detector with the full compliment of lead tape after A. Zylstra’s astrophysics campaign. The black tape was used to ensure the housing was light tight subsequent to the PMT change on F. Merrill’s shot day.

using a forward-fitting/folding technique utilising the known shape of the carbon signal (from the reaction history) and hohlraum gammas (geometrical + reaction history and estimated using Monte Carlo). Mounting in a TIM and locating at approximately 20 cm would increase solid angle by almost  $\times 100$  and combined with yields  $> 10 \times 10^{15}$  would negate the requirement for MCP amplification. A PADD1 design for NIF with improved shielding would not require a complex signal unfold to record  $\langle \rho R \rangle_{abl}$  during polar direct drive experiments. The PADD1 capability may also form part of a multi-diagnostic plan to measure particle stopping power during implosion experiments at Omega or NIF [97]. During  $D^3He$  implosions a mono-energetic 14.7 MeV proton source is generated during the burn. An existing charged particle spectrometer could be used to measure the induced energy

down-shift through the ablator. Dopants combined with a filtered X-ray detector could be used to measure the plasma conditions in the ablator. PADD1 could then be used to accurately measure the  $\langle \rho R \rangle_{abl}$  providing all the necessary observables to calculate stopping power. Unfortunately these experiments would only cover a small region of the temperature and density phase space. However the addition of a second target, possibly heated and compressed using a combination of short and long pulse lasers, could be used to cover a wider range of plasma conditions.

### 3.3.7 Conclusions

In summary a new technique has been demonstrated for measuring  $\langle \rho R \rangle_{abl}$  during direct drive ICF implosions using  $\gamma$  emission from inelastic neutron interactions with the ablator material. The technique has been developed into a new detector currently known as PADD1 at Omega. Conceptual design, Monte Carlo modelling and data analysis were performed by the author whilst LLE updated HXRD engineering drawings according to the PADD1 requirements. All engineering work was performed at LLE with materials and parts procured by AWE. Installation was performed in collaboration prior to the Knudsen campaign. Measured values from GCD2 in September 2013 compare well with data from the charged particle diagnostics and the  $\gamma$  reaction history diagnostic. The new PADD1 detector which heavily leveraged the existing HXRD at NIF and Omega has been designed in a multi-national collaboration between AWE, LLE and LANL and was fielded in preliminary status on three shot days during August 2014. A preliminary analysis of the PADD1 dataset shows strong correlation with signals recorded by GCD2 which was also fielded during the campaign. Several shielding modifications and minor changes to the glass and housing have been suggested as the project progresses to final design review in Autumn 2014. The benefit of the technique demonstrated in GCD2 and PADD1 in comparison with existing systems includes reduced statistical uncertainty and prompt analysis (no requirement for CR39 etching or Cherenkov null shot subtractions). Although a cross-calibration with charged particle detec-

tors has not been performed, PADD1 and GCD2 are also capable of making  $\langle \rho R \rangle_{abl}$  measurements for glass capsules, which GRH is unlikely to be able to perform. In addition the technique is applicable at NIF during polar direct drive experiments and, with further design and analysis effort, the PADD1 may be used to report  $\langle \rho R \rangle_{abl}$  during indirect drive implosions.

### 3.4 Super GCD design

During the latter part 2012 and through 2013 the design process began for the next generation Cherenkov detector currently name 'super GCD'. Unlike GCD1 and GCD2 this detector would be designed for fielding at both NIF and Omega which requires additional considerations including increased LPI X-ray energies and intensities due to the 1.8 MJ vs 25 kJ laser power, inelastic  $\gamma$  signals from the  $10\times$  higher shell  $\langle\rho R\rangle_{abl}$  values compared with Omega and the continuum and resonance  $\gamma$  emission from inelastic neutron interactions with the gold hohlraum. One objective for the super GCD detector is to measure the 5.5 MeV  $\gamma$  ray emitted during the fusion of hydrogen and deuterium, which is of critical importance for understanding the poorly understood solar proton-proton (P-P) reaction [98]. This mechanism is the dominant heating mechanism in low-mass stars such as our sun; in larger mass stars with higher core temperatures the carbon-nitrogen-oxygen (CNO) cycle and hot-CNO processes are more efficient methods of fusing hydrogen to helium.

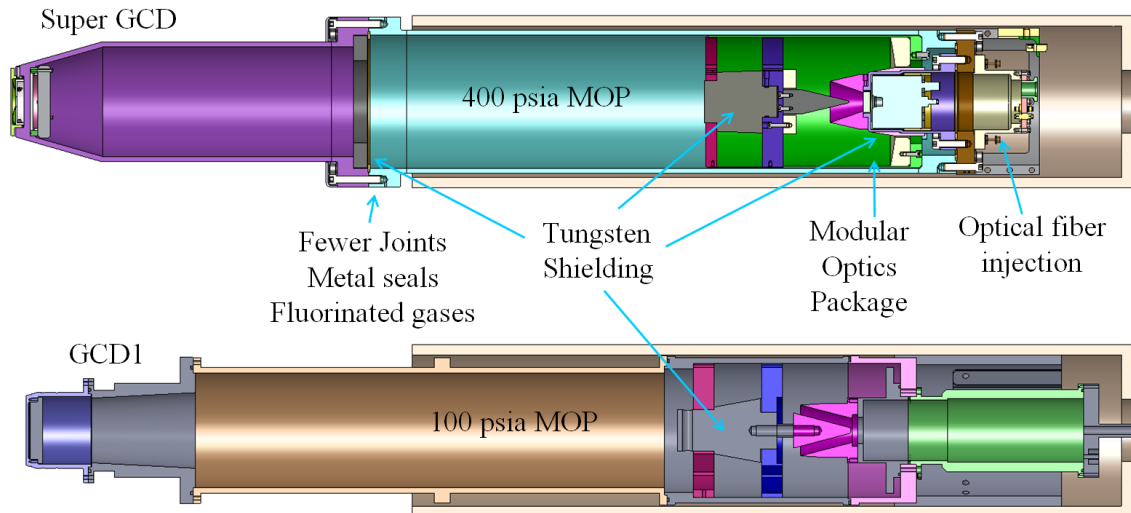


Figure 3.41: Cutaway view from the engineering CAD models of super GCD and GCD1 created using the SolidWorks eDrawings viewer [99]. MOP stands for Maximum Operating Pressure.

The first step in the P-P chain ( $p + p \rightarrow D + e^+ + \nu_e$ ) proceeds slowly as the

interaction is weak; consequently it is currently unfeasible to probe this reaction in the laboratory. This reaction eventually builds a suitable concentration of deuterium in the core to allow the second reaction in the chain to occur. This step ( $D + p \rightarrow {}^3\text{He} + \gamma (E_\gamma = 5.5 \text{ MeV})$ ) may be measurable at the Omega laser facility. The astrophysical S factor for this reaction has been calculated previously during several accelerator experiments [100]; the uncertainty in the combined dataset at ICF implosion temperatures of  $T_i = 3\text{-}15 \text{ keV}$  is approximately  $\times 3$ . Super GCD may be able to improve the uncertainty in this value to a level similar to the reported D-T branching ratio of  $\pm 50 \%$ . The three-body nature of the H-D reaction also makes ab initio calculations easier to compute when compared to DT, TT and  $D^3\text{He}$  reactions; constraining the S factor improves understanding of the nuclear theory.

Using all 60 beams with a total energy of 25 kJ, combined with a 1 mm diameter glass ( $3 \mu\text{m}$  thick) capsule filled with 15 atm of hydrogen (50 %) and deuterium (50 %), is calculated to produce  $T_i = 11 \text{ keV}$  and D-D and H-D yields of approximately  $1 \times 10^{11}$  and  $4 \times 10^6$  respectively. A similar setup with an  $870 \mu\text{m}$  diameter plastic ( $20 \mu\text{m}$  thick) capsule and 17 atm of the same fuel is calculated to produce  $T_i = 4 \text{ keV}$  and D-D and H-D yields of approximately  $2.5 \times 10^{10}$  and  $1 \times 10^6$  respectively. The 5.5 MeV  $\gamma$  is unobservable by GCD1 and GCD2 as it lies below the minimum threshold of  $E_\gamma = 6.3 \text{ MeV}$  at 100 psia. The GRH diagnostic can be filled to 215 psia  $\text{SF}_6$  with an associated  $E_\gamma = 2.95 \text{ MeV}$ ; the GRH however is located 187 cm from TCC outside the target chamber which reduces the solid angle by  $\times 90$  compared to GCD1 and GCD2 at 20 cm. Super GCD will support gas pressures up to 400 psia with  $E_{th} = 1.75 \text{ MeV}$  and will be located at 20 cm. The H-D reaction emits a 5.5 MeV  $\gamma$  during each reaction; combined with the relative super GCD solid angle of 0.0127 this amounts to 50800 ( $T_i = 11 \text{ keV}$ ) or 12700 ( $T_i = 4 \text{ keV}$ )  $\gamma$  photons interacting with the detector. The super GCD model discussed in the next section has been calculated by GEANT4 to have a response of 0.06 Cherenkov photons for  $E_\gamma = 5.5 \text{ MeV}$ , leading to approximately 3000 ( $T_i = 11 \text{ keV}$ ) or 740 ( $T_i = 4 \text{ keV}$ ) recorded Cherenkov photons; sufficient for a statistically significant observation. The observation is complicated by the emission of a 23.8 MeV  $\gamma$  during the D-

D reaction with a poorly understood branching ratio of approximately  $1 \times 10^{-7}$ ; again using the GEANT4 model the response at  $E_\gamma = 23.4$  MeV is calculated to be 0.52 leading to 66 ( $T_i = 11$  keV) or 17 ( $T_i = 4$  keV) recorded Cherenkov photons. Consequently the H-D signal should be approximately  $45 \times$  larger than the D-D background. In addition the D-D contribution can be subtracted using the D-D yield scaled data from a pure D<sub>2</sub> filled capsule designed to produce the same  $T_i$ . An additional complication is the contribution from neutron inelastic interaction with the plastic or glass ablator; the D-D neutrons in this case are lower in energy ( $E_n = 2.5$  MeV) compared with the 14.1 MeV fusion neutrons discussed in Section 3.3 and therefore shouldn't contribute a significant background. Nonetheless any background contributions can be investigated during the pure D-D calibration capsules.

### 3.4.1 GEANT4 output to LightTools 8.0

The super GCD GEANT4 model was modified to record the initial  $x$ ,  $y$ ,  $z$ ,  $E_\gamma$ ,  $P_x$ ,  $P_y$ ,  $P_z$  and  $t$  of each Cherenkov photon produced for a specific gas type and pressure.  $P_{x,y,z}$  here corresponds to the components of the momentum direction unit vector,  $t$  is the pre-step time in ns (pre-step is chosen instead of post to ensure the point of initial photon production relative to a  $\gamma$  photon being produced at target chamber centre (TCC)), and  $E_\gamma$  is the energy in eV of the optical photon required to assess the chromatic dependence of the optical system. The resulting data file then contains the full optical source term which can be used to design the mirror locations and curvatures of the diagnostic. The same algorithm was added to the GCD1 GEANT4 model to provide a direct comparison with a validated model.

Obtaining this information however is not simple. Each of the gas cells in the diagnostic were set as sensitive. In the sensitive detector class a logical statement was used to distinguish optical photons using the particle string name; each time a new photon was produced the aforementioned parameters were written to a stringstream buffer. The situation is complicated by the possibility of double counting the start-

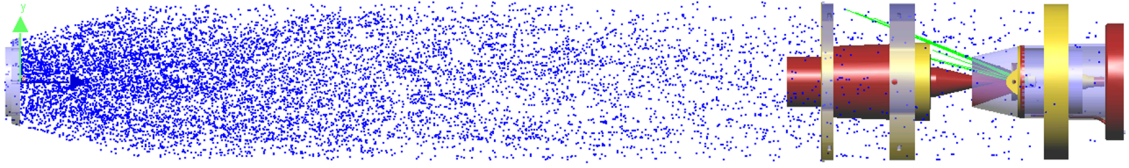


Figure 3.42: Image produced by LightTools showing the starting locations (blue from GEANT4) in super GCD for a gas pressure of 220 psia in SF<sub>6</sub>.



Figure 3.43: Image produced by LightTools showing the starting locations (blue from GEANT4) in GCD1 for a gas pressure of 100 psia in CO<sub>2</sub>.

ing location; the sensitive detector class provides the user access to many useful variables associated with the current step, there is however no boolean or integer to signal the current step is the first for a particular particle following an interaction. The chosen solution was to use three global integers: `stored_eventID`, `stored_trackID` and `stored_parentID` to determine whether the step was the first. The required parameters were only written to the stringstream buffer when at least one of the three global integers differs from the current `eventID`, `trackID` and `parentID`. If this condition is satisfied then the stored integers are updated to the current integers and the process begins again. This approach forms the basis for eliminating double counting throughout all the code written in this thesis.

The GEANT4 output files were combined with the optical ray tracing software LightTools [101] [102] produced by Synopsys by Robert Malone (National Security Technologies, Los Alamos, NM, USA). To combine the output files with LightTools a source template file was created by first running a dummy LightTools simulation containing the correct header format and input syntax. The contents of the GEANT4 output was then modified slightly using a text editor to conform to the

required file structure and subsequently copied into the optical source file and easily read by LightTools.

Figure 3.42 and 3.43 show the GEANT4 starting locations after being read into the LightTools package. Important points to note are the different tapers at the front of the two diagnostics. GCD1 has a much thinner gas cell immediately behind the converter compared to super GCD which opens up at a much larger angle; the taper is required in both detectors to ensure the geometry is within the diagnostic envelopes (line of sight required by laser systems and other diagnostics) at Omega and NIF. The light green lines on the super GCD image correspond to photons produced far down the gas cell interacting directly with the PMT and avoiding the Cassagrainian system; the intensity of the direct shine is less than 0.5 %. This agrees with the precursor investigations in Section 3.3.4 which showed that the vast majority of optical photons recorded prior to the minimum Cassagrainian time-of-flight are caused by Compton- and pair-produced electrons generating Cherenkov photons in the pressure windows and depositing energy into the PMT photocathode.

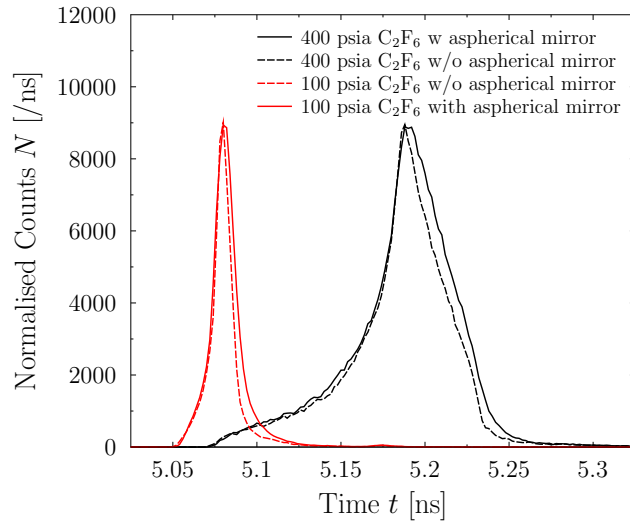


Figure 3.44: Temporal response of super GCD for 100 and 400 psia  $C_2F_6$  in red and black respectively. Broken lines correspond to the response with the aspherical mirror replaced with a flat mirror. The aspherical mirror offers slightly better light collection efficiency due to the collection of additional late-time paths.

As discussed in Section 3.1 understanding the diagnostic temporal response, also known as the impulse response function (IRF), is of great importance for measurements made at NIF and Omega for two primary reasons: a wide temporal response greater than 200 ps will smear out important features in the reaction history; relative delays introduced by varying the gas pressure and therefore refractive index will systematically change the reported bang time. Super GCD has been designed to handle pressures of 400 psia, almost  $2\times$  the maximum rating of the GRH diagnostic and  $4\times$  the GCD1 rating at Omega. As predicted in Figure 3.8 this will introduce significant broadening to the temporal response. Figure 3.44 shows the super GCD temporal response for 100 and 400 psia  $C_2F_6$  generated using a DT Hale source distribution. The 400 psia  $C_2F_6$  signal shows significant broadening at early time likely due to gammas converting further down the high-density gas cell;  $\gamma$  photons and electrons (a 12 MeV electron has  $\gamma = 12/0.511 = 23.5$  with  $v_{e^-}/c = \sqrt{1 - 1/\gamma^2} = 0.9991$ ) can travel at  $c$  whereas optical photons produced near the converter region must travel at the reduced SOL  $c/n$  which is significant at high pressures (approximately 1.033 at 400 psia  $C_2F_6$  compared to approximately 1.0063 at 100 psia  $C_2F_6$ ). At 100 psia  $C_2F_6$  the gas cell density of  $0.04 \text{ g/cm}^3$ , compared to  $0.22 \text{ g/cm}^3$  for 400 psia  $C_2F_6$ , is not sufficient to act as a continuous converter. It is difficult to describe the width of the 400 psia temporal response using a FWHM as the shape is asymmetric; the width at half maximum is approximately 50 ps however at the base the spread is as large as 150 ps, which is on the order of the response of the single and double stage Photek PMTs to be used in the detector. Consequently the temporal response will be an important component of the deconvolution and forward fitting routines developed at NIF to unfold reaction history [103].

### 3.4.2 Aspherical secondary mirror

A significant difference between super GCD and the existing axial Cherenkov detector GCD1 and GCD2 is the progression to an aspherical secondary instead of a flat

(GCD1) or spherical (GCD2) mirror. In GCD1 a significant fraction of the optical photons redirected by the primary mirror toward the outer edge of the secondary mirror are lost because the reflection angle is too small and the rays are lost to the tungsten bat ear shielding (shown in yellow in Figure 3.45). In super GCD the secondary mirror has an aspherical profile as shown in Figure 3.45 which expands the reflected angle at the edges and increases the amount of light recorded at the PMT. The shape was optimised by Bob Malone using the LightTools program. The aspherical shape developed and optimised by Bob Malone (LANL) using LightTools is shown in Figure 3.46 and is defined by the equation

$$z = \frac{Cy^2}{1 + \sqrt{1 - [(k + 1)C^2y^2]}} + Ay^4 + By^6, \quad (3.10)$$

where  $C = -5.5381 \times 10^{-4}$ ,  $A = 1.522 \times 10^{-7}$ ,  $B = 3.790 \times 10^{-11}$  and  $k = 0$ . No default GEANT4 CGS volume exists that comprises such a complicated aspherical surface therefore a different approach was required to create the mirror in the Monte Carlo geometry. The solution was to write an IDL routine which splits the aspherical surface into 50 linear sections along the Y axis. By splitting the problem into conical sections each can now be described by a CGS cut cone which is a default GEANT4 volume. The values at  $Y_{min}$  and  $Y_{max}$  were used to calculate the inner and outer radii of the cut cone and  $Z_{min}$  and  $Z_{max}$  were used to calculate the thickness. Logical statements were used to ensure the volumes were drawn correctly following the inflexion at  $Y = 27$  mm. Finally, a formatted print algorithm was used to write the cut cone values to a file in the required GEANT4 syntax. This file was read directly by the user detector geometry through an include statement. The splitting number of 50 was chosen to provide a good approximation to the surface whilst not over-complicating the geometry and reducing computational efficiency. Figure 3.45 (right) shows the resulting array of cut cones visualised using the HepRApp software. A similar formatted print to file routine and include method was used to give each cut cone reflective properties similar to those described in Section 1.7.11.

Figures 3.51 and 3.53 show the reduction caused by replacing the aspherical

mirror (broken black) with a flat mirror (broken red) for super GCD at 100 and 30 psia CO<sub>2</sub>. The reduction at both pressures is approximately 30 %. Figure 3.44 shows the additional signal recovered by the aspherical mirror (solid lines) comes at late time with respect to the detector temporal response; the additional signal broadens the response by 2-3 ps at 100 psia and 5-10 ps at 400 psia.

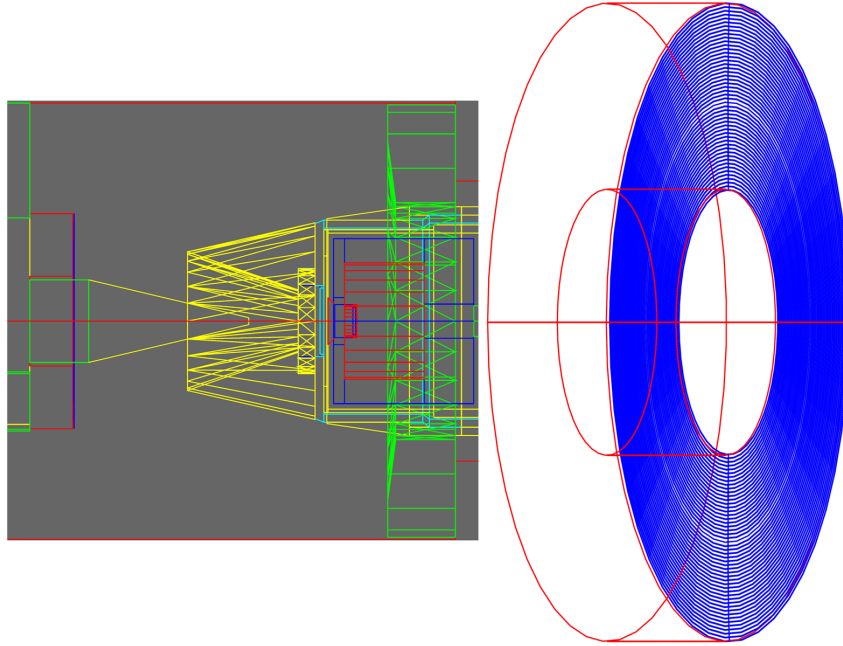


Figure 3.45: Isometric view of the super GCD aspherical mirror produced by the visualisation software HepRApp. The blue rings consist of 49 cut cone volumes in GEANT4 with each edge approximating the curve shown on the right.

### 3.4.3 Additional super GCD shielding

The increased inelastic  $\gamma$  signals producing Cherenkov light can be mitigated by increasing the  $\gamma$  threshold  $E_\gamma$  to 10 MeV (as opposed to  $E_\gamma=6.3$  MeV at Omega) above the majority of the inelastic spectrum; this does reduce the intensity response of the detector by a factor of approximately  $\times 15$  however the increased yields observed at NIF of ( $>10 \times 10^{15}$ ) more than make up for the drop in response; this solution has been implemented on the existing GRH diagnostic with good success [104].  $\gamma$  interactions that contribute signal to the precursor, as discussed in Section

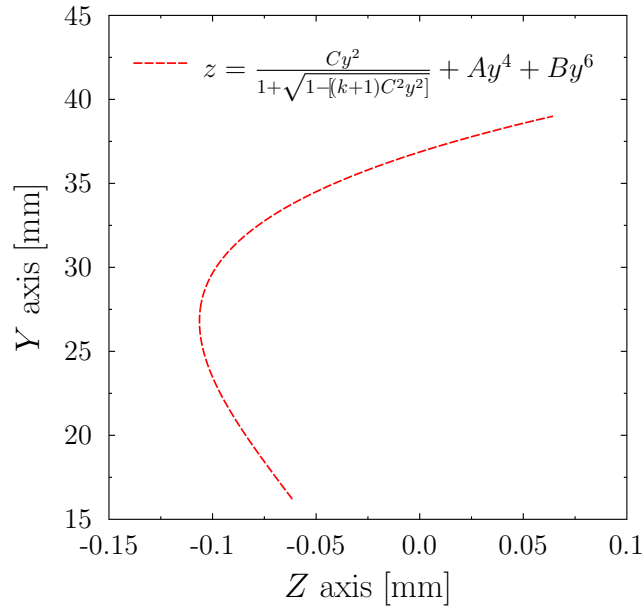


Figure 3.46: Plot showing the final aspherical mirror curvature optimised using the GEANT4 to LightTools technique. The aspherical coefficients are  $C = -5.5381 \times 10^{-4}$ ,  $A = 1.522 \times 10^{-7}$ ,  $B = 3.790 \times 10^{-11}$  and  $k = 0$ .

3.3.4 however can not be mitigated using this approach. In GRH the 3 off-axis parabolic mirrors and flat mirror separate the precursor and main Cherenkov signal by approximately 4-5 ns. In super GCD this separation is 0.8 ns as shown in Figure 3.51. The only approach that can be used to reduce the additional precursor is to insert high-Z shielding inside the diagnostic at specific locations designed to reduce Compton and pair electrons from reaching the PMT and pressure window without significantly impacting the intensity of the desired Cherenkov signal. In reality the amount of shielding that can be incorporated into the diagnostic depends on the mass and torque constraints associated with mounting the detector in a TIM or DIM. The weight limit of the detector is 100 lb and prior to this investigation the engineering team at LANL were close to this; therefore any shielding needed to be strategically and efficiently located.

Previous modelling of the GCD2 and GCD1 detectors have shown that the precursor signal originates primarily from electron-Cherenkov light in the glass pressure

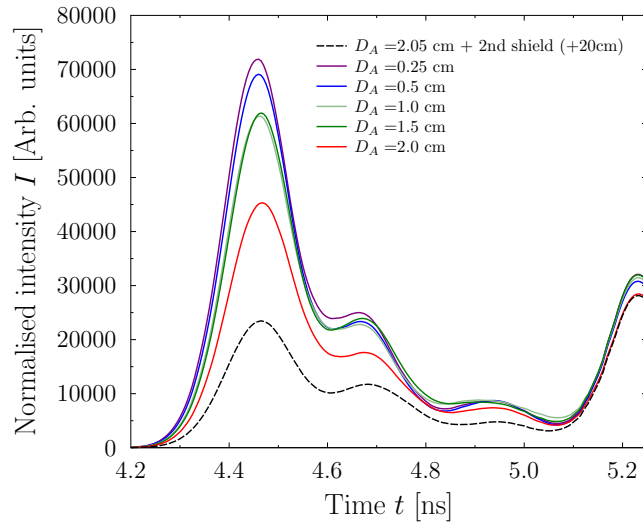


Figure 3.47: Plot showing the super GCD temporal response for several different annulus thicknesses at a CO<sub>2</sub> gas pressure of 30 psia. Raw GEANT4 data has been post-processed using the precursor model described in Section 3.3.3 and convolved with the impulse response function of a single stage Photek PMT (see Figure 4.3).

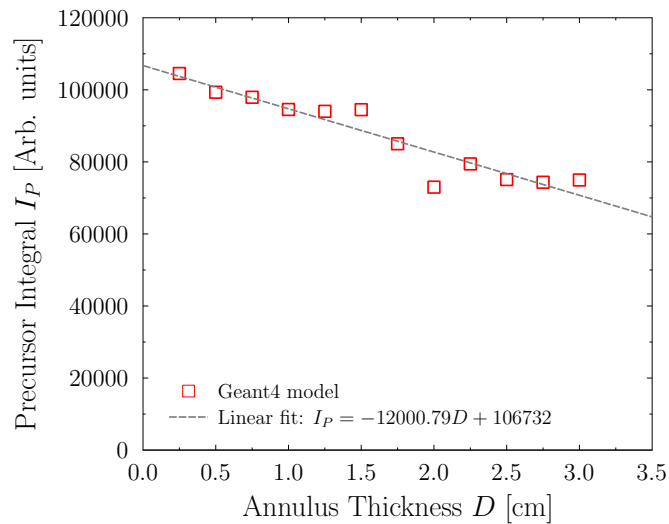


Figure 3.48: Plot showing the reduction in the precursor area as a function of annulus thickness. The plot shows that a 2 cm annulus drops the integral signal by  $> 20\%$ . The annulus does however reduce the signal more at later time therefore the improvement at the rising edge of the DT signal is better than 20%.

and input windows of the detector and PMT respectively. Originally the region between the primary Cassagrainian optic and pressure window / PMT housing was empty; the first additional tungsten shielding was located here to reduce the energy of any electrons scattering from the primary mirror (which is not shadowed by the central tungsten block) inward towards the PMT and pressure window. The second and most important additional tungsten shield was a 2.05 cm thick annulus placed approximately 37.5 cm from the right-hand side of the converter down the gas cell at the first bulkhead.

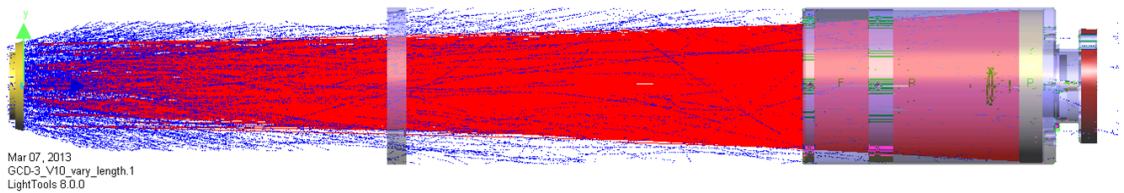


Figure 3.49: Side view of the super GCD model from LightTools. Blue dots represent the Cherenkov birth locations predicted by the GEANT4 model and the red lines are the light rays with initial momentum vector also from the GEANT4 model.

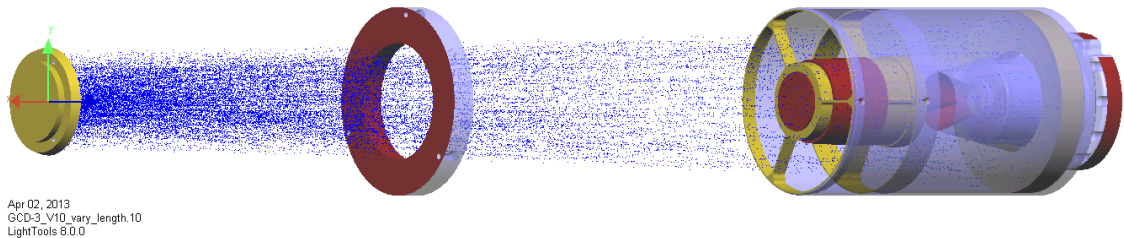


Figure 3.50: Isometric view of the super GCD model from LightTools clearly showing the position and impact of the annulus. Blue dots represent the Cherenkov birth locations predicted by the GEANT4 model.

Figure 3.48 shows the integral of the precursor as a function of annulus thickness for  $\langle \rho R \rangle_{abl}$  of  $33 \text{ mg/cm}^2$  and  $\text{CO}_2$  pressure of 100 psia. The reduction in precursor shows a definite linear relationship with annulus thickness. In addition, as can be seen in Figure 3.52 the improvement at the rising edge of the desired Cherenkov peak is approximately  $\times 2$  far better than the 25 % reduction predicted using the

precursor integral, suggesting that the annulus is reducing the precursor intensity more at late time. A similar result is obtained for the same  $\langle \rho R \rangle_{abl}$  and a CO<sub>2</sub> pressure of 30 psia shown in Figure 3.53.

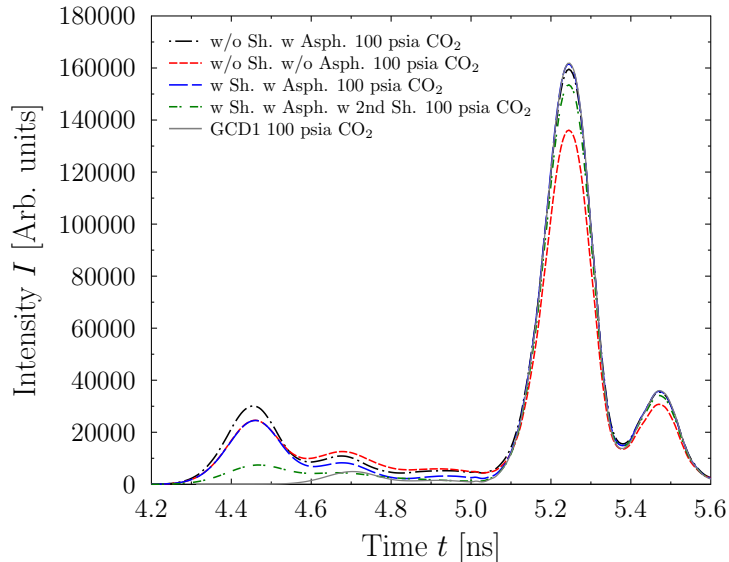


Figure 3.51: Plot highlighting the evolving precursor for several different shielding configurations with and without the aspherical mirror at a CO<sub>2</sub> gas pressure of 100 psia. Raw GEANT4 data has been post-processed using the precursor model described in Section 3.3.3 and convolved with the impulse response function of a single stage Photek PMT (see Figure 4.3). For comparison the GCD1 signal has been plotted in continuous grey.

An interesting result when performing these calculations was that the desired Cherenkov signal was not significantly reduced by the annulus despite the large solid angle subtended by the mass. The current inner radius of  $R_1 = 5$  cm was calculated by Robert Malone (LANL) to be the minimum that could be supported without losing any Cherenkov photons from the primary peak. The location of the tungsten annulus is shown in Figures 3.49 and 3.50 together with the Cherenkov birth locations and initial momentum vectors from the GEANT4 model. The red ray traces in Figure 3.49 clearly show that even with the tungsten in place no rays are blocked by the mass. It may also be the case that additional Cherenkov tracks are produced through the annulus acting as a  $\gamma$  to  $e^-$  converter. The added weight

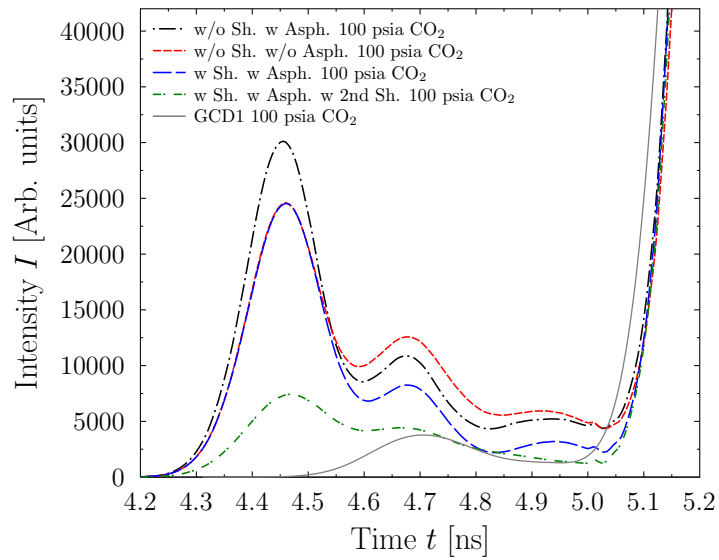


Figure 3.52: Plot highlighting the evolving precursor for several different shielding configurations with and without the aspherical mirror at a  $\text{CO}_2$  gas pressure of 100 psia. The plot is the same data as Figure 3.51 with the dependent axis expanded. Raw GEANT4 data has been post-processed using the precursor model described in Section 3.3.3 and convolved with the impulse response function of a single stage Photek PMT (see Figure 4.3). For comparison the GCD1 signal has been plotted in continuous grey.

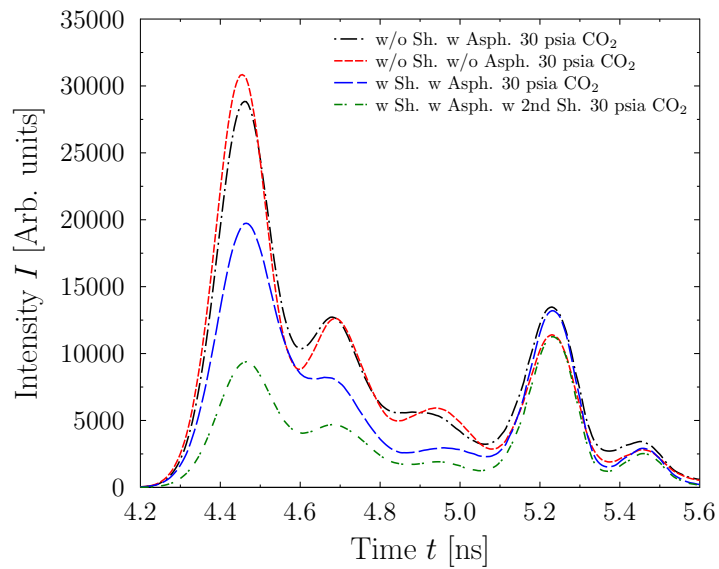


Figure 3.53: Plot highlighting the evolving precursor for several different shielding configurations with and without the aspherical mirror at a CO<sub>2</sub> gas pressure of 30 psia. Raw GEANT4 data has been post-processed using the precursor model described in Section 3.3.3 and convolved with the impulse response function of a single stage Photek PMT (see Figure 4.3). For comparison the GCD1 signal has been plotted in continuous grey.

that the 2.05cm thick annulus represents is  $\rho V = 19.25\pi (R_2^2 - R_1^2) = 4.8$  kg, where  $R_1=5$  cm and  $R_2=8$  cm are the inner and outer radii of the annulus respectively and  $l = 2.05$  cm is the annulus thickness. The shielding discussed earlier inside the primary Cassagrainian mirror represents less than a kg of additional mass. Figure 3.51 shows a comparison between the predicted super GCD signal compared to the GCD1 signal both calculated using the precursor model. Without shielding the precursor in super GCD is  $5\times$  larger in integral compared to GCD1; however the important region is the ratio of the intensities at the rising edge of the desired Cherenkov peak of approximately 3-4. With the shielding in place the precursor at the rising edge drops to within a factor of 2 compared to GCD1. Given the accuracy of the precursor model of a factor of 2-3 from Section 3.3.5, when applied to a different detector to GCD1, a prudent prediction for the super GCD precursor would be that it is likely to be similar in magnitude to the existing background observed by GCD1.

Figures 3.52 and 3.53 show that the precursor signal could be reduced even further by placing a second identical annulus 20 cm further down the gas cell; there is however a small associated reduction in the desired Cherenkov signal in this configuration and the mass constraints may further preclude inclusion.

### 3.4.4 Light output responses

Predicting the light output of the super GCD detector is important for planning future experiments such as the H-D reaction discussed previously. The light response is defined as the number of detected Cherenkov photons per incident  $\gamma$  at the PMT photocathode (PC); the PC is used instead of the glass input window to avoid double counting when combining the response with the PMT quantum efficiency curve (shown in Section 2.5). The algorithm used to record light response was the same as the methods used for GCD1, GCD2 and GRH; in short the response is the integral of all optical photons recorded at the PC (5 ps bin resolution) between 4.9 and 5.3 ns. The window is set late enough in time to avoid the precursor and

narrow enough to remove any low-intensity late-time reflections. Note that Figures, such as 3.51, 3.52 and 3.53 show GEANT4 data following convolution with the single-stage Photek PMT shown in Figure 4.3, and is consequently far broader than the raw GEANT4 output which shows negligible counts in the 400 ps spanning the precursor and Cherenkov peak.

Figure 3.54 shows super GCD responses (continuous lines) calculated using the GEANT4 model for several gas pressures as a function of  $E_\gamma$ . Also shown are two GCD1 responses at 100 and 30 psia CO<sub>2</sub> for comparison. Surprisingly the super GCD response as predicted by GEANT4 is lower than GCD1 by approximately 30 % across all gas configurations. This disagrees with the predictions made using LightTools using the GEANT4 birth locations which predicts super GCD to be higher by 25 %. This is likely due to the linear approximation to the aspherical mirror used in the GEANT4 model. GEANT4 predicts that the additional signal recovered by the aspherical surface is 25-30 % however LightTools suggest the mirror augments the recorded signal by  $\times 2$ . Good agreement is obtained between lightTools and GEANT4 when replacing the aspherical mirror with a flat mirror. Figure 3.55 shows the light response of the super GCD calculated by GEANT4 normalised to the response calculated by LightTools for the gas and source term configurations requested during the optics optimisation process. The responses in Figure 3.55 will form the basis of any future experiments using super GCD.

Figures 3.56 and 3.57 are binned Cherenkov birth locations (as used in the GEANT4 to LightTools technique) plotted against distance from converter in mm. This series of plots nicely shows how the nose region geometry of each detector impacts Cherenkov production in the gas cell. Figure 3.56 contains binned super GCD data for several gas pressures, shielding configurations and  $\gamma$  source definitions. The data shows that the geometry dominates the shape of Cherenkov production and only small variations are seen between the DT Hale source spectrum,  $E_\gamma = 5.5$  MeV and different gas pressures. This result provides confidence that the final Casagrainian optical configuration should provide good collection efficiency across a wide range of source terms and gas pressures. At approximately 400 mm the first

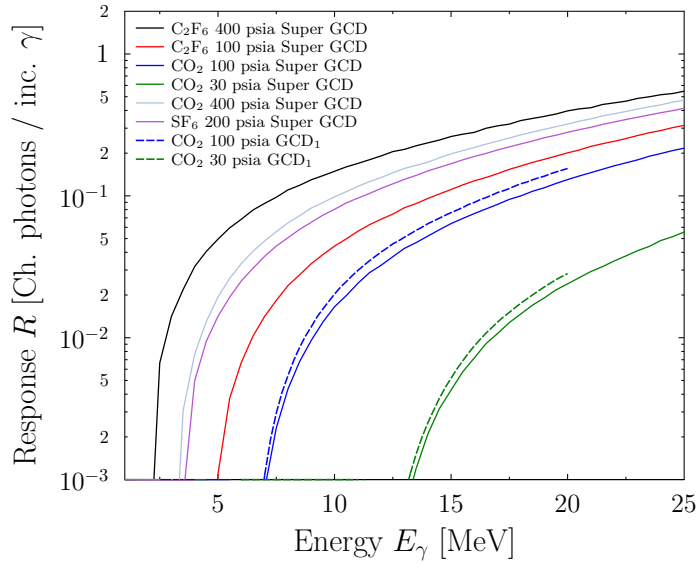


Figure 3.54: Super GCD light responses for several different gas pressures plotted as a function of incident  $\gamma$  energy. Also plotted (broken lines) are the same response calculations performed for GCD1.

bulkhead region (right hand side of the purple region in Figure 3.41 is evident as an abrupt increase in Cherenkov production. In all cases without the tungsten annulus the Cherenkov production increases at this point due to the expansion of the cell and the bulkhead acting as a  $\gamma$  to  $e^-$  converter. The higher pressure  $C_2F_6$  400 psia simulation shows the same trends as the lower pressures; the features at the bulkhead however are smeared out due to a smaller density discontinuity at the cell walls. With the shielding in place the opposite features are observed; the annulus reduces the diameter of the gas cell and attenuates any electrons converted in the bulkhead mass.

Figure 3.57 shows a comparison between the Cherenkov production locations for super GCD with GCD1. The shapes show a similar overall trend but contain subtle differences related to the different geometries. The birth locations are augmented near the GCD1 bulkhead at 200 mm for the same reasons as discussed previously for super GCD; the data shows that a significant amount of light is lost in the thinner nose cone of GCD1 relative to super GCD. There is however more Cherenkov

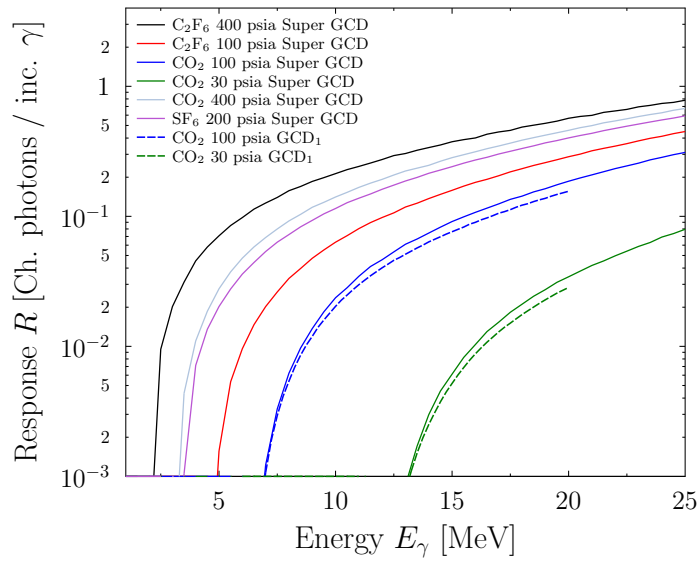


Figure 3.55: Super GCD light responses for several different gas pressures plotted as a function of incident  $\gamma$  energy. Also plotted (broken lines) are the same response calculations performed for GCD1. Between the GEANT4 model and LightTools model there is a slight difference in predicted intensity observed by the PMT (likely related to the GEANT4 aspherical mirror implementation). This plot shows the super GCD responses from Figure 3.54 normalised to the LightTools values.

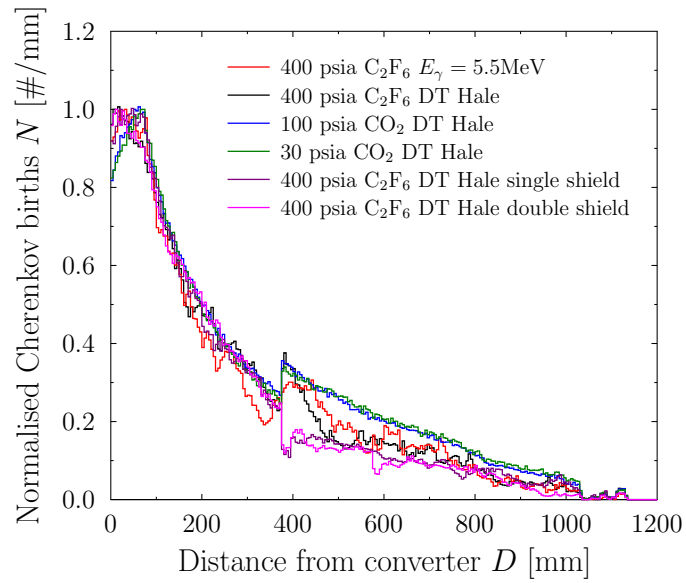


Figure 3.56: Figure showing a histogram of the Cherenkov birth locations for super GCD for several different gas types and pressures with and without the tungsten annulus in place. Also included is the histogram for a single line at 5.5 MeV.

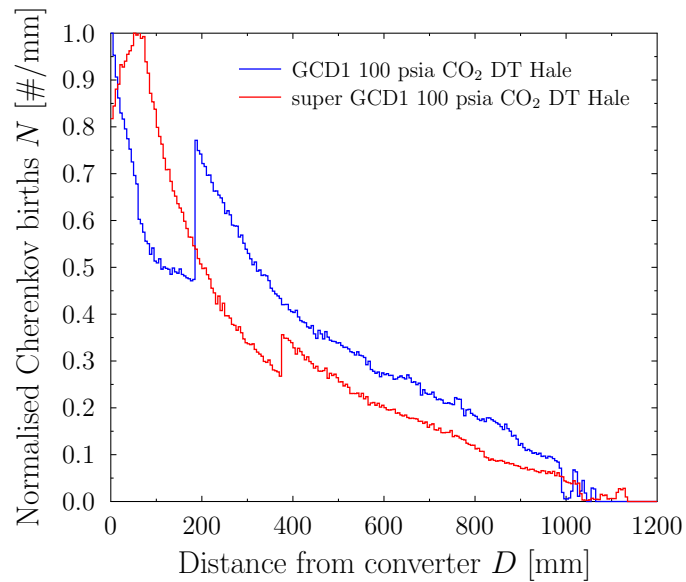


Figure 3.57: Figure showing a comparison between histogrammed Cherenkov birth locations super GCD (red) and GCD1 (blue) at a CO<sub>2</sub> gas pressure of 100 psia.

light produced by GCD1 further down the gas cell; this may be related to the 200 mm bulkhead which subtends a large solid angle relative to super GCD1 again acting as a converter. Again, this comparison confirms that the light production in each detector is dominated by the detector geometry with little dependence on gas conditions.

### 3.5 Summary

Chapter 3 discusses the design work performed using the Monte Carlo code GEANT4 in support of the Cherenkov detectors at Omega and NIF. The experimentally-validated codes from Section 2.5 were used to generate temporal impulse response functions (IRF)s for the GRH diagnostic at NIF. Analysis shows that gas pressure changes between 1 and 215 psia produce a peak centroid delay of 28 ps, a significant result considering the required  $\pm 50$  ps uncertainty in bang time measurements. The resulting IRFs are now part of the deconvolution and forward-fitting routines at LLNL used to unfold bang time from GRH raw data.

The following section describes an IDL routine developed by the author to calculate light collection efficiency as a function of gas type, pressure and  $\gamma$  energy for all the Cherenkov detectors. The complex phase space (light response, energy, gas pressure) required a grid interpolation routine and surface fitting algorithm. The completed IDL routine is currently in use at Lawrence Livermore and Los Alamos National laboratories for signal prediction and data analysis.

The next investigation proves the sensitivity of the Cherenkov detectors to neutron-induced inelastic  $\gamma$  emission from remaining ablator material at peak capsule compression. An undesired background signal had been observed consistently by the GCD1 and GCD2 detectors at Omega and speculated to originate from this interaction. Experiments were performed in September 2013 with an evacuated GCD2 to confirm the relation. The areal density was independently measured using the Charged Particle Spectrometer and Wedge Range Filter detectors. Good agreement was found between the GCD2 signal integral and independent measure-

ments. Consequently a permanent port-mounted detector initially named PADD1 (Prompt Areal Density Diagnostic 1) was designed with the author as Principle Investigator (PI). Conceptual design, data analysis and experimental setup form part of this thesis; engineering drawings and manufacture were performed by the Laboratory for Laser Energetics. PADD1 was successfully fielded in August 2014 and will be fully commissioned in May 2015.

The final section of this chapter discusses the GEANT4 design work used to optimise the next-generation Cherenkov detector super GCD. Output from the GEANT4 model was coupled to the optical ray tracing software LightTools. This included the 3D direction, 3D location and wavelength of every Cherenkov photon generated inside the super GCD gas cell for a variety of gas conditions,  $\gamma(E)$  distributions and engineering designs. Thus allowing the Cassagrainian optics and housing to be optimised with a realistic source term for the first time in this community. In addition a tungsten shielding annulus was designed as part of this work to reduce background signals from inelastic  $\gamma$  interactions. Using the GEANT4 model coupled to the LightTools package the background signal was reduced by a factor of approximately 3 over the non-shielded case, without impacting the primary signal.

### 3.5.1 Requirements for improved optical detectors

As mentioned throughout this thesis current MCP-based PMT technology limits the bandwidth of the Cherenkov detectors to approximately 100 ps FWHM, between  $2\times$  and  $10\times$  the intrinsic bandwidth of the gas cell and optics depending on the gas fill pressure and the detector variant. A Mach Zehnder interferometer system is used for signal transmission with bandwidth in the region of 30 ps, also significantly faster than the PMT. One option to increase bandwidth could be to replace the PMT with a photodiode, which is essentially a photomultiplier tube without the amplification dynode / micro-channel plate. This may be an option in circumstances where signal levels are large, such as the GRH diagnostic during NIF implosions with neutron yield greater than  $\times 10^{16}$  combined with a 200+ psia cell pressure. At the time

of writing there are plans to make this modification for one of the GRH channels at NIF. Unfortunately the observed signal when running GRH at high pressures (low Cherenkov threshold  $E_{th}$ ), is dominated by  $n, n'\gamma$  emissions from the shell and hohlraum. The individual contributions of each gamma source may be resolvable with a photodiode, making a direct measurement of  $\langle \rho R \rangle_{abl}$  possible; the burn history, which is the primary observable however, is smeared out by the inelastic gamma contributions. To measure the burn history the gas pressure needs to be set lower ( $E_{th} = 10$  MeV) to remove signal contamination. In this configuration and at currently achievable neutron yields the Cherenkov signals are too small to enable use of a photodiode. At current ICF yields the photon to electron conversion stage requires amplification by a minimum of  $\times 100$  to be useful across the current generation of Cherenkov detectors at NIF and OMEGA.

# Chapter 4

## Cherenkov light detection

### 4.1 Requirements for Cherenkov detectors

The optical focusing across the current generation of Cherenkov detectors at NIF and OMEGA is designed to produce a 10 mm diameter diverging beam at the input window location of the PMT. For compatibility, any novel photo-amplification device would require at least a 10 mm diameter window. For similar reasons the dimensions of the amplification device should be 63.9 mm diameter and 60.7 mm length for compatibility with the existing housings and feedthroughs; obviously for exceptional circumstances where significant bandwidth improvements are guaranteed modifications to the final optics and PMT housing can be made, but with large associated costs.

At present the burn width of implosions at NIF and Omega are approximately 100 ps, similar to the FWHM of the best single-stage PMTs available. As discussed in Section 1.6 important implosion structure is lost due to detector broadening at the PMT, therefore new technologies and approaches are required. In addition charge amplification of greater than  $\times 100$  is still required at currently achievable implosion neutron yields.

## 4.2 Review of detector technologies

The next section will discuss several of the existing technologies used for photon measurement and amplification, and applicability to the Cherenkov detectors.

### 4.2.1 Micro-channel plate photomultipliers

Microchannel plate (MCP) detectors have been used for several decades as an amplification element for image intensification devices [105]. The channel matrix is generally made from lead glass with a surface treated in such a way to optimise secondary electron emission and to provide semi-conductive properties for charge replenishment after discharge. Lead glass pores are created through multi-stage dragging and agglomeration of fibers with acid-soluble core. The entire block is cut at the desired chevron angle into single plates. The inner core is then chemically etched to produce multi-vein fibers. To obtain the desired semi-conducting properties the plates are baked in a hydrogen atmosphere to reduce the lead-oxide inner layer of each channel to a semi-conducting metal layer; the degree of reduction determines the final electrical and emissive properties [106]. Finally vacuum evaporation is used to coat electrical contacts onto the upper and lower surfaces of the plate; to maximise plate lifetime the plate must be polished and cleaned before the etching process and contacts are deposited.

The MCP itself can be used to measure radiation directly [105] albeit with low efficiency, or it can be coupled with a photocathode material and accelerating voltage to produce a photomultiplier tube [58]. The photocathode is manufactured to exhibit electron-conversion sensitivity to a specific region of the electromagnetic spectrum. There are numerous types of photocathode, for example the multi-alkali S20 [108] (sodium-potassium-antimony-caesium) cathode has good sensitivity in the blue region of the visible spectrum, the S25 [109] cathode manufactured using the same elements as the S20 cathode albeit with thicker layers of material has increased sensitivity in the red, and the solar blind [110] cathode (CsTe / CsI) has sensitivity in the UV range. Figure 4.1 shows the radiant efficiency in mA/W for a

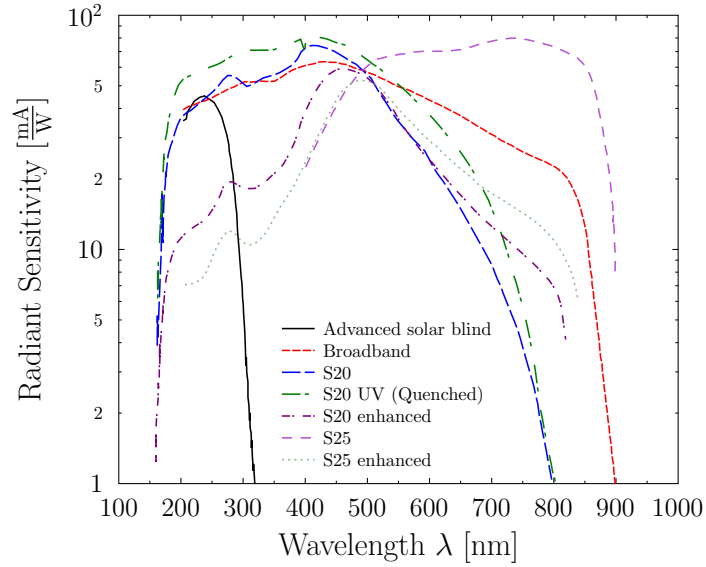


Figure 4.1: Plot showing the radiant sensitivity in mA/W for a range of photocathode materials [107].

range of different photocathode types. Cherenkov light is emitted with an intensity proportional to  $1/\lambda^2$ . Therefore the best choice of photocathode for the PMTs used in the Cherenkov detectors is the UV–quenched S20 cathode. One may consider increasing the signal by swapping to a solar blind cathode which extends deeper into the UV to sample the more intense region of the emission; the spectrum diminishes significantly below 200 nm due to the pressure window (sapphire / UV grade fused silica) between the gas cell and PMT.

### 4.2.2 Vacuum Photodiodes

A photodiode can be made by removing the MCP dynode stage from the PMT discussed previously. Removing the broadening introduced by the MCP will reduce the impulse response width of the system at the expense of amplification. This could be an option where the initial photon signal is large, such as the high pressure GRH cell at NIF. In this situation the photodiode would become an attenuator as the conversion process consists only of the photocathode quantum efficiency which is in

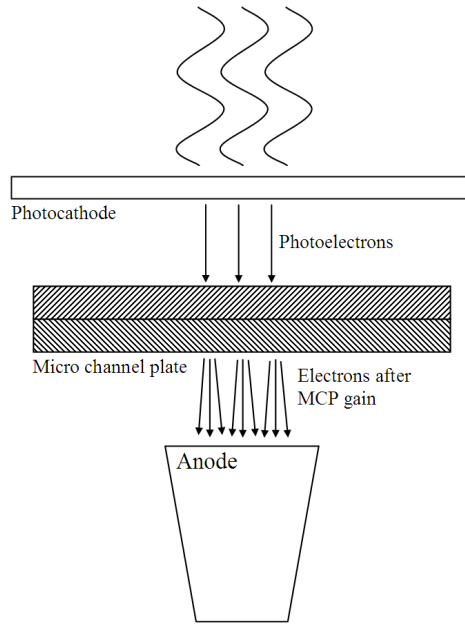


Figure 4.2: Diagram showing the layout and methodology of a MCP-based (two-stage in this diagram) photomultiplier tube (not to scale).

the region of 20 %. The impulse response of this configuration has not accurately been measured by Photek, as their light source can only supply a 45 ps pulse. Best estimates using quadrature subtraction suggest the FWHM is in the region of 50-60 ps. An issue with a photodiode of this kind is that the signal cannot be adjusted using a bias voltage, requiring an amplifier to be placed between diode and scope to tune the expected signal depending on estimated neutron yields. Nonetheless as yields increase at NIF, photodiodes may be an option.

An issue yet to be addressed for fast micro-channel plate PMTs and photodiodes is the difficulty of impedance matching the charge pulse generated by a photocathode and/or MCP with a high-bandwidth coaxial cable. Late-time oscillatory ringing from impedance mismatching is observed in the current generation of PMT and PDs, as shown in Figure 4.3 and will likely remain an issue as signals become faster.

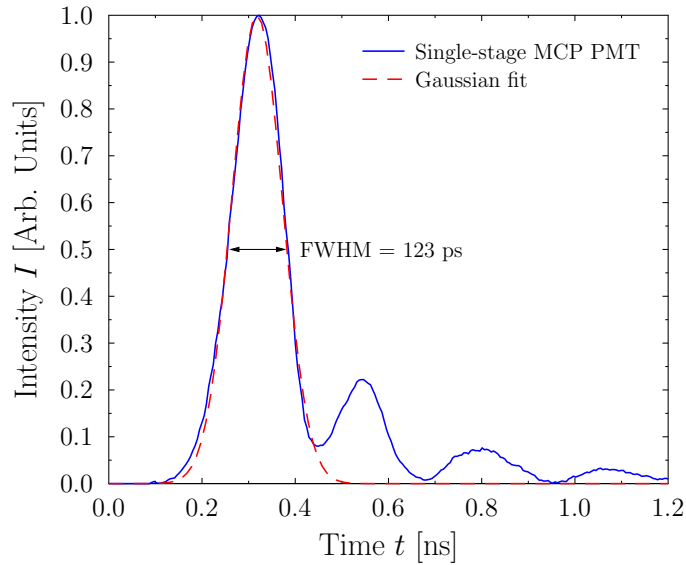


Figure 4.3: Unit response function (URF) of a single-stage MCP-based PMT with a FWHM of 123 ps. The URF in this case includes the 50' cableset used at the Omega laser facility. The coaxial line adds a small amount of broadening to the signal; this particular plot has been shown to highlight the general bandwidth of the system in this configuration. The actual minimum FWHM of the PMT by itself has been measured at approximately 88 ps.

### 4.2.3 Semi-conductor photodiodes

The conventional photodiode is made from a semi-conductor material, such as silicon with a band-gap of 1.1 eV [111]. Due to the small band gap, light incident on the wafer produces electron-hole pairs which are collected using a 50-100 V bias voltage. The ideal charge pulse produced by the diode is at best a 1:1 correspondence between incident photons and charge carriers; consequently the signal must be multiplied electronically using a preamp device. The fastest semi-conductor photodiodes combined with a preamp have bandwidths of a few hundred MHz, too slow for use in the Cherenkov detectors. In addition, signal-to-noise-ratio is poor as a result of the initial weak charge signal. Noise can be reduced through miniaturisation with a sacrifice in overall light collection efficiency. Silicon photodiodes may be best suited to imaging applications where many small wafer pixels with low

dark current can be assembled onto a chip; production of such devices leverages the existing computing industry infrastructure heavily. This may be of interest in the future at NIF when yields increase for time-integrated gamma images of the implosion.

The charge pulse from a conventional semi-conductor photodiode can be increased by applying a large voltage across the wafer and including a drift region. As the charge carriers accelerate in the large field ionisation interactions occur leading to the emission of further electron, in a process known as an avalanche. This modification is sufficient to increase the charge signal above the electronic noise; however the charge linearity has a strong dependence on temperature and bias voltage, both of which are difficult to maintain with large numbers of interactions occurring in such a small volume.

Further multiplication can be achieved in the semi-conductor photodiode by placing a photocathode prior to the wafer material and applying a large bias of approximately 10 kV between the two components. The resulting 10 keV electron subsequently produces a large amount of electron-hole pairs within the semi-conductor wafer. This configuration can generate gains of a few 1000. The benefit of such a system is that proportionality between the photon source signal and the resulting charge pulse is far improved relative to conventional PMTs. In addition the rise and fall times are less than 1 ns, and the absolute timing resolution 100 ps or better. These properties may still not be suitable for use in the Cherenkov detectors; they are however a significant improvement over the semi-conductor photodiode by itself.

### **4.3 An alternative high-speed technology**

To make the next leap in photomultiplier bandwidth is going to require new materials and a different approach. Modifying the existing configuration and materials through miniaturisation and novel MCP-coating techniques, such as Atomic Layer Deposition (ALD), respectively may lead to small improvements. These however will not provide the order of magnitude improvement in bandwidth required to

measure structure within an ICF reaction history. This section will introduce CVD diamond as a potential candidate for the future of PMTs in an ICF environment.

### **4.3.1 Design considerations**

#### **High-gain, low stage number discrete dynode device**

To make bandwidth improvements inside a photomultiplier one needs to minimise the number of different electron path lengths which can be taken through the device. The original box and grid PMTs consisted of a large number of dynode gain stages each generally with a gain of about 5. To achieve a  $\times 10^6$  requires approximately 9 dynode stages [111], the effect of which is to broaden the original photon signal by 10s of ns. Micro-channel plates were then developed which maintained the gain levels whilst minimising path lengths by making the entire length of a lead glass channel into a continuous dynode stage. Unfortunately the secondary electron yield of lead glass is between 1 and 3 therefore the plate needs to be thick (approximately  $160 \mu\text{m}$ ) to produce a gain of a few thousand. If a material could be found with a relatively large secondary electron yield compared to conventional materials, the number of hits required to produce a large gain could be reduced. This would be either by reducing dynode stages or by reducing the channel depth in a channel-plate-like device. Both approaches are investigated in the following chapter.

#### **Suitable dynode materials - CVD diamond**

Interest in diamond for charge amplification devices is primarily due to a large secondary electron yield (SEY) of approximately 80 [112] which can be obtained from hydrogen terminated and appropriately boron doped samples. Studies suggest low energy secondary electrons are able to migrate large distances due to a large 5.47 eV bandgap [113] between valance and conduction states; this reduces the inelastic scattering cross section for electrons in the conduction band and increases mean free path. At the surface a negative material-vacuum electron affinity allows conduction band electrons to leak out of the material without having to overcome

the large potential present in most materials. Diamond also has high thermal conductivity  $2 \times 10^3 \text{ Wm}^{-1}\text{K}^{-1}$ , important for components working in vacuum where heat dissipation can be a problem, and shows good radiation hardness essential for large scale fusion facilities, such as omega and NIF.

### 4.3.2 Operational modes

CVD diamond materials have currently not been incorporated into a traditional PMT design. Consequently it would be prudent to investigate which configuration yields the best timing and gain response. The solution may depend as much on ease of fabrication and cost as predicted temporal response, depending on the specific goals of the device. The specific quantitative aspects will be looked at in more detail later; the next few paragraphs however will introduce the terms involved.

#### Reflection

A reflection configuration consists of the secondary electron emission being optimised to emit from the surface into which the primary electron was injected. This is the traditional geometry used for multi-dynode PMTs. A benefit of this arrangement is the stage can be thick, which reduces costs for fabrication and removes the requirement for the dynode to be free-standing. This is in contrast with the transmission configuration which will be discussed in the next paragraph. An issue with a reflective configuration is that the first stage must be facing the photocathode whilst at the same time having a clear path to the second stage, which may include a curved trajectory as shown in Figure 4.4 due to the stages being progressively positively biased by a few hundred volts to draw the secondary emission from the initial dynode surface to subsequent stages. This complicates the design and leads to slow temporal responses due to the large number of possible path lengths through the system combined with the consecutive acceleration of low-energy secondary electrons between stages. A further issue is the possibility of electrons missing a dynode stage due to a wide starting trajectory further broadening the rising edge of the

detector response. If a novel design could be developed based on the linear-focused arrangement with a high-gain dynode material, the number of required stages could be reduced to 2 or 3, significantly reducing the overall transit time and multiple path length broadening.

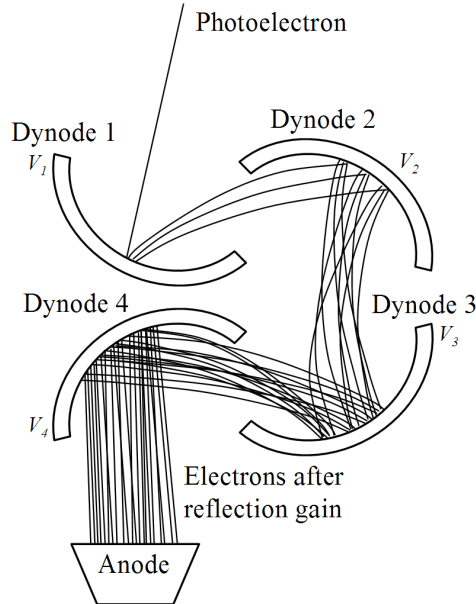


Figure 4.4: Schematic diagram of a reflection dynode configuration. Each successive dynode stage is biased progressively more positive than previous stages, drawing any secondary electrons through the system. The accelerating voltage is high enough for the secondary electrons to cause further amplification at the next stage.

The micro-channel plate is also an example of a dynode in reflection configuration. In this case the electrons interact with the inner surface of an angled channel running through a sheet of lead glass. One side of the glass is biased positively relative to the front surface, therefore electrons produced by the first hit early in the MCP liberate electrons which are drawn down the channel producing further secondary electrons in subsequent interactions. This specific reflection configuration has proved to be fast relative to traditional dynode geometries due to miniaturisation; however the secondary electron yield from lead glass is quite low at 1-3 (depending on interaction energy) requiring the plate to be thick (ap-

proximately 160  $\mu\text{s}$ ), and in some cases for several plates to be packed together, to generate a useful level of gain. At present fabrication techniques have not been developed to manufacture higher secondary electron yield materials with improved secondary electron transport properties, average ionisation energies and negative electron affinity (NEA) surfaces, into a microchannel plate configuration. This would allow similar gain characteristics at significantly reduced plate thickness, reducing path length broadening and overall impulse response.

### **Transmission**

In a transmission configuration the primary photoelectron is sufficiently accelerated to almost pass through the dynode, causing ionisation near the back surface as described in Figure 4.5. The bias voltage between photocathode and stage is tuned such that the generated secondary population inside the stage can efficiently migrate to the surface, whilst precluding the possibility of the primary electron penetrating all the way through which would broaden, or possibly impose an early time bump on, the rising edge of the response. A PMT with transmission geometry could be extremely fast ( $<10$  ps [114]) due to the axial nature of the design. Building a PMT with this approach is difficult as the dynode must be manufactured extremely thin at 200 nm or less (as demonstrated later in Figure 5.5 of Section 5.2.1). The stage can be made thicker, however the required accelerating voltage must increase proportionately. In addition a thicker stage will broaden the response due to variations in the scattering trajectory of the primary electron. If a dynode could be made thin enough for less than 5 kV accelerating voltage per stage then a fast multi-dynode PMT with a gain dependent on material and number of stages could be designed.

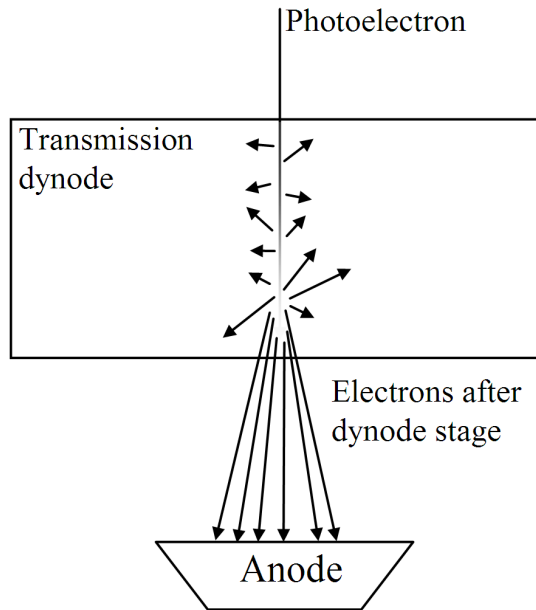


Figure 4.5: Schematic diagram of a transmission dynode configuration. The primary photoelectron is given sufficient energy to penetrate deep into the dynode material producing a large secondary population near the back surface. At the correct thickness and surface conditions the low energy secondaries can leak out of the surface where they can be accelerated towards the anode or into an additional dynode stage.

### Venetian blind

The Venetian blind (VB) configuration is another specific example of a reflection configuration; it can also be thought of as a 2-dimensional version of a micro-channel plate. Instead of an entire cylindrical channel being at an angle, the Venetian blind dynode has a single slanted surface. Additional stages are placed below the first at the opposing angle to keep the overall average trajectory of the secondary electron population along the axis of the photomultiplier tube, as shown in Figure 4.6. Traditional VB tubes were developed for use where the incident photon signal area is large and timing is less of a concern. In the past VB dynode stages have generally been thick due to fabrication limitations. Combined with the large collection area this produces relatively slow PMTs, when compared with linear-focused stages

[115] or MCP-based PMTs. Fabrication techniques have progressed however and techniques developed for the miniaturisation of silicon-based electrical components may allow development of a VB structure onto which a high-gain material, such as CVD diamond, could be grown. Silicon has been used extensively as a substrate for CVD diamond growth for its well-matched thermal expansion properties, high melting point (1683 K) and formation of an intermediate carbide layer which reduces strain across the diamond during thermal expansion of the substrate. Tungsten and molybdenum are alternative options for similar reasons [116].

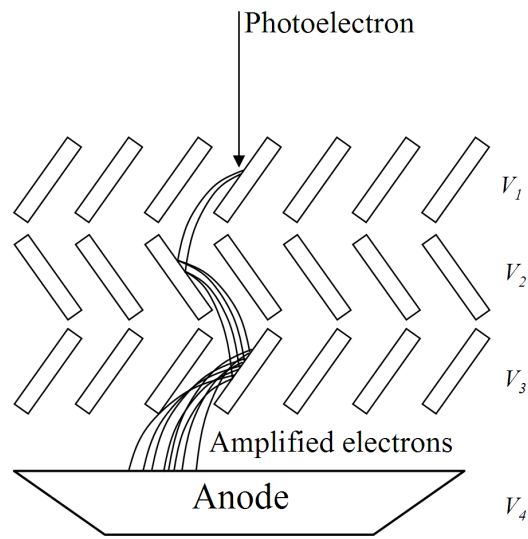


Figure 4.6: Schematic diagram of a Venetian blind dynode configuration. Each layer is angled opposite to the previous to allow a route through the amplification stage. The layers must be packed close enough to remove the direct line of sight. This geometry can be thought of as a 2-dimensional micro-channel plate.

### 4.3.3 Experimental characterisation

To ascertain the performance characteristics of the three potential PMT designs requires a dedicated experimental vacuum testing facility. The experimental setup used at the University of Leicester, Leicester, Leicestershire, UK, consists of an electron gun capable of producing a 0.25–5 keV beam, a combined roughing and

turbo-pump vacuum system, a flat target mount connected via BNC cables to a picoamp meter, and a large Faraday cup surrounding the target mount with a small hole to allow the electron beam through connected to a second picoammeter meter via BNC cables.

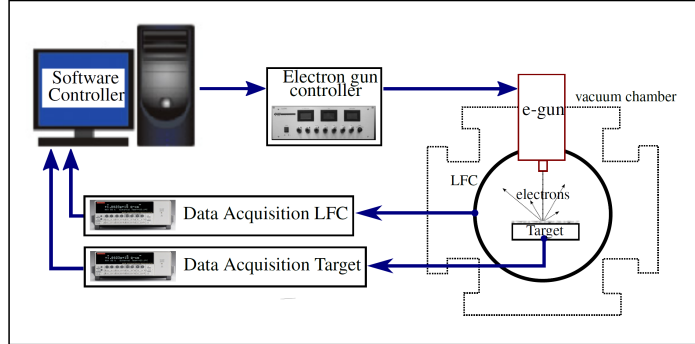


Figure 4.7: Schematic overview of the SEE characterisation equipment at Leicester University, used to measure the secondary electron emission properties of different dynode materials. Image courtesy of V. Taillandier (Leicester University). Photo courtesy of V. Taillandier of Leicester University [117].

Figures 4.7 and 4.8 contain a schematic overview of the system and communication, and several photos of the various components respectively. The secondary electron yield can be calculated by combining the target mount current and the large Faraday cup,

$$\delta = \frac{I_{LFC}}{I_{LFC} + I_{TM}}, \quad (4.1)$$

where  $\delta$  is the secondary electron yield,  $I_{LFC}$  is the large Faraday cup (LFC) current and  $I_{TM}$  us the target mount current [117]. The bakeable stainless steel chamber can maintain a vacuum level of  $2.5 \times 10^{-7}$  torr during measurements. The system is also designed to allow biasing of either the target mount or the large Faraday cup through an external DC supply; this allows electrons to be either repelled or attracted. Due to the ends of the LFC cylinder and the electron beam

hole some secondary electrons may be lost from the measurement. Applying a small positive bias of 10 - 20 V to the LFC is sufficient to collect all secondary electrons which would otherwise have been lost.

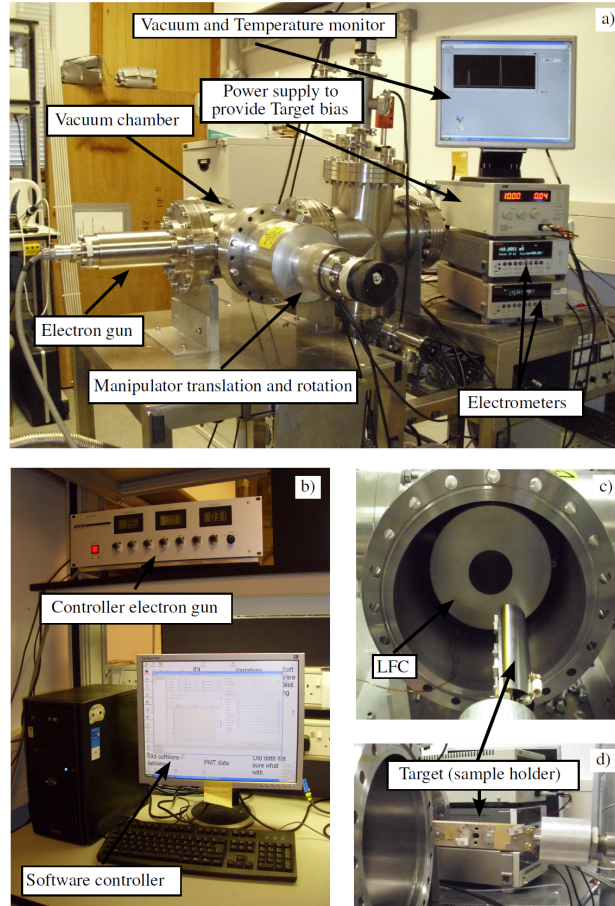


Figure 4.8: Photo of the equipment at Leicester University showing all the various components associated with the secondary electron emission measurement. Sub-image a) shows the exterior of the vacuum system, electrometers and vacuum monitoring sensors, b) shows the bespoke C++ software written by V. Taillandier (Leicester University) and PC, together with the electron gun controller unit. Sub-image c) shows the inside of the open vacuum chamber, Large Faraday Cup (LFC), target mounting holder and the associated manipulation arm and cabling.

## Measurement issues

Comparisons with simulation and existing published data have proved difficult. Fluctuations in SEE related to dose and dose rate have been observed during measurements at Leicester. Charge trapping and depletion, and surface modification are possible causes for these ageing effects, however further studies are required. Care must be taken to ensure that beam position and current density are selected such that subsequent readings are not affected. Consequently it is important to complement the experimental measurements with analytical models and Monte Carlo modelling to increase confidence and understanding. The next chapter focuses on the simulations and modelling developed alongside the measurements made at Leicester University.

## 4.4 Summary

This chapter has described the requirements for improved Cherenkov detector measurements and discussed the available technologies which could satisfy the specification. One technology showing potential is Chemical Vapour Deposition (CVD) diamond which could replace the micro-channel plate (MCP) component of existing Photomultiplier tubes (PMT)s.

Moderately-doped CVD diamond with a hydrogen-terminated surface has several characteristics which make it desirable as a dynode material. High surface secondary electron emission (SEE) is observed due to favourable internal secondary migration and a negative electron affinity (NEA) surface. Diamond shows good radiation hardness; a requirement for facilities such as NIF and Omega. High thermal conductivity makes diamond compatible with high-voltage vacuum environments. In addition CVD diamond has good strength making free-standing thin films 100–200 nm thick a possibility.

The preferred method of utilising CVD diamond in a PMT would be to replace the MCP dynode with several thin diamond membrane stages in a transmission type configuration, with an accelerating voltage of a few thousand kVs between

each. The axial design could increase bandwidth by limiting multiple path-length broadening whilst maintaining charge amplification. There are many free parameters in this system including: diamond thickness, accelerating voltage, boron doping levels, surface termination, crystallinity and growth substrate, to name a few. To narrow the large design phase space and aid understanding simulations and experimental measurements are required. The next chapter will initially discuss historic attempts to model secondary electron emission and then introduce a low-energy extension to the GEANT4 toolkit utilising recent theoretical approximations for electron transport in diamond.

# Chapter 5

## Diamond detector modelling using GEANT4

### 5.1 Existing SEE models

#### 5.1.1 Dionne approximation

Studies in the past have attempted to model secondary electron emission (SEE) in diamond using three stages: interaction of the primary electron to produce secondaries, transport of secondaries to the surface and escape from the surface. Dionne [118] [119], and later Shih [120], postulate that production of secondary electrons in the bulk material is related to the energy loss of the primary through the relation

$$n(x, E_0) = \frac{-1}{L} \frac{dE}{dx}, \quad (5.1)$$

where  $n(x, E_0)$  is the number of secondary electrons produced,  $E_0$  is the energy of the primary,  $dE/dx$  is the energy loss function and  $L$  is the average energy required to produce a secondary. Consequently the total number of internal secondary electrons is  $E_0/L$ . The energy loss function is approximated using either a power law or constant relationship; the latter was introduced in a later publication

to account for primary straggling

$$\frac{dE}{dx} = \frac{A}{E^{n-1}} \text{ or} \quad (5.2)$$

$$\frac{dE}{dx} = \frac{E_0}{d} \quad (5.3)$$

where  $A$ ,  $d$  and  $n$  are material dependent constants. Migration and escape of the secondary is modelled using a simple exponential approximation

$$f(x) = Be^{-\alpha x} \quad (5.4)$$

where  $\alpha$  is an absorption constant equivalent to an inverse diffusion length and  $B$  is the probability of escape at the surface, dependent on the termination type.  $F(x)$  assumes that the probability of a secondary electron escaping from the surface decays exponentially as a function of depth and that the interaction at the surface is independent of how far the secondary population has travelled. Note that in this model only the surface initially encountered by the primary is considered for secondary emission, this is known as a reflection configuration (RC). The observable used to constrain such models is the secondary electron yield  $Y_{1D}$  which can be obtained by

$$Y_{1D} = \int_0^d n(x, E_0) f(x) dx. \quad (5.5)$$

Substituting for the power loss function defined in equation 5.3 leads to

$$Y_{1D} = \frac{B}{L} \int_0^d e^{-\alpha x} \frac{A}{E(x)^{n-1}} dx. \quad (5.6)$$

Finding the solution to the power law differential equation  $E(x)^n = -nAx - Cn$

and then assuming the maximum penetration depth  $d$  occurs where  $E(d) = 0 = -nAd - Cn$  leads to  $E(x)^n = nAd - nAx$ . Finally substituting the initial primary electron energy  $E_0$  at  $x = 0$  leads to  $d = E_0^n/nA$ . Consequently  $E(x)^n = E_0^n - nAx$  and subsequently raising both sides to the power  $n/(n - 1)$  produces

$$E(x)^{n-1} = [An(d - x)]^{(n-1)/n}. \quad (5.7)$$

Combining equations 5.6 and 5.7 produces

$$Y_{1D} = \frac{B}{L} (An)^{1/n} \int_0^d \frac{e^{-\alpha x}}{n(d - x)^{(n-1)/n}} dx. \quad (5.8)$$

Equation 5.8 is the secondary electron yield assuming a power law for the stopping function and a one-dimensional decaying exponential with depth to represent the secondary electron migration to the surface. Dionne attempts to make 5.8 more physical by replacing the decaying exponential term  $Be^{-\alpha x}$  with a function that accounts for the 3D nature of the secondary diffusion. The assumption is that all secondaries disperse radially from creation into a solid angle fraction of  $4\pi$  where

$$\frac{d\Omega}{4\pi} = \frac{r^2 \sin \theta d\theta d\phi}{4\pi r^2}. \quad (5.9)$$

By integrating equation 5.9 over  $\theta = 0$  to  $\pi/2$  (corresponding to the population emitted backwards towards the surface) and  $\phi = 0$  to  $2\pi$ , and incorporating the linear exponential loss produces the modified secondary migration function

$$F(x) = \frac{1}{2} B \int_0^{\pi/2} \varepsilon^{-\alpha r} \sin \theta d\theta \quad (5.10)$$

where  $r = |x/\cos \theta|$  is the non-normal penetration depth of the primary at

an angle  $\theta$  and therefore  $x$  is the linear creation depth. Using the substitution  $\sin \theta \, d\theta = -d(\cos \theta)$  produces

$$F(x) = -\frac{1}{2}B \int_1^0 \varepsilon^{-\alpha|x/\cos\theta|} d(\cos \theta). \quad (5.11)$$

Note that  $d(\cos \theta)$  is an infinitesimal change in  $\cos \theta$  as opposed to the product of  $d$  and  $\cos \theta$ . A second substitution of  $\cos \theta = 1/z$  leads to

$$F(x) = \frac{1}{2}B \int_1^\infty \frac{\varepsilon^{-\alpha x|z|}}{z^2} dz. \quad (5.12)$$

Replacing the one dimensional secondary migration function  $B\varepsilon^{-\alpha x}$  in equation 5.8 with the 3D equivalent in equation 5.12 produces the 3D-corrected secondary electron yield

$$Y_{3D} = \frac{B}{L} (An)^{1/n} \int_0^d \int_1^\infty \frac{e^{-\alpha x|z|} dz dx}{2nz^2 (d-x)^{\frac{(n-1)}{n}}} \quad (5.13)$$

where  $d$  is the maximum penetration depth of the primary. Dionne presents the results of his equation in reduced form where only the ratio of the function to experimental data is presented, shown in Figure 5.1. To convert between absolute and reduced variables Dionne uses  $Y'_{3D} = Y_{3D}/K$ , where  $Y'_{3D}$  is the reduced secondary electron yield and  $K = \frac{B}{L} \left(\frac{An}{\alpha}\right)^{1/n}$ . This reduction removes the material-dependent parameters with the exception of  $n$ , allowing a single parameter to be investigated. Several values of  $n$  were used with 1.35 and 1.66 being closest to experimental data in the lower and higher energy regions of the experimental data respectively. Even in reduced form the plots fail to capture the underlying physics of the secondary electron emission process. Dionne also undertakes the same analysis for the constant loss stopping formalism; constant loss is suggested to compensate for large angle scattering of the primary as it navigates the material. Unfortunately the

resulting reduced secondary electron yield curves appear similar in magnitude and shape to the power law approach. The constant loss stopping function therefore also inadequately captures the underlying physics of secondary electron emission.

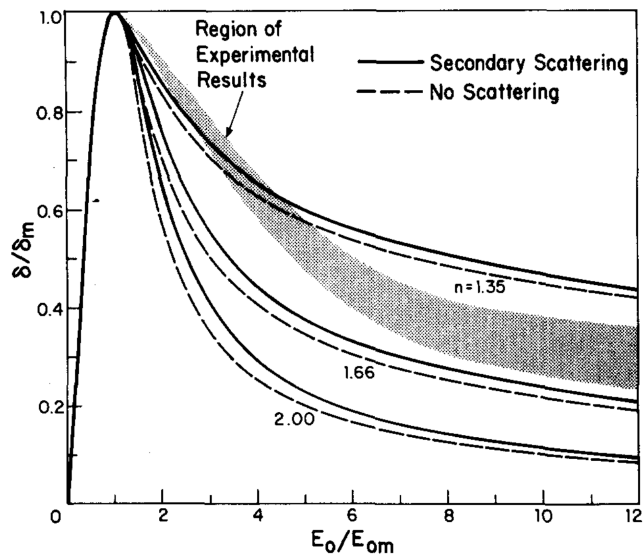


Figure 5.1: Dionne reduced yield curves plotted as a function of multiples of the maximum primary energy [118]. Solid/dotted lines are Dionne models and the filled region contains data from experiments.

### 5.1.2 Shih update to Dionne

Shih et al. later introduced a modification to the Dionne model to account for oblique primary trajectories [120]. The modification introduces an effective depth correction of  $\cos(\theta)$  to the integrals used by Dionne, where  $\theta$  is the angle between the surface normal and primary trajectory. If the primary electron beam is incident at an angle of  $0^\circ$  to the surface, the maximum penetration depth is reduced by a factor  $\cos(\theta)$  relative to that at normal incidence. Consequently, the yields are larger at more oblique angles. SEE increases with angle due to the shorter escape depth of secondary electrons required for emission. The effective depth correction for a molybdenum sample is shown in Figure 5.2. CVD diamond would show similar form but at higher intensities.

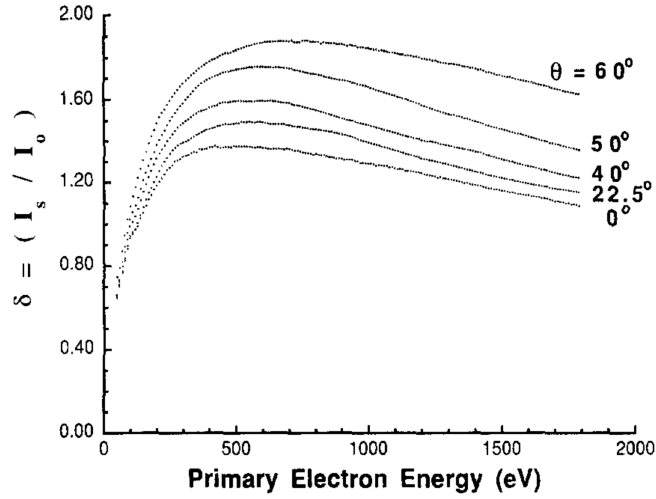


Figure 5.2: SEE emission as a function of primary electron energy for a molybdenum sample. Higher yields are observed at larger angles relative to the normal.

### 5.1.3 Dvorkin Model

A separate attempt to model secondary electron emission in diamond was made by Dvorkin using a stopping points functional form together with the assumption that the secondary electron-hole pair production distribution can be approximated using this function corrected by  $1/3E_g$ ; supported by Dvorkin's statement that the average energy required to produce an electron-hole pair is  $3E_g$  [121] [112] [122]. The electron-hole pair splitting energy of  $3E_g$  is extrapolated from  $\gamma$ , alpha and electron radiation-ionisation measurements by C. Klein in 1968 on various materials as a function of bandgap energy. The stopping points function is

$$n(z) = \frac{mz^{m-1}}{z_0^m} e^{-\left(\frac{z}{z_0}\right)^m}, \quad (5.14)$$

where  $z$  is the primary electron depth,  $m = 1.9$  is an empirically derived quantity and  $z_0$  is a unit of length ( $\mu\text{m}$ ) for the system related to the primary energy and diamond density. The migration of the secondary to the surface is treated using

the carrier diffusion length

$$l = \sqrt{D\tau}, \quad (5.15)$$

where  $D$  is the diffusion coefficient and  $\tau$  is the electron-hole pair recombination time approximately 1 ns. Using the Einstein relation [123] and a temperature of 300 K one obtains the diffusion length

$$l \approx \sqrt{\frac{\mu\tau}{40 [V^{-1}]}} \quad (5.16)$$

where  $\mu$  is the carrier mobility between 0.1-10  $\text{cm}^2\text{s}^{-1}\text{V}^{-1}$  for diamond membranes  $< 5 \mu\text{m}$  thick. This produces a diffusion length lying in the range 16 nm to 160 nm. In an RC the total electron yield using the Dvorkin model is

$$\kappa = \frac{BE_0}{3E_g} \left[ 1 - e^{\left[ -\left(\frac{L}{z_0}\right)^{1.9} \right]} \right] \quad (5.17)$$

where  $\kappa$  is the secondary electron yield and  $B$  is the probability of escape dependent on termination used to approximate emission at the surface. Dvorkin's RC yield calculation and stopping points function are shown in Figures 5.3(a) and 5.3(b). Agreement with experiment is good in Figure 5.3(b) however, the reference information associated with the stopping function could not be found therefore this method of calculating secondary emission locations was not considered for use in this work. There are however useful transport characteristics and values, such as the average ionisation required to produce an electron-hole pair, diffusion length range and various surface emission constants, which could be used in an alternative model.

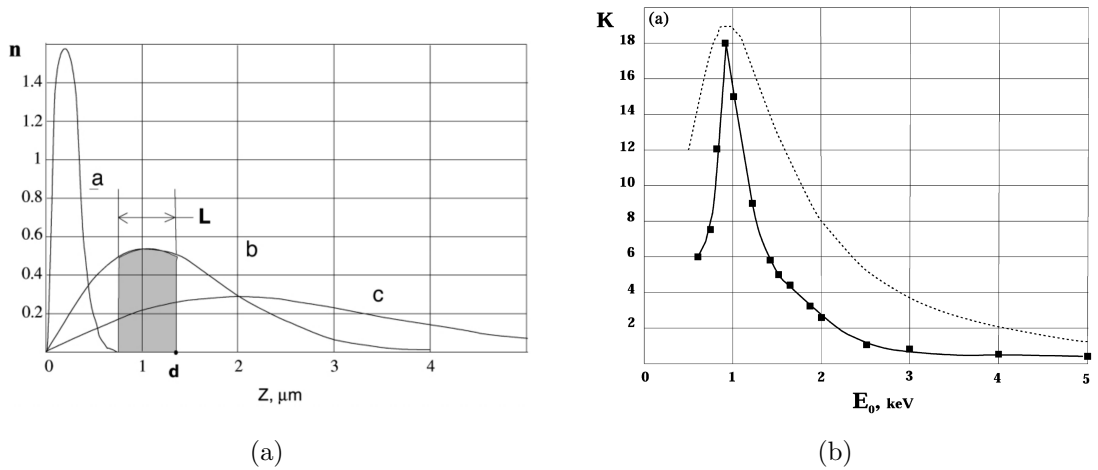


Figure 5.3: Dvorkin's stopping points model(a) for energies of 10 keV (a), 20 keV (b) and 30 keV (c) and yield calculation for a reflection configuration(b).

## 5.2 Electron transport considerations

The Monte-Carlo transport of electrons through homogeneous matter at intermediate and high energies (above 1 keV) is well understood [124]. The GEANT4 toolkit utilises models for ionisation [125] and bremsstrahlung, or dedicated stopping power tables from the International Commission on Radiation Units. Below 100 eV however, atomic shell effects and bandstructure significantly increases uncertainty in Monte Carlo codes, such as those discussed in Section 2, and therefore the models kill, or locally deposit the remaining kinetic energy of, the primary at approximately 100 eV. One consideration is whether to implement continuous energy loss using a stopping power  $dE/dX$  approach or to calculate separate cross sections for each pertinent physical process.

The first approach undertaken in this thesis involves stepping a particle through a material linearly and reducing the particle's energy by  $\delta x \times dE/dx$  for each step in the material, where  $\delta x$  is the step size. For diamond the average ionisation energy is  $3E_{gap} = 16.41$  eV [121]; the simulation would have to emit a secondary electron each time the cumulative energy loss reaches  $3E_{gap}$ . A model based on this approach is discussed in the next section.

### 5.2.1 Secondary electron emission in diamond simulation (SEEDS)

Using information from Dionne, Shih and Dvorkin, a code was written to estimate the number of electrons emitted from the surface of hydrogen terminated single crystal diamond. This approach calculates the stopping function analytically using a complex dielectric [126] function. Differential inverse mean free path [127] can be calculated using

$$\tau(E, \omega) = \frac{1}{\pi E a_0} \int_{q_-}^{q_+} \frac{dq}{q} \text{Im} \left[ \frac{-1}{\varepsilon(q, \omega)} \right], \quad (5.18)$$

where  $\tau$  is the differential inverse mean free path,  $E$  is the primary electron energy,  $a_0$  is the fine structure constant,  $q$  is electron momentum change,  $\hbar\omega$  is energy transferred by the primary particle to the background medium with  $\hbar$  being the reduced Planck constant and  $\text{Im}[-1/\varepsilon(q, \omega)]$  is the stopping function. The limits  $q_+$  and  $q_-$  are given by

$$q_{\pm} = k \left[ 1 \pm \sqrt{1 - (\hbar\omega/E)} \right], \quad (5.19)$$

where  $k$  is the wavevector associated with the incident electron.  $\text{Im} \left[ -\frac{1}{\varepsilon(q, \omega)} \right]$  is difficult to calculate from first principles; one method is to model the electronic properties of the material as a homogeneous free electron gas in the random phase approximation [128]. The complex longitudinal dielectric function is derived for a collisionless free electron plasma in the random phase approximation and at zero temperature. The result which is equivalent to the Lindhard dielectric function is

$$\varepsilon(k, \omega) = 1 + \frac{3\omega_p^2}{2k^2 v_F^2} [1 - g(\omega_+, k) + g(\omega_-, k)] \quad (5.20)$$

where  $v_F$  is the Fermi velocity,  $\omega_{\pm} = \omega \pm \frac{\hbar k^2}{2m_e}$ ,  $\omega_p$  is the plasma (free electron gas) frequency and

$$\operatorname{Re}\{g(k, \omega)\} = \frac{m_e(\omega^2 + k^2)v_F}{2\hbar k^3} \ln \left| \frac{\omega + kv_F}{\omega - kv_F} \right| \quad (5.21)$$

$$\operatorname{Im}\{g(k, \omega)\} = \begin{cases} 0 & \text{if } (\omega + kv_F) / (\omega - kv_F) > 0 \\ -\pi \frac{m_e(\omega^2 + k^2)v_F}{2\hbar k^3} & \text{if } (\omega + kv_F) / (\omega - kv_F) \leq 0 \end{cases} \quad (5.22)$$

Appendix B describes the Lindhard dielectric approach in further detail. To obtain the mean free path (MFP)  $\tau(E, \omega)$  must be integrated over all possible energy transfers

$$\lambda^{-1}(E) = \hbar \int_0^{E_0/\hbar} d\omega \tau(E, \omega). \quad (5.23)$$

Furthermore the linear energy loss per unit path length [127] or stopping power can be obtained by

$$S(E) = \hbar \int_0^{E_0/\hbar} d\omega \omega \tau(E, \omega). \quad (5.24)$$

The stopping function for diamond calculated using this approach is shown in Figure 5.4. An IDL code was written to propagate an electron through a diamond membrane in 0.01 nm step sizes, with the energy loss for each step computed from the four-part polynomial approximation to  $S(E)$ . The approximation was chosen to remove the computationally expensive integrals involved with calculating the stopping function during each iteration of the simulation. A 4-component fit was chosen to obtain close agreement where the function varies most. An alternative to the 4-component fit could have been to compute a high-resolution tabulated stopping function over the pertinent energy range in an algorithm separate to the

SEEDS code. This table could have then been read in at runtime and interpolated where required. The step size of 0.01 nm was decided after preliminary calculations of the stopping characteristics shown in Figure 5.5. A larger stepping value would poorly resolve the energy loss peak at maximum primary penetration depth and a smaller value would increase computation time with little added resolution. The simulation produces a secondary electron at the current penetration depth each time the cumulative energy loss reaches the experimentally-derived average ionisation energy of  $3E_g$  for diamond; the cumulative energy loss is subsequently reset to 0. The emission direction is sampled randomly from an isotropic distribution. Secondary emission length was linearly sampled from Dvorkins 16 nm - 160 nm range. Emission direction, length and depth determine whether the secondary can reach the surface. As the primary penetrates deeper into the diamond the solid angle subtended by the surface is determined by  $2\pi(1 - z/l)$  where  $z$  is the depth and  $l$  is the escape length. If the average emission length  $\bar{l} = (16 + 160)/2.0 = 88$  nm is assumed then the surface solid angle depends linearly (negatively) on the depth  $z$ . At  $z = \bar{l}$  the probability of the secondary reaching the surfaces drops to almost zero. Escape lengths  $l$  sampled higher than  $\bar{l}$  will still have a small chance of escaping. Dionnes probabilistic approximation,  $B = 0.4$  for hydrogen terminated diamond, was used to deduce whether the electron escapes the surface. The energy loss and secondary production profiles for SEEDS are shown in Figure 5.5. As expected SEEDS predicts the secondary electron production rate to increase with decreasing primary electron energy. Most secondaries are produced near the end of the primary trajectory. This suggests that the most efficient SEE primary energy would be a compromise between supplying sufficient energy to ionise a large population of secondaries whilst keeping the penetration depth small enough to allow a large fraction of that population to migrate to the surface. A transmission dynode with thickness tuned to the primary electron penetration depth would represent the most efficient method of achieving amplification with minimal temporal broadening. Figure 5.6 shows the SEE total surface emission as a function of primary energy for reflection and transmission configurations.

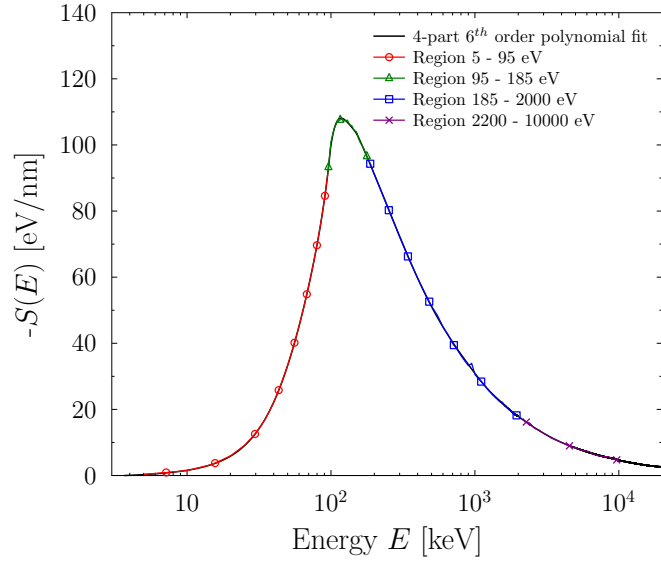


Figure 5.4: Stopping function computed using the Lindhard dielectric function, from RPA theory. A four component polynomial fit was produced to parameterise the shape for use in the SEEDS code.

As the primary energy  $E_p$  increases the penetration depth becomes too deep for efficient secondary migration to the surface, however, a small SEE is still observed from electrons produced earlier in the primary track. In RC, peak SEE production occurs at approximately 2 keV which is high compared with Shih and Dionne as shown in Figure 5.2 but low compared with some published data [129]. Nonetheless total SEE for RC compares well with data from Photek and with published data. No experimental data could be found for the transmission configuration. Despite varying levels of agreement with published data for bulk characteristics, SEEDS does not include the required physical processes to model SEE in fine detail. The Lindhard dielectric model for a free electron gas at  $T = 0$  is a good assumption for metals, such as aluminium, but may not work well for a semi-conducting material like diamond due to the subtle complexities of the band structure and indirect valance excitation. In addition primary electron transport is treated in one dimension separate to the secondary electron population. The associated momentum

transfer during inelastic scattering of the primary is neglected which in reality would scatter the primary away from the original trajectory, reducing the average distance of the primary relative to the surface and allowing a larger fraction of secondary electrons to escape. In addition elastic scattering is ignored which would provide additional scattering away from the one dimensional trajectory.

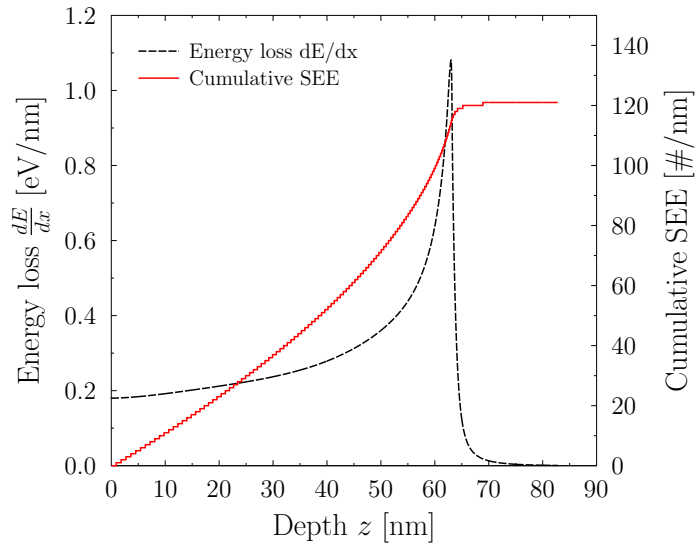


Figure 5.5: Energy loss relation and cumulative secondary electron emission predicted by the SEEDS model plotted as a function of depth, shown in broken black and red respectively. The SEEDS step resolution was 0.01 nm.

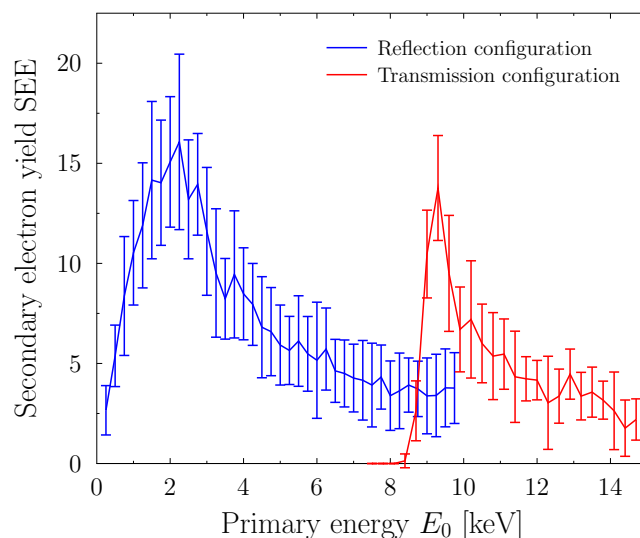


Figure 5.6: SEE for the reflection and transmission configurations, in blue and red respectively. The transmission simulation was performed for a 1  $\mu\text{m}$  thick diamond membrane.

Another important process absent from the SEEDS model is a suitable surface treatment beyond the constant coefficient of 0.4. This approach fails to address modification to the band structure of the crystal close to termination sites. One potential method could be to model the interface as a potential barrier, with potentials supplied from density function theory (DFT). Interactions with academic institutions capable of simulating these potentials, such as Cambridge University, are ongoing. In addition such institutions may be capable of calculating dielectric functions and band structure for diamond with different crystal structure (poly / single crystalline) and varying levels of boron doping. Finally, migration of the secondary is modelled crudely within SEEDS; in reality secondary electrons should be subject to the same physical interactions as the primary electron.

## 5.3 GEANT4 adaptations for secondary emission process

By default the GEANT4 toolkit gives the user the option to attach a wide range of physics packages to individual particles. Multiple packages may exist for the same process at different resolutions and extending over different energy regimes. In addition the C++ source files for each package are available to the user. This scenario allows the capability to modify existing processes or create entirely new processes from scratch, using an existing process as a template. Whilst extremely powerful and useful this situation can also lead to the wrong physics being applied to a particle, or errors/inaccuracies being introduced due to a poorly written physics process. Consequently any modifications need to be well-validated and tested before using for meaningful predictive simulations.

To model the secondary electron process required several new processes to be written for the GEANT4 toolkit. The existing processes unfortunately do not extend low enough, approximately 10 eV, to correctly describe the secondary emission process. Initial investigations using the default electromagnetic processes produce few secondary electrons from the surface of any material, even those traditionally used for electron multiplication purposes, such as BeO and MgO. Discussions with the GEANT4 community on the hypernews forum [130] suggested that the simplest physics process to modify is the G4GammaConversion process, commonly referred to as pair production. In short, two class files require modification to create a new process, these are the NAME\_process.cc file and the NAME\_model.cc file, where NAME is the name of the process. The former contains information regarding the energy range of the process, particles involved, and cross section bin size; the latter must contain algorithms for calculating the interaction cross section per atom as a function of energy and kinematics for all particles following the interaction.

## 5.4 Geant4 diamond model

In the next section the theory for calculating the interaction cross sections and probability distributions for an electron travelling through diamond will be introduced. The models will then be added as separate processes to the GEANT4 toolkit for electrons with energy below 2 keV travelling through carbon with diamond structure. The rationale for adding the process to GEANT4 instead of creating a new Monte-Carlo code is that the diamond implementation can be used alongside the existing intermediate-energy physics models for use in complex simulations of novel photomultiplier tubes and inertial fusion diagnostics. In addition, the GEANT4 toolkit already possesses a well-validated and powerful Monte-Carlo engine with many well-supported options for data analysis and visualisation.

### 5.4.1 Elastic scattering

Elastic scattering is the collision between two bodies resulting in a momentum shift of the projectile but no energy loss; this generally occurs when a light body collides with one much heavier, such as an electron interacting with the nucleus. The differential cross section [131] for elastic scattering with a spherically symmetric potential is

$$\frac{d\sigma_{el}}{d\theta}(E) = \frac{2\pi}{k^2} \left| \sum_{l=0}^{\infty} (2l+1) \sin(\delta_l) P_l(\cos(\theta)) \right|^2, \quad (5.25)$$

where  $k$  is the wave vector of the incident electron with energy  $E$ ,  $P_l$  is the Legendre polynomial series of order  $l$ ,  $\theta$  is the scattering angle and  $\delta_l$  is the phase shift for a given angular momentum exchange. Integrating this expression is straight forward if one knows the phase shifts  $\delta_l$ . Calculating  $\delta_l$  values requires solving the radial Schrödinger equation (RSE) for a spherically symmetric potential [131], where the nuclear potential must vanish to zero or a constant at some  $r$ . For a periodic material, such as diamond, a common approach is to approximate the repeating nuclear potential with a spherically symmetric Muffin Tin Potential (MTP);

MTPs can be calculated using density functional theory (DFT) which combines the cumulative interactions from the nucleus, inner shell and valence electrons with total energy minimisation and quantum mechanics to iteratively unfold the crystal potential [132]. The muffin-tin potential used in this work was obtained from [133] and is shown in Figure 5.7; this was combined with

$$\delta_l = \int_{r_0}^{\infty} dr \sqrt{k^2 - \frac{2me}{\hbar^2} V(r) - \frac{l(l+1)}{r^2}} - \int_{r_1}^{\infty} dr \sqrt{k^2 - \frac{l(l+1)}{r^2}} \quad (5.26)$$

to calculate the elastic scattering phase shifts [134], where  $r_0$  and  $r_1$  are the zeros of the respective integrals,  $V(r)$  is the muffin-tin potential,  $l$  is angular momentum,  $k$  is the electron wavevector,  $\hbar$  is the reduced Planck constant,  $m$  is the electron rest mass,  $e$  is the electron charge and  $r$  is distance away from the crystal lattice site. The MTP used in this work from 1971 was the only data available that could be found in the literature at the time of writing; MTPs computationally modelled using modern DFT techniques could provide a significant improvement to the accuracy of the elastic scattering cross sections calculating using this data. The differential cross section was calculated using equations 5.25 and 5.26; these are shown in contour form in Figures 5.8(a) and 5.8(a). The total elastic cross section is shown alongside the inelastic and phonon cross sections in Figure 5.9; the inelastic and phonon cross sections will be discussed later in this chapter.

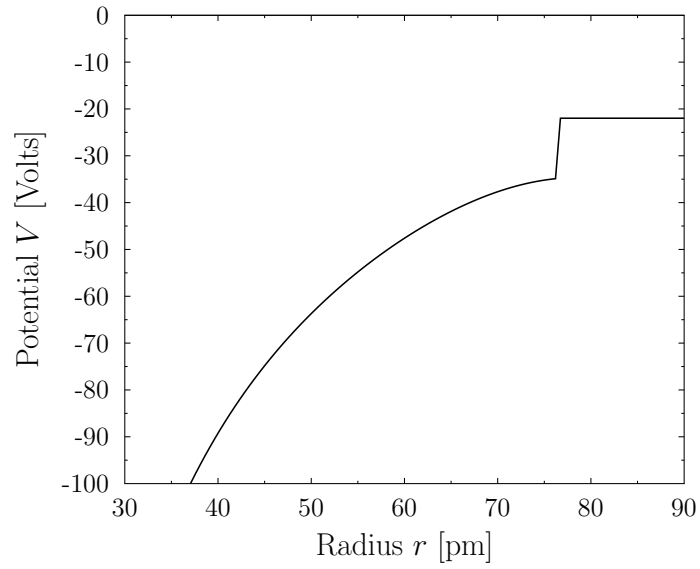
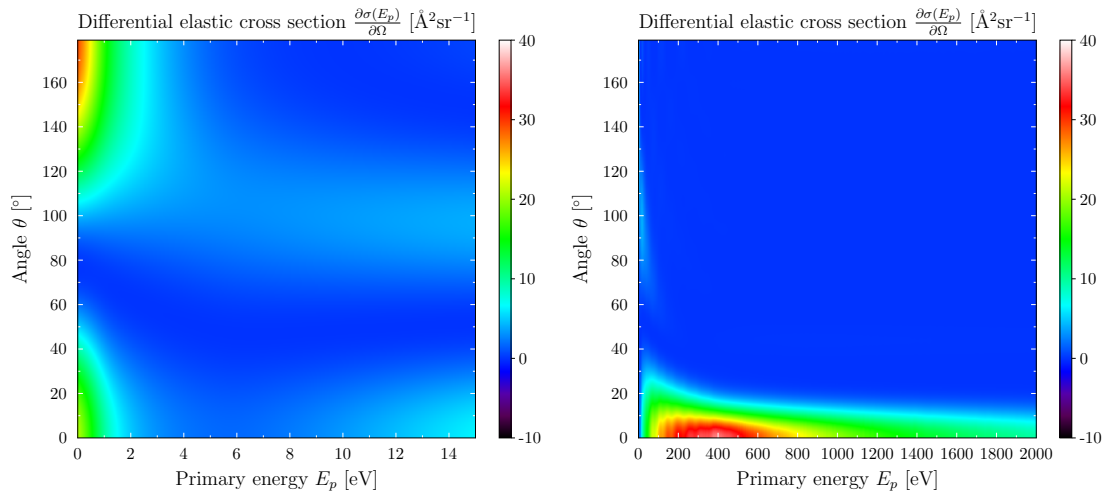


Figure 5.7: Muffin tin potential for diamond obtained from Painter et al., 1971 [133].



(a) Differential elastic cross section contour in the range 0 - 15 eV (b) Differential elastic cross section contour in the range 0 - 2000 eV

Figure 5.8: Figures (a) and (b) show the differential elastic cross section in contour form. At low energy the elastic scattering is almost isotropic, however as the primary electron energy increases elastic scattering becomes forward lobed.

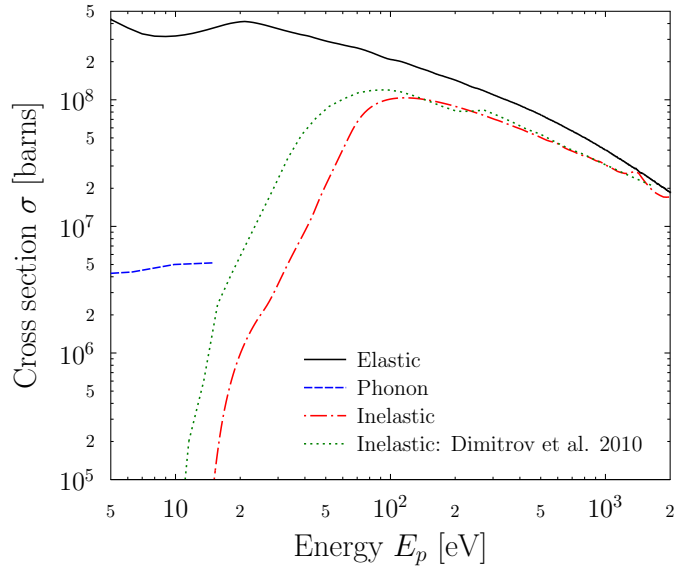


Figure 5.9: Elastic, inelastic and phonon cross sections calculated from this work compared with the inelastic cross section from Dimitrov et al [135].

### 5.4.2 Inelastic scattering

Inelastic scattering is the interaction of two bodies resulting in momentum exchange and energy loss, such as the ionisation of an atom by a passing electron. One method of calculating the transport of low-energy electrons through diamond is to combine the photonic Energy Loss Function (ELF) with knowledge of the band structure near the conduction band minimum [136]. The photonic energy-loss distribution is obtained by measuring the downshift of X-rays through diamond over the energy range of interest; this is known as the  $k \approx 0$  limit due to the small amount of momentum that can be transferred by a photon to the background medium during individual scattering interactions. As discussed previously in section 5.2.1 the basis for calculating stopping power is

$$\tau(E, \omega) = \frac{1}{\pi E a_0} \int_{q_-}^{q_+} \frac{dq}{q} \text{Im} \left[ \frac{-1}{\varepsilon(q, \omega)} \right], \quad (5.27)$$

Predicted energy loss and momentum transfer consequently depend on the creation of plasmons within the electron plasma [137]. If the underlying data supplied to this equation spans the pertinent energy regime it should be used for transport of both primary and secondary. This approach has been utilised for modelling the electron transport in metals; however for a semiconductor with wide bandgap the method is inadequate. Instead  $\text{Im}\left[\frac{-1}{\varepsilon(q,\omega)}\right]$  was obtained from [135] and is shown in Figure 5.10.

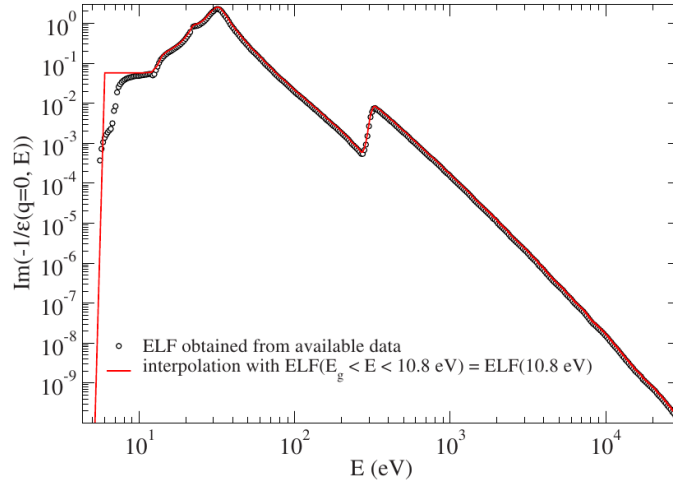


Figure 5.10: Plot of the diamond ELF in the  $q = 0$  limit from [135].

To obtain the electron inverse mean free path, and by inverse proportionality the inelastic interaction cross section, equation 5.27 must be integrated between 0 and the incident electron energy  $\hbar\omega$  over frequency space,

$$\frac{1}{\lambda(E)} = \int_0^{\frac{E}{\hbar}} \tau(\omega, E) d\omega, \quad (5.28)$$

where  $\lambda(E)$  is the electron inelastic mean free path. The remaining issue pertains to the  $q = 0$  condition in Figure 5.10. At present an electron propagated using equations 5.27 through 5.28 would lose energy but would not transfer momentum to the diamond, there would be no straggling. A method for expanding the ELF is needed and this is obtained using an approach developed by Ashley *et al*

[138] [139]. In this case the momentum transfer is obtained assuming the inelastic interaction is occurring at the plasmon frequency  $\omega_p$  as predicted by the Lindhard single-pole free-electron-gas dielectric function. Using the approach developed by Ashley and equations 5.27 through 5.28 an equation for the inverse mean free path can be obtained,

$$\frac{1}{\lambda(E)} = \frac{1}{\pi E a_0} \int_0^{\frac{E}{\hbar}} d\omega \int_{q-}^{q+} \frac{dq}{q} \frac{(\omega - \hbar q^2/2m)}{\omega} \text{Im} \left( -\frac{1}{\varepsilon^{\text{EXP}}(q=0, \omega - \hbar q^2/2m)} \right), \quad (5.29)$$

where  $\varepsilon^{\text{EXP}}(q=0, \omega)$  is the optical ELF obtained from X-ray experiments. Using equation 5.29 and the ELF shown in Figure 5.10 the MFP was calculated. Figure 5.11 shows the MFP from this work together with MFPs from Ashley [136], a fitted approximation from Ziaja [140] [141], and calculations from Tanuma, Penn and Powell [142]. The data from this work (green) was calculated between 15 and 2000 eV and shows varying levels of agreement with previous calculations. The data used for this work were transcribed directly from the literature which may have introduced a small amount of uncertainty; this process however was carried out several times using different sources at progressively higher levels of precision and produced little impact on the shape of the calculated IMFP. In addition significant effort was made to optimise the integration routines and again produced a negligible impact on the shape. The IMFP from Ziaja's fitting equation (solid black line) are significantly smaller for electron energies between 10 and 100 eV. This will increase scattering of the primary at low energy thereby reducing the maximum penetration depth and will also reduce the ability of low energy secondary electrons to migrate to the surface. The interaction cross section can be calculated from equation 5.29 using  $\sigma = 1/N\lambda$  together with the diamond atom density  $N = \rho/M_C = 3520 \text{ [Kg]} / (12u) = 1.766 \times 10^{29} \text{ m}^{-3}$ , where  $u$  is the atomic mass unit  $1.66 \times 10^{27} \text{ [Kg]}$ ; the cross section is shown in Figure 5.9

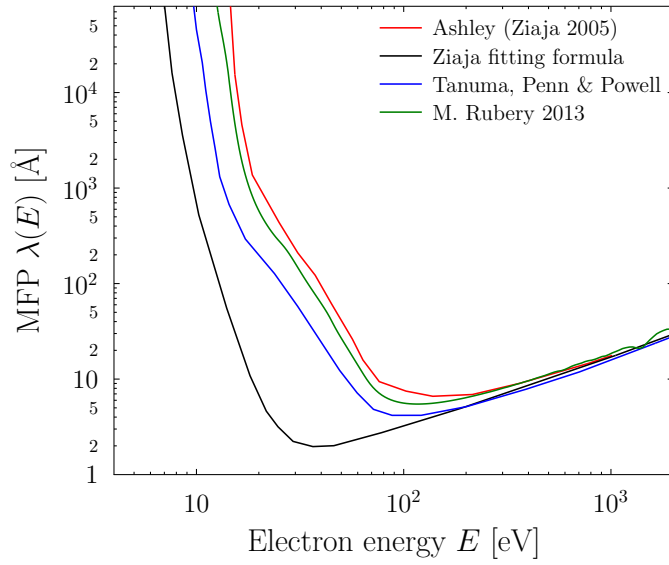


Figure 5.11: Calculated inelastic mean free paths (IMFP) for diamond from this work, Ziaja [140] [141], Ashley [136] and Tanuma [142].

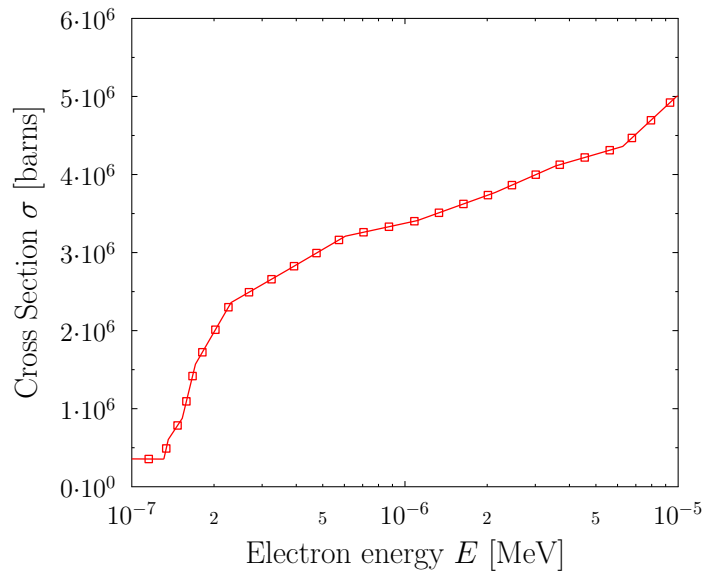


Figure 5.12: Optical phonon scattering cross section obtained from Dimitrov's scattering rate data [143].

### 5.4.3 Energy-loss probability distribution

To create a Monte Carlo simulation one needs to go further than calculating the cross section for interaction. At the point of scattering probability distributions associated with energy loss and momentum transfer need to be calculated. The approach used in this work was to iterate through the pertinent energy range (0-2000 eV) at a resolution of 1 eV and calculate the probability distribution at each energy with high resolution for  $dk$  and  $d\omega$ . The resulting grid is read into the GEANT4 model at runtime and interpolated during the simulation to increase computational efficiency which is important where large numbers of secondary tracks are generated. The first probability distribution to be calculated is the energy-loss; as will be shown later the probability distribution for momentum change depends on the energy loss. The probability distributions come from the double differentiation of the cross section [144] [145]

$$\frac{\partial^2 \sigma_{in}(q, \omega, E)}{\partial q \partial \omega} = \frac{1}{N\pi a_0 E q} \text{Im}(-\varepsilon^{-1}(q, \omega)), \quad (5.30)$$

which can be derived from 5.29. To calculate the energy-loss probability distribution  $\tau(E, \omega)$  is calculated for all  $\omega$  values up to  $\omega_{max} = E/\hbar$ ; each  $\tau(\omega, E)$  value is essentially the probability of a specific energy loss  $\omega$ . When the distribution of  $\tau(\omega, E)$  values is divided by the cross section  $\sigma_{in}$  the distribution becomes a normalised probability distribution,

$$P(\omega, E) = \frac{\tau(\omega, E)}{\sigma_{in}}. \quad (5.31)$$

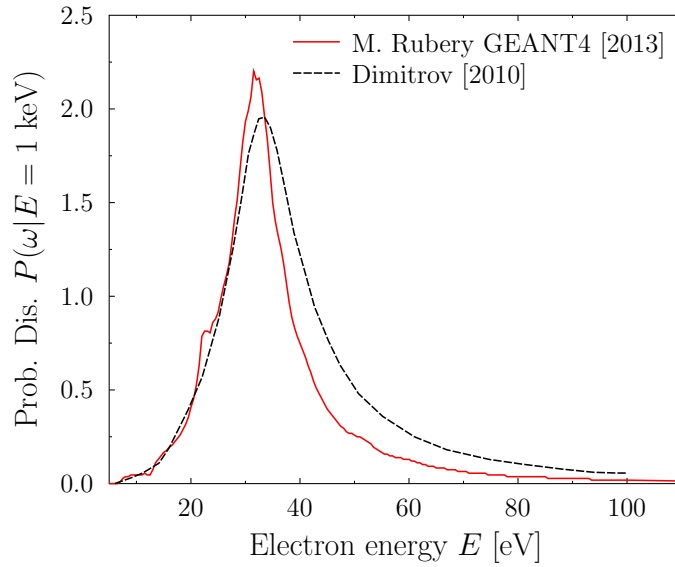


Figure 5.13: Probability distribution calculated for a 1 keV electron using equation 5.31 compared with the analytical result reported by Dimitrov [143].

Figure 5.13 shows analytical results from Dimitrov [143] compared with a Monte Carlo check of the algorithms included in the GEANT4 model. The calculated energy-loss probability distributions for a 1 keV incident electron show qualitative agreement; differences are likely due to approximations made in the GEANT4 integration routines which at present are simply based on trapezium rule. In the future these will be modified to incorporate a Gauss-quadrature or Newton-Cotes approach to improve accuracy. As mentioned previously to calculate the momentum transfer probability distribution the energy loss must already be known. The probability distribution [144] [145] is defined as

$$P(q|\omega, E) = \frac{\frac{\partial^2 \sigma_{in}(q|\omega, E)}{\partial q \partial \omega}}{\int_{q_-}^{q_+} \frac{\partial^2 \sigma_{in}(q'|\omega, E)}{\partial q' \partial \omega} dq'}. \quad (5.32)$$

Comparisons between the GEANT4 model and the Dimitrov analytical results show similar qualitative characteristics in Figure 5.13. A current issue with the code is how to handle primaries and secondaries with energies between  $E_g$  and 10

eV, the inelastic scattering cross section cut-off. In this energy range the dominant energy-loss mechanism is optical and acoustic phonon scattering. At present a treatment for phonon scattering is not implemented in any detail within the model. A cross section obtained from Dimitrov [143] is used for the process together with an energy-loss of 0.16 eV per scatter event. The origin of the phonon interaction is electron-phonon intervalley scattering which rapidly decreases the energy of a free charge carrier at low energies and reduces the probability of generating additional secondary electrons via impact ionisation. The angular dependence is assumed to be isotropic which is unlikely to be the case as phonons cannot carry a large amount of momentum relative to the electron and the energy transfer is small. This assumption will likely have the effect of shortening the escape depth of electrons at scattering energies dominated by photon interactions, and therefore reducing the overall secondary electron yield of the material.

#### 5.4.4 Geometry and physics implementation

To implement the physics discussed in Section 5.2 the gamma conversion class was modified. Two distinct models for inelastic and elastic scattering were created based on this approach. The first required task is to alter the cross section generator from the Bethe-Heitler differential cross section to those shown in Figure 5.9. Linear splines were performed on the cross section data and exported to text files which are read into 2D arrays at startup by the main C++ program. The 'ComputeCrossSectionPerAtom' is called for all processes that have been added and in the case of bespoke physics it is up to the user to inform the process manager of the minimum and maximum energy range and the number of logarithmic cross section samples to be performed. For inelastic scattering these were set to 10-2000 eV and 215 samples and for elastic scattering 1-2000 eV and 215 samples. A for-loop together with linear interpolation algorithm was written to return the correct cross section in barns to the 'ComputeCrossSectionperAtom' method for both processes. Once the cross section has been registered the next task is to update the 'SampleSecon-

daries' method in which modifications to the primary particle energetics (incident electron) are made and secondaries produced. This method gives the user access to the primary particle energy, momentum three-vector, current volume and material.

To obtain the change in energy  $\Delta E_{e-}$  equation 5.31 is used together with the incident electron energy and a uniform random number  $r_1$  between 0 and 1. The probability distribution is calculated for the current incident electron energy  $E_{e-}$  and stored in a 2-dimensional array. An additional column is added to the array containing the integral of the probability distribution over the same independent range; the same algorithm also returns the maximum value of the integral  $I_{max}$ . To sample from this distribution we use  $P_v = I_{max}r_1$  to define a location somewhere on the dependent axis of the integrated probability distribution. The selected electron energy loss  $\Delta E_{e-}$  is then calculated by identifying the unique location on the independent axis (energy) that corresponds with  $P_v$ . Once  $\Delta E_{e-}$  is known the sample sampling methodology is applied to equation 5.32. The energy loss and momentum change are now known for the incident electron; however this is not enough information to emit a secondary and modify the kinematics of the primary.

To calculate the final unit vector of the primary electron  $V_p$  and the emission unit vector of the secondary  $V_s$  we use the conservation of energy and momentum in 2 dimensions  $X''$  and  $Z''$  assuming that the incident electron  $U_p$  is down the  $Z''$  axis. Note that  $Z''$  differs from the laboratory  $Z$  axis. The primary electron scattering angle  $\theta_p$  is

$$\theta_p = \cos^{-1} \frac{[|V_p^2| + |U_p^2| - |V_s^2|]}{2|V_p||U_p|}, \quad (5.33)$$

similarly the secondary scattering angle can be calculated using

$$\theta_s = \sin^{-1} \left( \frac{-V_p \sin \theta_p}{V_s} \right), \quad (5.34)$$

where  $V_s$  the magnitude of the secondary velocity is

$$V_s = \sqrt{|U_p^2| - |V_p^2|}. \quad (5.35)$$

The 2-vector for the primary are calculated using

$$V_x'' = \sin \theta_p, \quad (5.36)$$

$$V_z'' = \cos \theta_p. \quad (5.37)$$

Two diagrams Figure C.1 and C.2 are shown in appendix C to illustrate the steps involved in calculating the scattered primary electron emission vector and the subsequent Euler rotations used to transform the emission vector from the reference frame of the primary electron to the laboratory frame. The scattering problem is extended into 3-dimensions by randomly choosing a value for  $\phi_p = 2\pi r_2$  where  $r_2$  is a uniform random number between 0 and 1. To calculate the new 3-vector using  $\phi_p$  and the original 2-dimensional  $V_{x/z}''$  we use a single Eulerian rotation around the Z axis by the angle  $\phi_p$ ,

$$V_x' = \sin \theta_p \cos \phi_p, \quad (5.38)$$

$$V_y' = \sin \theta_p \sin \phi_p, \quad (5.39)$$

$$V_z' = \cos \theta_p. \quad (5.40)$$

This 3-vector is the scattered electron direction relative to the incident primary electron, when the absolute velocity vector of the primary electron points down the  $Z''$  axis. To obtain the unit emission vector in the laboratory frame, which is required by the 'sampleSecondaries' method, a double Eulerian rotation is required. This modifies the vector  $V_{x/y/z}'$  such that  $Z'$  (primary electron vector) points down the laboratory Z axis. To calculate the Eulerian angles for this rotation we require  $\theta_e$  and  $\phi_e$ , the primary electron polar angles in the laboratory frame. The literature generally describes this transformation in the opposite direction to the situation required; consequently the equations for transforming the laboratory Z axis vector to primary electron vector will be described. The Euler angles however are multiplied by  $-1$  to switch the direction of the transform. The rotation first requires a rotation around the  $Z'$  axis from  $X'$  such that the new Y axis lies in the plane defined by

the laboratory Z axis and the primary electron vector  $U_p$ ; the required Euler angle including the transformation direction change is  $\phi_{Euler} = -(\pi/2 - \phi_e)$ . Secondly a rotation around the new X axis is performed such that the resulting Z axis points in the same direction as the primary electron; the Euler angle after reversing the transformation direction is  $\theta_{Euler} = -\theta_e$ . Using these angles together with the standard Euler transformation matrices leaves

$$V_x = V'_x \cos \phi_{euler} - V'_y \cos \theta_{Euler} \sin \phi_{Euler} + V'_z \sin \theta_{Euler} \sin \phi_{Euler} \quad (5.41)$$

$$V_y = V'_x \sin \phi_{euler} - V'_y \cos \theta_{Euler} \cos \phi_{Euler} + V'_z \sin \theta_{Euler} \cos \phi_{Euler} \quad (5.42)$$

$$V_z = V'_y \sin \theta_{euler} - V'_z \cos \theta_{Euler}. \quad (5.43)$$

After calculating the updated primary electron 3-vector in the laboratory frame and the new primary electron energy  $E'_p = E_p - \Delta E_{e-}$ , the secondary emission 3-vector and energy can be trivially calculated using conservation of momentum,  $V_p$  and  $U_p$ . The individual vectors of  $U_p$  are  $U_x = \sin \theta_e \cos \phi_e$ ,  $U_y = \sin \theta_e \sin \phi_e$  and  $U_z = \cos \theta_e$ . Equating the momentum before and after the scattering event in X, Y, and Z leads to

$$V_{sx} = U_x - V_x, \quad (5.44)$$

$$V_{sy} = U_y - V_y, \quad (5.45)$$

$$V_{sz} = U_z - V_z. \quad (5.46)$$

The electron masses cancel during the conservation calculation. We now have the emission unit vectors for the primary electron  $V_p$  and the secondary  $V_s$ ; the primary energy and secondary energies are  $E'_p$  and  $\Delta E_{e-}$  respectively. Note that if  $\Delta E_{e-}$  is  $< 5.47$  eV, the diamond band-gap, the secondary particle is not emitted and the energy is assumed to be lost to the material instead.

## 5.5 Results and discussions

### 5.5.1 Relation to incident primary angle

An important validation that the tracking algorithm in the GEANT4 is working correctly is to investigate how the yield varies with increasing incident electron angle. The linear theory discussed in Section 5.1.2 suggests that the yield and primary energy at which the maximum SEE occurs should both increase as the incident primary angle  $\theta_p$  increases; the primary angle is defined as the angle between the electron incident vector and the sample surface normal. The source term for the GEANT4 model was modified to give the fractional momentum vectors  $P_x=\sin(\theta_p)$ ,  $P_y=0$  and  $P_z=\cos(\theta_p)$ ; SEE values were recorded using a tally sphere placed around the diamond sample. Figure 5.14 shows how the GEANT4 model predicts the SEE to change with  $\theta_p$  plotted next to values for molybdenum experimentally measured by Shih and Hor [146]. The set up used by Shih and Hor consisted of a large Faraday cup placed around the sample to subtend almost  $2\pi$  steradians, with a small hole to allow the electron beam to hit the sample, all placed inside a vacuum system. The molybdenum sample was kept at a bias of -72 eV to propel secondary electrons towards the Faraday cup. This represents a less complex approach compared to the LEED grids however for integrated yield measurements it is sufficient. Despite the comparison being for different sample materials, the angular angle trends should be similar. From a qualitative perspective increasing the angle of incidence should reduce the effective depth of the primary track thereby allowing a greater proportion of the internal secondary electron population to migrate to the surface. The GEANT4 data does produce the same trends observed in the measured molybdenum data; the peak SEE occurs at the largest incident angle, and the  $E_p$  at which the peak occurs does shift to higher energies with increasing incident angle. The difference between each incident angle in the GEANT4 model however is significantly reduced compared with the molybdenum experimental data. This may be related to the large secondary electron escape depth in diamond compared with materials, such as molybdenum, which exhibit low SEE. A useful exercise would

have been to supply the GEANT4 simulation with equivalent elastic, inelastic and phonon parameters for molybdenum thereby increasing the relevance of the primary angle comparison. This would constrain whether the differences observed between the two materials are computational or real. Unfortunately the literature study required to identify the relevant physical parameters could not be performed due to time constraints.

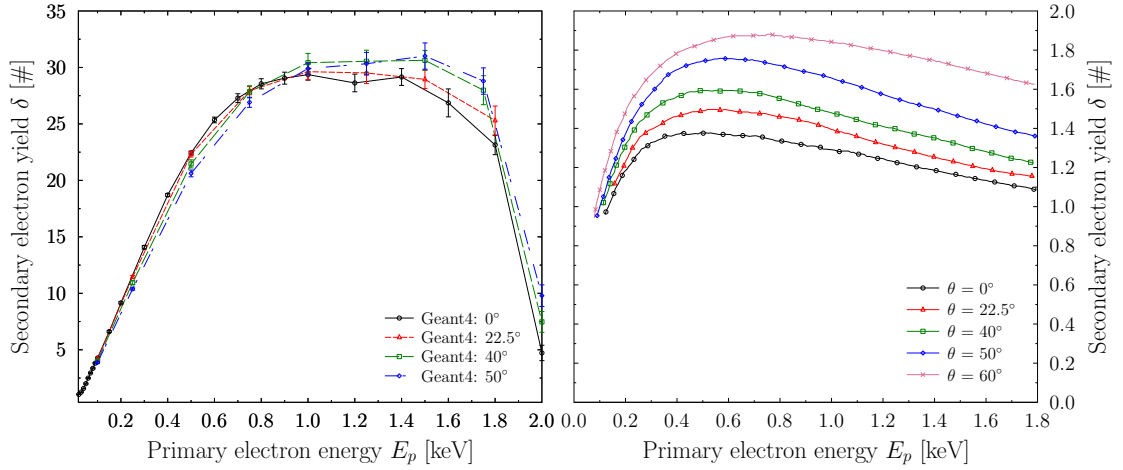


Figure 5.14: Plot showing the SEE ( $\delta$ ) curve for moderately doped diamond at several incident electron angles predicted by the GEANT4 model; the second plot shows measured SEE data by Shih and Hor [146] for a molybdenum sample. Note the surface coefficient for hydrogen-terminated diamond of 0.4 has not been applied to the GEANT4 data as the comparison is between two different materials and investigates the trend with angle not the absolute secondary yields.

## 5.5.2 SEE yield curve

Figure 5.15 contains a visualisation of a single 500 eV electron scattering in the GEANT4 model produced by the HepRapp visualisation software. The image highlights the fractal, and therefore computationally expensive, nature of the electron lifetime inside the diamond material. The secondary electron emission of 31 is shown as straight lines emanating from the front surface to the left. Figures 5.16 and 5.17 show reflection SEE and the individual scattering totals for each sub-process as a function of incident primary electron energy. Yields in Figure 5.16

compare favourably in shape and intensity with measurements made at Leicester University in the dedicated characterisation facility discussed earlier in Section 4.3.3 and with published data [120]. The multiplier of 0.4 shown in Figure 5.16 is to correct for the lack of a surface treatment in the model; this is generally treated as a constant attenuation for hydrogen-terminated diamond and is related to electron tunnelling from the conduction band to the vacuum [121]. Above 2.05 keV the novel low energy model switches over to the standard GEANT4 electromagnetic processes; consequently the number of internal secondaries decreases rapidly beyond this point and the SEE drops. Surprisingly the GEANT4 model is observed to drop off significantly 200 eV below the 2.05 keV transition point. This is in part due to the elastic scattering formulation shown in Figure 5.8. At low energies below 25 eV elastic scattering is isotropic; at higher energies however elastic scattering becomes increasingly forward –biased and despite undergoing elastic collisions the primary electron can penetrate deep into the material, reducing the probability of secondaries navigating to the surface. Figure 5.16 also shows the reflection configuration SEE curve predicted by the SEEDS code discussed in Section 5.2.1 of this thesis. As described earlier the maximum SEE predicted by SEEDS is in likely serendipitous agreement with experimental data but the shape and therefore the underlying electron transport physics disagrees.

Figure 5.17 shows that elastic scattering is by far the dominant process in the model followed by phonon scattering. Inelastic scattering represents the least number of interactions for a given primary energy; once the electron reduces to energies just above the band gap only phonon scattering can reduce the energy further and therefore significantly more interactions are required to drop the electron into the valance band. This is one of the reasons that diamond has such a high SEE. Unfortunately the mean ionisation energy of approximately 23 eV in Figure 5.17 is high when compared to published values [135]. This is likely due to the inelastic cross section from this work in Figure 5.9 tending to zero at a higher energy than seen in other models. Figure 5.17 illustrates the necessity for a more sophisticated phonon scattering model. Significant effort was made in this chapter to produce a valid

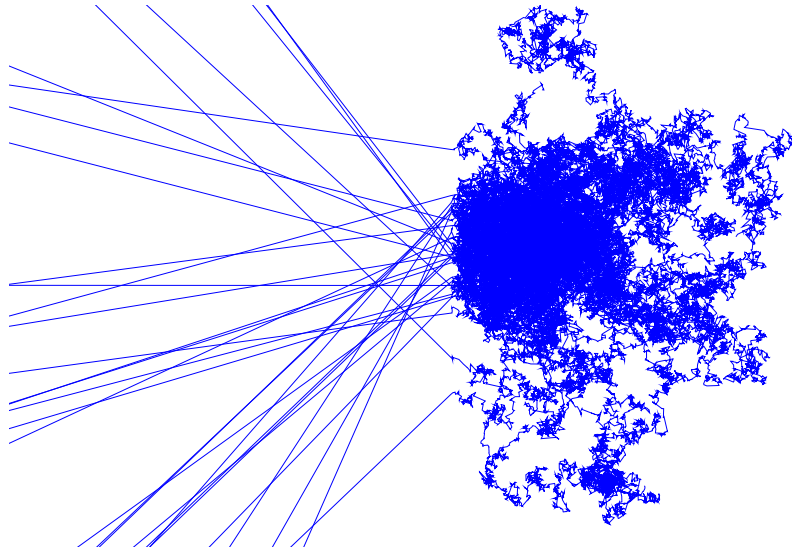


Figure 5.15: Visualisation of a 500 eV electron from the Geant4 model. The visualisation tool used was HepRApp [60].

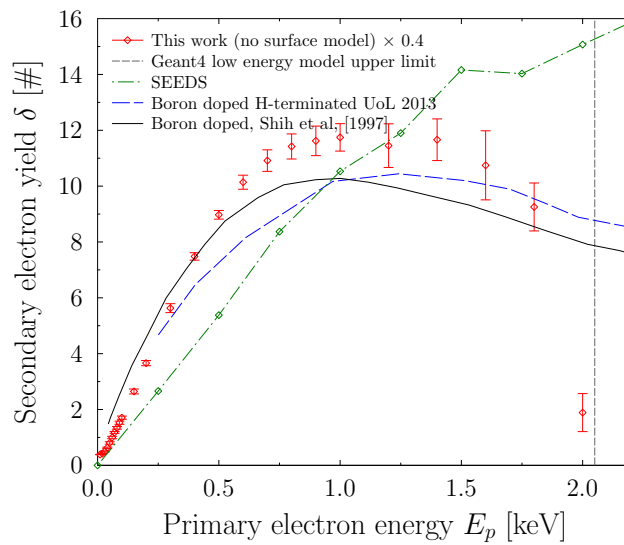


Figure 5.16: Comparison of the GEANT4 model (single crystal moderately boron doped diamond) with SEE measurements from Leicester University (polycrystalline, moderately boron doped and hydrogen terminated diamond) and Shih et al [120] (hydrogen terminated and moderately boron doped diamond). The SEEDS code discussed in Section 5.2.1 is shown in broken green for comparison.

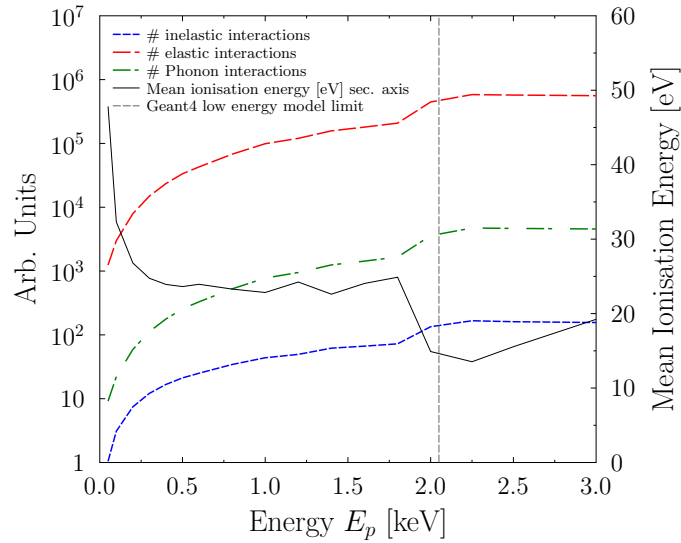


Figure 5.17: Plot showing the individual scattering totals for each process from the Geant4 model as a function of primary electron energy. The mean ionisation in eV (black) has also been included on the secondary axis.

model for inelastic scattering as this is the sole process that can generate secondary electrons. However the individual scattering yields plot clearly emphasises that the elastic and phonon interactions are at least equal in importance when considering an integrated variable such as surface secondary electron yield. Future developments to the GEANT4 model should address the out-dated MTP used to derive the elastic scattering cross section, and realistic scattering interactions should be developed beyond the isotropic and constant 0.16 eV loss approach for electron-phonon interactions. A further issue with the GEANT4 model is the discontinuity at 1.75 keV for all processes and the mean ionisation energy in Figure 5.17. The maximum energies for the inelastic, elastic and phonon models were set at 2050 eV and the low energy activation thresholds for the G4UrbanMscModel93, G4MollerBhabhaModel and G4SeltzerBergerModel were all set at 2050 eV. Consequently the GEANT4 simulation should smoothly switch to the processes outlined in this chapter at 2050 eV. Unfortunately it is evident that the transition has not been implemented as desired and the electron transport is not being calculated correctly between 1750 and

2050 eV, much lower than the transition value would suggest. This may go some way to explaining the sharp drop off in secondary electron emission above 1750 eV in Figure 5.16. The transition region requires investigation in future developments of the GEANT4 model.

### 5.5.3 Secondary energy distribution

Figure 5.19 shows the energy spectrum predicted from the GEANT4 model compared to experimental data from Shih et al using a low-energy electron diffraction (LEED) with retarding field analyser, housed inside a  $\mu$  metal shield with solid angle of  $2\pi$  sr (same as GEANT4 tallying algorithm for RC observations) [120] [147]. The LEED system uses retarding fields to screen out electrons below a specific energy; through multiple measurements a series of integrals are produced, the secondary electron energy distribution can be calculated from the derivative of these integrals.

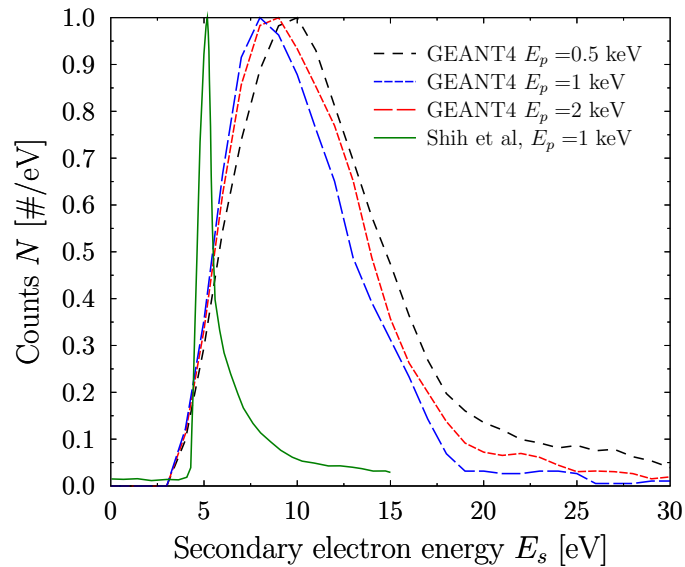


Figure 5.18: Plot showing the secondary electron energy distribution for moderately doped diamond predicted by the GEANT4 model at several different primary energies  $E_p$ . In addition the secondary electron distribution measured by Shih et al [120] [147] has been plotted for comparison. The differences highlight the need for a surface model treatment in the GEANT4 model.

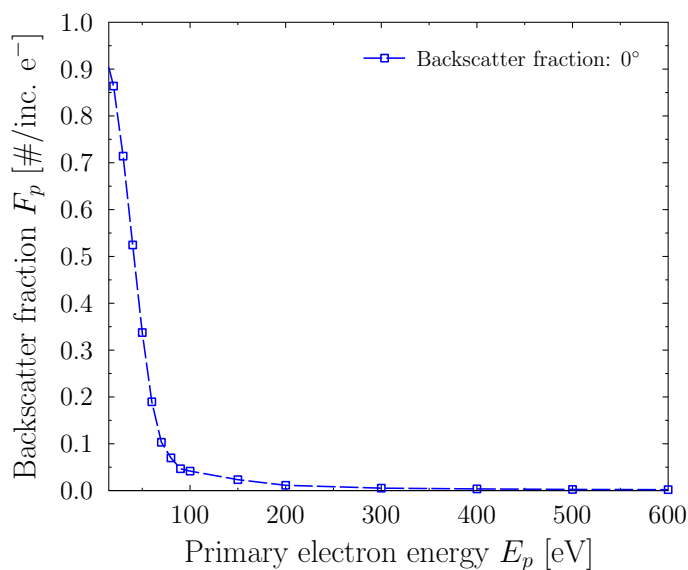


Figure 5.19: Plot showing the fraction of primaries backscattered from the diamond as a function of primary energy  $E_p$  predicted by the GEANT4 model. Simulation suggests that the backscatter fraction reduces to less than 5 % at energies below 100 eV.

The GEANT4 results shown in Figure 5.19 produce a secondary electron energy distribution similar in shape to the energy loss function in Figure 5.10; this is expected as the energy loss function forms the basis of the inelastic scattering algorithm. Compared to the experimental data from Shih et al however, the spectra are more broad and higher in energy. This is to be expected as the GEANT4 model does not include a treatment for the surface which is likely to down-shift the secondary population. The GEANT4 model does exhibit the correct shift to a lower average secondary electron energy with increasing  $E_p$ . This is due to the primary electron penetrating deeper into the diamond requiring the secondary electron population to propagate further to reach the surface, allowing additional inelastic and phonon interactions to occur. In the future it may be possible to unfold a transfer function from the difference between the GEANT4 secondary electron distribution and experiments utilising the LEED approach.

## 5.6 Summary

Chapter 5 has briefly discussed historical models and recent theory for electron transport in diamond. The analytical models by Dionne in the 1970s and Shih/Yater in the 1990s are useful for qualitatively describing the competing processes governing secondary electron emission, specifically primary electron migration and relation to stopping function  $dE/dx$ , secondary production and relation to average ionisation energy, and surface penetration. The models however compare poorly with experimental data when considering secondary electron emission yield, even in reduced form. In addition these models do not allow calculation of secondary emission properties, such as energy and angular emission distributions, useful in the design of a PMT.

Recent efforts using dielectric functions in the  $k = 0$  limit calculated from X-ray transmission experiments extended into the  $k \neq 0$  limit using Lindhard free-electron-gas theory show more promise for generating the complex models required to support PMT design. Such theory was incorporated into the GEANT4 toolkit as a parameterised low-energy extension to the existing models. Initial testing of the model shows qualitative agreement with measurements at Leicester University and results from literature. Several issues require further work however. The transition from default electromagnetic processes does not occur smoothly at 2.05 keV and significantly reduces secondary electron yield above 1.75 keV. The phonon scattering and surface models are simple and require significant work. In addition the model is only valid for the boron concentration used originally during the X-ray transmission experiment. Consequently due to time constraints the GEANT4 low-energy extension is not mature enough to begin narrowing the PMT design phase space. Collaborations with Cambridge University in the area of density functional theory (DFT) may yield the transport algorithms and data required to model phonon scattering and surface emission.

In the future the GEANT4 SEE model may allow optimisation of a novel CVD diamond-based PMT in transmission configuration. It is hoped that such a design

with three dynode stages could produce a PMT with rise time in the region of 1–10 ps and a gain of a few thousand, improving Cherenkov detector system bandwidth by almost an order of magnitude.

# Chapter 6

## Summary

The long-awaited possibility of cheap and clean energy from fusion may still be several decades away; improvements however in plasma and nuclear understanding, target fabrication, laser facility technology and diagnostic development at the NIF and Omega suggest the community is heading in the right direction.

This thesis has concentrated on the important modelling support for the Cherenkov detectors at NIF and Omega, and the possibility of using diamond to improve detector temporal resolution by an order of magnitude. The GEANT4 and ACCEPT codes were initially benchmarked for consistency in the relevant energy regime using simple test geometries and sources and showed extremely good agreement for the Compton scattering, pair production and photo-electric effect processes. The two codes were then validated at the absolutely calibrated high-intensity  $\gamma$  source facility at DUKE University; a series of translational and pressure scan measurements were conducted and compared to code with agreement never exceeding a factor of  $\times 2$ . The confidence obtained from the HI $\gamma$ S validation enabled a series of investigations to be performed looking at hard-to-measure detector characteristics, such as the dependence of detector temporal response and output intensity on gas pressure and incident  $\gamma$  energy, the feasibility of measuring  $\langle \rho R \rangle_{abl}$  using a routinely observed and undesired background signal, and the design and optimisation of the next-generation super GCD detector currently under construction at Los Alamos National Laboratory. The latter required direct coupling of GEANT4

output with the optics package LightTools. This allowed the benefits of the particle physics Monte Carlo simulation to be combined with the individual optical component optimisation capabilities of the ray tracing software for the first time in this environment; ultimately improving several characteristics of the next-generation Cherenkov detector. In this respect the validated Monte Carlo codes have added significant value to the Cherenkov detector collaboration. The NIF  $\gamma$  reaction history Cherenkov diagnostic has been one of the primary methods for reporting nuclear bang-time and burn-width at NIF since its commissioning in 2010 and in addition, has evolved the capability of reporting  $\langle \rho R \rangle_{abl}$  using the multi-channel thresholding technique. Without input from the Monte Carlo codes, reported values would comprise larger and less-understood error bars due to uncharacterised detector effects from gas pressure changes, and the next generation of Cherenkov detectors would suffer less-favourable signal-to-noise ratio. Fundamental detector developments and investigations are critical for diagnosing the failure modes which have plagued the first years of the ignition campaign. In the future, GEANT4, MCNP and ACCEPT will continue to supply detector parameters and insights to the Cherenkov detector collaboration adding a small but important contribution to the quest for inertial fusion energy.

A novel technique has also been demonstrated for measuring remaining shell areal density  $\langle \rho R \rangle_{abl}$  during direct drive ICF implosions using the  $\gamma$  emission from inelastic neutron interactions with ablator material. An initial experiment was performed using the GCD2 detector and good proportionality was observed between measured GCD2 signals and reported  $\langle \rho R \rangle_{abl}$  values from the Charged Particle Spectrometer (CPS) and Wedge Range Filter (WRF) diagnostics. The concept was subsequently developed into a new detector currently known as PADD1 at Omega as part of a collaboration between AWE, Laboratory for Laser Energetics (LLE) and Los Alamos National Laboratory (LANL). Conceptual design, Monte Carlo modelling and data analysis were performed by the author with LLE and LANL providing engineering resources and support equipment respectively. Preliminary analysis of the PADD1 dataset from the initial fielding shows strong correlation

with signals recorded by the GCD2 during the same shots. The PADD1 system will benefit the community by providing prompt post-shot results (no requirement for CR39 etching or Cherenkov null shot subtractions) and reduced error bars. In addition the novel detector can measure  $\langle \rho R \rangle_{abl}$  during both glass and plastic implosions, which is not currently possible using the GRH.

Also discussed in this thesis was the possibility of using diamond as a dynode material inside a photomultiplier tube, for eventual use inside a Cherenkov detector, potentially improving bandwidth and gain. Diamond has many favourable characteristics that make its use desirable, such as large secondary electron yields, high thermal conductivity and radiation hardness. At present there are no publicly available codes that adequately describe the propagation of electrons through diamond; combined with the complexity of different boron doping levels and surface termination types it quickly became apparent that a model should be created and combined with the GEANT4 package to allow full simulations of the Cherenkov detectors to be performed. Using existing theory based on experimentally-derived dielectric functions, elastic scattering from quantum mechanics and an existing phonon scattering formalism, a model was created and added to the existing GEANT4 package as a low-energy extension below 2.01 keV. Due to time constraints it was not possible to create a complex quantum surface treatment as originally planned; at the cessation of the project the model utilises a constant loss at the surface in line with other 1-dimensional approaches from the literature. In addition, it was originally desired that the experimentally-derived dielectric function for moderately boron-doped single crystal diamond used to calculate electron stopping would be augmented using density functional theory (DFT). It may be possible to create a range of  $k = 0$  dielectric functions each with a different boron doping concentration using DFT which could then be selected at run-time in the GEANT4 model and used to perform large-scale PMT optimisation studies. Nonetheless the GEANT4 model does show qualitative agreement with measurements made at Leicester University and with data from the literature. In the future it is hoped that the GEANT4 model can help optimise the design of a novel CVD diamond-based PMT in transmission

configuration with 2–3 dynode stages. Such a system may produce a PMT with rise time in the region of 10 ps and a gain of a few thousand, potentially improving Cherenkov detector system bandwidth by almost an order of magnitude.

# Appendices

# Appendix A

## Cherenkov Detector Gas Parameters

The threshold to incident gamma radiation can be calculated [71] using

$$E_\gamma = \left[ \frac{1}{\sqrt{1 - \frac{1}{n(\lambda, T, P)^2}}} - \frac{1}{2} \right] m_e c^2, \quad (\text{A.1})$$

where  $n$  is refractive index (RI),  $m_e$  is the electron rest mass and  $c$  is the speed of light. The situation is complicated by the dispersion of the RI as a function of wavelength; for a given pressure the RI is not constant and generally increases with reducing wavelength. Consequently the actual gamma threshold for a specific pressure occurs at the shortest observable wavelength of the PMT; this occurs at approximately 200 nm. Alternative photocathode materials and pressure windows could be used which would extend the lower limit; the  $\gamma$  threshold  $E_\gamma$  however would become increasingly less well defined. Equation A.1 relies on knowledge of the RI as a function of both pressure, wavelength and temperature. Before calculating RI as a function of the aforementioned parameters, the relation between pressure and density must be understood; the refractivity  $\eta = n - 1$  is generally proportional to density

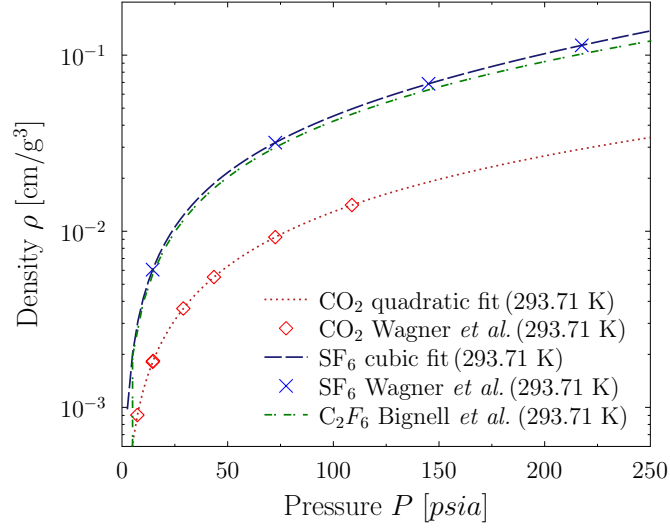


Figure A.1: Plot showing density scaling with respect to gas pressure for a temperature of 293.71 K, the NIF target hall nominal temperature.

Measurements undertaken by Wagner for CO<sub>2</sub> [148] and SF<sub>6</sub> [149] show the  $P(\rho)$  relation from sub-atmospheric pressure up to the gas-liquid phase transition for a temperature of 293.71 K. Using a nested interpolation routine it was possible to calculate the scaling relation for density as a function of pressure, with the scaling parameters themselves dependent on temperature. For CO<sub>2</sub> the full phase space relation was based on 2nd order polynomials and was calculated to be

$$\rho_{CO_2} = A_{CO_2} P_{CO_2}^2 + B_{CO_2} P_{CO_2} + C_{CO_2} \quad (\text{A.2})$$

where

$$A_{CO_2} = 3.313 \times 10^{-12} T^2 - 2.669 \times 10^{-9} T + 5.477 \times 10^{-7} \quad (\text{A.3})$$

$$B_{CO_2} = 1.504 \times 10^{-9} T^2 - 1.308 \times 10^{-9} T + 3.784 \times 10^{-4} \quad (\text{A.4})$$

$$C_{CO_2} = -2.151 \times 10^{-9} T^2 + 1.276 \times 10^{-6} T - 1.872 \times 10^{-4}. \quad (\text{A.5})$$

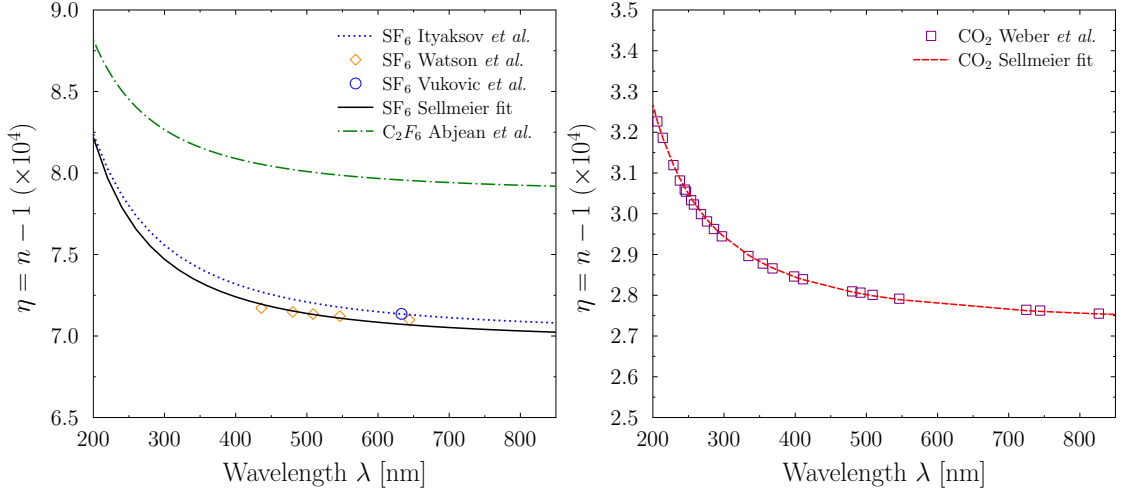


Figure A.2: Plot of the refractive index of SF<sub>6</sub> and C<sub>2</sub>F<sub>6</sub> (left) and CO<sub>2</sub> (right) at 1 atm. The Sellmeier fit for SF<sub>6</sub> was formed using a least-squares approximation to three separate experimental datasets.

For SF<sub>6</sub> the full phase space relation was based on 3rd order polynomials and was calculated to be

$$\rho_{SF_6} = A_{SF_6} P_{SF_6}^3 + B_{SF_6} P_{SF_6}^2 + C_{SF_6} P + D_{SF_6} \quad (\text{A.6})$$

where

$$A_{SF_6} = -2.389 \times 10^{-12} T^2 + 1.334 \times 10^{-9} T - 1.833 \times 10^{-7} \quad (\text{A.7})$$

$$B_{SF_6} = 1.173 \times 10^{-9} T^2 - 6.8353 \times 10^{-7} T + 9.9466 \times 10^{-5} \quad (\text{A.8})$$

$$C_{SF_6} = -1.0124 \times 10^{-7} T^2 + 5.7549 \times 10^{-5} T - 7.7228 \times 10^{-3} \quad (\text{A.9})$$

$$D_{SF_6} = 1.6525 \times 10^{-6} T^2 - 9.6553 \times 10^{-4} T + 1.4056 \times 10^{-4}. \quad (\text{A.10})$$

Figure A.1 shows the interpolated CO<sub>2</sub> and SF<sub>6</sub> measurements together with quadratic and cubic fits across the working pressure range of the GCD 1 and GRH. The temperature of 293.71 K corresponds to measurements made inside the gas

cell at NIF; Omega gas-cell temperatures (not shown) are measured at 298 K. The next requirement for calculating a specific gamma threshold is to obtain  $\eta(\lambda)$  for the desired gas at close to standard temperature and pressure (STP). The STP constraint is to allow use of the ideal gas relation (IGR) to correct  $\eta(\lambda)$  for the small temperature deviations observed at NIF and Omega with minimal error. At STP the gases used in this work are low enough in density and temperature that small changes to the internal energy increase only the molecular kinetic energy and thus pressure, and do not contribute significantly to rotational and vibrational molecular modes or inter-molecular correlations which would cause a deviation from IGR. After  $\eta(\lambda)$  has been corrected for a given temperature it can be scaled to a given pressure using the  $P(\rho)$  relation; the relation between  $\eta$  and  $\rho$  is linear over the range of interest to this work and therefore

$$\frac{\rho}{\rho_{STP}} = \frac{\eta}{\eta_{STP}}, \quad (\text{A.11})$$

where  $\eta$  is the desired refractivity,  $\eta_{STP}$  is the known refractivity at STP,  $\rho$  is the density calculated using  $P(\rho)$  and  $\rho_{STP}$  is the density at STP; the single unknown is the desired refractivity. STP measurements of refractivity were found in the literature for CO<sub>2</sub> [150] and SF<sub>6</sub> [151] [152] [153] and were approximated with Sellmeier [154] equations to produce Figure A.2. A third gas C<sub>2</sub>F<sub>6</sub> is also used to generate Cherenkov radiation in gamma detectors; the pressure-density scaling and refractive index were generated using a slightly different approach. The linear temperature relation  $B_{C_2F_6} = 1.97 \times 10^{-6}T - 8.473667 \times 10^{-4}$  was generated using measured second virial coefficients at 290, 300 and 310 K from the literature [155]. Using this relation the density as a function of pressure can be calculated from

$$\rho_{C_2F_6} = \frac{1 \times 10^{-3}PC_{C_2F_6}}{RT + B_{C_2F_6}P}, \quad (\text{A.12})$$

where  $P$  is the pressure in psia,  $C_{C_2F_6} = 0.13801$  Kg/mol is the molar mass of  $C_2F_6$ ,  $R$  is the molar gas constant and  $B_{C_2F_6}$  is the temperature dependent second virial coefficient described previously. The refractive index as a function of wavelength was obtained from [156] and is shown in Figure A.2. With  $\eta(\lambda)$  known as a function of wavelength and pressure for all three gases the gamma threshold relation can be calculated using equation A.1 and  $\eta(P, T, \lambda = 200 \text{ nm})$ . The gamma threshold curves for  $CO_2$ ,  $SF_6$  and  $C_2F_6$  are shown in Figure A.3;  $C_2F_6$  is the best option if sensitivity to low-energy gammas is required, such as the carbon 4.4 MeV resonance.  $SF_6$  transitions to a liquid phase at a much lower pressure than  $CO_2$  and  $C_2F_6$ . In reality the choice of gas may depend on cost and COSHH restrictions applied by individual ICF facilities. At present the GCD1 at Omega is approved for use with  $CO_2$ . The GRH at Omega is approved for use with both  $CO_2$  and  $SF_6$ ; however  $SF_6$  is generally used. At NIF the four GRH detectors can be used with either  $CO_2$  or  $SF_6$ ,  $SF_6$  is chosen again for sensitivity. The next generation 'super' GCD to be initially fielded at Omega will be designed for use with all three gases and at higher pressures of up to 400 psia.

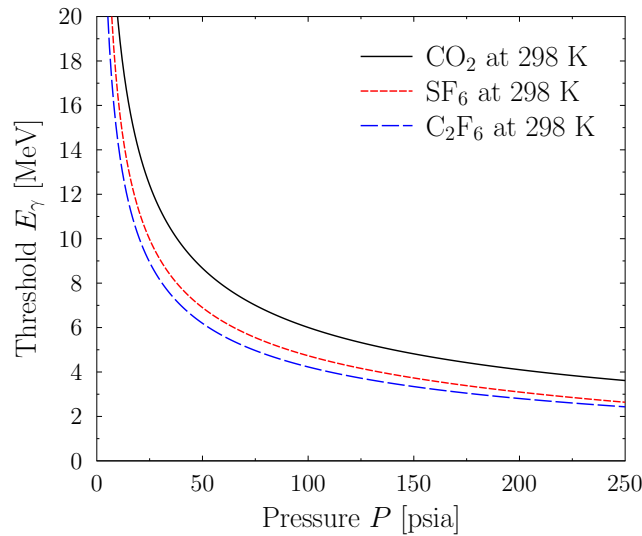


Figure A.3: Plot showing gamma energy threshold as a function of gas pressure.

As shown in Figures 1.19 and 1.20 each diagnostic has several mirrors and a

pressure window separating the high pressure gas cell from the PMT. The optical properties of each of these components will strongly impact the spectrum observed by the PMT. Cherenkov radiation itself is generated with intensity proportional to  $1/\lambda^2$ ; to calculate the spectrum seen by the PMT this shape must be folded with the wavelength-dependent reflectance and transmittance of all mirrors and pressure windows respectively. Transmission and reflection profiles for UV grade crystal sapphire  $\text{Al}_2\text{O}_3$  [157] (GRH) with AR coating and polished  $\text{SiO}_2$  [158] (GCD 1) respectively are shown in Figure A.4; general profiles from the literature have been used in this work as no direct optical measurements have been made for these components. The  $\text{SiO}_2$  input window to the PMT was omitted from calculations as any reflection/transmission effects are accounted for during measurements of the PMT quantum efficiency, which will be discussed later. Transmission reduces significantly below 200 nm for the window glasses, the air separating the pressure window and PMT; consequently any analysis involving Cherenkov radiation, including Monte Carlo modelling are truncated at 200 nm. All Cherenkov diagnostics utilise optical routing systems: GRH employs three polished-Al off-axis parabolic (OAP) mirrors and a single flat mirror, and GCD 1 polished  $\text{SiO}_2$  Cassagrainian optics; reflectance profiles for each mirror type used in the GEANT4 models are shown in Figure A.4.

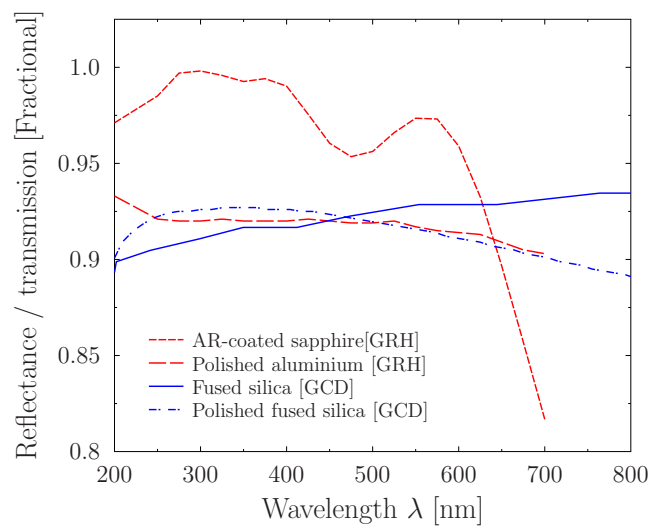


Figure A.4: Plot showing the transmission and reflection spectra used in the models of GRH and GCD 1. Dotted lines represent pressure window transmissions and solid lines mirror reflectances.

# Appendix B

## Lindhard Dielectric Function

This appendix contains a description of the Lindhard dielectric formalism of dense plasma, such as those encountered in metals. The concept of the dielectric function is introduced by considering the screening of interactions in the model electron gas [159]. Assistance was provided by D. Chapman (AWE) throughout this section.

The initial assumptions for the Lindhard dielectric function in the random phase approximation are that a free electron gas at  $T = 0$  is the medium and that interactions between electrons occur according the Coulomb potential  $V_{ee}(r) = \frac{e^2}{4\pi\epsilon_0 r}$ . The potential energy associated with interactions between particles in a dielectric medium can be described using

$$W_{ab}(1, 2) = V_{ab}(1, 2) + \sum_{cd} \int d(3, 4) V_{ac}(1, 3) \Pi_{cd}(3, 4) W_{db}(4, 2), \quad (\text{B.1})$$

where  $W_{ab}(1, 2)$  is the effective potential,  $a, b, c$  and  $d$  are species labels,  $V_{ab}(1, 2)$  is the Coulomb potential,  $d(3, 4)$  is notation used to represent the integration over dummy / internal spatial and temporal coordinate and  $\Pi_{cd}(3, 4)$  is a polarisation function. The latter characterises the density response of species 'c' due to the effective potential associated with species 'd'. In the case of the electron gas model, one has

$$W_{ee}(1, 2) = V_{ee}(1, 2) + \int_0^\infty d(3, 4) V_{ee}(1, 3) \Pi_{ee}(3, 4) W_{ee}(4, 2), \quad (\text{B.2})$$

which contains contributions from electron–electron interactions only. Performing a Fourier transform with respect to the microscopic variables  $\vec{r} = \vec{r}_1 - \vec{r}_2$  and  $\tau = \tau_1 - \tau_2$  eliminates the integral and leaves

$$W_{ee}(\vec{k}, \omega) = V_{ee}(\vec{k}) + V_{ee}(\vec{k}) \Pi_{ee}(\vec{k}, \omega) W_{ee}(\vec{k}, \omega). \quad (\text{B.3})$$

The result can then be readily manipulated to give the well-known expression

$$W_{ee}(\vec{k}, \omega) = \frac{V_{ee}(\vec{k})}{1 - V_{ee}(\vec{k}) \Pi_{ee}(\vec{k}, \omega)} \equiv \frac{V_{ee}(\vec{k})}{\varepsilon(\vec{k}, \omega)}, \quad (\text{B.4})$$

where  $\varepsilon(\vec{k}, \omega)$  is the retarded dielectric function. This result shows that the screened potential is essentially the bare Coulomb field reduced by the retarded dielectric function. The Coulomb interaction in Fourier space is given by

$$V_{ee}(\vec{k}) = \int_0^\infty e^{-i\vec{k}\cdot\vec{r}} V_{ee}(\vec{r}) d\vec{r}. \quad (\text{B.5})$$

It can be shown that this expression cannot be evaluated analytically due to the indeterminate behaviour of the sinusoid at infinity. Thus we consider writing  $V_{ee}(\vec{r}) = \lim_{\alpha \rightarrow 0} V_{ee}(\vec{r}) e^{-\alpha \vec{r}}$ . Reconstructing this equation for spherical coordinates and replacing  $V_{ee}$  with the Coulomb potential leads to

$$V_{ee}(k) = \lim_{\alpha \rightarrow 0} \frac{1}{2} \int_0^\infty r \int_0^{2\pi} e^{-\alpha r} e^{-kr \cos \theta} \frac{e^2}{\varepsilon_0} \sin \theta d\theta d\phi. \quad (\text{B.6})$$

Making the substitution  $x = -\cos\theta$  and therefore  $dx = \sin\theta d\theta$  produces

$$V_{ee}(k) = \lim_{\alpha \rightarrow 0} \frac{e^2}{2\varepsilon_0} \int_0^\infty r dr \int_{-1}^1 e^{-\alpha r} e^{ikrx} dx. \quad (\text{B.7})$$

Evaluating the  $dx$  integral and using the Euler relation  $e^{ix} = \cos x + i \sin x$  produces the result

$$V_{ee}(k) = \lim_{\alpha \rightarrow 0} \frac{e^2}{k\varepsilon_0} \int_0^\infty e^{-\alpha r} \sin kr dr. \quad (\text{B.8})$$

Evaluating the integral produces the result

$$V_{ee}(k) = \lim_{\alpha \rightarrow 0} \frac{e^2}{\varepsilon_0(k^2 + \alpha^2)} \quad (\text{B.9})$$

Taking the limit therefore yields the Fourier transform of the Coulomb potential

$$V_{ee}(k) = \frac{e^2}{\varepsilon_0 k^2} \quad (\text{B.10})$$

which is one term calculated in equation B.4 which can now be written

$$\varepsilon(\vec{k}, \omega) = 1 - \frac{e^2}{\varepsilon_0 k^2} \Pi_{ee}(\vec{k}, \omega). \quad (\text{B.11})$$

This leaves only the polarisation function  $\Pi_{ee}(\vec{k}, \omega)$  to be calculated. The polarisation function in the random phase approximation is

$$\Pi_{ee}^{RPA}(\vec{k}, \omega) = \int \frac{d\vec{k}'}{(2\pi)^3} \frac{f_e(\vec{k}' + k) - f_e(\vec{k}')}{E_e(\vec{k}' + k) - E_e(\vec{k}') + \hbar(\omega + i\eta)} \quad (\text{B.12})$$

where  $E_e(\vec{k}') = \frac{\hbar^2(\vec{k}')^2}{2m_e}$  is the kinetic energy of a free electron in the electron gas,  $F_e(\vec{k}) = \frac{1}{e^{\beta(E-\mu)} + 1}$  is the Fermi-Dirac distribution with  $\beta = 1/k_B T$  and  $\mu$  being the chemical potential.  $\hbar(\omega + i\eta)$  is the complex frequency of the density fluctuations ( $\eta \rightarrow 0$  is taken formally, in reality it yields Landau damping). As discussed earlier the assumption is that  $T = 0$  therefore the occupation function has states filled from the ground state up with no vacancies or excitations, producing  $f_e(\vec{k}) = \Theta(k - k_f)$  where  $k_f = (3\pi^2 n_e)^{1/3}$  is the Fermi wave vector with  $n_e$  being the electron number density. Combining the free electron kinetic energy with the  $T = 0$  case of the Fermi-Dirac distribution leads to an approximation to the polarisation function within the RPA

$$\Pi_{ee}^{RPA}(\vec{k}, \omega) = -\frac{3\varepsilon_0\omega_p^2}{2e^2v_f^2} [1 - g(\omega_+, k) + g(\omega_-, k)], \quad (\text{B.13})$$

where  $\omega_{\pm} = \omega \pm \frac{\hbar k^2}{2m_e}$ . Combining equations B.11 and B.13 produces the final result which is used in section 5.2.1 of this thesis. Note that the result beginning with equation B.12 and leading to B.13 was obtained from the reference; the boundary conditions for the free electron energy and electron distribution are stated in the previous paragraph for clarity and to provide insight into the limitations of the result.

# Appendix C

## Euler rotations

This short appendix section contains two schematics illustrating the steps involved with firstly calculating the scattered primary electron vector  $V'(x', y', z')$  and the required Euler rotations to transform  $V'(x', y', z')$  from the primary reference frame to the laboratory frame [160], as required by the GEANT4 Monte Carlo code. These diagrams have been created to facilitate understanding of the methodology in section 5.4.4.

Define the primary electron reference frame and generate primary scattering vector

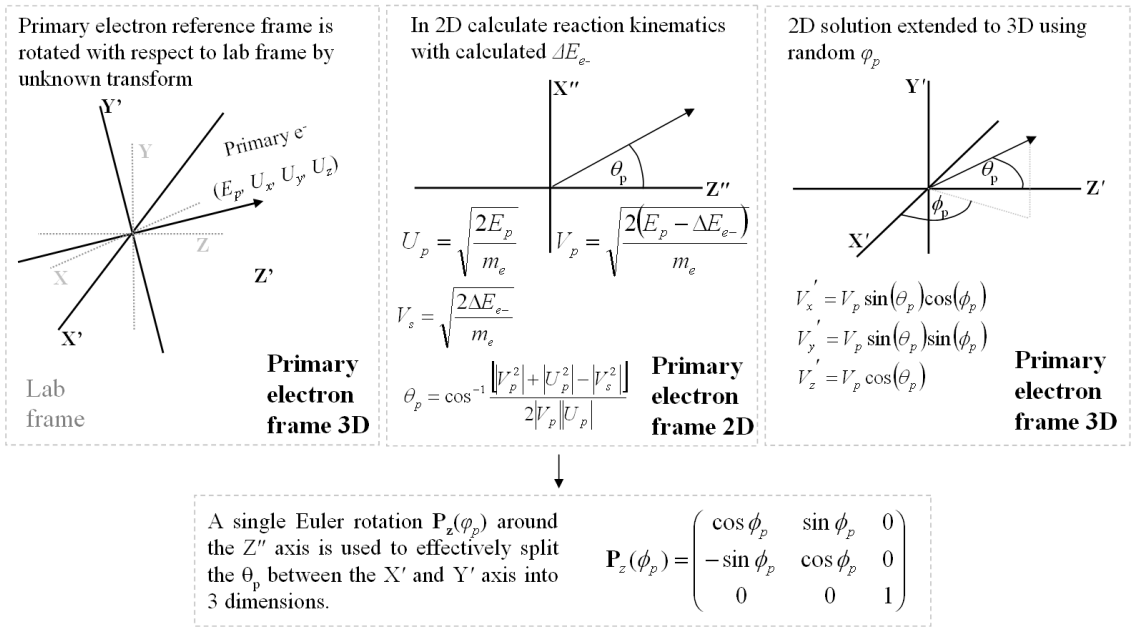
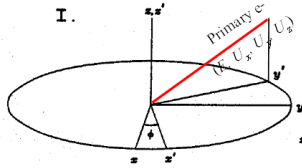


Figure C.1: Diagram illustrating the primary electron and laboratory reference frames together with the 2D and 3D stages in the calculation of the scattered primary vector  $V'(x', y', z')$  [160].

**Transform the new primary vector  $V_{x'}$ ,  $V_{y'}$  and  $V_{z'}$  from the primary electron reference frame to the laboratory frame.**

Firstly we need to rotate around the Z-axis (from X) so that the new Y' axis lies in the plane defined by the lab frame Z axis and the primary electron vector. This angle is:

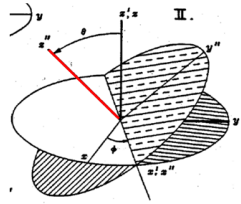
$$\phi_{euler} = -\left(\frac{\pi}{2} - \phi_e\right)$$



The full angle between  $x$  and  $y'$  is just  $\phi_e$  but we only need the difference between  $y$  and  $y'$  which is where  $\pi/2$  comes from. The negative is because we are going in the opposite direction (eventually).

Secondly we need to rotate around the X' axis such that the new Z axis points in the direction of the primary electron vector. This angle is:

$$\theta_{euler} = -(\theta_p)$$



In this diagram the previous  $z'$  axis (or  $z$  axis they are identical) is rotated around the new  $x'$  axis by  $\theta_e$  such that the new  $z''$  axis points in the direction of the primary electron. The negative is introduced because we are again going in the opposite direction.

We require the multiplication of matrices  $P_z$  and  $P_{x'}$  (below) using  $\phi_{Euler}$  and  $\theta_{Euler}$ :

$$P_z(\phi_{Euler}) = \begin{pmatrix} \cos \phi_{Euler} & \sin \phi_{Euler} & 0 \\ -\sin \phi_{Euler} & \cos \phi_{Euler} & 0 \\ 0 & 0 & 1 \end{pmatrix}$$

$$P_{x'}(\theta_{Euler}) = \begin{pmatrix} 1 & 0 & 0 \\ 0 & \cos \theta_{Euler} & \sin \theta_{Euler} \\ 0 & -\sin \theta_{Euler} & \cos \theta_{Euler} \end{pmatrix}$$

The operator for transforming the new primary vector  $V$  into the laboratory from is thus:

$$V_x = V'_x \cos(\theta_{Euler}) - V'_y \cos(\theta_{Euler}) \sin(\phi_{Euler}) + V'_z \sin(\theta_{Euler}) \sin(\phi_{Euler})$$

$$V_y = V'_x \sin(\theta_{Euler}) + V'_y \cos(\theta_{Euler}) \cos(\phi_{Euler}) - V'_z \sin(\theta_{Euler}) \cos(\phi_{Euler})$$

$$V_z = V'_y \sin(\theta_{Euler}) + V'_z \cos(\theta_{Euler})$$

Figure C.2: Diagram outlining the two steps involved with transforming the scattered primary electron vector  $V'(x', y', z')$  from the primary electron frame to  $V(x, y, z)$  in the laboratory frame [160].

# Bibliography

- [1] John D. Lindl, Robert L. McCrory, and E. Michael Campbell. Progress toward Ignition and Burn Propagation in Inertial Confinement Fusion. *Physics Today*, 45(9):3240, 1992.
- [2] S Atzeni. Laser driven inertial fusion: the physical basis of current and recently proposed ignition experiments. *Plasma Physics and Controlled Fusion*, 51(12):124029, 2009.
- [3] John D Lindl, Peter Amendt, Richard L Berger, S Gail Glendinning, Siegfried H Glenzer, Steven W Haan, Robert L Kauffman, Otto L Landen, and Laurence J Suter. The physics basis for ignition using indirect-drive targets on the national ignition facility. *Physics of Plasmas*, 11:339, 2004.
- [4] William L Kruer. Interaction of plasmas with intense lasers. *Physics of Plasmas*, 7:2270, 2000.
- [5] David H Sharp. An overview of rayleigh-taylor instability. *Physica D: Non-linear Phenomena*, 12(1):3–18, 1984.
- [6] RK Kirkwood, JD Moody, J Kline, E Dewald, S Glenzer, L Divol, P Michel, D Hinkel, R Berger, E Williams, et al. A review of laser–plasma interaction physics of indirect-drive fusion. *Plasma Physics and Controlled Fusion*, 55(10):103001, 2013.

- [7] John Lindl. Development of the indirect-drive approach to inertial confinement fusion and the target physics basis for ignition and gain. *Physics of Plasmas*, 2(11):3933–4024, 1995.
- [8] Stefano Atzeni and Jürgen Meyer-ter Vehn. *The Physics of Inertial Fusion: BeamPlasma Interaction, Hydrodynamics, Hot Dense Matter: BeamPlasma Interaction, Hydrodynamics, Hot Dense Matter*. Number 125. Oxford University Press, 2004.
- [9] VN Goncharov, JP Knauer, PW McKenty, PB Radha, TC Sangster, S Skupsky, R Betti, RL McCrory, and DD Meyerhofer. Improved performance of direct-drive inertial confinement fusion target designs with adiabat shaping using an intensity picket. *Physics of Plasmas*, 10:1906, 2003.
- [10] J. D. Anderson, C. C. Gardner, J. W. McClure, M. P. Nakada, and C. Wong. Inelastic scattering of 14-mev neutrons from carbon and beryllium. *Phys. Rev.*, 111:572–574, Jul 1958.
- [11] V. N. Goncharov, T. C. Sangster, T. R. Boehly, S. X. Hu, I. V. Igumenshchev, F. J. Marshall, R. L. McCrory, D. D. Meyerhofer, P. B. Radha, W. Seka, S. Skupsky, C. Stoeckl, D. T Casey, J. A. Frenje, and R. D. Petrasso. Demonstration of the highest deuterium-tritium areal density using multiple-picket cryogenic designs on omega. *Phys. Rev. Lett.*, 104:165001, Apr 2010.
- [12] HF Robey, BJ MacGowan, OL Landen, KN LaFortune, C Widmayer, PM Celliers, JD Moody, JS Ross, J Ralph, S LePape, et al. The effect of laser pulse shape variations on the adiabat of nif capsule implosions. *Physics of Plasmas*, 20:052707, 2013.
- [13] Paul J Wegner, Jerome M Auerbach, Thomas A Biesiada Jr, Sham N Dixit, Janice K Lawson, Joseph A Menapace, Thomas G Parham, David W Swift, Pamela K Whitman, and Wade H Williams. Nif final optics system: frequency conversion and beam conditioning. In *Society of Photo-Optical Instrumentation Engineers (SPIE) Conference Series*, volume 5341, pages 180–189, 2004.

- [14] D. T. Casey. *Diagnosing Inertial Confinement Fusion Implosions at OMEGA and the NIF Using Novel Neutron Spectrometry*. PhD thesis, Massachusetts Institute of Technology, January 2012.
- [15] JA Paisner, EM Campbell, and WJ Hogan. The national ignition facility project. *Fusion Technology*, 26(3):755–766, 1994.
- [16] B. Remington. Science and technology review. Web, August 2007.
- [17] WJ Hibbard, MD Landon, MD Vergino, FD Lee, and JA Chael. Design of the national ignition facility diagnostic instrument manipulator. *Review of Scientific Instruments*, 72(1):530–532, 2001.
- [18] JD Lindl and EI Moses. Special topic: Plans for the national ignition campaign (nic) on the national ignition facility (nif): On the threshold of initiating ignition experiments. *Physics of Plasmas*, 18(5):050901, 2011.
- [19] SW Haan, JD Lindl, DA Callahan, DS Clark, JD Salmonson, BA Hammel, LJ Atherton, RC Cook, MJ Edwards, S Glenzer, et al. Point design targets, specifications, and requirements for the 2010 ignition campaign on the national ignition facility. *Physics of Plasmas*, 18:051001, 2011.
- [20] EM Campbell, JT Hunt, ES Bliss, DR Speck, and RP Drake. Nova experimental facility. *Review of Scientific Instruments*, 57:2101, 1986.
- [21] RPJ Town, MD Rosen, PA Michel, L Divol, JD Moody, GA Kyrala, MB Schneider, JL Kline, CA Thomas, JL Milovich, et al. Analysis of the national ignition facility ignition hohlraum energetics experiments. *Physics of Plasmas*, 18:056302, 2011.
- [22] E. L. Dewald, J. L. Milovich, P. Michel, O. L. Landen, J. L. Kline, S. Glenn, O. Jones, D. H. Kalantar, A. Pak, H. F. Robey, G. A. Kyrala, L. Divol, L. R. Benedetti, J. Holder, K. Widmann, A. Moore, M. B. Schneider, T. Döppner, R. Tommasini, D. K. Bradley, P. Bell, B. Ehrlich, C. A. Thomas, M. Shaw,

- C. Widmayer, D. A. Callahan, N. B. Meezan, R. P. J. Town, A. Hamza, B. Dzenitis, A. Nikroo, K. Moreno, B. Van Wonterghem, A. J. Mackinnon, S. H. Glenzer, B. J. MacGowan, J. D. Kilkenny, M. J. Edwards, L. J. Atherton, and E. I. Moses. Early-time symmetry tuning in the presence of cross-beam energy transfer in icf experiments on the national ignition facility. *Phys. Rev. Lett.*, 111:235001, Dec 2013.
- [23] DE Hinkel, MD Rosen, EA Williams, AB Langdon, CH Still, DA Callahan, JD Moody, PA Michel, RPJ Town, RA London, et al. Stimulated raman scatter analyses of experiments conducted at the national ignition facility. *Physics of Plasmas*, 18:056312, 2011.
- [24] J. Edwards. Nif: Recent progress and future plans. NIF Management Advisory Council, December 2013.
- [25] Andy Mackinnon. Performance of high-density-carbon (hdc) ablator implosion experiments on the national ignition facility (nif). *Bulletin of the American Physical Society*, 58, 2013.
- [26] D Ho, S Haan, J Milovich, J Salmonson, G Zimmerman, L Benedict, J Biener, C Cerjan, D Clark, E Dewalds, et al. High-density carbon (hdc) ablator for ignition capsules. *Bulletin of the American Physical Society*, 58, 2013.
- [27] DC Wilson, AN Simakov, SA Yi, JL Kline, JD Salmonson, DS Clark, JL Milovich, MM Marinak, and DA Callahan. Optimizing fuel adiabat and thickness for beryllium ignition targets. *Bulletin of the American Physical Society*, 58, 2013.
- [28] RL McCrory, R Betti, TR Boehly, DT Casey, TJB Collins, RS Craxton, JA Delettrez, DH Edgell, R Epstein, JA Frenje, et al. Progress towards polar-drive ignition for the nif. *Nuclear Fusion*, 53(11):113021, 2013.
- [29] TR Boehly, DL Brown, RS Craxton, RL Keck, JP Knauer, JH Kelly, TJ Kessler, SA Kumpan, SJ Loucks, SA Letzring, et al. Initial performance

- results of the omega laser system. *Optics Communications*, 133(1):495–506, 1997.
- [30] TR Boehly, RS Craxton, TH Hinton, JH Kelly, TJ Kessler, SA Kumpan, SA Letzring, RL McCrory, SFB Morse, W Seka, et al. The upgrade to the omega laser system. *Review of Scientific Instruments*, 66:508, 1995.
- [31] Laboratory for Laser Energetics University of Rochester. *OMEGA System Operations Manual Volume 1 - System Description*. Revision A (February 2003).
- [32] Kenneth S. Krane. *Introductory Nuclear Physics*. Wiley, November 1987.
- [33] alpcentauri. Binding energy and nuclear forces. Online image, Dec 2013.
- [34] Michael Steven Rubery. An investigation into nuclear reactions using proton emission from a laser irradiated thin metal foil. Master's thesis, University of Surrey, 2008.
- [35] Y. Kim, J. M. Mack, H. W. Herrmann, C. S. Young, G. M. Hale, S. Caldwell, N. M. Hoffman, S. C. Evans, T. J. Sedillo, A. McEvoy, J. Langenbrunner, H. H. Hsu, M. A. Huff, S. Batha, C. J. Horsfield, M. S. Rubery, W. J. Garbett, W. Stoeffl, E. Grafel, L. Bernstein, J. A. Church, D. B. Sayre, M. J. Rosenberg, C. Waugh, H. G. Rinderknecht, M. Gatu Johnson, A. B. Zylstra, J. A. Frenje, D. T. Casey, R. D. Petrasso, E. Kirk Miller, V. Yu Glebov, C. Stoeckl, and T. C. Sangster. Determination of the deuterium-tritium branching ratio based on inertial confinement fusion implosions. *Phys. Rev. C*, 85:061601, Jun 2012.
- [36] J. M. Mack, S. E. Caldwell, S. C. Evans, T. J. Sedillo, D. C. Wilson, C. S. Young, C. J. Horsfield, R. L. Griffith, and R. A. Lerche. Multiplexed gas Cherenkov detector for reaction-history measurements. *Review of Scientific Instruments*, 77(10):10E728, October 2006.

- [37] DC Wilson, PA Bradley, CJ Cerjan, JD Salmonson, BK Spears, SP Hatchet II, HW Herrmann, and V Yu Glebov. Diagnosing ignition with dt reaction history). *Review of Scientific Instruments*, 79(10), 2008.
- [38] A. M. McEvoy, H. W. Herrmann, C. J. Horsfield, C. S. Young, E. K. Miller, J. M. Mack, Y. Kim, W. Stoeffl, M. Rubery, S. Evans, T. Sedillo, and Z. A. Ali. Gamma bang time analysis at OMEGA. *Review of Scientific Instruments*, 81(10):10D322, 2010.
- [39] H. W. Herrmann, S. E. Caldwell, D. Drew, S. C. Evans, V. Y. Glebov, C. J. Horsfield, J. M. Mack, G. S. Macrum, E. K. Miller, P. Sanchez, T. Sedillo, C. Stoeckl, D. C. Wilson, and C. S. Young. Improved gamma bang time measurements on Omega. *Journal of Physics: Conference Series*, 112(3):032084, 2008.
- [40] V. Yu. Glebov, C. Stoeckl, T. C. Sangster, S. Roberts, G. J. Schmid, R. A. Lerche, and M. J. Moran. Prototypes of National Ignition Facility neutron time-of-flight detectors tested on OMEGA. *Review of Scientific Instruments*, 75(10):3559–3562, 2004.
- [41] CJ Forrest, PB Radha, V Yu Glebov, VN Goncharov, JP Knauer, A Pruyne, M Romanofsky, TC Sangster, MJ Shoup, C Stoeckl, et al. High-resolution spectroscopy used to measure inertial confinement fusion neutron spectra on omega. *Review of Scientific Instruments*, 83(10):10D919, 2012.
- [42] Gary W Cooper and Carlos L Ruiz. Nif total neutron yield diagnostic. *Review of Scientific Instruments*, 72:814, 2001.
- [43] Cris W Barnes, Thomas J Murphy, and John A Oertel. High-yield neutron activation system for the national ignition facility. *Review of Scientific Instruments*, 72(1):818–821, 2001.
- [44] FH Séguin, JA Frenje, CK Li, DG Hicks, S Kurebayashi, JR Rygg, B-E Schwartz, RD Petrasso, S Roberts, JM Soures, et al. Spectrometry of charged

- particles from inertial-confinement-fusion plasmas. *Review of Scientific Instruments*, 74(2):975–995, 2003.
- [45] JA Frenje, DT Casey, CK Li, JR Rygg, FH Séguin, RD Petrasso, V Yu Glebov, DD Meyerhofer, TC Sangster, S Hatchett, et al. First measurements of the absolute neutron spectrum using the magnetic recoil spectrometer at omega. *Review of Scientific Instruments*, 79(10):10E502, 2008.
- [46] R. K. Kirkwood, T. Mccarville, D. H. Froula, B. Young, D. Bower, N. Sewall, C. Niemann, M. Schneider, J. Moody, G. Gregori, F. Holdener, M. Chrisp, B. J. MacGowan, S. H. Glenzer, and D. S. Montgomery. Calibration of initial measurements from the full aperture backscatter system on the National Ignition Facility. *Review of Scientific Instruments*, 75(10):4174–4176, 2004.
- [47] JD Moody, P Datte, K Krauter, E Bond, PA Michel, SH Glenzer, L Divol, C Niemann, L Suter, N Meezan, et al. Backscatter measurements for nif ignition targets. *Review of Scientific Instruments*, 81:10D921, 2010.
- [48] David H. Munro, Peter M. Celliers, Gilbert W. Collins, David M. Gold, Luiz B. Da Silva, Steven W. Haan, Robert C. Cauble, Bruce A. Hammel, and Warren W. Hsing. Shock timing technique for the National Ignition Facility. *Physics of Plasmas*, 8(5):2245–2250, 2001.
- [49] BJ Kaufman, S Montelongo, EW Ng, RB Robinson, TW Tunnell, PW Watts, and PG Zapata. Imaging visar diagnostic for the national ignition facility (nif). 2004.
- [50] E. L. Dewald, K. M. Campbell, R. E. Turner, J. P. Holder, O. L. Landen, S. H. Glenzer, R. L. Kauffman, L. J. Suter, M. Landon, M. Rhodes, and D. Lee. Dante soft x-ray power diagnostic for National Ignition Facility. *Review of Scientific Instruments*, 75(10):3759–3761, 2004.
- [51] John L Kline, K Widmann, A Warrick, RE Olson, CA Thomas, AS Moore, LJ Suter, O Landen, D Callahan, S Azevedo, et al. The first measurements of

- soft x-ray flux from ignition scale hohlraums at the national ignition facility using dante. *Review of Scientific Instruments*, 81(10):10E321, 2010.
- [52] J. W. McDonald, R. L. Kauffman, J. R. Celeste, M. A. Rhodes, F. D. Lee, L. J. Suter, A. P. Lee, J. M. Foster, and G. Slark. Filter-fluorescer diagnostic system for the National Ignition Facility. *Review of Scientific Instruments*, 75(10):3753–3755, 2004.
- [53] John A Oertel, Robert Aragonéz, Tom Archuleta, Cris Barnes, Larry Casper, Valerie Fatherley, Todd Heinrichs, Robert King, Doug Landers, Frank Lopez, et al. Gated x-ray detector for the national ignition facility. *Review of scientific instruments*, 77(10):10E308, 2006.
- [54] H. W. Herrmann, C. S. Young, J. M. Mack, Y. H. Kim, A. McEvoy, S. Evans, T. Sedillo, S. Batha, M. Schmitt, D. C. Wilson, J. R. Langenbrunner, R. Malone, M. I. Kaufman, B. C. Cox, B. Frogget, E. K. Miller, Z. A. Ali, T. W. Tunnell, W. Stoeffl, C. J. Horsfield, and M. Rubery. ICF gamma-ray reaction history diagnostics. *Journal of Physics: Conference Series*, 244(3):032047, 2010.
- [55] R. B. Firestone. *Table of Isotopes*. Wiley VCH, 8th edition edition, May 1996.
- [56] H. W. Herrmann, N. Hoffman, D. C. Wilson, W. Stoeffl, L. Dauffy, Y. H. Kim, A. McEvoy, C. S. Young, J. M. Mack, C. J. Horsfield, M. Rubery, E. K. Miller, and Z. A. Ali. Diagnosing inertial confinement fusion gamma ray physics (invited). *Review of Scientific Instruments*, 81(10):10D333, 2010.
- [57] C. J. Horsfield, M. S. Rubery, J. M. Mack, C. S. Young, H. W. Herrmann, S. E. Caldwell, S. C. Evans, T. J. Sedilleo, Y. H. Kim, A. McEvoy, J. S. Milnes, J. Howorth, B. Davis, P. M. O’Gara, I. Garza, E. K. Miller, W. Stoeffl, and Z. Ali. Development and characterization of sub-100 ps photomultiplier tubes. *Review of Scientific Instruments*, 81(10):10D318, 2010.

- [58] J Milnes and J Howorth. Picosecond time response characteristics of micro-channel plate pmt detectors. In *Proc. of SPIE Vol*, volume 5580, page 731, 2005.
- [59] S. Agostinelli, J. Allison, K. Amako, J. Apostolakis, H. Araujo, P. Arce, M. Asai, D. Axen, S. Banerjee, G. Barrand, F. Behner, L. Bellagamba, J. Boudreau, L. Broglia, A. Brunengo, H. Burkhardt, S. Chauvie, J. Chuma, R. Chytracsek, G. Cooperman, G. Cosmo, P. Degtyarenko, A. Dell’Acqua, G. Depaola, D. Dietrich, R. Enami, A. Feliciello, C. Ferguson, H. Fesefeldt, G. Folger, F. Foppiano, A. Forti, S. Garelli, S. Giani, R. Giannitrapani, D. Gibin, J. J. Gomez Cadenas, I. Gonzalez, G. Gracia Abril, G. Greeniaus, W. Greiner, V. Grichine, A. Grossheim, S. Guatelli, P. Gumplinger, R. Hamatsu, K. Hashimoto, H. Hasui, A. Heikkinen, A. Howard, V. Ivanchenko, A. Johnson, F. W. Jones, J. Kallenbach, N. Kanaya, M. Kawabata, Y. Kawabata, M. Kawaguti, S. Kelner, P. Kent, A. Kimura, T. Kodama, R. Kokoulin, M. Kossov, H. Kurashige, E. Lamanna, T. Lampn, V. Lara, V. Lefebvre, F. Lei, M. Liendl, W. Lockman, F. Longo, S. Magni, M. Maire, E. Medernach, K. Minamimoto, P. Mora de Freitas, Y. Morita, K. Murakami, M. Nagamatu, R. Nartallo, P. Nieminen, T. Nishimura, K. Ohtsubo, M. Okamura, S. O’Neale, Y. Oohata, K. Paech, J. Perl, A. Pfeiffer, M. G. Pia, F. Ranjard, A. Rybin, S. Sadilov, E. Di Salvo, G. Santin, T. Sasaki, N. Savvas, Y. Sawada, S. Scherer, S. Sei, V. Sirotenko, D. Smith, N. Starkov, H. Stoecker, J. Sulkimo, M. Takahata, S. Tanaka, E. Tcherniaev, E. Safai Tehrani, M. Tropeano, P. Truscott, H. Uno, L. Urban, P. Urban, M. Verderi, A. Walkden, W. Wander, H. Weber, J. P. Wellisch, T. Wenaus, D. C. Williams, D. Wright, T. Yamada, H. Yoshida, and D. Zschiesche. Geant4a simulation toolkit. *Nuclear Instruments and Methods in Physics Research Section A: Accelerators, Spectrometers, Detectors and Associated Equipment*, 506(3):250–303, 2003.
- [60] J. Allison, M. Asai, G. Barrand, M. Donszelmann, K. Minamimoto, J. Perl,

- S. Tanaka, E. Tcherniaev, and J. Tinslay. The Geant4 Visualisation System. *Computer Physics Communications*, 178(5):331–365, 2008.
- [61] GEANT Collaboration. Physics reference manual. *obtainable from the GEANT4 website: <http://geant4.cern.ch>*, 2007.
- [62] J.A. Halbleib, R.P. Kensek, G.D. Valdez, S.M. Seltzer, and M.J. Berger. ITS: the integrated TIGER series of electron/photon transport codes-Version 3.0. In *Nuclear Science Symposium and Medical Imaging Conference, 1991.*, *Conference Record of the 1991 IEEE*, page 1036 1041 vol.2, November 1991.
- [63] Brian C Franke, Ronald P Kensek, and Thomas W Laub. Its version 5.0: The integrated tiger series of coupled electron/photon monte carlo transport codes with cad geometry revision 1. *Sandia National Laboratories, Tech. Rep. SAND2004-5172*, 2005.
- [64] Walter Guber, Roger Nagel, Robert Goldstein, Phillip S Mittelman, and Malvin H Kalos. A geometric description technique suitable for computer analysis of both the nuclear and conventional vulnerability of armored military vehicles. Technical report, DTIC Document, 1968.
- [65] J Kenneth Shultis and RE Faw. An mcnp primer. *Dept. of Mechanical and Nuclear*, 2006.
- [66] LANL. A general monte carlo n-particle (mcnp) transport code. Online, Dec 2013. Produced by Monte Carlo Code Group.
- [67] C. S. Young J. Mack. Private communication, 2009.
- [68] Y. K. Wu. Performance and Capabilities of Upgraded High Intensity Gamma-Ray Source at Duke University. In *Proceedings of the 23rd Particle Accelerator Conference*, 2009.
- [69] Edward I. Moses. The National Ignition Facility (NIF): A path to fusion energy. *Energy Conversion and Management*, 49(7):1795–1802, July 2008.

- [70] R.L. McCrory, R.E. Bahr, R. Betti, T.R. Boehly, T.J.B. Collins, R.S. Craxton, J.A. Delettrez, W.R. Donaldson, R. Epstein, J. Frenje, V.Yu. Glebov, V.N. Goncharov, O.V. Gotchev, R.Q. Gram, D.R. Harding, D.G. Hicks, P.A. Jaanimagi, R.L. Keck, J.H. Kelly, J.P. Knauer, C.K. Li, S.J. Loucks, L.D. Lund, F.J. Marshall, P.W. McKenty, D.D. Meyerhofer, S.F.B. Morse, R.D. Petrasso, P.B. Radha, S.P. Regan, S. Roberts, F. Sguin, W. Seka, S. Skupsky, V.A. Smalyuk, C. Sorce, J.M. Soures, C. Stoeckl, R.P.J. Town, M.D. Wittman, B. Yaakobi, and J.D. Zuegel. OMEGA ICF experiments and preparation for direct drive ignition on NIF. *Nuclear Fusion*, 41(10):1413–1422, October 2001.
- [71] M. S. Rubery, C. J. Horsfield, H. W. Herrmann, Y. Kim, J. M. Mack, C. S. Young, S. E. Caldwell, S. C. Evans, T. J. Sedilleo, A. McEvoy, E. K. Miller, W. Stoeffl, Z. Ali, and J. Toebbe. GEANT4 simulations of Cherenkov reaction history diagnostics. *Review of Scientific Instruments*, 81(10):10D328, October 2010.
- [72] R. M. Malone, B. C. Cox, S. C. Evans, B. C. Frogget, H. W. Herrmann, M. I. Kaufman, Y. H. Kim, J. M. Mack, K. D. McGillivray, M. Palagi, W. Stoeffl, A. Tibbitts, T. W. Tunnell, and C. S. Young. Design and construction of a Gamma reaction history diagnostic for the National Ignition Facility. *Journal of Physics: Conference Series*, 244(3):032052, 2010.
- [73] R. R. Berggren, S. E. Caldwell, Jr. J. R. Faulkner, R. A. Lerche, J. M. Mack, K. J. Moy, J. A. Oertel, and C. S. Young. Gamma-ray-based fusion burn measurements. *Review of Scientific Instruments*, 72(1):873–876, 2001.
- [74] Y. Kim, J. M. Mack, H. W. Herrmann, C. S. Young, G. M. Hale, S. Caldwell, N. M. Hoffman, S. C. Evans, T. J. Sedillo, A. McEvoy, J. Langenbrunner, H. H. Hsu, M. A. Huff, S. Batha, C. J. Horsfield, M. S. Rubery, W. J. Garbett, W. Stoeffl, E. Grafil, L. Bernstein, J. A. Church, D. B. Sayre, M. J. Rosenberg, C. Waugh, H. G. Rinderknecht, M. Gatu Johnson, A. B. Zylstra, J. A. Frenje,

- D. T. Casey, R. D. Petrasso, E. Kirk Miller, V. Yu Glebov, C. Stoeckl, and T. C. Sangster. D-T gamma-to-neutron branching ratio determined from inertial confinement fusion plasmas. *Physics of Plasmas*, 19(5):056313, 2012.
- [75] Michael Rubery, Colin Horsfield, Hans Herrmann, Yongho Kim, Joe Mack, Carl Young, Scott Evans, Tom Sedillo, Kirk Miller, Wolfgang Stoeffl, et al. Geant4 supplied parameters for gamma reaction history at nif. *Bulletin of the American Physical Society*, 56, 2011.
- [76] RA Lerche and TJ Murphy. Geometry compensation for improving speed and efficiency of scintillator-based neutron time-of-flight detectors. *Review of Scientific Instruments*, 63:4880, 1992.
- [77] RA Lerche and DW Phillon. Rise time of bc-422 plastic scintillator; 20 ps. In *Nuclear Science Symposium and Medical Imaging Conference, 1991., Conference Record of the 1991 IEEE*, pages 167–170. IEEE, 1991.
- [78] Saint-Gobain Crystals. Bc-418, bc-420, bc-422 premium plastic scintillators. Online brochure, Dec 2013.
- [79] Hans W Herrmann, Joseph M Mack, Carlton S Young, Robert M Malone, Wolfgang Stoeffl, and Colin J Horsfield. Cherenkov radiation conversion and collection considerations for a gamma bang time/reaction history diagnostic for the nif. *Review of Scientific Instruments*, 79(10):10E531, 2008.
- [80] M. Goettlich. Private communication. Online discussion, October 2009.
- [81] R. Lerche. Private communication, July 2009.
- [82] V. V. Zhuk. Light collection efficiency from thin plastic scintillators, December 2005. Published by the Paul Scherrer Institute.
- [83] S. Le Pape. Private communication, September 2009.
- [84] Colin Horsfield, Michael Rubery, Herrmann Hans, Joseph Mack, Carl Young, Steven Caldwell, Evans Scott, Thomas Sedillo, Yongho Kim, Gerry Hale, et al.

- Estimates of the dt fusion gamma spectrum using an energy thresholding gas cherenkov detector. *Bulletin of the American Physical Society*, 56, 2011.
- [85] Colin Horsfield, Michael Rubery, Yong Ho Kim, Hans Herrmann, Joseph Mack, Carlton Young, Jamie Langenbrunner, Scott Evans, Thomas Sedillo, Aaron McEvoy, et al. Investigation of the dt fusion gamma spectrum with an energy thresholding gas cherenkov detector. *Bulletin of the American Physical Society*, 55, 2010.
- [86] H. Herrmann J. Church. Preliminary analysis of nif grh data. Private Communication (LLNL & LANL), September 2013.
- [87] NM Hoffman, HW Herrmann, YH Kim, HH Hsu, CJ Horsfield, MS Rubery, EK Miller, E Grafil, W Stoeffl, JA Church, et al. Measurement of areal density in the ablators of inertial-confinement-fusion capsules via detection of ablator ( $n, n'\gamma$ ) gamma-ray emission. *Physics of Plasmas*, 20:042705, 2013.
- [88] N. M. Hoffman, D. C. Wilson, H. W. Herrmann, and C. S. Young. Using gamma-ray emission to measure areal density of inertial confinement fusion capsules. *Review of Scientific Instruments*, 81(10):10D332, 2010.
- [89] MB Chadwick, P Obložinský, M Herman, NM Greene, RD McKnight, DL Smith, PG Young, RE MacFarlane, GM Hale, SC Frankle, et al. Endf/b-vii. 0: Next generation evaluated nuclear data library for nuclear science and technology. *Nuclear Data Sheets*, 107(12):2931–3060, 2006.
- [90] MS Rubery, CJ Horsfield, H Herrmann, Y Kim, JM Mack, C Young, S Evans, T Sedillo, A McEvoy, SE Caldwell, et al. Monte carlo validation experiments for the gas cherenkov detectors at the national ignition facility and omega. *Review of Scientific Instruments*, 84(7):073504, 2013.
- [91] Kim Molvig, Nelson M Hoffman, BJ Albright, Eric M Nelson, and Robert B Webster. Knudsen layer reduction of fusion reactivity. *Physical Review Letters*, 109(9):095001, 2012.

- [92] S Kerry Wilson and Patrick Delay. A method to improve cathode ray oscilloscope accuracy. *Instrumentation and Measurement, IEEE Transactions on*, 43(3):483–486, 1994.
- [93] FJ Marshall, JA Delettrez, V Yu Glebov, RPJ Town, B Yaakobi, RL Kremens, and M Cable. Direct-drive, hollow-shell implosion studies on the 60-beam, uv omega laser system. *Physics of Plasmas*, 7:1006, 2000.
- [94] C. K. Li, F. H. Séguin, J. A. Frenje, S. Kurebayashi, R. D. Petrasso, D. D. Meyerhofer, J. M. Soures, J. A. Delettrez, V. Yu. Glebov, P. B. Radha, S. P. Regan, S. Roberts, T. C. Sangster, and C. Stoeckl. Effects of fuel-shell mix upon direct-drive, spherical implosions on omega. *Phys. Rev. Lett.*, 89:165002, Sep 2002.
- [95] C Stoeckl, V Yu Glebov, DD Meyerhofer, W Seka, B Yaakobi, RPJ Town, and JD Zuegel. Hard x-ray detectors for omega and nif. *Review of Scientific Instruments*, 72:1197, 2001.
- [96] Freecad 0.13: parametric 3d modeler, September 2014.
- [97] Nelson M Hoffmann, Robert L Singleton, Hans W Herrman, Yong Ho Kim, Johan Frenje, Fredrick Seguin, Alex Zylstra, and Sean Regan. Simultaneous gamma-ray, charged-particle, and x-ray observations of capsule implosions for charged-particle stopping power measurements. Technical report, Los Alamos National Laboratory (LANL), 2011.
- [98] J . Frenje. Nuclear science using high-energy-density plasmas (hedp) – a new area of research. 11<sup>th</sup> International Conference on Nucleus-Nucleus Collisions, 2012.
- [99] H. W. Herrmann. Private communication, May 2013.
- [100] Carmen Angulo, Marcel Arnould, Marc Rayet, Pierre Descouvemont, D Baye, C Leclercq-Willain, Alain Coc, S Barhoumi, P Aguer, C Rolfs, et al. A

- compilation of charged-particle induced thermonuclear reaction rates. *Nuclear Physics A*, 656(1):3–183, 1999.
- [101] Synopsis. Lighttools, 2013.
- [102] R. M. Malone. Private communication, November 2013.
- [103] George R Labaria, Judith A Liebman, Daniel B Sayre, Hans W Herrmann, Essex J Bond, and Jennifer A Church. Multi-objective optimization for the national ignition facility’s gamma reaction history diagnostic. In *SPIE LASE*, page 86020C. International Society for Optics and Photonics, 2013.
- [104] Siegfried H Glenzer, Brian K Spears, M John Edwards, Ethan T Alger, Richard L Berger, Darren L Bleuel, David K Bradley, Joseph A Caggiano, Debra A Callahan, Carlos Castro, et al. First implosion experiments with cryogenic thermonuclear fuel on the national ignition facility. *Plasma Physics and Controlled Fusion*, 54(4):045013, 2012.
- [105] Joseph Ladislav Wiza. Microchannel plate detectors. *Nuclear Instruments and Methods*, 162(1):587–601, 1979.
- [106] Walter B Morrow Jr, John Rennie, and William Markey. Development and manufacture of the microchannel plate (mcp). Technical report, DTIC Document, 1988.
- [107] Stanford Computer Optics. Image intensifier: Photocathode. Website, December 2014.
- [108] BP Varma and C Ghosh. Some optical properties of a multialkali (s20) photocathode and the processing parameters. *Journal of Physics D: Applied Physics*, 6(5):628, 1973.
- [109] Lei Liu and Benkang Chang. Spectral matching factors between super-S25 and new S25 photo cathodes and reflective radiation of objects. *Applied optics*, 43(3):616–619, 2004.

- [110] JW Campbell. Developmental solar blind photomultipliers suitable for use in the 1450–2800 Angstrom region. *Applied Optics*, 10(6):1232–1240, 1971.
- [111] Glenn F Knoll. *Radiation detection and measurement*. John Wiley & Sons, 2010.
- [112] J.E. Yater, J.L. Shaw, K.L. Jensen, T. Feygelson, R.E. Myers, B.B. Pate, and J.E. Butler. Secondary electron amplification using single-crystal {CVD} diamond film. *Diamond and Related Materials*, 20(56):798–802, 2011.
- [113] Paul W. May. Diamond thin films: a 21st-century material. *Philosophical Transactions of the Royal Society of London. Series A:Mathematical, Physical and Engineering Sciences*, 358(1766):473495, 2000.
- [114] J. Lapington. Potential rise timsystem cvd diamond transmission dynode system. Private communication, January 2015.
- [115] KK Hamamatsu Photonics. Photomultiplier tubes: Basics and applications. *Edition 3a*, 2006.
- [116] Paul W May. Cvd diamond: a new technology for the future? *Endeavour*, 19(3):101–106, 1995.
- [117] Virgil Taillandier. *High speed imaging detectors with diamond dynode materials*. Phd thesis, Department of Physics and Astronomy, 2014.
- [118] Gerald F Dionne. Effects of secondary electron scattering on secondary emission yield curves. *Journal of Applied Physics*, 44(12):5361–5364, 1973.
- [119] Gerald F Dionne. Origin of secondary-electron-emission yield-curve parameters. *Journal of Applied Physics*, 46:3347, 1975.
- [120] A. Shih, J. Yater, C. Hor, and R. Abrams. Secondary electron emission studies. *Applied Surface Science*, 111(0):251–258, 1997.

- [121] V. V. Dvorkin, N. N. Dzbanovsky, N. V. Suetin, E. A. Poltoratsky, G. S. Rychkov, E. A. Il'ichev, and S. A. Gavrilov. Secondary electron emission from CVD diamond films. *Diamond and Related Materials*, 12(12):2208–2218, 2003.
- [122] Claude A Klein. Bandgap dependence and related features of radiation ionization energies in semiconductors. *Journal of Applied Physics*, 39(4):2029–2038, 1968.
- [123] Setsuo Ichimaru. *Statistical plasma physics*. Westview, 2004.
- [124] H. A. Bethe. Moliere's Theory of Multiple Scattering. *Phys. Rev.*, 89(6):1256–1266, March 1953.
- [125] H. Messel and D.F. Crawford. *Electronphoton Shower Distribution Function: Tables for Lead, Copper, and Air Absorbers*. Pergamon Press, 1970.
- [126] Jens Lindhard. On the properties of a gas of charged particles. *Kgl. Danske Videnskab. Selskab Mat.-Fys. Medd.*, 28, 1954.
- [127] Albert C Thompson, Douglas Vaughan, et al. *X-ray data booklet*. Lawrence Berkeley National Laboratory, University of California Berkeley, CA, 2001.
- [128] Evgenii Mikhailovich Lifshitz, Lev Petrovich Pitaevskii, and Lev Davidovich Landau. *Physical kinetics*, volume 60. Pergamon press Oxford, 1981.
- [129] JE Yater and A Shih. Secondary electron emission characteristics of single-crystal and polycrystalline diamond. *Journal of Applied Physics*, 87(11):8103–8112, 2000.
- [130] SLAC. Geant4 hypernews forum, August 2014.
- [131] David Griffiths. *Introduction to Quantum Mechanics*. Pearson Education, 2005.

- [132] Beata Ziaja, David van der Spoel, Abraham Szke, and Janos Hajdu. Auger-electron cascades in diamond and amorphous carbon. *Phys. Rev. B*, 64(21):214104, November 2001.
- [133] G. S. Painter, D. E. Ellis, and A. R. Lubinsky. *Ab Initio* Calculation of the Electronic Structure and Optical Properties of Diamond Using the Discrete Variational Method. *Phys. Rev. B*, 4:3610–3622, Nov 1971.
- [134] Yasuyuki Suzuki. *Structure and reactions of light exotic nuclei*. CRC Press, 2003.
- [135] D. A. Dimitrov, R. Busby, J. R. Cary, I. Ben-Zvi, T. Rao, J. Smedley, X. Chang, J. W. Keister, Q. Wu, and E. Muller. Multiscale three-dimensional simulations of charge gain and transport in diamond. *Journal of Applied Physics*, 108(7), 2010.
- [136] Beata Ziaja, Abraham Szke, David van der Spoel, and Janos Hajdu. Space-time evolution of electron cascades in diamond. *Phys. Rev. B*, 66(2):024116, July 2002.
- [137] P. Nozières and D. Pines. Electron Interaction in Solids. Characteristic Energy Loss Spectrum. *Phys. Rev.*, 113(5):1254–1267, March 1959.
- [138] J. C. Ashley. Energy loss rate and inelastic mean free path of low-energy electrons and positrons in condensed matter. *Journal of Electron Spectroscopy and Related Phenomena*, 50(2):323–334, 1990.
- [139] J. C. Ashley. Energy-loss probabilities for electrons, positrons, and protons in condensed matter. *Journal of Applied Physics*, 69(2):674–678, January 1991.
- [140] Beata Ziaja, Richard A. London, and Janos Hajdu. Unified model of secondary electron cascades in diamond. *Journal of Applied Physics*, 97(6):064905, March 2005.

- [141] Beata Ziaja, Richard A. London, and Janos Hajdu. Ionization by impact electrons in solids: Electron mean free path fitted over a wide energy range. *Journal of Applied Physics*, 99(3):033514, February 2006.
- [142] C. J. Powell S. Tanuma and D. R. Penn. Calculations of Electron Inelastic Mean Free Paths II. Data for 27 Elements over the 50-2000 eV Range. *Surface Interface Analysis*, 17(911), 1991.
- [143] D. A. Dimitrov. Modeling Seconda Electron Generation and Charge Transport in Diamond with VORPAL 3D. In *Tech-X, Boulder*, 2010.
- [144] Michael Dingfelder, Detlev Hantke, Mitio Inokuti, and Herwig G Paretzke. Electron inelastic-scattering cross sections in liquid water. *Radiation physics and chemistry*, 53(1):1–18, 1999.
- [145] Michael Dingfelder. Track-structure simulations for charged particles. *Health physics*, 103(5), 2012.
- [146] Arnold Shih and Charles Hor. Secondary emission properties as a function of the electron incidence angle. *Electron Devices, IEEE Transactions on*, 40(4):824–829, 1993.
- [147] Arnold Shih, Joan Yater, C Hor, and RH Abrams. Secondary electron emission properties of oxidized beryllium cfa cathodes. *Electron Devices, IEEE Transactions on*, 41(12):2448–2454, 1994.
- [148] R. Span and W. Wagner. A New Equation of State for Carbon Dioxide Covering the Fluid Region from the Triple-Point Temperature to 1100 K at Pressures up to 800 MPa. *Journal of Physical and Chemical Reference Data*, 25:1509–1596, November 1996.
- [149] C. Guder and W. Wagner. A Reference Equation of State for the Thermodynamic Properties of Sulfur Hexafluoride (SF6) for Temperatures from the Melting Line to 625 K and Pressures up to 150 MPa. *Journal of Physical and Chemical Reference Data*, 38:3394, March 2009.

- [150] Marvin J. Weber. *Handbook of Optical Materials*. CRC Press, September 2002.
- [151] D. Ityaksov, H. Linnartz, and W. Ubachs. Deep-UV Rayleigh scattering of N<sub>2</sub>, CH<sub>4</sub> and SF<sub>6</sub>. *Molecular Physics*, 106(21-23):2471–2479, 2008.
- [152] D Vukovic, G A Woolsey, and G B Scelsi. Refractivities of and at wavelengths of 632.99 and 1300 nm. *Journal of Physics D: Applied Physics*, 29(3):634–637, March 1996.
- [153] H. E. Watson and K. L. Ramaswamy. The Refractive Index Dispersion and Polarization of Gases. *Proceedings of the Royal Society of London. Series A - Mathematical and Physical Sciences*, 156(887):144–157, August 1936.
- [154] Gorachand Ghosh. *Handbook of Optical Constants of Solids, Five-Volume Set: Handbook of Optical Constants of Solids: Handbook of Thermo-Optic Coefficients of Optical Materials with Applications*. Academic Press, 1 edition, May 1998.
- [155] CM Bignell and Peter J Dunlop. Second virial coefficients for seven fluoroethanes and interaction second virial coefficients for their binary mixtures with helium and argon. *The Journal of chemical physics*, 98:4889, 1993.
- [156] R Abjean, A Bideau-Mehu, and Y Guern. Refractive index of hexafluoroethane C<sub>2</sub>F<sub>6</sub> in the 300-150 nm wavelength range. *Nuclear Instruments and Methods in Physics Research Section A: Accelerators, Spectrometers, Detectors and Associated Equipment*, 354(2):417–418, 1995.
- [157] I. S. P. Optics. *Sapphire Transmission Specification*. 2012.
- [158] I. S. P. Optics. *Fused Silica UV Grade*. 2012.
- [159] Dietrich Kremp, Thomas Bornath, Manfred Schlanges, and Wolf-Dietrich Kraeft. *Quantum statistics of nonideal plasmas*, volume 25. Springer, 2006.

- [160] George W Collins et al. The foundations of celestial mechanics. *The Foundations of Celestial Mechanics, by George W. Collins, II. Tucson, AZ, Pachart Publishing House (Pachart Astronomy and Astrophysics Series. Volume 16), 1989, 158 p., 1, 1989.*